SPECTROSCOPIC INVESTIGATIONS INTO THE ACTIVE SITE STRUCTURE AND THE MECHANISMS OF RADICAL SAM ENZYMES

by

Krista Ann Shisler

A dissertation submitted in partial fulfillment
of the requirements for the degree

of

Doctor of Philosophy

in

Biochemistry

MONTANA STATE UNIVERSITY
Bozeman, Montana

January 2016

©COPYRIGHT

by

Krista Ann Shisler

2016

All Rights Reserved

DEDICATION

For my husband Greg, son Ike, and all my family and friends who have supported me.

ACKNOWLEDGEMENTS

I would especially like to thank my Ph.D. advisor Dr. Joan Broderick for taking me under her wing and for all her valuable insights and encouragement during my graduate career. Thanks to all my past and present committee members: Dr. John Peters, Dr. Martin Lawrence, Dr. Valérie Copié, Dr. Behrad Noudoost, Dr. Richard Smith, and Dr. Robert Szilagyi. I would also like to thank all our collaborators Dr. Brian Hoffman and his colleagues Dr. Masaki Horitani, Dr. George Cutsail III, and Dr. Amy Marts. I would especially like to thank Masaki for conducting all ENDOR and RFQ experiments and helping me understand all the ENDOR results. Thanks to all the past Broderick lab members that worked on PFL-AE for they started some of the projects that I was able to refine. I would also like to thank all present Broderick lab members for their support and insights into my projects.

Thanks so much to my family and friends, especially my husband Greg and son Ike. Greg really encouraged me throughout my graduate career. Thanks for sticking with me. I want to thank my parents and my in-laws for all their support and love.

TABLE OF CONTENTS

1. INTRODUCTION 1

Fe-S Clusters in Biological Systems 1
Fe-S Cluster Function and Structure 1
Radical SAM Enzymes 3
Structural Motif of Radical SAM Enzymes 4
A Common Radical Initiation Reaction 6
Functional Diversity of Radical SAM Enzymes 8
The Radical SAM Enzyme PFL-AE 10
PFL-AE as a Model for Radical SAM Enzymes 10
Unusual Aspects of PFL-AE 12
Pyruvate Formate Lyase 14
Research Goals 15
References 19

2. GENERAL METHODS 23

Growth and Purification of PFL-AE 23
Growth and Purification of PFL 26
Protein and Iron Quantification 29
Synthesis and Purification of SAM 30
Preparation of EPR and ENDOR Samples 32
Activity Assays 33
References 37

3. MATERIALS AND METHODS 38

Spectroscopic Methods for Radical SAM Enzymes:
Fe-S Cluster Characterization 38
Electron Paramagnetic Resonance Spectroscopy 38
Theoretical Background 39
Population Difference is Key for an EPR Absorption Event 41
Electrons in Molecules 42
Anisotropy 43
Hyperfine Interactions: The Effect of Nuclear Spin 45
Advantages and Disadvantages of EPR Spectroscopy 47
Electron Nuclear Double Resonance Spectroscopy 48
What ENDOR Spectroscopy Can Detect 49
General Theory 50
Different ENDOR Spectroscopic Techniques 52
CW ENDOR. 52
Pulsed ENDOR Spectroscopy 53

TABLE OF CONTENTS – CONTINUED

Optimizing an ENDOR Experiment for Metalloproteins 55
Advantages and Disadvantages of ENDOR Spectroscopy 55
EPR and ENDOR Spectroscopic Applications for Fe-S Clusters 57
Electron Delocalization and Spin States of Fe-S Clusters 57
EPR and ENDOR Spectroscopic Considerations for Fe-S Clusters 59
Temperature and Power Effects on Fe-S Clusters 60
References 62

4. EMERGING THEMES IN RADICAL SAM CHEMISTRY 64

Contribution of Authors and Co-Authors 64
Manuscript Information Page 65
Abstract 66
Introduction 66
Structural Insights into the Radical SAM Superfamily 66
Binding Diverse Substrates with a Common Fold 66
Positioning SAM and Substrate for Catalysis 68
The SAM–Cluster Interaction and Implications for Mechanism 68
Novel Chemistry for Radical SAM Enzymes 69
Emerging Themes in Radical SAM Chemistry 71
Multiple Fe–S Clusters 71
Unexpected Cysteine Motifs 72
Reductive Cleavage of Alternate C–S Bonds of SAM 72
Concluding Remarks 72
Acknowledgements 72
References and Recommended Reading 72

5. GLYCYL RADICAL ACTIVATING ENZYMES: STRUCTURE, MECHANISM, AND SUBSTRATE INTERACTIONS 76

Contribution of Authors and Co-Authors 76
Manuscript Information Page 77
Abstract 78
Introduction 78
The Glycyl Radical Enzymes: Substrates for the GRE–AEs 78
Pyruvate Formate Lyase 80
Anaerobic Ribonucleotide Reductase 81
Benzylsuccinate Synthase 81
B_{12}-Independent Glycerol Dehydratase 82

TABLE OF CONTENTS – CONTINUED

4-Hydroxyphenylacetate Decarboxylase 82
CutC 82
PFL-AE as a Model for the GRE–AEs 82
Interaction of PFL-AE and PFL 82
Nature of the Iron–Sulfur Cluster in PFL-AE and its Interaction with SAM 83
The State of the Iron–Sulfur Cluster *In Vivo* 83
Interaction with *In Vivo* Electron Donors 83
Conclusions 84
Acknowledgments 84
References 84

6. EPR AND ENDOR ANALYSIS OF SMALL MOLECULES INDUCING VALENCE LOCALIZATION IN PFL-AE 85

Contribution of Authors and Co-Authors 85
Manuscript Information Page 86
Introduction 87
Materials and Methods 90
Materials 90
Expression of PFL-AE 90
PFL-AE Purification 91
PFL-AE Variants 92
Synthesis of [Ribose-$^{13}C_5$]-AMP 93
Preparation of EPR Samples 93
Preparation of ENDOR Samples 94
EPR and ENDOR Spectroscopy 95
Docking Studies 96
Results 97
EPR Spectroscopy of WT PFL-AE 97
EPR Spectroscopy of Variant PFL-AE 100
The PFL-AE H37A Variant 102
The PFL-AE H202A Variant 103
Additional PFL-AE Variants 105
ENDOR Spectroscopy of Isotopically Labeled Small Molecules 105
^{31}P ENDOR 106
^{13}C and ^{15}N ENDOR 107
^{1}H ENDOR 108
Docking AMP into the Active Site of PFL-AE 110
A SAM-Like Binding Model 110

TABLE OF CONTENTS – CONTINUED

A π-Cation Binding Model 111
A Rotated SAM-Like Model 113
Discussion 114
Supplementary Information 120
SI Figures 120
References 125

7. THE ACTIVATION OF THE RADICAL SAM ENZYME PYRUVATE FORMATE LYASE ACTIVATING ENZYME IS STIMULATED BY POTASSIUM 127

Contribution of Authors and Co-Authors 127
Manuscript Information Page 129
Keywords 130
Abstract 130
Introduction 131
Materials and Methods 134
Refinement of Alternative Species in the Putative Metal Site 134
Expression and Purification of PFL and PFL-AE and Generation of Variants 135
PFL-AE Activity Assays 139
EPR Sample Preparation and Spectroscopy 140
Circular Dichroism 141
Results 142
Refinement of Alternative Species in the Putative Metal Site 142
Effect of Cations on PFL-AE Activity 144
Effect of Cations on the Electronic Structure of PFL-AE 145
Altering the Cation Binding Site 147
Discussion 148
Acknowledgements 156
Figures 157
Supplementary Information 174
SI Figures 174
References 178

8. AN EPR AND ENDOR INVESTIGATION OF THE CATION SITE IN PFL-AE 181

Introduction 181

TABLE OF CONTENTS – CONTINUED

Materials and Methods 185
Materials 185
Expression and Purification of PFL-AE 185
PFL-AE Activity Assays 185
EPR and ENDOR Sample Preparation 186
Results 188
Specific Activity of PFL-AE in the Presence of K^+, Na^+, and Tl^+ 188
EPR Spectroscopy of PFL-AE in the Presence of Tl^+ 189
ENDOR Spectroscopy of the Cation Site 192
SAM Coordination Differences Observed by ENDOR Spectroscopy 194
Discussion 198
Supplementary Figures 203
References 205

9. WHY NATURE USES RADICAL SAM ENZYMES SO WIDELY: ELECTRON NUCLEAR DOUBLE RESONANCE STUDIES OF LYSINE 2,3-AMINOMUTASE SHOW THE 5′-DADO• "FREE RADICAL" IS NEVER FREE 207

Contribution of Authors and Co-Authors 207
Manuscript Information Page 209
Abstract 210
Introduction 210
Materials and Methods 212
Materials 212
Preparation of LAM 212
Preparation of anSAM 213
Preparation of ENDOR Samples 213
EPR and ENDOR Spectroscopy 213
Results 214
EPR Measurements and Analysis for Stochastic ^1H ENDOR for anAdo• Radical 214
Substrate ^{13}C ENDOR Measurements 214
Analysis of 2-^{13}C ENDOR Response 215
Pauli Spin Delocalization 215
Mims ENDOR from ^2H-Lys 216
Distance from C5′ Methyl-^{13}C Methionine of anSAM 216
Constraints on the Distances from C5′ to Other Lys Nuclei 217
Discussion 217
Structural Consequences of SAM Cleavage 217

TABLE OF CONTENTS – CONTINUED

Lessons from LAM about Coenzyme B_{12} Enzymes 218
Associated Content 219
Author Information 219
Acknowledgments 219
References 220
Supplementary Information 221

10. A RAPID FREEZE QUENCH ENDOR STUDY OF AN ORGANOMETALLIC RADICAL INTERMEDIATE IN PFL-AE 233

Contribution of Authors and Co-Authors 233
Manuscript Information Page 235
Introduction 236
Materials and Methods 238
Materials 238
Protein Growth and Purification 238
SAM Purification 239
Rapid Freeze Quench Sample Preparation 239
Static EPR Sample Preparation 243
EPR and ENDOR Analysis 243
Annealing 243
Results 244
RFQ Reveals a Unique Signal 244
Optimization of the Intermediate Signal 245
Annealing Studies Reveal Progression to the Glycyl Radical 247
ENDOR Analysis of ^{57}Fe Labeled PFL-AE 249
ENDOR Analysis of Isotopically Labeled SAM Molecules 250
Discussion 254
Supplementary Information 262
SI Figures 262
References 265

11. CONCLUSIONS 267

References 277

REFERENCES CITED 278

LIST OF TABLES

Table Page

SI 6.1. Specific activity of PFL-AE WT and variants 124

SI 6.2. Distances for SAM-like docking models of AMP 124

7.1. B-factor comparison after refinement in CNS 170

7.2. B-factor comparison after refinement in REFMAC 170

7.3. B-factor and occupancy comparison 171

7.4. Distances between sodium and nearby atoms 171

7.5. Distance between modeled potassium and nearby atoms 171

7.6. Specific activities of PFL-AE in the presence of different monovalent and divalent cations 172

7.7. Simulated g values of PFL-AE in the presence of different monovalent cations 172

7.8. Simulated g values of the PFL-AE variants D104A and D129A 173

7.9. Simulated g values of the PFL-AE variants D104A and D129A with SAM 173

9.1. Calculated distances from C5' to specific nuclei of lysine 217

9.2. Distances between C5' of SAM and target C in radical SAM enzymes 218

SI 9.1. Coupling constants for ^{2}H in labeled lysine 232

LIST OF FIGURES

Figure Page

1.1. Representative Fe-S clusters 2

1.2. Crystal structures of BioB, LAM and PFL-AE 4

1.3. SAM coordination to the [4Fe-4S] cluster 6

1.4. SAM cleavage reaction 7

1.5. Cleavage of anSAM 8

1.6. Representative radical SAM enzyme reactions 9

1.7. Mössbauer spectra of whole cells and purified PFL-AE 13

1.8. Crystal structure of PFL 14

1.9. Reaction of PFL 15

2.1. A representative chromatogram from a PFL-AE purification 25

2.2. Representative chromatogram from a PFL purification on an anion exchange column 27

2.3. Representative SDS-PAGE gels of a PFL purification 28

2.4. Representative chromatogram from a PFL purification on a hydrophobic column 29

2.5. Representative chromatogram of a SAM purification 31

2.6. The PFL-AE activity assay 34

3.1. EPR energy level diagram 40

3.2. Representative EPR signals from S = ½ systems 44

3.3. Origin of hyperfine interactions 46

LIST OF FIGURES – CONTINUED

Figure Page

3.4. ENDOR energy level diagram 50

3.5. The pulse sequence for Mims and Davies ENDOR 54

3.6. SAM coordination to the [4Fe-4S] cluster 56

3.7. Localization and delocalization patterns of Fe-S clusters 58

3.8. Delocalization of spin for a symmetric Fe^{2+}-Fe^{3+} dimer 59

4.1. Reductive cleavage of SAM 67

4.2. Crystal structures of radical SAM enzymes 67

4.3. Representative radical SAM reactions 70

4.4. Proposed biosynthesis pathway for HydA 71

5.1. SAM coordinated to the [4Fe-4S] cluster 79

5.2. SAM cleavage reactions 79

5.3. Crystal structure of PFL-AE 79

5.4. Mechanism for activation of GREs 80

5.5. Crystal structures of GREs 80

5.6. Active site of PFL 80

5.7. Reactions catalyzed by GREs 81

6.1. Reductive cleavage of SAM and the activation of PFL 88

6.2. Representations of a valence delocalized and localized $[4Fe\text{-}4S]^{2+}$ cluster 89

6.3. EPR spectra of PFL-AE in the presence of small molecules that induce valence localization 98

LIST OF FIGURES – CONTINUED

Figure Page

6.4. EPR spectra of PFL-AE in the presence of small molecules that do not induce valence localization 100

6.5. PFL-AE active site with amino acids involved in SAM binding.....101

6.6. EPR spectra of the H37A PFL-AE variant in the presence of small molecules 103

6.7. EPR spectra of the H202A PFL-AE variant in the presence of small molecules 104

6.8. Isotopically labeled AMP and Ado molecules.....106

6.9. Mims 13C ENDOR spectra of labeled AMP and adenosine 108

6.10. ^{1}H ENDOR spectra of PFL-AE prepared in $^{2}H_2O$ and $^{1}H_2O$ 109

6.11. SAM-like docking of AMP into the active site of PFL-AE.....111

6.12. The π-cation docking model of AMP 112

6.13. Rotated SAM-like docking model of AMP 114

6.14. AMP docking into NosL.....118

SI 6.1. EPR spectra of PFL-AE in the presence of small molecules and different monovalent cations.....120

SI 6.2. EPR spectra comparing native PFL-AE and the PFL-AE variants H37A and H202A.....121

SI 6.3. EPR spectra of the PFL-AE variants Y201A, R166A, and D104A 122

SI 6.4. Mims ^{15}N and ^{31}P ENDOR spectra of labeled AMP.....123

LIST OF FIGURES – CONTINUED

Figure Page

7.1. Crystal structure of PFL-AE with cation bound 157

7.2. The PFL crystal structure 158

7.3. Putative metal site with sodium modeled 159

7.4. Refinement of different ions/molecules in the putative metal site 160

7.5. PFL-AE specific activity in different cations 161

7.6. The effect of [K^+] on PFL-AE activity 162

7.7. EPR spectra of PFL-AE in the presence of different monovalent cations and SAM 163

7.8. CD spectra of PFL-AE in the presence of monovalent cations and SAM 164

7.9. CD spectra of PFL-AE in the presence of varying KCl concentrations 165

7.10. EPR spectra of the PFL-AE variant D104A 166

7.11. EPR spectra of the PFL-AE variant D129A 167

7.12. Surface representation of the PFL-AE active site 168

7.13. Sequence alignment of PFL-AE and other radical SAM enzymes 169

SI 7.1. EPR spectra of PFL-AE in the presence of monovalent cations 174

SI 7.2. EPR spectra of PFL-AE in the presence of divalent cations 175

SI 7.3. EPR spectra of PFL-AE in the presence of divalent cations and SAM 176

LIST OF FIGURES – CONTINUED

Figure Page

SI 7.4. CD spectra of PFL-AE in the presence of monovalent cations 177

8.1. Cation site in PFL-AE....183

8.2. Specific activity of PFL-AE in the presence of K^+, Na^+, and Tl^+ 188

8.3. EPR spectra of PFL-AE in the presence of K^+, Na^+, and Tl^+ 190

8.4. X-band and Q-band EPR spectra of PFL-AE in the presence of Tl^+ and SAM 191

8.5. Mims $^{203}Tl/^{205}Tl$ ENDOR spectra....193

8.6. Mims ^{23}Na ENDOR spectra....194

8.7. Methionine bidentate ring structure of SAM bound to the [4Fe-4S] cluster....195

8.8. Davies ^{14}N ENDOR spectra of SAM bound to PFL-AE 196

8.9. Mims ^{13}C ENDOR spectra of methyl-13C-SAM bound to PFL-AE in the presence of K^+, Na^+, and Tl^+ 198

8.10. Superposition of the PFL-AE structures to show disordered SAM interactions with the cation....201

SI 8.1. Splitting values in the X-band and Q-band EPR spectrum 203

SI 8.2. Comparison of the ENDOR spectra of PFL-AE in the presence of K^+ and Na^+ 204

9.1. Steps in the reaction catalyzed by LAM 211

9.2. Active site structure of LAM and EAL....212

LIST OF FIGURES – CONTINUED

Figure Page

9.3. Davies ^{13}C ENDOR spectra of LAM with anSAM and labeled lysine 214

9.4. Calculated distances from anAdo• to lysine atoms.....215

9.5. ^{2}H Mims ENDOR spectra of LAM with anSAM and labeled lysine 216

9.6. ^{13}C Mims ENDOR spectra of LAM with labeled anSAM.....217

9.7. Inferred motion of 5'-dAdo• post cleavage 218

SI.9.1. EPR and ^{1}H ENDOR spectra of LAM with anSAM and lysine 222

SI.9.2. ^{13}C Davies ENDOR spectra of LAM, anSAM, and lysine.....223

SI.9.3. ^{13}C Mims ENDOR simulation.....224

SI.9.4. ^{13}C Mims ENDOR simulation of [1,2-^{13}C]-Lys.....225

SI.9.5. ^{13}C Davies ENDOR (small range) spectra 225

SI.9.6. PESTRE technique for LAM with [U-^{13}C]-Lys.....226

SI.9.7. ^{13}C Mims ENDOR simulation of [^{13}C-methyl]-anSAM 227

SI.9.8. ^{15}N Mims ENDOR simulation 228

SI.9.9. ^{15}N Mims ENDOR simulation of [2-^{15}N]-Lys 229

SI9.10. Illustration of the constraint within the LAM active site 230

SI.9.11. Electron density map of LAM active site.....231

LIST OF FIGURES – CONTINUED

Figure Page

10.1. Reductive cleavage of SAM 236

10.2. Activation of PFL by PFL-AE 237

10.3. EPR spectra of 500 ms quench in comparison to PFL-AE with SAM and the gly radical 245

10.4. Comparison of the intermediate signal with SAM and anSAM 247

10.5. Annealing studies of the 500 ms quench 248

10.6. EPR and ENDOR spectra of the 500 ms quench with ^{57}Fe labeled PFL-AE 249

10.7. Isotopically labeled SAM molecules 250

10.8. EPR spectra of the 500 ms quench with different isotopically labeled SAM molecules 251

10.9. ^{13}C ENDOR spectrum of the 500 ms quenched sample with [U-$^{13}C_{10}$,$^{15}N_5$-adeonsine]-SAM 252

10.10. Carbon based radicals 253

10.11. Mims ^{13}C ENDOR spectra of the 500 ms quench sample with labeled SAM 254

10.12. Timeline of observed paramagnetic species in PFL-AE 255

10.13. Proposed intermediate in PFL-AE 256

10.14. Proposed intermediates in IspH and IspG 257

10.15. A proposed mechanism for intermediate production 259

10.16. A second proposed mechanism for the intermediate production 260

LIST OF FIGURES – CONTINUED

Figure Page

SI 10.1. EPR spectra of different quench times 262

SI 10.2. Comparison of the 500 ms quenched and the empty cavity 263

SI 10.3. EPR power saturation and temperature dependence of the intermediate signal 263

SI 10.4. 500 ms quench with PFL variants 264

LIST OF SCHEMES

Scheme Page

9.1. SAM cleavage reaction 210

9.2. Reaction catalyzed by LAM 211

9.3. anSAM cleavage reaction 212

LIST OF CHARTS

Chart Page

9.1. Isotopically ^{13}C labeled lysine molecules 214

9.2. Isotopically ^{2}H labeled lysine molecules 216

LIST OF ABBREVIATIONS

ADP – adenosine 5’-diphosphate
AMP – adenosine 5’monophosphate
anAdo• – 5’-deoxy-3’,4’-anhydroadenosine-5’-yl radical
anSAM – *S*-3’,4’-anhydroadenosyl-L-methionine
AdoCbl – adenosylcobalamin
ATP – adenosine 5’-triphosphate
dAdo or 5’-dAdo – 5’-deoxyadenosine
dAdo• or 5’-dAdo• – 5’-deoxyadenosyl radical
ENDOR – electron nuclear double resonance
EPR – electron paramagnetic resonance
LAM – lysine 2,3-aminomutase
MTA – 5′-deoxy-5′-(methylthio)adenosine
PFL – pyruvate formate lyase
PFL-AE – pyruvate formate lyase activating enzyme
RFQ – rapid freeze quench
SAM – *S*-adenosyl-L-methionine
TIM – triosephosphate isomerase

ABSTRACT

The radical *S*-adenosyl-L-methionine (SAM) superfamily of enzymes carry out diverse and complex reactions through generation of a 5'-deoxyadenosyl (5'-dAdo•) radical followed by transfer to substrate. These enzymes contain a [4Fe-4S] cluster which binds and transfers an electron to SAM. The exact mechanism of 5'-dAdo• generation is unknown and the studies herein provide further investigation into pyruvate formate lyase activating enzyme (PFL-AE) and lysine 2,3-aminomutase (LAM) pre and post SAM cleavage.

To understand the active site of PFL-AE prior to SAM cleavage, cation and small molecule effects were examined by electron paramagnetic resonance (EPR) and electron nuclear double resonance (ENDOR) spectroscopies. Previously, PFL-AE had been observed to contain a valence localized cluster in the presence of small molecules and this work used EPR and ENDOR spectroscopy to further probe the effects of these molecules. These studies determined that these molecules do not directly bind the cluster but rather an H_xO species occupies the unique Fe site. The crystal structure of PFL-AE revealed a cation site and to probe this site, EPR and ENDOR spectroscopies were employed. Monovalent cations stimulated PFL-AE activity, with the greatest activity in the presence of potassium. The identity of the cation perturbed the EPR signal of PFL-AE which was more pronounced in the presence of SAM. ENDOR spectroscopy determined that SAM coordination differed depending on the monovalent cation.

Due to its high reactivity, 5'-dAdo• has never been spectroscopically observed. In order to examine any intermediate states, a SAM analog and rapid freeze quench (RFQ) techniques were employed in conjunction with EPR and ENDOR spectroscopies. LAM can cleave the SAM analog, *S*-3',4'-anhydroadenosyl-L-methionine, to produce a stable allylic radical which was coupled with isotopically labeled lysine for ENDOR analysis. It was determined that radical generation is highly controlled with little movement towards its substrate upon 5'-dAdo• production. During RFQ techniques on PFL-AE, an organometallic intermediate species was observed. To probe this intermediate, isotopically labeled SAM and an ^{57}Fe labeled cluster were coupled with the unknown paramagnetic species. It was determined that this intermediate was an unprecedented organometallic Fe-adenosyl bound species post SAM cleavage.

CHAPTER 1

INTRODUCTION

Fe-S Clusters in Biological Systems

Iron is the fourth most abundant element in the earth's crust [1], and as such, has made its way into many diverse roles in biology. One major and ancient use for iron is formation of Fe-S clusters which are composed of iron and inorganic sulfide and are some of the most functionally versatile and ubiquitous prosthetic groups in proteins [2]. Fe-S clusters were first characterized in the 1960's in ferredoxins for electron transfer and the since then, the discovery of Fe-S clusters in other biological systems has expanded into a vast array of biological functions.

Fe-S Cluster Function and Structure

The basic structure of Fe-S clusters is the Fe_2S_2 rhomb which can be combined to form [2Fe-2S], [4Fe-4S], [3Fe-4S] clusters (Figure 1.1) and even more complex structures. The Fe_2S_2 rhombs can be considered the building blocks of assembly: for example, the cubane [4Fe-4S] clusters can be assembled from two [2Fe-2S] units whereas the [3Fe-4S] clusters are formed from the loss of one Fe from the [4Fe-4S] cluster. These prosthetic groups are ligated to the protein generally through cysteine side chains to complete a tetrahedral sulfur coordination at each iron site. Other residues, such as histidine, and to a lesser extent glutamine, serine, arginine, or even aspartate have also been found to ligate clusters to proteins [3-5]. Fe-S cluster containing proteins range

in size from 6 kDa to over 500 kDa, have been found to contain up to 9 clusters, and are present in a vast array of cellular functions and cellular compartments [4]. The Fe-S clusters themselves are intrinsically oxygen-sensitive but the extent of this oxygen sensitivity is dependent on the protein and their polypeptide matrix.

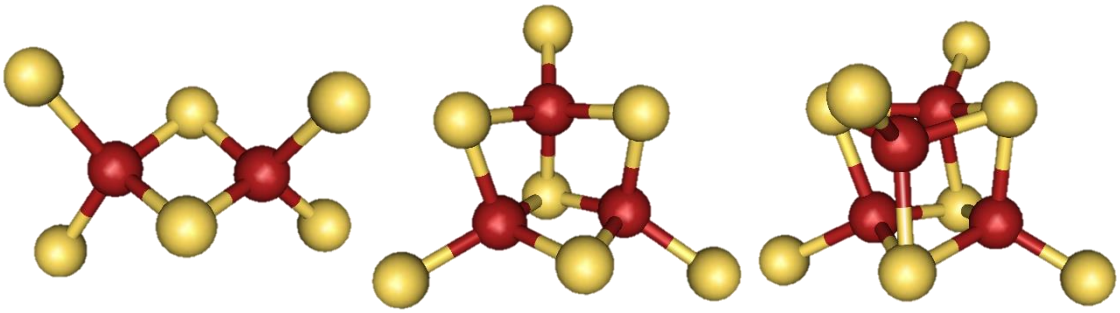


Figure 1.1. Representative Fe-S clusters with a [2Fe-2S] cluster on the left, a [3Fe-4S] cluster in the middle, and a [4Fe-4S] on the right. Each Fe is ligated by an inorganic sulfur and a protein cysteine.

Aside from electron transfer, Fe-S clusters have versatile functions in metalloproteins which include substrate binding and activation, Fe or cluster storage, regulation of gene expression, structural roles, enzyme regulation, and sulfur donation, just to name a few [3-5]. In these metalloenzymes, the cluster structure can vary from [2Fe-2S] clusters to the more complex clusters such as the H-cluster of hydrogenase [6].

The flexibility of electron transfer of Fe-S clusters stems from their ability to delocalize the electron density over all the iron atoms of the cluster. The surrounding protein environment influences the redox potentials of the Fe-S cluster, allowing for electron carrier proteins to operate over a wide range of oxidation-reduction potentials [5,7]. Remarkably, the reduction potentials for Fe-S clusters spans a range of approximately -700 mV to 400 mV due to the versatility of the protein environment [2,4].

The primary mode of Fe-S cluster assembly are the Isc (iron sulfur cluster) and Suf pathways which function under normal and oxidative stress conditions, respectively [5,8,9]. The Nif pathway is also required for the FeMo-cofactor biosynthesis in nitrogenase [5]. These pathways contain multiple proteins for the delivery of inorganic sulfide, the assembly of the clusters, and delivery of the complete clusters. Sulfide is generated through the activity of a cysteine desulfurase enzyme (NifS, IscS, or SufS) and pyridoxal phosphate containing enzymes. These enzymes utilize cysteine as a substrate and deliver the inorganic sulfide via a protein-bound persulfide to a scaffold protein (NifU, IscU, or SufU) where Fe-S cluster assembly occurs. SufA and SufB (in a SufBCD complex) can also serve as a scaffolds and/or carriers in the Suf pathway [9-12]. The Isc machinery also includes the chaperone proteins HscA ATPase and HscB to facilitate cluster transfer from IscU to the target protein [9,13]. The actual mode of sulfide and iron transfer to these assembly proteins is still under debate but it is believed that the cluster is fully assembled and transferred to its target protein [9].

Radical SAM Enzymes

One of the largest superfamily of enzymes is the radical *S*-adenosyl-L-methionine (SAM) enzymes that are found in all kingdoms of life and catalyze a diverse set of reactions [14]. They contain a [4Fe-4S] cluster which binds SAM and directs electron transfer for radical generation on substrate. They perform similar radical chemistry as the adenosylcobalamin (AdoCbl) dependent enzymes which initiate difficult transfer of unreactive hydrogen atoms through the production of a highly reactive

5’-deoxyadenosinyl radical (5’-dAdo•) by homolytic cleavage of the Co-C5’ bond of the AdoCbl cofactor [15,16]. Radical SAM enzymes, on the other hand, carry out more diverse reactions through homolytic cleavage of the much simpler cofactor SAM [15,17].

Structural Motif of Radical SAM Enzymes

Radical SAM enzymes all contain a similar fold, either a partial $(\alpha/\beta)_6$ triosephophate isomerase (TIM) in most cases or full $(\alpha/\beta)_8$ TIM barrel in other cases [14,18]. This core domain is highly conserved in radical SAM enzymes. The [4Fe-4S] cluster is housed at the base of the TIM barrel (Figure 1.2) and is ligated to the protein in a tri-cysteine $CX_3CX\Phi C$ motif where Φ is an aromatic residue and X is any residue [18,19]. Variations of this motif have been found in other radical SAM enzymes such as

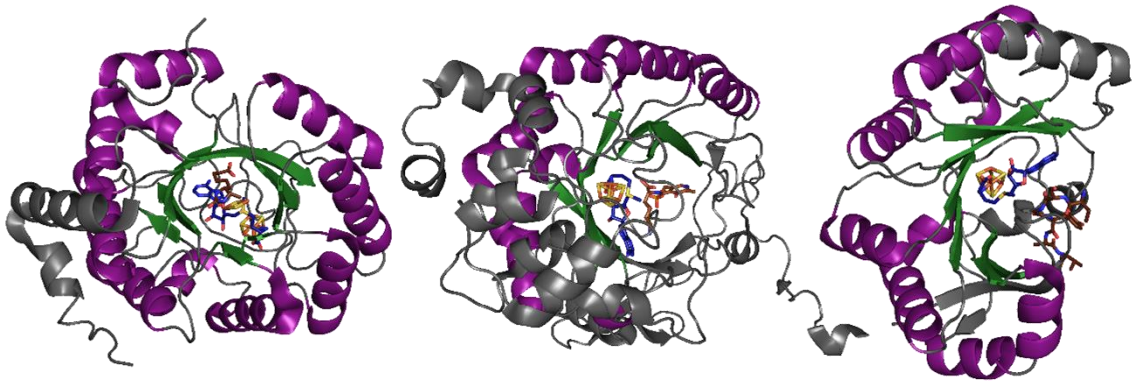


Figure 1.2. The radial SAM enzymes BioB (left), LAM (middle) and PFL-AE (right). The α-helixes (purple) and β-strands (green) that comprise the partial $(\alpha/\beta)_6$ (PFL-AE and LAM) or the full $(\alpha/\beta)_8$ TIM barrel are highlighted for each structure. SAM (blue carbons) and substrates (brown carbons), or the 7-mer peptide in the case of PFL-AE, increase from left to right coinciding with an increase of barrel size from left to right.

ThiC and HmdB which contain CX_2CX_4C and CX_5CX_2C motifs, respectively [20,21].

In the structurally solved radical SAM enzymes, the protein overall size and TIM

barrel type reflects the magnitude of substrate [18,22]: larger substrates coincide with a smaller protein and a partial TIM barrel that is more splayed such as in the case of the smallest crystallized enzyme pyruvate formate lyase activating enzyme (PFL-AE) (Figure 1.2) whose substrate is a large homodimeric protein [23]. Smaller substrates correlate with enzymes that contain either a more enclosed barrel or a full TIM barrel. Biotin synthase (BioB), whose substrate is the small molecule biotin, contains a full TIM barrel (Figure 1.2) [24]. Barrel size is thought to protect the highly reactive radicals produced during catalysis. Additional protein elements in the C-terminal region and sometimes the N-terminal region, another molecule, or substrate can contribute to blocking or plugging the active site [18].

In addition to the common fold of radical SAM enzymes, SAM coordinates the cluster similarly in all characterized radical SAM enzymes [14,18]. Since the cluster is only bound to the protein via three cysteines, a unique iron is available to bind SAM through its amino and carboxyl groups (Figure 1.3) which was first characterized through electron nuclear double resonance (ENDOR) techniques on the radical SAM enzyme PFL-AE [25]. This binding of SAM was later verified in the crystal structures of radical SAM enzymes. Since SAM binds across the top of the TIM barrel in the loop regions between β-strands, it is difficult to identify specifically conserved residues, or SAM binding motifs, that are consistent with all radical SAM enzymes. A glycine-rich region, a GGE motif, has been identified as a SAM binding motif which hydrogen bonds with the amino group of the methionine portion of SAM while a GxIxGxxE motif is utilized for adenine coordination [26]. Each radical SAM enzymes seems to contain a unique SAM

coordination system which may reflect the diversity of the substrates and how SAM must abstract a hydrogen atom from these vastly different substrates in this large superfamily of enzymes.

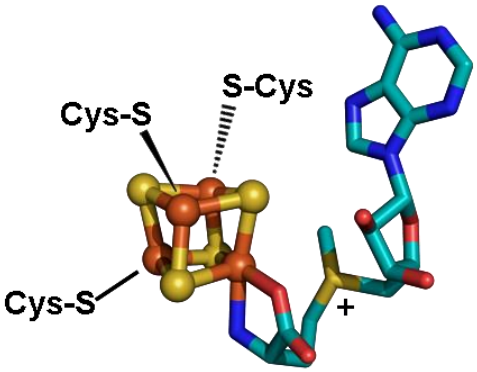


Figure 1.3. SAM coordination to the [4Fe-4S] cluster in radical SAM enzymes.

A Common Radical Initiation Reaction

Radical SAM enzymes initiate catalysis using a proposed common mechanism. SAM is bound through its amino and carboxyl moieties to a unique Fe of a [4Fe-4S] cluster. The $[4Fe\text{-}4S]^{2+}$ cluster is reduced to the $[4Fe\text{-}4S]^{+}$ state via an external source, such as flavodoxin *in vivo*. Inner sphere electron transfer from the cluster to SAM promotes homolytic cleavage of the S-C5' bond of SAM, producing methionine and a highly reactive 5'-deoxyadenosyl radical (5'-dAdo•). This radical can then abstract a hydrogen atom from substrate to form a substrate radical and 5'-deoxyadenosine (5'-dAdoH) [15]. This substrate radical can then undergo other radical-mediated reactions. The SAM molecule can either be utilized as a cofactor where SAM is regenerated or as a co-substrate. When SAM acts a co-substrate, SAM is used catalytically and methionine and 5'-dAdoH must leave the active site and a new SAM

molecule must enter for another round of catalysis (Figure 1.4). When SAM acts as a cofactor, on the other hand, the substrate radical re-abstracts a H-atom from 5'-dAdoH to produce the 5'-dAdo• radical which subsequently combines with methionine to form SAM and the electron is donated back to the cluster (Figure 1.4). The majority of the radical SAM enzymes characterized

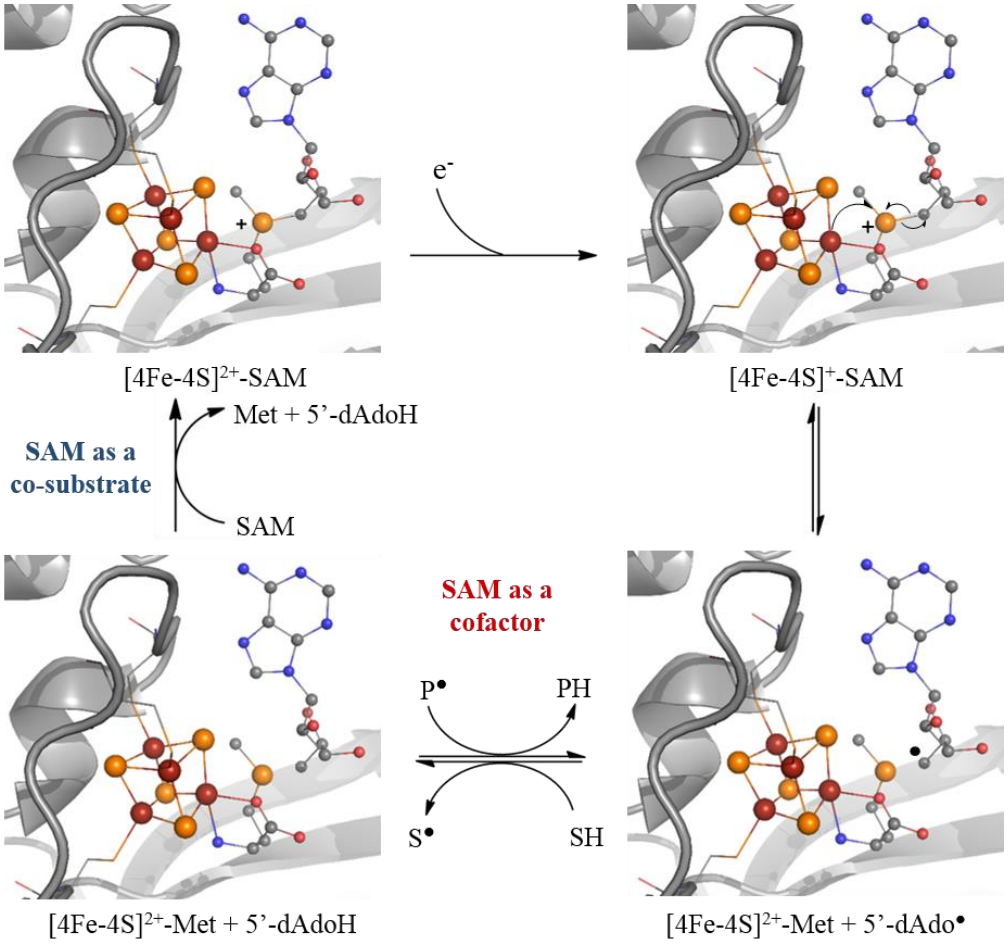


Figure 1.4. SAM cleavage by radical SAM enzymes. The reaction is initiated by SAM binding to the $[4Fe\text{-}4S]^{2+}$ cluster and reduction to the $[4Fe\text{-}4S]^{+}$ cluster. SAM is homolytically cleaved to produce the 5'-dAdo• radical and cluster bound methionine. When SAM is a co-substrate, the substrate radical (S•) is formed and 5'-dAdoH and methionine leave the active site, allowing a new SAM molecule to bind. In the cofactor case, the product radical (P•) abstracts a hydrogen from 5'-dAdoH, producing 5'-dAdo• which recombines with methionine to from SAM (modified from [22]).

thus far utilize SAM as a co-substrate with only a few known cases as a cofactor [22].

Currently, the 5'-dAdo• radical intermediate has never been observed but a stabilized allylic radical with the use of a SAM analogue has been spectroscopically analyzed. The radical SAM enzyme, lysine 2,3-aminomutase (LAM), is able to homolytically cleave the SAM analogue *S*-3',4'-anhydroadenosylmethionine (anSAM) to produce the stable 5'-deoxy-3',4'-anhydroadenosine-5'-yl (anAdo•) radical (Figure 1.5) [27,28]. LAM can turnover α-lysine to β-lysine with anSAM, albeit with only ~0.25% activity of that observed in the presence of SAM, showing that the 5'-dAdo• radical is an intermediate in radical SAM catalysis [27,28].

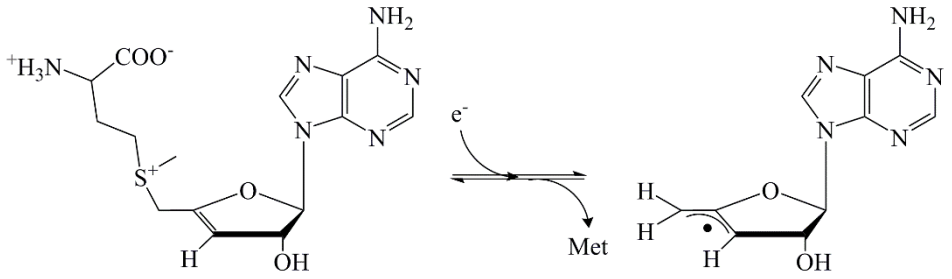


Figure 1.5. Reaction of *S*-3',4'-anhydroadenosylmethionine (anSAM) to the stable 5'-deoxy-3',4'-anhydroadenosine-5'-yl (anAdo•) radical and methionine.

Functional Diversity of Radical SAM Enzymes

Even though all radical SAM enzymes initiate catalysis through radical generation of 5'-dAdo•, the substrates and products vary greatly between enzymes. A few examples of the different reactions are shown in Figure 1.6 which include activating a substrate protein through H-atom abstraction, isomerization, sulfur insertion, cofactor biosynthesis, antibiotic synthesis, and post-translational and post-transcriptional modifications.

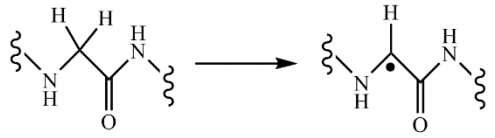
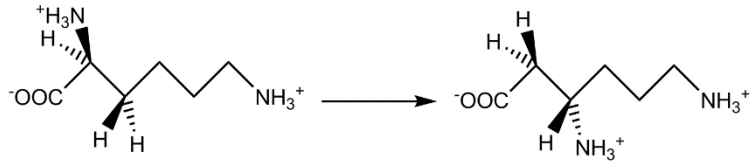
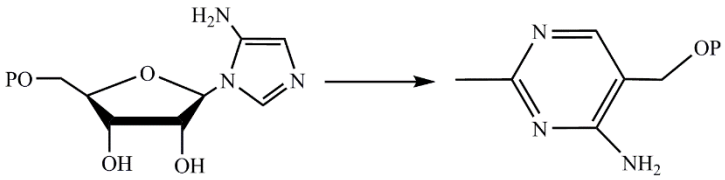
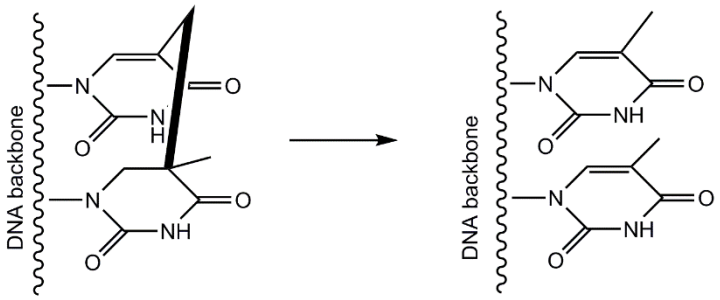
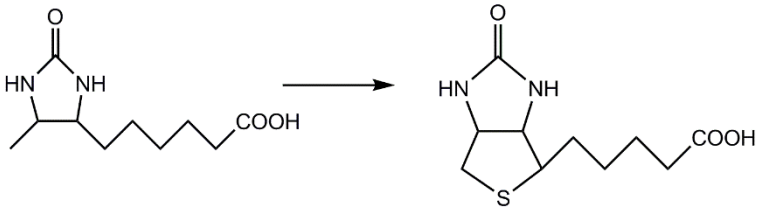
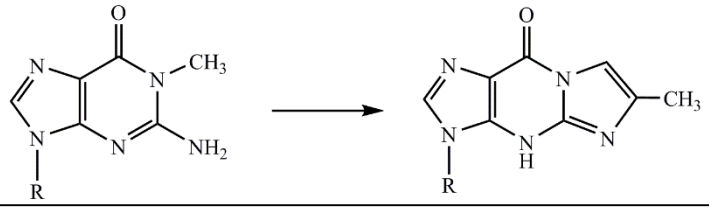
Enzyme	Reaction Catalyzed	Role of SAM
Activating enzymes		Co-substrate
LAM		Cofactor
ThiC		Co-substrate
SPL		Cofactor
BioB		Co-substrate
TWY1		Co-substrate

Figure 1.6. Representative radical SAM enzyme reactions and the role of SAM as a co-substrate or cofactor in each enzyme.

As mention above, radical SAM enzymes all contain the same TIM barrel domain, but what gives them this ability to carry out such diverse reactions is the

versatility of the 5'-dAdo• radical which can abstract a hydrogen from almost any substrate.

The Radical SAM Enzyme PFL-AE

Pyruvate formate lyase activating enzyme (PFL-AE) (Figure 1.2) is the one of the most highly characterized radical SAM enzymes. It belongs to a group of radical SAM enzymes known as the glycyl radical enzyme activating enzymes (GRE-AE) whose substrates are glycyl radical enzymes (GRE). GRE-AE utilize 5'-dAdo• to abstract a hydrogen from a GRE, activating its respective GRE. PFL-AE activates the homodimeric GRE protein pyruvate formate lyase (PFL) through abstraction of the pro-*S* hydrogen on a glycine residue (G734) [29].

PFL-AE as a Model for Radical SAM Enzymes

PFL-AE was first discovered as an unknown activase of PFL that required iron, SAM and a reductant [30,31]. PFL-AE was later found to introduce an unprecedented organic free radical localized on a PFL residue [16]. A sequence analysis later revealed three cysteine residues that were thought to be significant for the Fe-binding property of the enzyme: the conical CX_3CX_2C [4Fe-4S] cluster binding motif [32]. Initial UV-vis spectroscopic analysis revealed that PFL-AE contains an Fe-S cluster and, upon further analysis with Resonance Raman, electron paramagnetic resonance (EPR), and Mössbauer spectroscopies, revealed that as-isolated protein contained a mixture of $[2Fe\text{-}2S]^{2+}$, $[3Fe\text{-}3S]^{+}$, and $[4Fe\text{-}4S]^{2+}$ clusters which could be reduced to a $[4Fe\text{-}4S]^{+}$ cluster upon

dithionite reduction [33-35]. Later, using EPR techniques, it was discovered that the $[4Fe\text{-}4S]^{+}$ cluster is the active state of the enzyme and that the cluster is oxidized to the $[4Fe\text{-}4S]^{2+}$ state concomitant with substrate turnover [36].

Since PFL-AE only contains three cysteines in the cluster binding motif, it was proposed that a unique, site-differentiated Fe was present similar to the enzyme aconitase which also contains a site-differentiated Fe site. Analysis of the radical SAM enzyme lysine 2,-3 aminomutase (LAM) showed that there indeed is a labile Fe site and the cluster converts to a [3Fe-4S] cluster upon oxygen exposure but could convert back to the [4Fe-4S] state once anaerobic and mild reducing conditions were implemented [37]. Using these results, Broderick and coworkers were able to utilize Mössbauer spectroscopy and strategic ^{57}Fe labeling of the unique Fe site to determine that this unique Fe site binds SAM [38]. SAM binding to the cluster wasn't resolved until electron nuclear double resonance (ENDOR) was conducted on PFL-AE. In ENDOR, a paramagnetic species is coupled to an NMR active nuclei (such as ^{13}C, ^{15}N, or ^{14}N) to analyze how these two sites are interacting. A reduced cluster was coupled with different isotopically labeled SAM molecules, namely ^{17}O and ^{13}C-labling in the carboxyl group and ^{15}N in the amino group of methionine, and revealed that SAM binds the unique Fe via the amino and the carboxyl oxygen (Figure 1.3) [25,39]. SAM binds to the cluster in the same geometry in both the +1 and +2 states of the clusters as shown though cryoreduction of a frozen $[4Fe\text{-}4S]^{2+}$ sample reduced to the EPR active $[4Fe\text{-}4S]^{+}$ state [40]. This SAM binding scheme was later verified in the crystal structure of PFL-AE in

the $[4Fe\text{-}4S]^{2+}$ state [41] and in all other radical SAM enzymes, verifying that SAM binding plays a pivotal role in catalysis.

Unusual Aspects of PFL-AE

To investigate PFL-AE *in vivo*, Mössbauer spectroscopy was conducted on *E. coli* whole cells overexpressing PFL-AE under aerobic and anaerobic conditions. It was concluded that under aerobic conditions, about 44% of the total iron was present in $[4Fe\text{-}4S]^{2+}$ clusters while 6% was in $[2Fe\text{-}2S]^{2+}$ clusters and the remainder 50% as noncluser Fe^{II} and Fe^{III} species. Once these cells were introduced to anaerobic conditions, about 75% of the iron was present in $[4Fe\text{-}4S]^{2+}$ clusters with the remaining 25% found as noncluster species with no $[2Fe\text{-}2S]^{2+}$ clusters [42] suggesting that these $[2Fe\text{-}2S]^{2+}$ clusters either undergo reductive coupling to form $[4Fe\text{-}4S]^{2+}$ clusters or that the $[2Fe\text{-}2S]^{2+}$ clusters are scavenged and converted to $[4Fe\text{-}4S]^{2+}$ clusters under anaerobic conditions.

An unprecedented observation of the whole cell Mössbauer results showed that 100% of the $[4Fe\text{-}4S]^{2+}$ clusters contain a valence localized Fe^{II}-Fe^{III} pair (Figure 1.7a) [42]. Purified protein only exhibits two valence delocalized $Fe^{2.5+}$-$Fe^{2.5+}$ pairs (Figure 1.7). It was proposed that a small molecule must be interacting with the unique Fe *in vivo* to cause a charge buildup and molecules containing adenosine moieties were added to purified protein to induce this unusual result. Only in the presence of methylthioadenosine (MTA), 5'-deoxyadenosine, adenosine monophosphate (AMP), and adenosine diphosphate (ADP) did the purified protein contain a valence localized cluster (Figure 1.7b); however, not 100% of the purified protein was valence localized. AMP

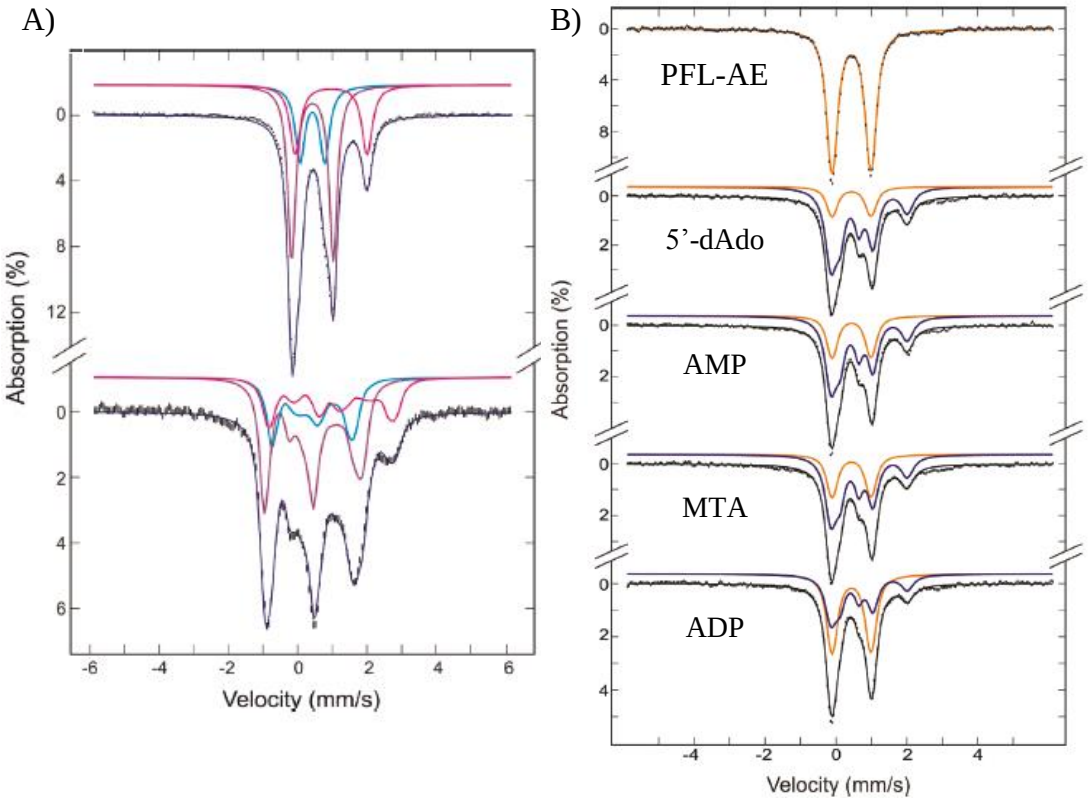


Figure 1.7. Mössbauer spectra of whole cells (a) and purified PFL-AE in the absence and presence of different adenosine containing molecules (b). A) PFL-AE exhibits a valence delocalized $Fe^{2.5+}$-$Fe^{2.5+}$ pair (purple) and a valence localized Fe^{2+}-Fe^{3+} pair with the cluster Fe^{2+} contribution shown in magenta and the cluster Fe^{3+} contribution in cyan. The upper spectrum has a 50 mT applied field while the bottom has a 6 T applied field. B) The purified protein contains only delocalized $Fe^{2.5+}$-$Fe^{2.5+}$ pairs (orange) while the adenosine molecules contain an additional signal (blue) which is comprised of one $Fe^{2.5+}$-$Fe^{2.5+}$ pair and one localized Fe^{2+}-Fe^{3+} pair. Figure taken from [42].

was proposed to be the source of the valence localization *in vivo* because it is the only adenosine containing molecule with high enough abundance in the cell to bind 100% of PFL-AE [42].

Pyruvate Formate Lyase

The substrate for PFL-AE is the GRE pyruvate formate lyase (PFL) which is a homodimeric protein with half-site reactivity on one of its 85 kDa monomers (Figure 1.8) [43,44]. PFL catalyzes the reaction of pyruvate and coenzyme A (CoA) to produce

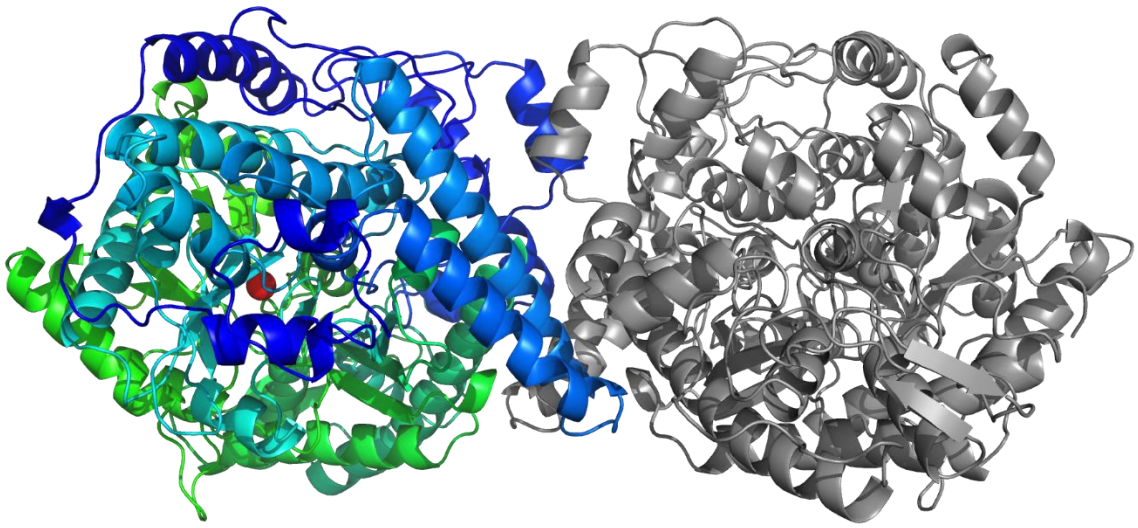


Figure 1.8. Crystal structure of PFL. Only one of its monomers (illustrated in color) is activated by PFL-AE by the abstraction of a hydrogen on G734 (orange circle).

formate and acetyl-CoA (Figure 1.9), providing the sole source of acetyl-CoA under anaerobic conditions [29,45,46]. During catalysis, the 5'-dAdo• radical abstracts the pro-*S* hydrogen from G734 on PFL, producing a glycyl radical. This glycine is located on a highly dynamic loop which has been shown to move into an "open" conformation to interact with PFL-AE for H-atom abstraction and a "closed" conformation where the glycyl radical is used to produce formate and acetyl-CoA [47]. In the closed conformation, the glycyl radical abstracts an H-atom from an interior cysteine, C419. This thiyl radical is then transferred to C418 which then attacks the carbonyl carbon on pyruvate, promoting C–C bond cleavage [43,44]. The resulting formate anion radical re-

abstracts an H-atom from G734 to produce a glycyl radical ready for another round of catalysis. The acetyl moiety residing on C418 then reacts with CoA to produce acetyl-CoA (Figure 1.9) [45,46,48].

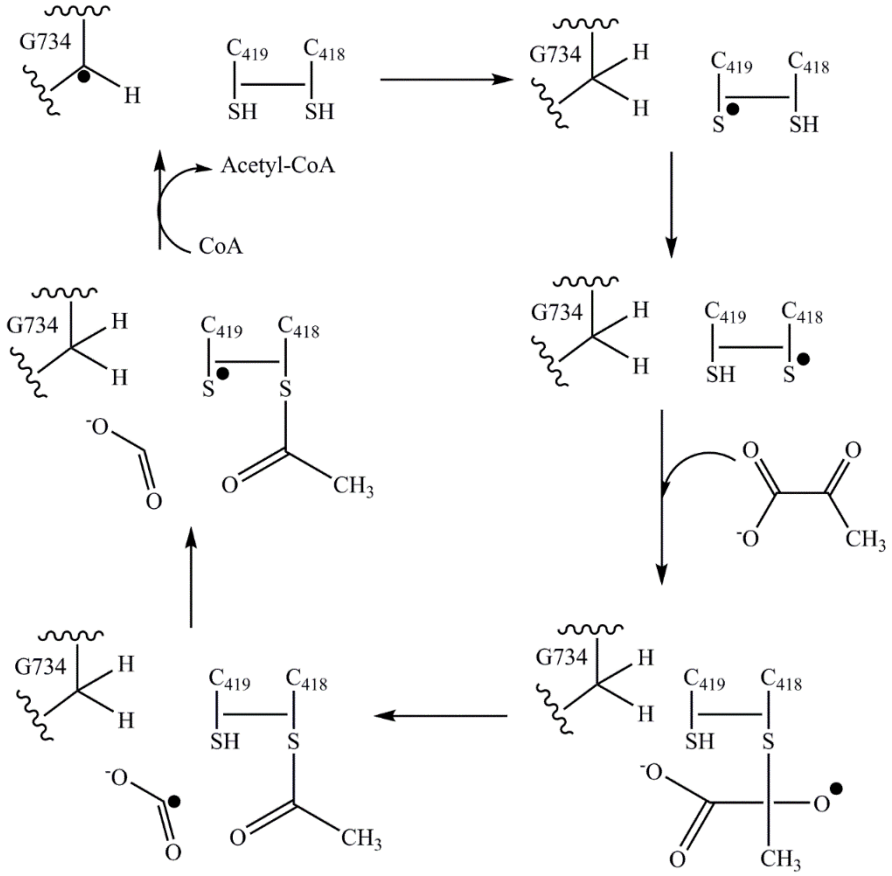


Figure 1.9. Reaction of PFL after activation by PFL-AE. During catalysis, PFL converts pyruvate and CoA to formate and acetyl-CoA through the production of two thiyl radicals on C419 followed by C418.

Research Goals

Although extensive research has been conducted on PFL-AE, unknown details into the mechanism still exist. For my research, I wanted to utilize spectroscopic

techniques to explore the active site of PFL-AE prior to SAM cleavage and intermediates during SAM cleavage.

Two of my research goals focused on PFL-AE prior to SAM cleavage to explore some of the peculiarities of PFL-AE. The first goal explored how small molecules are interacting with PFL-AE to induce a valance localized $[4Fe\text{-}4S]^{2+}$ cluster through the use of EPR and ultimately ENDOR spectroscopy. Since PFL-AE is difficult to crystallize, I wanted to use ENDOR spectroscopy to obtain a 3D rendering of how AMP and adenosine are interacting with the cluster to induce a valence localized state. Mutagenesis was carried out on amino acids that were proposed to interact with the small molecules followed by EPR analysis. EPR spectroscopy and mutagenesis work was conducted at Montana State University while ENDOR samples were shipped to Brian Hoffman's lab at Northwestern University. The second goal was a continuation of a cation effect on PFL-AE. Refinement of the crystal structure of PFL-AE revealed a cation in the active site of PFL-AE and the identity of this cation affects the activity and electronic structure of the [4Fe-4S] cluster. I wanted to perform activity assays and other spectroscopic techniques with strictly cation free (M^+-free) PFL-AE. PFL-AE is typically purified in a NaCl containing buffer and previous lab members tried to buffer exchange PFL-AE into M^+-free buffer for activity assays and EPR analysis. They still observed a stimulatory effect on activity even after buffer exchange. Thus, I wanted to use PFL-AE purified in the absence of any cation for activity assays and EPR and circular dichroism (CD) spectroscopic analysis to observe changes in the signals with the addition of different monovalent cations. I also wanted to conduct ENDOR spectroscopy

to observe any coupling between the cluster and different monovalent cations in addition to observing whether SAM coordination is changed in the presence of different monovalent cations. To investigate this cation binding site, activity assays and EPR experiments were conducted on PFL-AE variants. These variants contained a change from the two aspartate residues of the cation binding site to an alanine to restrict cation binding in the active site.

The other half of my research goals focused on SAM cleavage mechanisms. The highly reactive 5'-dAdo• has never been spectroscopically observed but the SAM analogue (anSAM) can produce a stabilized anAdo• radical. PFL-AE has not been shown to cleave anSAM but LAM can cleave anSAM. Thus, LAM was used to study the movement of anSAM with respect to the cluster and substrate (α-lysine) after cleavage and production of anAdo•. In order to observe the movement of anAdo•, I purchased different isotopically labeled lysine molecules and made ENDOR samples with these labeled lysine molecules and anSAM along. Another lab member synthetized [methyl-^{13}C]-anSAM which was also used in ENDOR sample preparation. ENDOR spectroscopy was conducted at Northwestern University. Another goal in my graduate research focused on an intermediate species previously isolated in PFL-AE. During rapid freeze quench (RFQ) techniques on PFL-AE, an unknown EPR signal was observed that was not a $[4Fe\text{-}4S]^{+}$ cluster nor a glycyl radical on PFL. To conduct RFQ, PFL-AE was isolated from SAM and PFL and mixed for a specified amount of time after which the reaction was quenched by freezing to isolate any intermediate states. I first wanted to optimize the experimental parameters to obtain a stronger EPR signal. Next, in order to

understand the origin of this novel intermediate signal, I synthesized isotopically labeled SAM molecules and used an ^{57}Fe labeled cluster in PFL-AE for ENDOR analysis. In order to perform RFQ experiments, I traveled to Northwestern University and all ENDOR analysis was conducted by the Hoffman laboratory at Northwestern University.

References

1. Tan, L.; Chi-lung, Y. *Int. Geol. Rev.* **1970**, *12*, 778-786.

2. Beinert, H. *J. Biol. Inorg. Chem.* **2000**, *5*, 2-15.

3. Beinert, H.; Holm, R. H.; Munck, E. *Science* **1997**, *277*, 653-659.

4. Meyer, J. *J. Biol. Inorg. Chem.* **2008**, *13*, 157-170.

5. Johnson, D. C.; Dean, D. R.; Smith, A. D.; Johnson, M. K. *Annu. Rev. Biochem.* **2005**, *74*, 247-281.

6. Peters, J. W.; Lanzilotta, W. N.; Lemon, B. J.; Seefeldt, L. C. *Science* **1998**, *282*, 1853-1858.

7. Kiley, P. J.; Beinert, H. *Curr. Opin. Microbiol.* **2003**, *6*, 181-185.

8. Frazzon, J.; Dean, D. R. *Curr. Opin. Chem. Biol.* **2003**, *7*, 166-173.

9. Peters, J. W.; Broderick, J. B. *Annu. Rev. Biochem.* **2012**, *81*, 429-450.

10. Ayala-Castro, C.; Saini, A.; Outten, F. W. *Microbiol. Mol. Biol. Rev.* **2008**, *72*, 110-125, table of contents.

11. Chahal, H. K.; Dai, Y.; Saini, A.; Ayala-Castro, C.; Outten, F. W. *Biochemistry* **2009**, *48*, 10644-10653.

12. Fontecave, M.; Ollagnier-de-Choudens, S. *Arch. Biochem. Biophys.* **2008**, *474*, 226-237.

13. Bonomi, F.; Iametti, S.; Morleo, A.; Ta, D.; Vickery, L. E. *Biochemistry* **2008**, *47*, 12795-12801.

14. Broderick, J. B.; Duffus, B. R.; Duschene, K. S.; Shepard, E. M. *Chem. Rev.* **2014**, *114*, 4229-4317.

15. Frey, P. A.; Magnusson, O. T. *Chem. Rev.* **2003**, *103*, 2129-2148.

16. Knappe, J.; Neugebauer, F. A.; Blaschkowski, H. P.; Ganzler, M. *Proc. Natl. Acad. Sci. USA* **1984**, *81*, 1332-1335.

17. Frey, P. A. *FASEB J.* **1993**, *7*, 662-670.

18. Vey, J. L.; Drennan, C. L. *Chem. Rev.* **2011**, *111*, 2487-2506.

19. Sofia, H. J.; Chen, G.; Hetzler, B. G.; Reyes-Spindola, J. F.; Miller, N. E. *Nucleic Acids Res.* **2001**, *29*, 1097-1106.

20. Chatterjee, A.; Li, Y.; Zhang, Y.; Grove, T. L.; Lee, M.; Krebs, C.; Booker, S. J.; Begley, T. P.; Ealick, S. E. *Nat. Chem. Biol.* **2008**, *4*, 758-765.

21. McGlynn, S. E.; Boyd, E. S.; Shepard, E. M.; Lange, R. K.; Gerlach, R.; Broderick, J. B.; Peters, J. W. *J. Bacteriol.* **2010**, *192*, 595-598.

22. Duschene, K. S.; Veneziano, S. E.; Silver, S. C.; Broderick, J. B. *Curr. Opin. Chem. Biol.* **2009**, *13*, 74-83.

23. Vey, J. L.; Yang, J.; Li, M.; Broderick, W. E.; Broderick, J. B.; Drennan, C. L. *Proc. Natl. Acad. Sci. USA* **2008**, *105*, 16137-16141.

24. Berkovitch, F.; Nicolet, Y.; Wan, J. T.; Jarrett, J. T.; Drennan, C. L. *Science* **2004**, *303*, 76-79.

25. Walsby, C. J.; Ortillo, D.; Broderick, W. E.; Broderick, J. B.; Hoffman, B. M. *J. Am. Chem. Soc.* **2002**, *124*, 11270-11271.

26. Nicolet, Y.; Drennan, C. L. *Nucleic Acids Res.* **2004**, *32*, 4015-4025.

27. Magnusson, O. T.; Reed, G. H.; Frey, P. A. *J. Am. Chem. Soc.* **1999**, *121*, 9764-9765.

28. Magnusson, O. T.; Reed, G. H.; Frey, P. A. *Biochemistry* **2001**, *40*, 7773-7782.

29. Frey, M.; Rothe, M.; Wagner, A. F.; Knappe, J. *J. Biol. Chem.* **1994**, *269*, 12432-12437.

30. Knappe, J.; Blaschkowski, H. P.; Edenharder, R. *Enzyme-dependent activation of pyruvate formate-lyase of Escherichia coli*; Springer: Berlin Heidelberg New York, 1972.

31. Knappe, J.; Schacht, J.; Mockel, W.; Hopner, T.; Vetter, H., Jr.; Edenharder, R. *Eur. J. Biochem.* **1969**, *11*, 316-327.

32. Rödel, W.; Plaga, W.; Frank, R.; Knappe, J. *Eur. J. Biochem.* **1988**, *177*, 153-158.

33. Broderick, J. B.; Duderstadt, R. E.; Fernandez, D. C.; Wojtuszewski, K.; Henshaw, T. F.; Johnson, M. K. *J. Am. Chem. Soc.* **1997**, *119*, 7396-7397.

34. Broderick, J. B.; Henshaw, T. F.; Cheek, J.; Wojtuszewski, K.; Smith, S. R.; Trojan, M. R.; McGhan, R. M.; Kopf, A.; Kibbey, M.; Broderick, W. E. *Biochem. Biophys. Res. Commun.* **2000**, *269*, 451-456.

35. Krebs, C.; Henshaw, T. F.; Cheek, J.; Huynh, B.; Broderick, J. B. *J. Am. Chem. Soc.* **2000**, *122*, 12497-12506.

36. Henshaw, T. F.; Cheek, J.; Broderick, J. B. *J. Am. Chem. Soc.* **2000**, *122*, 8331-8332.

37. Petrovich, R. M.; Ruzicka, F. J.; Reed, G. H.; Frey, P. A. *Biochemistry* **1992**, *31*, 10774-10781.

38. Krebs, C.; Broderick, W. E.; Henshaw, T. F.; Broderick, J. B.; Huynh, B. *J. Am. Chem. Soc.* **2002**, *124*, 912-913.

39. Walsby, C. J.; Ortillo, D.; Yang, J.; Nnyepi, M. R.; Broderick, W. E.; Hoffman, B. M.; Broderick, J. B. *Inorg. Chem.* **2005**, *44*, 727-741.

40. Walsby, C. J.; Hong, W.; Broderick, W. E.; Cheek, J.; Ortillo, D.; Broderick, J. B.; Hoffman, B. M. *J. Am. Chem. Soc.* **2002**, *124*, 3143-3151.

41. Nicolet, Y.; Amara, P.; Mouesca, J. M.; Fontecilla-Camps, J. C. *Proc. Natl. Acad. Sci. USA* **2009**, *106*, 14867-14871.

42. Yang, J.; Naik, S. G.; Ortillo, D. O.; Garcia-Serres, R.; Li, M.; Broderick, W. E.; Huynh, B. H.; Broderick, J. B. *Biochemistry* **2009**, *48*, 9234-9241.

43. Becker, A.; Fritz-Wolf, K.; Kabsch, W.; Knappe, J.; Schultz, S.; Volker Wagner, A. F. *Nature structural biology* **1999**, *6*, 969-975.

44. Becker, B. F.; Gilles, S.; Sommerhoff, C. P.; Zahler, S. *J. Biol. Chem.* **2002**, *383*, 1821-1826.

45. Parast, C. V.; Wong, K. K.; Lewisch, S. A.; Kozarich, J. W.; Peisach, J.; Magliozzo, R. S. *Biochemistry* **1995**, *34*, 2393-2399.

46. Plaga, W.; Frank, R.; Knappe, J. *Eur. J. Biochem.* **1988**, *178*, 445-450.

47. Peng, Y.; Veneziano, S. E.; Gillispie, G. D.; Broderick, J. B. *J. Biol. Chem.* **2010**, *285*, 27224-27231.

48. Plaga, W.; Vielhaber, G.; Wallach, J.; Knappe, J. *FEBS Lett.* **2000**, *466*, 45-48.

CHAPTER 2

GENERAL METHODS

Growth and Purification of PFL-AE

The pCAL-n-EK plasmid containing the PFL-AE gene (*E. coli* gene *pflA*) was expressed in *E. coli* BL21(DE3)pLysS (Stratagene) cells. One colony from a LB-ampicillin (50 μg/mL amp) plate was used to inoculate a 50 mL LB and 50 μg/mL ampicillin starter culture which was grown overnight. This 50 mL starter culture was then used to inoculate 10 L of minimal media in a bench-top fermentor (New Brunswick) which also contained 50 μg/mL ampicillin and a solution of glucose and vitamins. Included in the minimal media was 100 g Casamino acids, 84.2 g MOPS, 8.0 g Tricine, 14.7 g NaCl, 16.0 g KOH, 5.1 g NH_4Cl and 9.8 L of water. A glucose solution was sterile filtered prior to addition to the fermentor and contained the following: 50 g of glucose in 200 mL water; 25 mL of an "O" solution; 25mL of 1 M KH_2PO_4; 12.5 mL of 276 mM K_2SO_4; and 62.5mL of 0.1 M $CaCl_2$. The "O" solution was prepared with 0.1 g $FeCl_2 \cdot 4H_2O$ dissolved in 10 mL of 12 M HCl, 2.68 g $MgCl_2 \cdot 6H_2O$, and 1 mL "T" solution (18.4 mg $CaCl_2 \cdot 2H_2O$, 64 mg H_3BO_3, 40 mg $MnCl_2 \cdot 4H_2O$, 18 mg $CoCl_2 \cdot 6H_2O$, 4 mg $CuCl_2 \cdot 2H_2O$, 340 mg $ZnCl_2$, and 605 mg $Na_2MoO_4 \cdot 2H_2O$ diluted to 100 mL with H_2O) and the "O" was brought up to a final volume of 50 mL with H_2O. Additionally, 10 mg of the vitamins biotin, pantothenic acid, vitamin B_{12}, thiamine, folic acid, riboflavin, niacinamide, thioctic acid, and pyridoxine were added to the fermentor along with the glucose solution. The growth was incubated at 37°C, agitated at 250 rpm with a flow of

5 L/min of compressed air. Once the cells reached an OD_{600} of ~0.5, 0.5 mM (final concentration) of isopropyl-β-D-thiogalactopyranoside (IPTG) was added along with 0.75 g of $Fe(NH_4)_2(SO_4)_2 \cdot 6H_2O$. After ~2 hours, the cells were cooled and purged with N_2 once the culture was ~ 30°C to stimulate anaerobic conditions. Once the culture was ~20°C, another addition of 0.75 g of $Fe(NH_4)_2(SO_4)_2 \cdot 6H_2O$ was added. The culture was purged with N_2 overnight in a 4°C fridge. The cells were harvested after ~16 hours of overnight purging by centrifugation at 6,000 rpm and 4°C for 10 minutes in 1 L centrifuge bottles. The pellet was flash frozen in liquid nitrogen and stored in a -80°C freezer until purification.

PFL-AE cell pellets were purified in an anaerobic Coy chamber. The cell pellets were lysed in a 50 mM Tris, pH 7.5 buffer wtih 100 mM NaCl containing 5% w/v glycerol, 1% w/v Triton X-100, and 10 mM $MgCl_2$. Additionally, 18 mg of PMSF, 78 mg of DTT, 16 mg of lysozyme, and ~0.2 mg of DNase and RNase were added to 100 mL of lysis buffer. Approximately 2 mL of lysis buffer was added per 1 g of cell pellet and the cells were allowed to lyse on ice for ~1 hour. When needed, a needle and syringe were used to break up the cell pellet. After an hour, the lysis was centrifuged at 18,000 rpm and 4°C for 30 minutes, which was repeated if necessary. The supernatant was applied to a Superdex-75 resin equilibrated with 2 L of gel filtration buffer via a superloop at 3 mL/min. The gel filtration buffer (50 mM Tris, pH 7.5 with 100 mM NaCl and 1 mM DTT) was washed over the column at 5 mL/min and the dark brown fractions were pooled and concentrated using a 10K MWCO Millipore Amicon Ultra centrifugal

concentrator at ambient Coy chamber temperatures. Fractions eluted after ~2 hours (550-600 mL) (Figure 2.1).

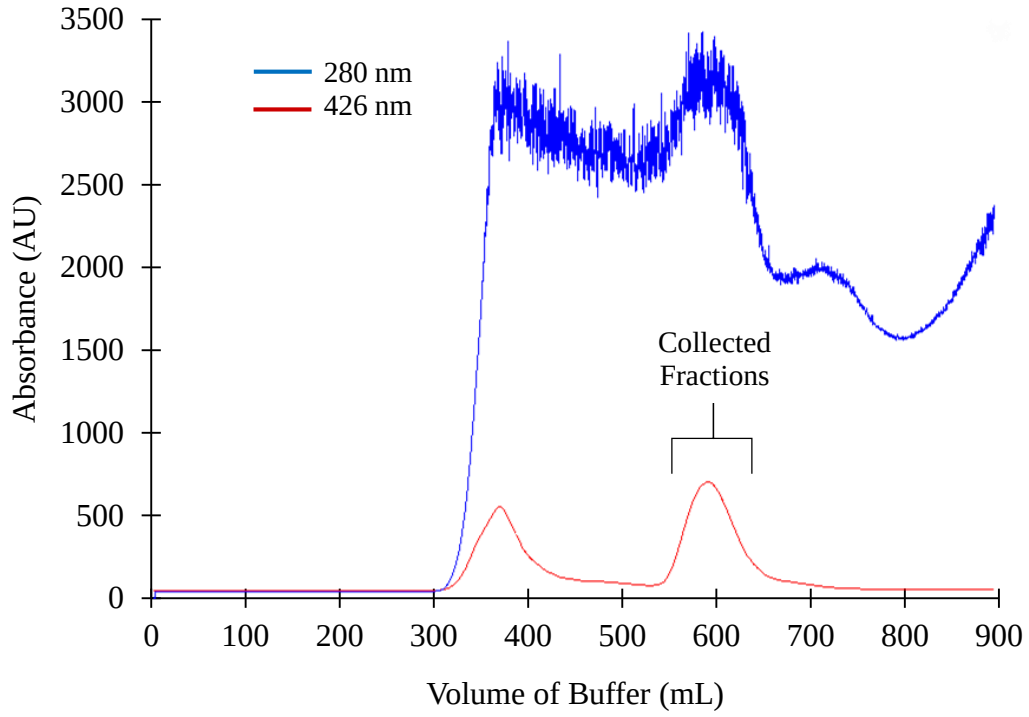


Figure 2.1. A representative chromatogram from the first PFL-AE column purification using size exclusion Superdex 75 resin and a 50 mM Tris, pH 7.5 buffer with 200 mM NaCl. The blue line is the absorbance at 280 nm while the red line is the absorbance at 426 nm pertaining to the Fe-S cluster content. The fractions with the darkest brown color, which came off around 550 mL to 625 mL (bracket) were concentrated.

The column was equilibrate again with another round of 2 L of gel filtration buffer, after which the concentrated protein was run over the column a second time and the fractions with the highest 426/280 nm ratio were pooled and concentrated using a 10K MWCO Millipore Amicon Ultra centrifugal concentrator. Cutoff 426/280 nm ratios depended on the purification but a typical ratio for the best protein was >0.160 Protein

was aliquoted into screw-top tubes and frozen in liquid nitrogen immediately following removal from the Coy chamber and stored at -80°C.

Growth and Purification of PFL

PFL was purified from BL21(DE3)pLysS cells containing the pKK223-3 plasmid expressing the *E. coli* gene *pflB.* The cells were grown aerobically in a benchtop fermentor. A single colony from an LB-ampicilin (50 μg/mL) plate was used to inoculate a 50 mL LB and 50 μg/mL ampicillin starter culture which was grown overnight and used to inoculate 10 L of LB and 50 μg/mL ampicillin. The culture was incubated at 37°C with 300 rpm agitation and air flow at 5 mL/min from a compressed air tank. Once the culture reached an OD_{600} of ~0.8, sterile filtered IPTG was added to a final concentration of 1 mM to induce the cells. After 3 hours, the cells were harvested by centrifugation at 6,000 rpm and 4°C for 10 minutes in a 1 L centrifuge bottle. Again, the cells were flash frozen in liquid nitrogen and stored at -80°C.

Cell pellets were lysed aerobically in a 20 mM Tris, pH 7.2 buffer containing 5% w/v glycerol, 1% w/v Triton X-100, and 10 mM $MgCl_2$. To 100 mL of lysis buffer, 18 mg of PMSF, 16 mg of lysozyme, and ~0.2 mg of DNase and RNase were added. Like PFL-AE, approximately 2 mL of lysis buffer per 1 g of cell pellet was added to the cells which stirred at 4°C for ~1 hour upon which the lysate was centrifuged at 18,000 rpm and 4°C for 30 minutes. The supernatant was applied to a Waters AP-5 300 mm column containing Accell Plus QMA resin equilibrated with Buffer A (20 mM Tris, pH 7.2 with 1 mM DTT) via a superloop at 3 mL/min. The column was washed with 300 mL of

Buffer A followed by a 900 mL linear gradient to 100% Buffer B (20 mM Tris, pH 7.2 with 500 mM NaCl and 1 mM DTT), and ending with 300 mL of 100% Buffer B. The absorbance at 280 nm was monitored during the program. PFL eluted around 50% Buffer B (Figure 2.2) and fractions were collected and analyzed via SDS-PAGE (Figure 2.3).

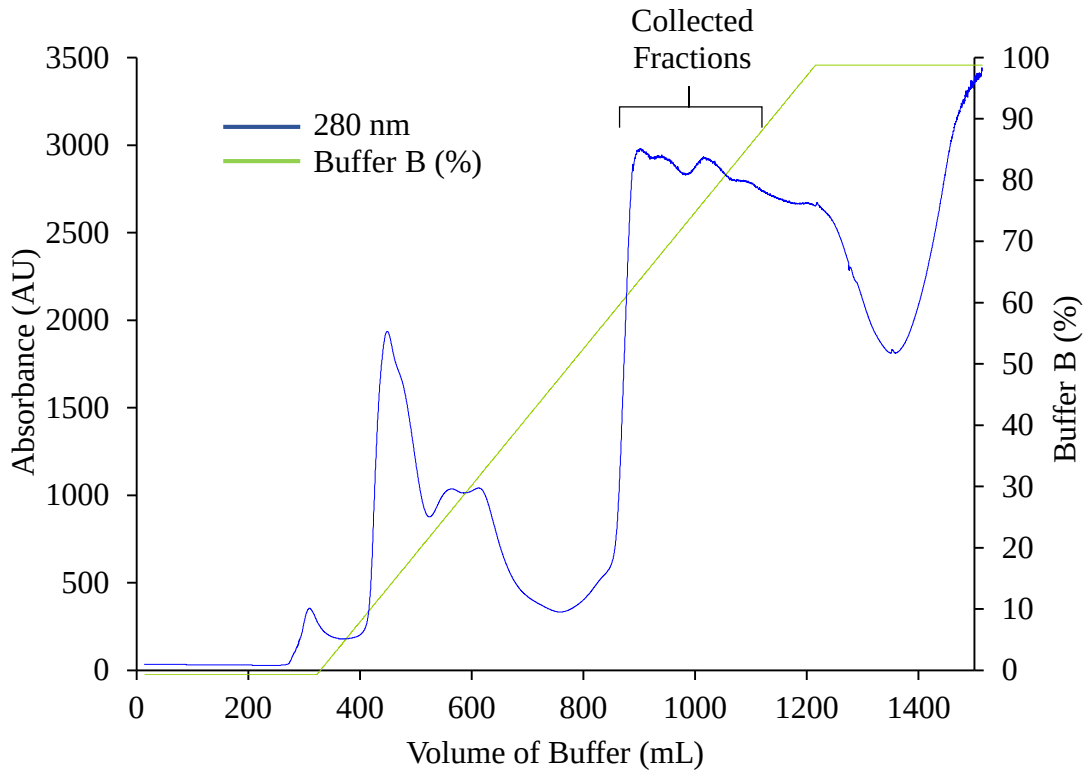


Figure 2.2. Representative chromatogram from the QMA anion exchange column from a PFL purification. The absorbance at 280 nm is shown in blue and the percent Buffer B (20 mM Tris, pH 7.2 with 500 mM NaCl and 1 mM DTT) is shown in green. Fractions, analyzed by gel chromatography, are collected after about 900 mL, or approximately 60% Buffer B.

Most abundant and the purest fractions were pooled, concentrated, and buffer exchanged into a high salt buffer (10 mM Tris, pH 7.2 with 1 M $(NH_4)_2SO_4$ and 1 mM

DTT). To buffer exchange PFL, the fractions was concentrated as much as possible using a 10 K (or a 30 K) MWCO Millipore Amicon Ultra centrifugal concentrator at 4°C. Due to precipitation at high concentrations, PFL was concentrated to about 3-5 mL in the 15 mL centrifugal concentrator. High salt buffer was added up to 15 mL and PFL was

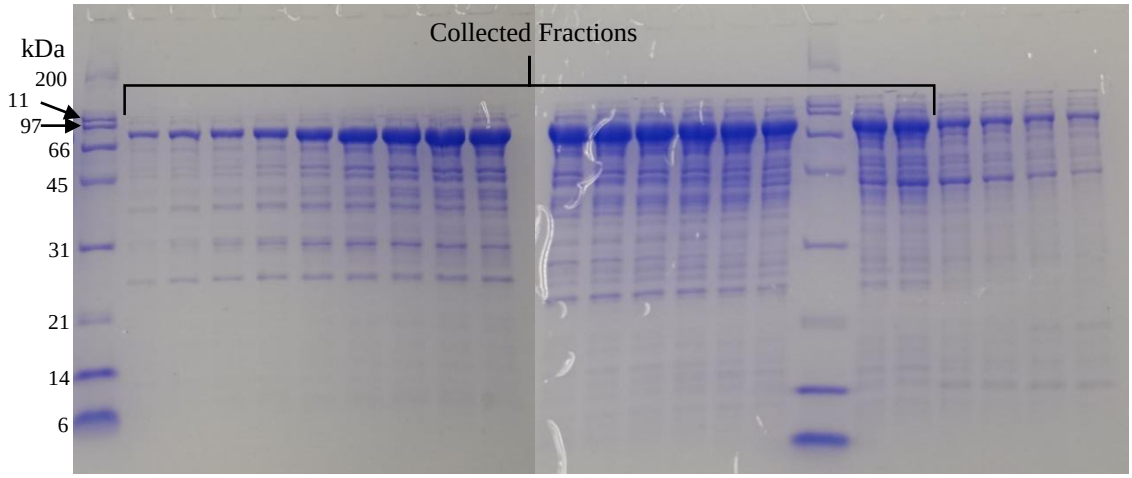


Figure 2.3. Representative SDS-PAGE gels from an anion exchange PFL purification. The protein ladder is labeled in kDa (far left). The fractions that were collected and pooled are bracketed. Fractions with an increase of the band around 40 kDa were excluded from the pool.

concentrated down again. This process was repeat about 8-10 times. After buffer exchanging PFL and concentrating to less than 5 mL, the protein was loaded onto a HighLoad High Performance 16/10 phenyl sepharose column equilibrated in high salt buffer via a superloop at 1 mL/min. The column was washed with 50 mL of the high salt buffer followed by a 50 mL linear gradient to 100% Buffer A (20 mM Tris, pH 7.2 with 1 mM DTT) and ended with a 50 mL wash of Buffer A. PFL eluted at 100% Buffer A (Figure 2.4) and again was analyzed via SDS-PAGE. PFL was buffer exchanged into a 20 mM Tris, pH 7.2 buffer to remove excess M^+ from purification and then degassed on a

Schlenk line. It was then taken into the MBraun anaerobic glovebox where O_2 levels are maintained at ≤1 ppm, aliquoted into screw-top tubes, flash frozen in liquid nitrogen upon removal from the MBraun chamber, and stored at -80°C.

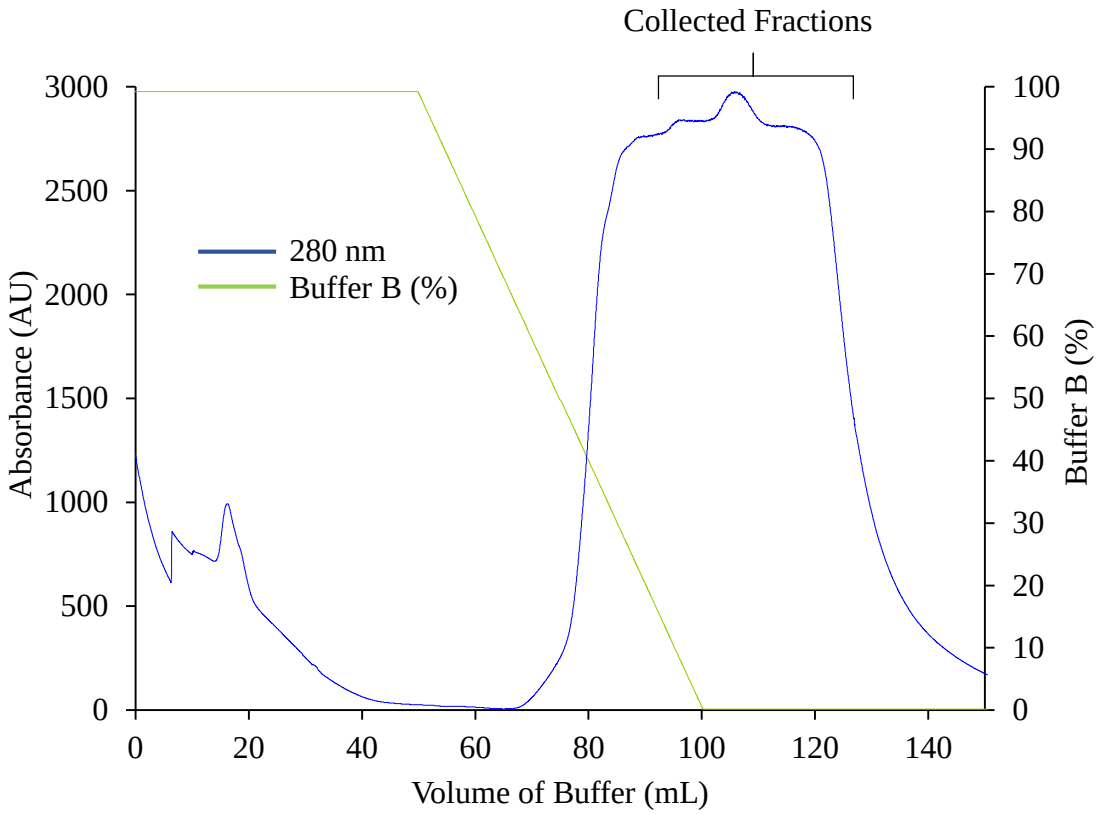


Figure 2.4. Representative chromatogram from the hydrophobic phenyl sepharose column from a PFL purification. The absorbance at 280 nm is shown in blue and the percent Buffer B (20 mM Tris, pH 7.2 with 1 mM DTT) is shown in green. Fractions, analyzed by gel chromatography, are collected after 0% Buffer B has been reached.

Protein and Iron Quantification

Protein concentrations were determined using the method of Bradford [1] using dye reagent from Biorad. Bovine serum albumin (BSA) was used to produce a standard curve (0, 1, 2, 3, 4, 5, and 6 μg) and PFL-AE was diluted appropriately to fit on the

curve. A correction factor, determined by acid hydrolysis [2], was utilized in the final calculations of PFL-AE concentration. Iron content was determined using atomic absorption (AA) spectroscopy or by the method of Beinert [3]. For both methods, a standard curve (0, 0.4, 0.8, 1.2, 1.6, and 2.0 μg) was made from a 1,000 ppm Fe standard (purchased from Ricca Chemical Company) and PFL-AE was diluted appropriately to fit on the standard curve. For the determination via AA spectroscopy, 2 mL of standard or protein sample was prepared. For the Beinert assay, standards and protein samples were diluted to appropriate concentrations for a final volume of 1 mL. To each solution, 500 μL of a 1:1 ratio of 1.2 M HCl:4.5% $KMnO_4$ was added and samples incubated for 2 hours in a 65°C water bath. Then, 100 μL of reagent B (4.9 g ammonium acetate, 4.4 g ascorbic acid, 40 mg neocuproine, and 40 mg ferrozine were added to a total of 12.5 mL H_2O) was added to the samples and vortexed periodically over 30 minutes. The absorbance at 562 nm was recorded and Fe content was calculated using the standard curve.

Synthesis and Purification of SAM

SAM was synthesized in the laboratory and purified prior to experiments. In a scintillation vial, the following was added in order: 8.275 mL of a 100 mM Tris, pH 8 buffer; 37 mg KCl; 53 mg $MgCl_2$; 18 μL 0.5 M EDTA; 73 mg ATP; 18 mg L-methionine; 800 μL β-mercaptoethanol (βME); 1-5 μL inorganic phosphatase (depending on the stock of enzyme); and 1 mL SAM synthetase crude lyase. The reaction was stirred overnight, for about 15-16 hours, at ambient temperatures after which

the reaction is quenched with 1 mL of 1 M HCl. The solution was centrifuged at 18,000 rpm and 4°C for 30 minutes. Half of the supernatant (5 mL) is applied to a Source15S cation exchange column equilibrated with H_2O via a superloop at 1 mL/min. The SAM program was run with buffer A (H_2O) and buffer B (1 M HCl) under the following sequence at 2 mL/min: 1) 26 mL 0% buffer B; 2) a linear gradient of 16 mL up to 10% buffer B; 3) 14 mL of 10% buffer B; 4) linear gradient of 104 mL up to 100% buffer B; 5) 20 mL of 100% buffer B; 6) linear gradient of 8 mL to 0% buffer B; 7) 40 mL of 0% buffer B. Absorbance was monitored at 280 nm and SAM eluted after about 50% Buffer B (Figure 2.5). The program is run again with the second half of the supernatant and both purifications were pooled into a round bottom flask.

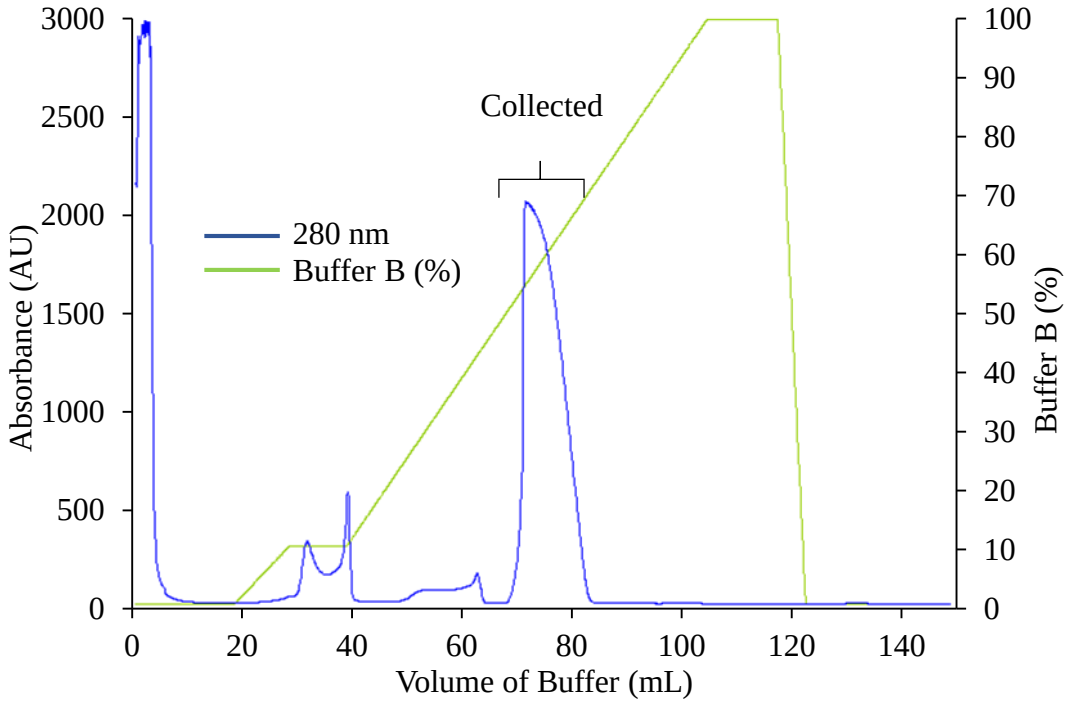


Figure 2.5. Representative chromatogram of a SAM purification on a Source 15S cation exchange column. SAM was collected (bracket) after about 50% Buffer B (1 M HCl).

SAM was rotovapped down to ~1-5 mL after which it was lyophilized on the Schlenk line overnight. For reconstitution, the lyophilized SAM was brought into an anaerobic MBraun glovebox where a degassed 100 mM Tris, pH 8 buffer was added. The pH was adjusted to be between 7.0 and 7.5 with addition of degassed 1 M NaOH after which degassed water was added to bring the concentration of the buffer to 50 mM Tris. SAM was aliquoted into screw-top vials, flash frozen in liquid nitrogen, and stored at -80°C. The concentration of SAM was determined by the absorbance at 260 nm and the molar extinction coefficient of 16,000 M^{-1} cm^{-1}.

Preparation of EPR and ENDOR Samples

EPR and ENDOR samples were prepared in an anaerobic MBraun glovebox with $\leq$1 ppm O_2. A "stock" of PFL-AE was photoreduced (as discussed below) and aliquoted for addition of small molecule. For EPR experiments, a total volume of 250 μL was required while for ENDOR experiments, about 75-100 μL is required but 100 μL was generally loaded into Q-band tubes. For the "stock" of photoreduced PFL-AE, the protein was premixed in Eppendorf tubes in a Tris buffer (usually 50-100 mM Tris, pH 7.5 and 1 mM DTT) containing the appropriate salt (100-200 mM KCl or cation of choice) and 5-deazariboflavin (100 μM final concentration) and pipetted into a shortened NMR tube. The 5-deazariboflavin was added last and the tube(s) were kept covered with a glove or aluminum foil. Photoreduction was accomplished by placement of the sample in a glass dish containing an ice bath and illumination of the sample with a 300 W halogen lamp for an hour. Bath water was changed to maintain temperatures of ~0°C.

After photoreduction, the sample was placed in an Eppendorf tube and the evaporated volume was accounted for by addition of buffer. A small molecule, such as SAM, was added to bring the final concentration of PFL-AE to 200 μM. If no small molecule was added, buffer was added to bring the final concentration of PFL-AE to 200 μM. PFL-AE was generally photoreduced at a higher concentration to allow dilution to 200 μM with addition of small molecules. The samples were pipetted into X-band EPR tubes (a total volume of 250 μL) via a pulled glass Pasteur pipette or Q-band ENDOR tubes (a total volume of 100 μL) via a glass Pasteur pipette, capped with rubber septa, taken out of the MBraun chamber, and flash frozen in liquid nitrogen. EPR samples were kept in a liquid nitrogen dewer until EPR was run while ENDOR tubes were placed in individual cryotubes with a small amount of glass wool at the top and bottom of the cryotube to keep the samples from moving. The samples were then shipped to Brian Hoffman's laboratory at Northwestern University in a dry shipping dewer.

Activity Assays

Activity of PFL-AE was determined via a coupling assay (Figure 2.6). In a Unilab MBraun anaerobic chamber containing ≤ 1 ppm O_2, a 450 μL "activation solution" was mixed containing 0.05 μM PFL-AE, 5 μM PFL, 0.1 mM SAM, 10 mM oxamate, 8 mM DTT, 25 μM 5-deazariboflavin (added last in the dark) and 100 mM Tris, pH 7.6 with 100 mM KCl buffer (all concentrations given are final concentrations). For determination of activity in the presence of different monovalent cations, 100 mM of the specific monovalent cation was added while for a divalent cation, 1 mM of different

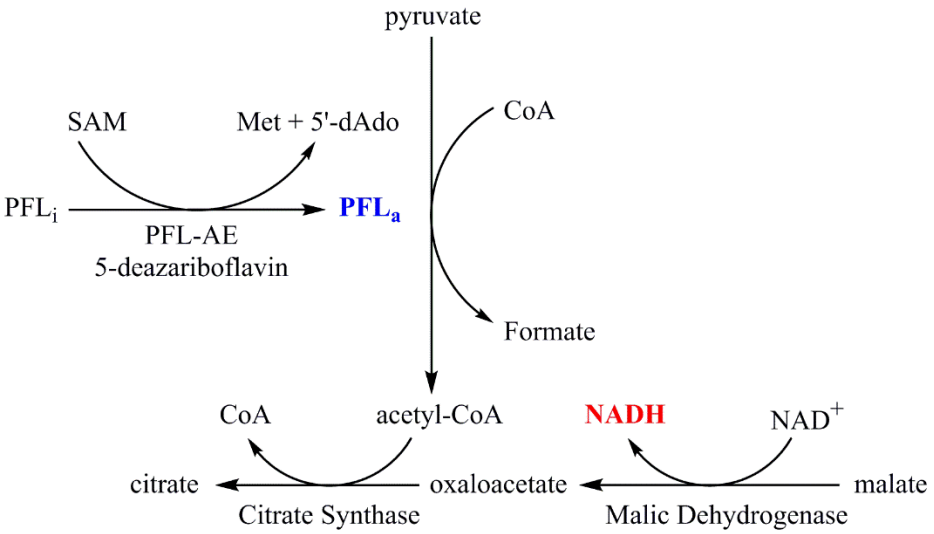


Figure 2.6. The PFL-AE coupled activity assay. In the activation solution, which is applied to the lid of an anaerobic cuvette, inactivated PFL (PFL_i) is activated (PFL_a) by PFL-AE through the cleavage of SAM and production of the glycyl radical on PFL. A coupling solution containing the coupling enzymes citrate synthase and malic dehydrogenase, the substrate for malic dehydrogenase (malate), and the substrates for PFL (pyruvate and CoA) are placed in the cuvette. When the cuvette is inverted just prior to placement into the UV-vis spectrometer, pyruvate and CoA are turned over to formate and acetyl-CoA, respectively. Malic dehydrogenase turns over malate to oxaloacetate through the reduction of NAD^+ to NADH (red) which is monitored via UV-vis spectroscopy. Citrate synthase turns over acetyl-CoA and oxaloacetate which increases PFL turnover and malic dehydrogenase turnover to produce more NADH.

divalent cations were added. This activation solution was photoreduced by illumination with a 300 W halogen lamp and the protein was kept in a 30°C ± 2°C water bath for 5 minutes (or another desired amount of illumination time) and then covered with foil to prevent further reduction. To assay the activity, 5 µL of the resulting activation solution was placed on a lid of an anaerobic cuvette containing 895 µL of coupling solution containing 3 mM NAD^+, 55 µM CoA, 0.05 mg/mL BSA, 10 mM pyruvate, 10 mM malate, 2 U/mL citrate synthase, 30 U/mL malic dehydrogenase, 10 mM DTT, and 100 mM Tris, pH 8.1 (all final concentrations after mixing of activation solution and coupling

solution which was 900 μL) prior to sealing the cuvette and removing it from the chamber. The two solutions were mixed by inverting the cuvette just prior to placing in a thermostatted (30°C) Cary 60 UV-vis spectrophotometer. The production of NADH was monitored at 340 nm for 90 seconds. Rates were calculated from the slope of absorbance vs. time from 18 seconds to 90 seconds, when the slopes stabilized and were the most linear. One unit of PFL activity corresponds to the production of one μmole of pyruvate per minute, and 35 units of PFL is equivalent to 1 nmole of PFL active sites [4]. The definition of one unit of PFL-AE activity is the amount that catalyzes the production of 1 nmole of active PFL per minute (Equation 1-5) [5]. The units of active PFL (PFL_{ac}) in the 1 mL cuvette is calculated as follows (Equation 1):

$$\left(\frac{AU}{\min}\right)\left(\frac{\frac{mol}{L}}{6200\ AU}\right)(9.0\ \times 10^{-4}\ L\ assay\ vol)\left(\frac{10^{6}\mu Mol}{mol}\right) = \frac{\mu mol\ pyruvate}{\min} = U\ PFL_{ac} \quad (1)$$

where AU/min is the rate of NADH production during a 1.5 minute (90 second) scan, 6200 AU mol^{-1} L^{-1} is the molar absorptivity of NADH, and 9.0×10^{-4} L assay vol is the total assay volume in the cuvette after mixing. This equation holds true assuming 1 NADH molecule produced equals one molecule pyruvate turned over by PFL. The total units of PFL_a in the activation solution is calculated as follows (Equation 2):

$$\left(\frac{U\ PFL_{ac}}{5\ \mu L}\right)(450\ \mu L) = U\ PFL_a \quad (2)$$

where 5 μL is the volume of the activation solution on the lid of the cuvette and 450 μL is the total volume of activation solution illuminated. The specific activity for PFL-AE from units of PFL can be calculated as follows for a 5 minute photoillumination time to reduce PFL-AE (Equations 3-5):

$$(UPFL_a)\left(\frac{1\ nmol\ PFL_a}{35\ U}\right) = nmol\ PFL_a \quad (3)$$

$$\frac{nmol\ PFL_a}{5\ min} = U\ PFL\text{-}AE \quad (4)$$

$$Specific\ Activity\ (PFL\text{-}AE) = (U\ PFL\text{-}AE)/(mg\ PFL\text{-}AE) \quad (5)$$

References

1. Bradford, M. M. *Anal. Biochem.* **1976**, *72*, 248-254.

2. Broderick, J. B.; Duderstadt, R. E.; Fernandez, D. C.; Wojtuszewski, K.; Henshaw, T. F.; Johnson, M. K. *J. Am. Chem. Soc.* **1997**, *119*, 7396-7397.

3. Beinert, H. *Methods Enzymol.* **1978**, *54*, 435-445.

4. Kulzer, R.; Pils, T.; Kappl, R.; Huttermann, J.; Knappe, J. *J. Biol. Chem.* **1998**, *273*, 4897-4903.

5. Broderick, J. B.; Henshaw, T. F.; Cheek, J.; Wojtuszewski, K.; Smith, S. R.; Trojan, M. R.; McGhan, R. M.; Kopf, A.; Kibbey, M.; Broderick, W. E. *Biochem. Biophys. Res. Commun.* **2000**, *269*, 451-456.

CHAPTER 3

MATERIALS AND METHODS

Spectroscopic Methods for Radical SAM Enzymes: Fe-S Cluster Characterization

Many different spectroscopic techniques can be used to analyze Fe-S clusters such as UV-vis, resonance Raman, Mössbauer, electron paramagnetic resonance (EPR), and electron nuclear double resonance (ENDOR) spectroscopies. Ligand to metal transfer bands occur between 305-450 nm for Fe-S clusters which are dependent on the type of cluster and oxidation state. [2Fe-2S] and [4Fe-4S] exhibit absorptions in this range in the oxidized state but become bleached in the reduced states [1]. Mössbauer spectroscopy can determine the cluster type, oxidation state of the Fe, and the delocalization patterns within a cluster [2,3]. Resonance Raman spectroscopy can distinguish between the cluster types and identify ligands [4]. The type of cluster, its coordination environment, and oxidation state can be explored through EPR and ENDOR spectroscopic techniques [1,4,5]. The background of EPR and ENDOR spectroscopies will be discussed in detail below along with how they are used to study Fe-S clusters.

Electron Paramagnetic Resonance Spectroscopy

Electron paramagnetic resonance (EPR) spectroscopy is a technique that probes specific aspects of an unpaired electron's environment through the interaction of the paramagnetic center and an applied magnetic field. EPR spectroscopy is only applicable

to species with one or more unpaired electrons such as inorganic and organic free radicals, triplet states, and transition metal ions [4,6]. This technique has been widely used in the analysis of metalloenzymes that contain transition metal centers.

Theoretical Background

In a typical EPR experiment, the microwave (mw) frequency (ν) is held constant and the magnetic field strength (B_o) is varied. It is also possible to carry out EPR experiments wherein the magnetic field is held constant and the frequency is varied until a transition occurs. When the appropriate magnetic field is reached to split the M_S states to allow for an absorption event of the applied microwave frequency, an EPR spectrum is produced. The most common EPR experiments are performed at a microwave frequency of about 9.3 GHz, known as X-band. Q-band (35 GHz) and W-band (95 GHz) are common and P-band (15 GHz) and K-band (18 GHz) have also been used. EPR spectrometers are tuned to detect signals that change amplitude as the field changes, resulting in a signal which is output as the first derivative (Δ signal amplitude / Δ magnetic field) of an absorption spectrum [4,6].

An isolated electron in the absence of outside forces has an intrinsic angular momentum spin (S) and since an electron is charged, the angular motion of the charged particle generates its own magnetic field. Due to its charge and angular momentum, the electron acts like a small bar magnet, or magnetic dipole, with a magnetic moment, μ, and $S \propto \mu$. Like a bar magnet, the magnetic moment of an electron has no preferred direction in space, but when an electron is placed under an external magnetic field, it experiences Zeeman interactions. A bar magnet, like a compass needle that points north, tends to

orient in an external magnetic field (B_o) into two orientations: a more favored orientation and a least favored orientation with an infinite number of states in between. An electron, on the other hand, has a set intrinsic angular momentum of $S = ½$. Therefore, an electron only has two orientations in an external field: $M_S = ½$ and $M_S = -½$ (Figure 3.1). The lower energy level, $M_S = -½$, is aligned with the magnetic field (stabilized) and the higher

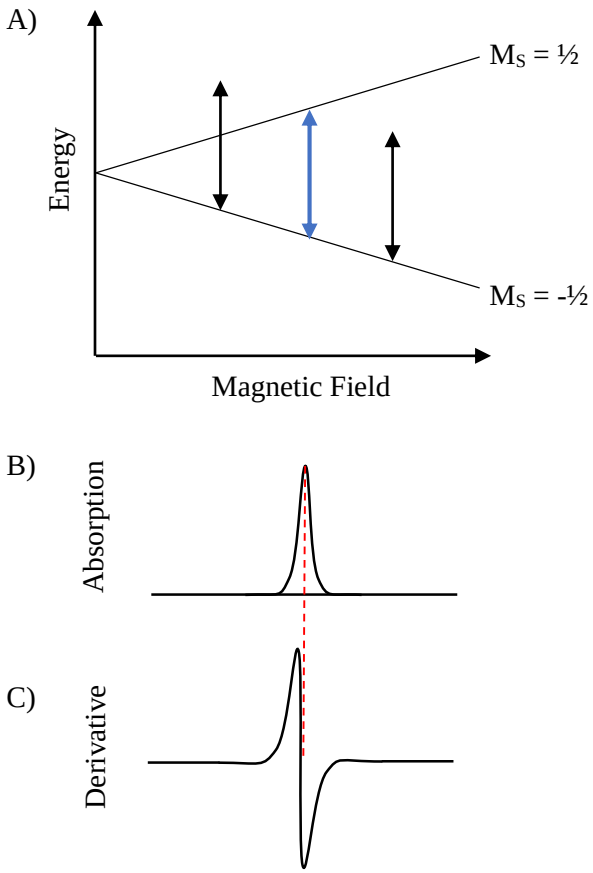


Figure 3.1. A simple energy level diagram in the presence of a magnetic field and a representative absorption and derivative spectrum. A) The splitting of the two $M_S = \pm ½$ energy levels in the presence of a magnetic field is shown. The double headed arrows represent the microwave quantum and when the difference in energy levels is equal to the microwave quantum (blue arrow), an absorption of microwave energy occurs and an absorption spectrum is generated (b). The derivative of the absorption (c) is generally reported by the spectrometer.

energy level, M_S = ½, is aligned against the magnetic field (destabilized) [7]. The interaction of an electron with a magnetic field to induce splitting of the energy levels is called the Zeeman interaction. The energy of an electron with $M_S = \pm$ ½ is (Equation 1):

$$E_{\pm 1/2} = \pm \frac{1}{2} g_e \beta B_o \quad (1)$$

where β is the Bohr magneton, the natural unit of an electron's magnetic moment, and g_e is the spectroscopic g-factor of the free electron with the value g_e = 2.0023 [4,6,7]. When a uniform magnetic field is applied to a paramagnetic species, the ground state levels are split into $E_{1/2}$ and $E_{-1/2}$, separated by ΔE (Equation 2):

$$\Delta E = E_{1/2} - E_{-1/2} = \left(\frac{1}{2} g \beta B_o\right) - \left(-\frac{1}{2} g \beta B_o\right) = g \beta B_o \quad (2)$$

In order for a transition to occur, or a spin flip from the lower energy level to the higher energy level, energy (ΔE) is required and is given by Equation 3:

$$\Delta E = h\nu = g \beta B_o \quad (3)$$

where h is Planck's constant and ν is the microwave frequency. When Equation 3 is satisfied, the sample is in resonance and absorption of the microwave energy occurs (Figure 3.1). For an EPR transition, ΔM_S can only change by $\pm$ 1 unit [4,6,7].

Population Difference is
Key for an EPR Absorption Event

In order for absorption of a microwave to occurring during an EPR experiment, there needs to be a net difference in population between the more-stable (M_S = -½) and the less-stable (M_S = ½) states. This requires that the number of transitions from the more-stable to less-stable states (by flipping the spin) exceed those in the opposite direction, by either relaxation or emission to the M_S = -½ state [6].

Since X-band microwaves are used to irradiate samples, the separation between the energy levels is small (~0.3 cm^{-1} for X-band) which causes the difference of spins between the two M_S levels to also be small. At room temperature, there is only ~0.5% net excess of spins in the lower level [4]. With the application of microwaves, the populations tend to equalize and thus decrease the observed absorption. During a spectral scan, the radiation-induced $M_S = -½ \rightarrow M_S = ½$ transition has the same probability of occurring as the opposite direction. Although there is an equal probability for a transition in either direction, a net absorption is observed because there is more spin in the lower level initially. Thus, the number of spins in the upper level will increase relative to the lower level, resulting in a decrease in a population difference between M_S states and consequently decreasing the net absorption, which is also known as saturation. A difference between the levels is maintained through non-radiative spin relaxation processes, known as spin-lattice relaxation, which will decrease the number of spins in the upper level. As long as the spin-lattice relaxation rate is greater than the rate of radiation-induced transitions, the population difference will be maintained, absorption can occur, and an EPR spectrum will be produced [6].

Electrons in Molecules

A paramagnetic species in a biological environment is surrounded by amino acids, solvent, and other molecules, causing the unpaired electron to possess some orbital angular momentum (*L*) in addition to its intrinsic spin angular momentum (*S*). The magnetic moment depends on the total paramagnetism which involves both the spin and the orbital angular moment. Generally, the orbital angular moment is approximately zero

for an electron in the ground state where a spin-only system exists with an effective *g*-factor equal to that of a free electron (g_e = 2.0023). However, in most systems, mixing of this ground state with excited states by spin-orbit coupling gives back some orbital angular momentum, or a coupling contribution. The magnitude of the spin-orbit coupling contribution is dependent on the size of the nucleus that the unpaired electron resides. In the case of organic free radicals, such as a radical on H, O, C, and N atoms, a small contribution from spin-orbit coupling is observed and its *g*-factor will be close to g_e. If an unpaired electron is associated with larger elements, such as transition metals, the *g*-factor may be significantly perturbed from g_e [4].

Anisotropy

Deviation from the g-factor of a free electron (g_e) arises from the spin-orbit coupling between the ground and excited states. Since orbitals are oriented in a molecule, the magnitude of mixing is direction-dependent, or anisotropic [6]. In a solution, the anisotropy is averaged out. However, in a fixed orientation, such as a crystal, the *g*-factor would change as you rotated the crystal in the spectrometer due to *g* anisotropy. In frozen samples, on the other hand, the paramagnets are not rapidly rotating as in a solution nor are they aligned in a set direction like a crystal but they are fixed in all possible orientations.

For each paramagnetic species, there is a unique axis system called the principal axis and the *g*-factors measured along this axis are called the principal g-factors (g_x, g_y, and g_z). An EPR spectrum can be classified as one of three spectral types: isotropic, axial, or rhombic (Figure 3.2). In an isotropic spectrum, the principal *g*-factors are the

same ($g_x = g_y = g_z$), the magnetic moment is independent of orientation, and the resultant spectrum is a single symmetric line. In an axial spectrum, there is a unique axis that differs from the other two ($g_x = g_y \neq g_z$). The unique g value is parallel to the axis, called $g_{\parallel}$, while the two common g values that are perpendicular to it are referred to as $g_{\perp}$. Since the $g_{\perp}$ value has twice the probability of occurring than the $g_{\parallel}$ does, the spectrum is more intense in the $g_{\perp}$ region. A rhombic spectrum, on the other hand, occurs when all the g-factors differ ($g_x \neq g_y \neq g_z$) [4].

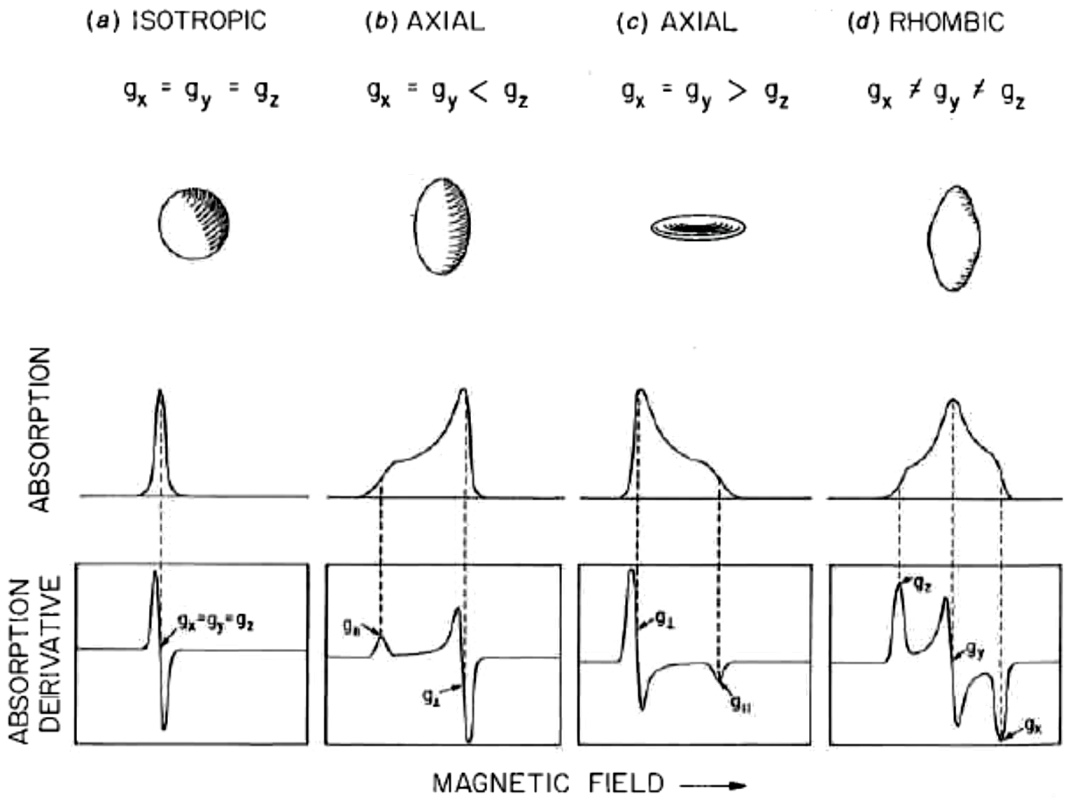


Figure 3.2. Representative EPR signals originating from $S = ½$ systems. The columns (a-d) give the spectral type, the associated pattern of g anisotropy, a symmetry diagram as a solid body, and the graphical absorption and derivatives. The isotropic symmetry body is spherical while the axial symmetry can either be prolate (like a football) or oblate (like a discus). The rhombic body is more like a partially inflated football. In the absorption and derivative graphs, the dashed line correlate to the absorption peaks to its perspective derivative feature. Figure taken from [4].

Hyperfine Interactions:
The Effect of Nuclear Spin

In most systems, the paramagnetic species can be affected by neighboring magnetic nuclei and these interactions are known as hyperfine interactions. Going back to a classical bar magnet, a magnet will align itself with an external magnetic field (Zeeman interactions). But the energy of the bar magnet can also be influenced by interactions with a neighboring bar magnet (Figure 3.3) and the magnitude of these interactions is dependent on the distance of separation and the alignment of the two magnets [7]. An analogous interaction can occur between a paramagnetic species and a neighboring magnetic nucleus ($I > ½$), known as the hyperfine interaction. The effect of the hyperfine interaction can be added as a term to the energy expression for an EPR transition (Equation 4):

$$\Delta E = h\nu = g\beta B_o + hAM_I \quad (4)$$

where A is the hyperfine coupling constant (measured in cm^{-1} or MHz) and M_I is the magnetic quantum number for the nucleus. Since there are $2I + 1$ possible values of M_I, the hyperfine interaction thus splits the Zeeman transition into $2I + 1$ lines of equal intensity (Figure 3.3b) [6]. For examples, the interaction of an electron with a proton ($I = ½$) will produce an EPR spectrum which contains two lines ($M_I = ½, -½$) while interaction with ^{14}N ($I = 1$) contains three lines ($M_I = 1, 0, -1$). The energy separation between these lines is equal to hA but is termed the hyperfine splitting constant (a) and is measured and expressed in magnetic field units (Gauss or Tesla) [4]. These interactions are the basis of ENDOR spectroscopy which will be discussed later.

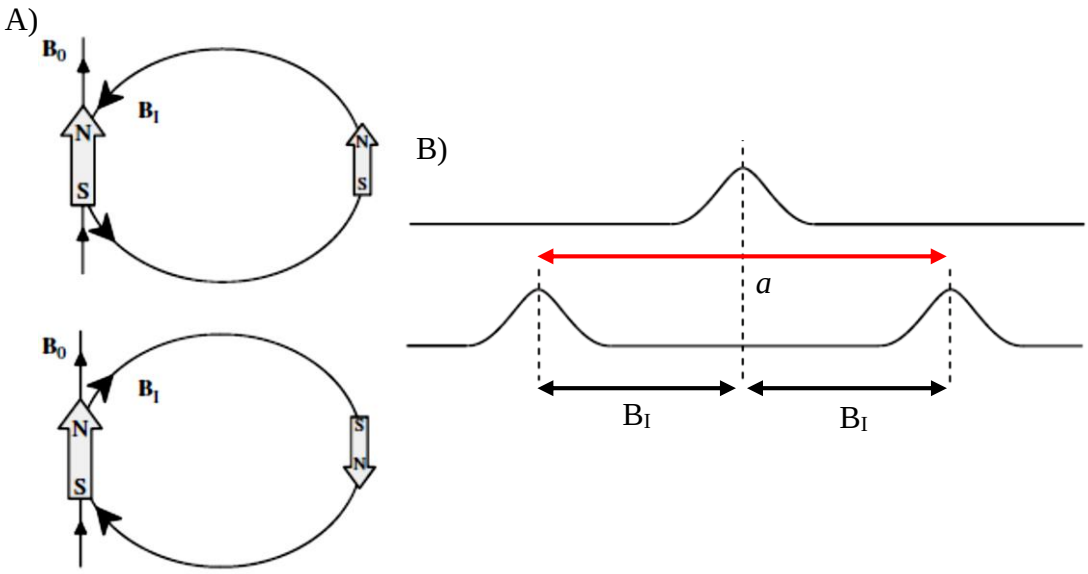


Figure 3.3. Origin of a hyperfine interaction with a bar magnetic representation (a). A magnetic moment of a nucleus produces a magnetic field (B_I) at the electron. This field either opposes (top) or adds (bottom) to the applied magnetic field (B_0) depending on the alignment of the nucleus. When B_I adds to the magnetic field, less applied magnet field is required and the resonance field is lowered by B_I; while if B_I opposes the laboratory field, the opposite is true, producing two absorption peaks (b). The spacing between the two absorption peaks for an $I = ½$ system is equal to the hyperfine splitting constant a (red arrow). Figure taken and modified from [7].

In addition to hyperfine interactions, a paramagnetic species can interact with "satellite" magnetic nuclei rather than the parent nucleus, which is known as super-hyperfine interactions. An example is an organic radical where the unpaired electron is found in an orbital delocalized over a large aromatic framework, and thus might be under the influence of a number of nuclei. Another example is when a paramagnetic metal complex contains ligands with nuclear spin. For an unpaired electron exposed to n equivalent nuclei, the number of lines the spectrum is split into is equal to $2nI + 1$ but the intensity of the individual lines vary. For an $I = ½$ nucleus, the intensity distribution is

predicted by Pascal's triangle where the four line pattern has the relative intensities 1:3:3:1 [4,6].

Advantages and Disadvantages of EPR Spectroscopy

Like most spectroscopic techniques, EPR does have its downsides. As discussed above, there are many conditions that must be fulfilled in order to obtain an EPR spectrum. To begin, the system studied must contain a paramagnetic species. Most metalloenzymes contain transition metals in their active sites which are, in most states, paramagnetic. Secondly, the temperature of the sample is important. Most EPR samples must be frozen and kept frozen during an experiment since most are prepared in aqueous solutions that absorb microwaves, causing the sample to heat up. In order to maintain a population difference between M_S states, the sample must be run at the lowest temperature possible, while keeping in mind that the optimal temperature does need to be determined because samples can saturate at low temperatures and exhibit line broadening at high temperatures [7]. The paramagnetic center must have a fast enough relaxation time to maintain the population difference between M_S energy levels or the sample reaches saturation. Lowering the temperature can decrease the relaxation rate for some systems. The appropriate microwave power must be also be optimized. If the power is too high, too much absorption occurs and the system will become saturated. Many other considerations must be taken for individual samples/systems.

For most metalloproteins, the advantages outweigh the disadvantages. EPR spectroscopy can reveal information about the ground state, oxidation state, the local

symmetry of the metal center, and geometric and electronic structure of the metal site. Only a paramagnetic signal is visible in an EPR experiment, such as an active site metal ion, while the rest of the protein is silent. Thus, in EPR, only the active site environment gives rise to a signal and we can look at how the active site changes throughout its catalytic process (with and without substrates, products, or inhibitors).

Electron Nuclear Double Resonance Spectroscopy

Many paramagnetic metalloproteins exhibit a broad, low symmetry (either an axial or rhombic) EPR spectrum that can provide generic information about the metalloprotein but it provides little detailed information. These systems are great candidates for ENDOR spectroscopic investigation to provide more detail on the metal coordination environment and possible mechanistic insight not obtainable from EPR alone [8-10]. ENDOR spectroscopy can provide information related to the electronic and magnetic properties of a metal site(s), insight into enzyme mechanisms such as transition states, protein dynamics, and structural information such as coordination geometry, valency of the metal site, and identification of ligands [9-11].

Metalloproteins generally don't have well defined hyperfine splitting which creates line broadening. In contrast, NMR exhibits narrow lines from a specific nucleus that contains chemical shift and spin coupling information, but NMR is insensitive since the nuclear magnetic moment is much smaller in comparison to an electron. Therefore, ENDOR combines EPR and NMR by detection of the NMR resonances by observing their effect on an EPR signal (EPR-detected NMR) [9]. The EPR signal is measured at a

fixed magnetic field (a specific *g* value) and its intensity is varied by scanning an applied radio frequency (rf) to probe the NMR active sites.

What ENDOR Spectroscopy Can Detect

ENDOR spectroscopy is used to study the magnetic interactions of an unpaired electron with the spins of a magnetic nucleus, or the hyperfine interactions. It monitors the actual NMR transitions induced by an rf field but does not directly detect the transitions. With the application of a fixed microwave frequency, a specific EPR transition (one g value) is promoted. When the rf field is applied and swept through a selected range, the NMR transitions are monitored as a change in the EPR signal intensity at this transition. The resulting spectrum has orders of magnitude better resolution than an EPR spectrum at a specific *g* center. Thus, ENDOR spectroscopy can be used to characterize hyperfine and quadrupole interactions of systems that show little or no hyperfine splitting [4,11,12]. The nucleus, which contains a nuclear spin of $I \geq ½$, can either be the parent molecule where the unpaired electron resides or on a nearby nucleus which has orbital overlap with the unpaired electron.

The hyperfine coupling interaction between a paramagnetic center and a nucleus can provide a wealth of information. Hyperfine coupling is related to the electron spin delocalized onto a given nucleus, providing information on the type of bond, the geometry, and structural information.

General Theory

In an ENDOR experiment, a fixed magnetic field (for a specific *g* value) is chosen and the EPR signal is saturated or partially saturated. The ENDOR signal can be described as an NMR-induced desaturation of this EPR saturated signal. An example of an energy level diagram is depicted in Figure 3.4 for the simplest system with one paramagnetic species with $S = ½$ and one nuclear spin with $I = ½$. During application of a magnetic field, the ground state levels are split into two levels: $M_S = -½$ and $M_S = ½$ (the Zeeman interactions as discussed in the EPR discussion). When a nucleus with a

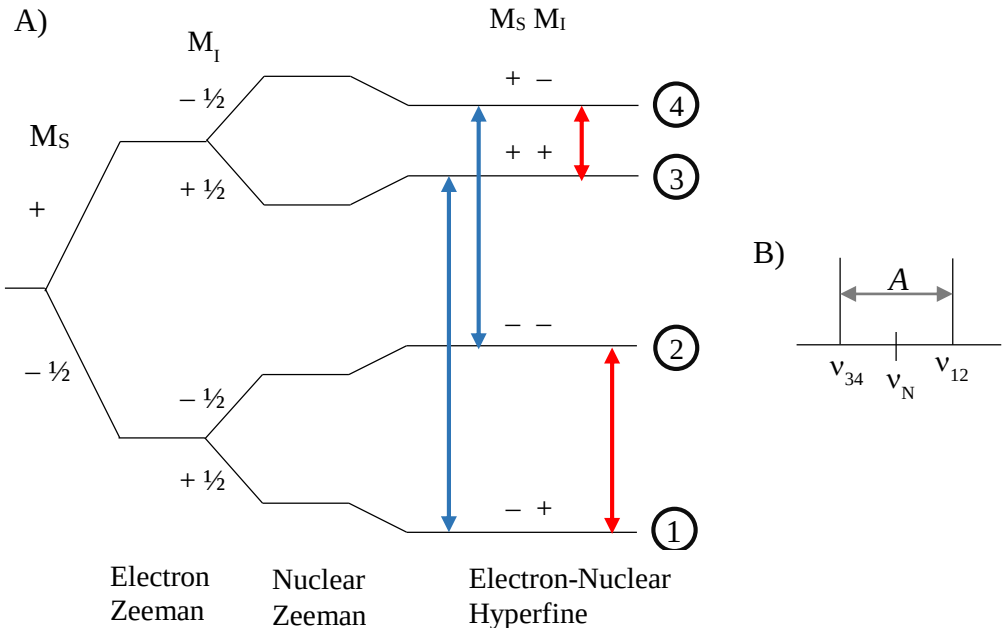


Figure 3.4. The energy level diagram for an $S = ½$ paramagnetic species interacting with an $I = ½$ nuclear spin (a). EPR transitions are shown in blue while NMR (ENDOR) transitions are shown in red. B) A simple stick representation of a weakly coupled paramagnetic species and a nucleus for the energy diagram in (a). The numbered frequencies ($\nu_{\#\#}$) represent a transition (red arrows in (a)) between the corresponding numbered energy level. The lines are split by the hyperfine constant (*A*) and centered at the Larmor frequency (ν_N). See text for more detail.

nuclear spin $I \geq ½$ is present (hyperfine interactions), the M_S levels are further split into two M_I levels, $M_I = -½$ and $M_I = ½$. An EPR allowed transition has the selection rules $\Delta M_S = \pm 1$ and $\Delta M_I = 0$ while an NMR allowed transition has the selection rules of $\Delta M_S = 0$ and $\Delta M_I = \pm 1$. Following these selection rules, an EPR transition shown in Figure 3.4 is represented as a solid blue arrow and the NMR (ENDOR) transitions are represented as a solid red arrow. During an ENDOR experiment, the magnetic field is set to a specific EPR transition between 2 and 4, for example. This signal is saturated with microwave power, equalizing the electron spin populations on these two levels. When the rf field is scanned and the energy matches that of an NMR transition between 3 and 4, an NMR transition occurs, increasing the population in level 4. The populations in levels 2 and 4 will no longer be equal, or the EPR levels are no longer saturated, and an EPR absorption can occur. This new population difference allows for a net absorbance of the microwave frequency in the EPR transition and thus an ENDOR signal is produced [13].

Figure 3.4b shows a simplified ENDOR stick spectrum that would occur for the simple $S = ½$, $I = ½$ system. A nuclear transition in the upper levels from 3 → 4 (red arrow from Figure 3.4a), will produce one ENDOR line while a transition between the lower levels from 1 → 2 will produce another ENDOR line. Each unique nucleus ($I > ½$) will produce two ENDOR peaks (a doublet) and the number of ENDOR lines for a nucleus with spin I is given by the rule of $4I$ lines ($2I$ NMR lines for each of the two Ms states) [4]. The rf frequencies where these NMR transitions can occur ($\nu_{\pm}$) are related to the Larmor frequency of the nucleus (ν_N), which is specific for each nucleus, and the hyperfine coupling constant (A) (Equation 7):

$$\nu_{\pm} = |\nu_N \pm \frac{A}{2}| \quad (7)$$

In cases where the nuclear Zeeman splitting is dominant (also known as weak coupling), the doublet is centered at the Larmor frequency and the peaks are split by *A*. When the hyperfine splitting is dominant (or strong coupling), the signals are centered at *A*/2 and split by $2\nu_N$ (twice the Larmor frequency). Generally, weak coupling is typical for a ^{1}H ($I = ½$) that has a large nuclear *g*-factor (g_N). A strong coupling is typically found for ^{57}Fe, which has a small g_N value but large hyperfine coupling since, in most cases, the paramagnetic species resides on the transition metal [10,11].

Different ENDOR Spectroscopic Techniques

There are two different types of ENDOR experiments: continuous wave (CW) and pulsed techniques. CW ENDOR of metalloenzymes most often has better sensitivity than pulsed because generally, a microwave pulse cannot flip all the electron spins in a sample. On the other hand, pulsed ENDOR experiments often give better line shapes and resolution and one can vary the pulse sequences to optimize for a given sample [10].

CW ENDOR. CW ENDOR spectroscopy is generally more sensitive than pulsed techniques but with the expense of resolution [9]. Usually, CW experiments are done first to investigate what signals are present in a sample before pulsed techniques are employed to obtain higher resolution. Some signals are too weak for CW analysis and other techniques are required. The CW experiment is conducted by the saturation of an EPR signal through an increase in mw power. The recovery of this signal is then monitored as a function of the frequency of continuously irradiated rf waves (as

described above). When the rf matches the nuclear transition, the populations of the energy levels are changed and microwaves can then be absorbed and this absorption is detected [12].

Pulsed ENDOR Spectroscopy. Pulsed ENDOR techniques are based on the electron spin echo (ESE) effect. An echo signal is created through the application of a microwave pulse. An rf pulse is applied during a "mixing period" between microwave pulses which drives nuclear spin transitions and changes the ESE intensity. The ENDOR signal is then measured as the amplitude of this change when the rf is scanned. There are two widely used pulsed techniques called Mims and Davies that are used to probe different degrees of coupling between the paramagnetic center and the target nucleus.

The Mims pulsed technique is ideal for providing high resolution spectra of a nucleus that has small hyperfine couplings (weak coupling, generally less than 2 MHz, with the paramagnetic center). Good candidates for Mims are ^{2}H, ^{13}C, and ^{15}N from specifically labeled molecules which are interacting with a paramagnetic site via longer range dipole coupling [9]. A Mims pulsed sequence is shown in Figure 3.5a. Both EPR transitions are excited by a microwave pulse ($\pi/2$). A delay time is present between the first mw pulse after which there is a mixing period. During this mixing period, a frequency-swept rf pulse is applied to cause transfer between the electronic and nuclear transitions. A third mw pulse then generates the ESE which is observed during the detection period. Usually this sequence is repeated for a sample (~20 pulsed sequences). There is a delay time between repeats which ideally restores the EPR energy levels.

Another pulsed technique termed Davies is useful for detection of strongly coupled systems. A sequence is shown in Figure 3.5b. An initial mw pulse is applied which inverts the EPR transition followed by the mixing period where a frequency-swept rf pulse is applied to stimulate nuclear transitions. When the rf frequency is equal to a nuclear frequency, a nuclear transition occurs, changing the population in the nuclear levels, thus affecting the population of the EPR transitions as well. This effect is detected by the echo intensity through the final part of the pulse sequence (π/2-τ-π-τ-echo).

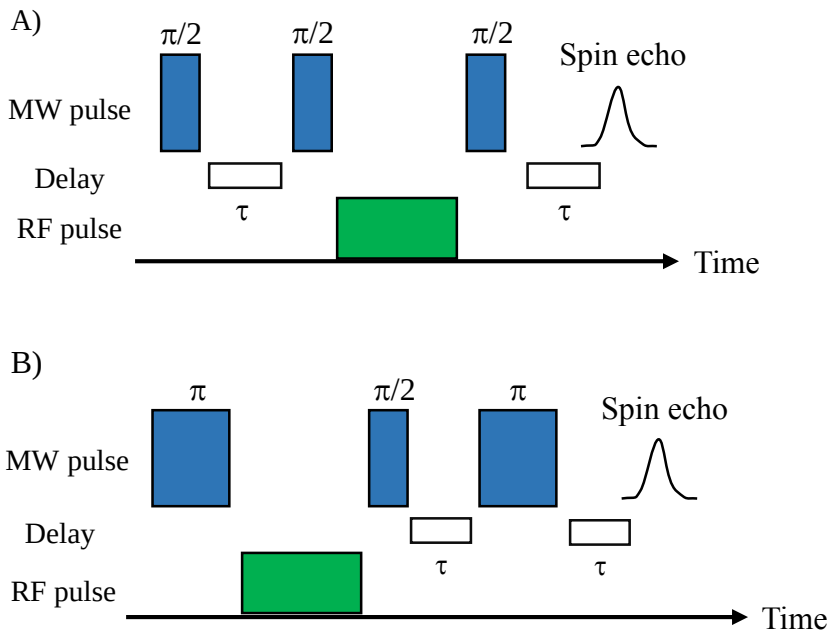


Figure 3.5. The pulse sequence for Mims (a) and Davies (b) ENDOR. Each technique has a different sequence of microwave (mw) pulses (blue boxes) to induce EPR transitions and radiofrequency (rf) pluses (teal boxes) to induce NMR transitions. A wait time, or delay time (white boxes) occurs at different times for each technique. After each sequence, a spin echo is recorded.

Optimizing an ENDOR Experiment for Metalloproteins

Most metalloprotein systems do not contain just one nucleus with $I > ½$ but rather contain multiple nuclei which ligate the metal center. Many nuclei have Larmor values at low frequencies (less than 5 MHz) and thus assignments are often complicated due to overlapping signals [14]. A shit from X-band (9-10 GHz) to Q-band (35 GHz) frequency is usually sufficient to move and separate the field-dependent Larmor frequency of a proton, for example, from a nitrogen. The field-dependent hyperfine component is unaffected.

Advantages and Disadvantages of ENDOR Spectroscopy

ENDOR spectroscopy has similar advantages and disadvantages as an EPR experiment but the information retrieved from an ENDOR experiment can be very valuable and cannot be obtained from any other spectroscopic technique.

ENDOR spectroscopy can also give information about a metal containing active site and it can discriminate against nuclei that are not part of the active site: signals only arise from a nucleus that has hyperfine interactions with the electron-spin system under observation, such as only the active site atoms. For example, it is possible to examine ^{57}Fe resonances from one Fe-S cluster without interference from other unlabeled Fe-S clusters or from excess ^{57}Fe not bound to protein [10].

As stated previous, in order to have an ENDOR signal, there needs to be a nucleus with $I > ½$ coupled to a paramagnetic species. Not all naturally abundant isotopes have nuclear spin, which can actually be advantageous. Through isotopic labeling, one can

characterize every atom associated with a paramagnetic center individually [9]. For example, in radical SAM enzymes, the SAM molecule can be isotopically labeled on select carbon molecules with ^{13}C. Any ^{12}C molecules ($I = 0$) cannot couple with [4Fe-4S]$^{+}$ cluster and do not produce an ENDOR signal. Multiple ENDOR experiments can be conducted with individual ^{13}C labeled SAM sites and the distances of each carbon can be determined. This was done with the radical SAM enzyme PFL-AE with [methyl-^{13}C]-SAM and [carboxyl-^{13}C]-SAM to determine how SAM was coordinated to the cluster prior to SAM cleavage [15,16] (Figure 3.6).

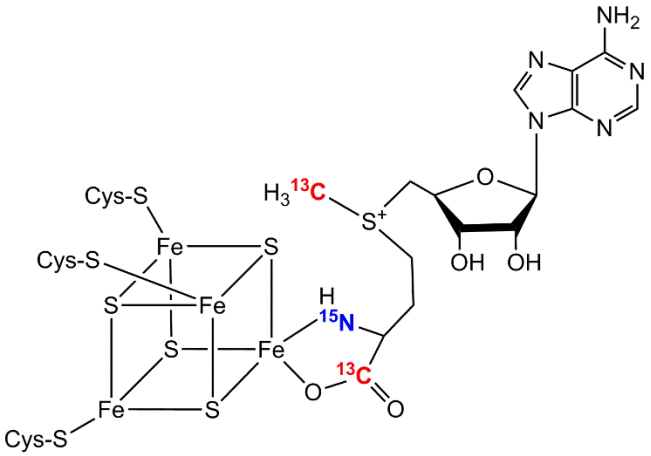


Figure 3.6. SAM coordination to the [4Fe-4S] cluster determined with ENDOR spectroscopy of PFL-AE in the presence of different isotopically labeled SAM molecules. Colored ^{13}C (red) and ^{15}N (blue) isotopes were labeled in different SAM molecules which were used for subsequent ENDOR experiments.

Isotope effects can also be monitored with ENDOR spectroscopy to determine if a molecule is interacting with (or directly coordinated to) the paramagnetic center. An example includes preparing samples in $^{2}H_2O$ which Werst *et al.* performed on the [4Fe-4S] cluster containing protein aconitase [17]. When samples were prepared in

$^{2}H_2O$, a strongly coupled ^{1}H ENDOR signal disappeared and a new strongly coupled ^{2}H signal appeared. The authors concluded that an H_xO species was coordinated to the [4Fe-4S]$^{+}$ cluster in the presence and absence of substrate [17]. Another example in radical SAM enzymes is with PFL-AE and an isotopically labeled ^{15}N-amino-SAM (Figure 3.6). With the addition of the ^{15}N-amino SAM, the strongly coupled ^{14}N signal disappeared and shifted to become a strongly coupled ^{15}N signal [16].

ENDOR spectroscopy can also obtain valuable information about intermediate states during catalysis in metalloproteins that cannot be observed by other methods such as x-ray crystallography. ENDOR spectroscopy, in conjunction with other techniques such as rapid freeze quench, can trap and identify reaction intermediates.

EPR and ENDOR Spectroscopic Applications for Fe-S Clusters

EPR and ENDOR spectroscopic techniques can be applied to Fe-S containing metalloproteins to obtain information about the cluster type and its coordination environment, which will be discussed below. Due to the different oxidation states of Fe-S clusters, only some oxidation states are paramagnetic, or EPR active, which will also be discussed below.

Electron Delocalization and Spin States of Fe-S Clusters

The localization and delocalization patterns in Fe-S clusters are summarized in Figure 3.7. In the simple case of an oxidized [2Fe-2S]$^{2+}$ cluster, two Fe^{3+} atoms are present in the cluster, each containing a 5/2 spin which are antiparallel and are

antiferromagnetically coupled with a resulting spin of 0, an EPR silent state. In the one electron reduced state, a $[2Fe\text{-}2S]^{+}$ cluster, the electron settles on one Fe, producing a Fe^{2+} and Fe^{3+} pair. These local spins, 4/2 (or 2) and 5/2, couple antiferromagnteically with a resulting spin of ½ (Figure 3.8) which can be observed with EPR techniques. In the case of an oxidized $[4Fe\text{-}4S]^{2+}$ cluster, there are $2Fe^{3+}$ and $2Fe^{2+}$ resulting in two mix-valence pairs (two Fe^{2+}-Fe^{3+} pairs) with spins of 9/2 which are antiferromagnetically coupled, resulting in a net spin of 0. These clusters can be thought of as containing two

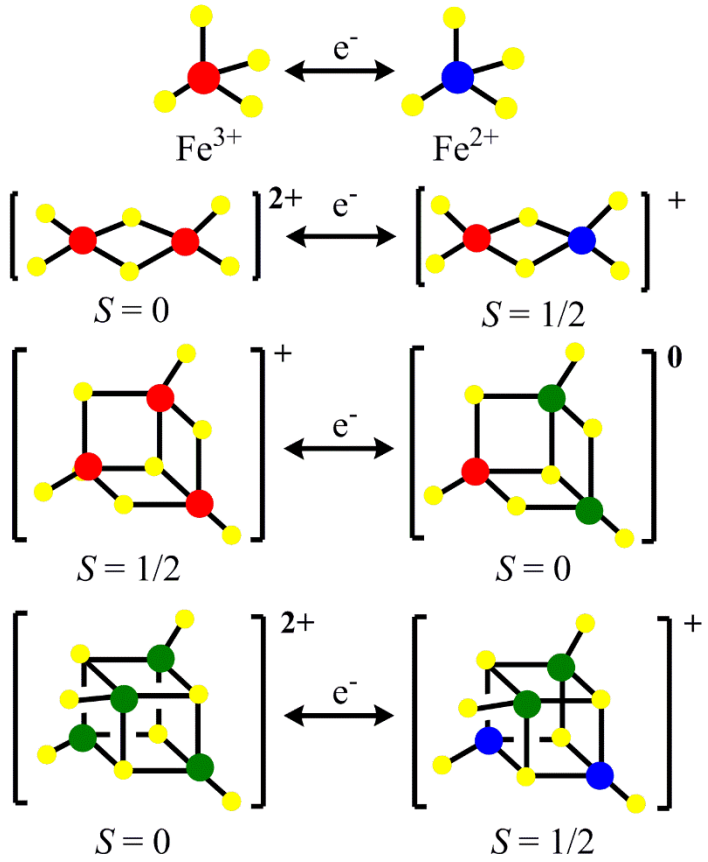


Figure 3.7. Localization and delocalization patterns of Fe-S clusters in different cluster oxidation states as indicated with brackets. The localized Fe^{3+} (red circles) and Fe^{2+} (blue circles) sites and delocalized $Fe^{2.5+}$-$Fe^{2.5+}$ pairs (green circles) are shown with bound sulfur atoms (yellow circles). The overall spin state is shown below each cluster.

delocalized $Fe^{2.5+}$-$Fe^{2.5+}$ pairs. Upon one electron reduction to the $[4Fe\text{-}4S]^{+}$ state, a mix-valence pair ($Fe^{2.5+}$-$Fe^{2.5+}$ pair) and a Fe^{2+}-Fe^{2+} pair are each ferromagnetically coupled yielding spins of 9/2 and 8/2 (4), respectively. These pairs are then antiferromagnetically coupled, resulting in a net ½ spin for the cluster [18].

The advantage of a delocalized Fe-S cluster is that an electron delocalized over a metal cluster can be transferred more efficiently than from a single metal site [18]. The delocalization spreads the electron out over a larger structure, reducing the reorganization energy that is required for the interconversion between the oxidized and reduced structures.

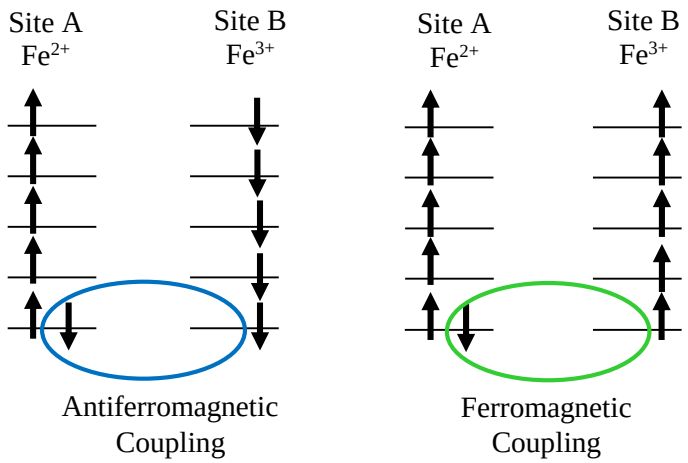


Figure 3.8. Delocalization of spin for a symmetric Fe^{2+}-Fe^{3+} dimer. Antiferromagnetic coupling spin alignments are shown on the left and ferromagnetic coupling is shown on the right.

EPR and ENDOR Spectroscopic Considerations for Fe-S Clusters

Fe-S clusters usually contain non-isotropic EPR signals with line broadening due to their lower symmetry, coordination environment within metalloenzymes which

complicates an EPR spectrum. Nonetheless, EPR spectroscopy of Fe-S clusters can provide information about the structure and biological function that other techniques cannot. For example, $[3Fe\text{-}4S]^{+}$ clusters exhibit isotropic signals while $[2Fe\text{-}2S]^{+}$ and $[4Fe\text{-}4S]^{+}$ clusters have axial or rhombic signals. The electronic structures of the clusters can be investigated through hyperfine interactions with isotopically labeling the clusters with ^{57}Fe and ^{33}S and analysis by ENDOR spectroscopy. The redox states of clusters can also be determined under different conditions along with the midpoint redox potentials [19-21]. The type of Fe-S cluster present in a metalloenzyme can be determined since each type of cluster produces a unique signal with different relaxation properties that are affected by different temperatures and mw power (discussed below).

In a system with only one Fe-S cluster, the only possible interactions are the superhyperfine interactions with a magnetic nucleus present in the second and higher coordination spheres, such as ^{1}H, naturally abundant ^{13}C (1.11% abundance), and ^{14}N from coordinated residues and added substrates. In standard CW EPR spectroscopy, the hyperfine splitting from ligands are not usually resolved and thus contribute to inhomogeneous line broadening.

Temperature and Power Effects on Fe-S Clusters

The EPR signals of Fe-S clusters are affected by temperature and mw power to varying degrees depending on Fe-S cluster type. This property can be very useful in determining the type of cluster(s) in the system of interest and extracting the individual signal components from proteins that contain a complicated, multi-cluster spectrum. In

general, Fe-S clusters are easily saturated with microwave power at lower temperatures but less at higher temperatures since the relaxation times increase. But these relaxation properties can be dependent on the Fe-S cluster. At higher temperatures, the excited states (M_s = ½) becomes more populated which causes the signals to disappear, particularly the signals from $[4Fe\text{-}4S]^+$ clusters [5]. $[4Fe\text{-}4S]^+$ clusters will only produce an EPR signal below 30 K while $[2Fe\text{-}2S]^+$ will produce a signal for temperatures $\leq$ 100 K [22]. At low temperatures ($\leq$ 15K) $[2Fe\text{-}S]^+$ clusters are more susceptible to power saturation with high mw power settings, while $[4Fe\text{-}4S]^+$ clusters are more resistant and do no exhibit signal saturation effects under these conditions [22]. These effects are due to a more efficient electron-spin relaxation in $[4Fe\text{-}4S]^+$ clusters and their ability to delocalize the unpaired electron over two [2Fe-2S] rhombs which are antiferromagnetically coupled. However, the rate of relaxation is dependent on the geometry and the environment of the cluster and these effects can be an over-simplification.

EPR and ENDOR spectroscopies are powerful techniques that can analyze metalloproteins throughout the different stages of catalysis and can be used in conjunction with other spectroscopic techniques to obtain a more complete picture of its active site. EPR and ENDOR spectroscopies can be applied to a wide range of metalloproteins, not just Fe-S containing enzymes, which contain a transition metal which is paramagnetic in at least one oxidation state to provide information about the coordination of metal.

References

1. Sweeney, W. V.; Rabinowitz, J. C. *Annu. Rev. Biochem.* **1980**, *49*, 139-161.

2. Beinert, H.; Holm, R. H.; Munck, E. *Science* **1997**, *277*, 653-659.

3. Pandelia, M. E.; Lanz, N. D.; Booker, S. J.; Krebs, C. *Biochim. Biophys. Acta* **2015**, *1853*, 1395-1405.

4. Que, L. J. *Physical Methods in Bioinorganic Chemistry : Spectroscopy and Magnetism*; University Science Books: Sausalito, CA, 2000.

5. Cammack, R.; MacMillan, F. In *Metals in Biology: Applications of High-Resolution EPR to Metalloenzymes*; Hanson, G., Berliner, L., Eds.; Springer: New York, 2010; Vol. 29.

6. Hales, B. J. In *Applications of Physical Methods to Inorganic and Bioinorganic Chemistry*; Scott, R. A., Lukehart, C. M., Eds.; John Wiley and Sons, Ltd.: England, 2007, p 40-53.

7. Eaton, G. R.; Eaton, S. S.; Barr, D. P.; Weber, R. T. *Quantitative EPR*; Springer Vienna, 2010.

8. Hoffman, B. M. *Acc. Chem. Res.* **1991**, *24*, 164-170.

9. Hoffman, B. M. *Proc. Natl. Acad. Sci. USA* **2003**, *100*, 3575-3578.

10. Hoffman, B. M. *Acc. Chem. Res.* **2003**, *36*, 522-529.

11. Telser, J. In *Applications of Physical Methods to Inorganic and Bioinorganic Chemistry*; Scott, R. A., Lukehart, C. M., Eds.; John Wiley and Sons, Ltd.: England, 2007, p 99-124.

12. Kulik, L.; Lubitz, W. *Photosynth. Res.* **2009**, *102*, 391-401.

13. Van Doorslaer, S.; Vinck, E. *Phys. Chem. Chem. Phys.* **2007**, *9*, 4620-4638.

14. Murphy, D. M.; Farley, R. D. *Chem. Soc. Rev.* **2006**, *35*, 249-268.

15. Walsby, C. J.; Hong, W.; Broderick, W. E.; Cheek, J.; Ortillo, D.; Broderick, J. B.; Hoffman, B. M. *J. Am. Chem. Soc.* **2002**, *124*, 3143-3151.

16. Walsby, C. J.; Ortillo, D.; Broderick, W. E.; Broderick, J. B.; Hoffman, B. M. *J. Am. Chem. Soc.* **2002**, *124*, 11270-11271.

17. Werst, M. M.; Kennedy, M. C.; Beinert, H.; Hoffman, B. M. *Biochemistry* **1990**, *29*, 10526-10532.

18. Beinert, H. *J. Biol. Inorg. Chem.* **2000**, *5*, 2-15.

19. Cutsail, G. E., 3rd; Telser, J.; Hoffman, B. M. *Biochim. Biophys. Acta* **2015**, *1853*, 1370-1394.

20. Kappl, R.; Bracic, G.; Huttermann, J. In *High Resolution EPR: Applications to Metalloenzymes and Metals in Medicine*; Hanson, G., Berliner, L., Eds.; Springer: New York, 2009; Vol. 28, p 63-103.

21. Lund, A.; Shiotani, M.; Shimada, S. *Principles and Applications of ESR Spectroscopy*; Springer: New York, 2011.

22. Rupp, H.; Rao, K. K.; Hall, D. O.; Cammack, R. *Biochim. Biophys. Acta* **1978**, *537*, 255-269.

CHAPTER FOUR

EMERGING THEMES IN RADICAL SAM CHEMISTRY

Contribution of Authors and Co-Authors

Manuscript(s) in Chapter(s) 4, 5, 6, 7, 9, 10

Author: Krista A Shisler

Contributions: Wrote manuscript and generated figures.

Co-Author: Joan B Broderick

Contributions: Aided in preparation of manuscript and figures.

Manuscript Information Page

Krista A Shisler and Joan B Broderick
Current Opinion in Structural Biology
Status of Manuscript:
____ Prepared for submission to a peer-reviewed journal
____ Officially submitted to a peer-review journal
____ Accepted by a peer-reviewed journal
__X__ Published in a peer-reviewed journal

Published by Elsevier
Published online November 8, 2012
In Catalysis and Regulation Themed Issue Volume 22, 701-710 (2012)

Available online at www.sciencedirect.com

SciVerse ScienceDirect

Current Opinion in Structural Biology

Emerging themes in radical SAM chemistry

Krista A Shisler and Joan B Broderick

Enzymes in the radical SAM (RS) superfamily catalyze a wide variety of reactions through unique radical chemistry. The characteristic markers of the superfamily include a [4Fe–4S] cluster coordinated to the protein via a cysteine triad motif, typically CX_3CX_2C, with the fourth iron coordinated by *S*-adenosylmethionine (SAM). The SAM serves as a precursor for a 5′-deoxyadenosyl radical, the central intermediate in nearly all RS enzymes studied to date. The SAM-bound [4Fe–4S] cluster is located within a partial or full triosephosphate isomerase (TIM) barrel where the radical chemistry occurs protected from the surroundings. In addition to the TIM barrel and a RS [4Fe–4S] cluster, many members of the superfamily contain additional domains and/or additional Fe–S clusters. Recently characterized superfamily members are providing new examples of the remarkable range of reactions that can be catalyzed, as well as new structural and mechanistic insights into these fascinating reactions.

Address
Department of Chemistry & Biochemistry and the Astrobiology Biogeocatalysis Research Center, Montana State University, Bozeman, MT 59717, United States

Corresponding author: Broderick, Joan B (jbroderick@chemistry.montana.edu, jtbbroderick@gmail.com)

Current Opinion in Structural Biology 2012, **22**:701–710

This review comes from a themed issue on **Catalysis and regulation**

Edited by **Thomas Carell**

For a complete overview see the Issue and the Editorial

Available online 8th November 2012

0959-440X/$ – see front matter, Published by Elsevier Ltd.

http://dx.doi.org/10.1016/j.sbi.2012.10.005

Introduction

The radical *S*-adenosylmethionine (radical SAM, hereafter RS) superfamily of enzymes carry out a wide variety of biological functions including synthesis of cofactors, modification of RNA, DNA repair, and synthesis of antibiotics [1]. There are currently tens of thousands of predicted RS superfamily members spanning the phylogenetic kingdom; however, only a small fraction of these have been characterized. Although the chemistry they catalyze is diverse, the RS enzymes utilize a common mechanism for initiation of catalysis that involves generation of a primary carbon-centered radical intermediate, the 5′-deoxyadenosyl radical (dAdo$^{\bullet}$), which abstracts a hydrogen atom from the substrate [2–4,5$^{\bullet\bullet}$]. The substrate radical can then undergo radical-mediated and often complex transformations to generate product.

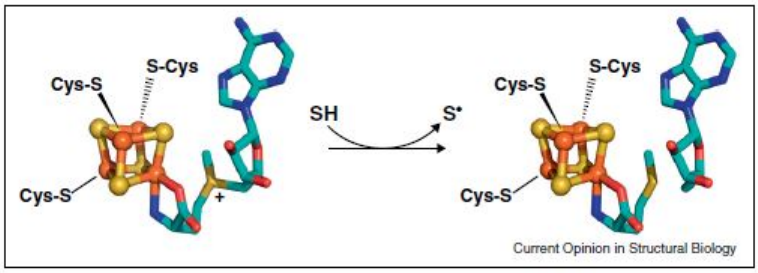
In order to generate the dAdo$^{\bullet}$ radical from SAM, RS enzymes utilize an enzyme-bound [4Fe–4S] cluster. Three of the four irons in the [4Fe–4S] cluster are coordinated by cysteine thiolates (C or Cys) present in a triad motif, generally CX_3CX_2C although variations exist. The fourth iron of the cluster, often referred to as the unique iron due to its distinct coordination, has no cysteine ligand but rather is coordinated by SAM (Figure 1). The iron–sulfur cluster is active in its reduced $[4Fe–4S]^{+}$ state, from which it can transfer an electron to the sulfonium of SAM to promote homolytic cleavage of the S–5′C bond of SAM, producing methionine and a 5′-deoxyadenosyl radical intermediate that abstracts a hydrogen atom from substrate (Figure 1) [6]. The highly reactive nature of the dAdo$^{\bullet}$ radical intermediate [7] confers on these enzymes the ability to carry out diverse and difficult chemical transformations requiring abstraction of a hydrogen atom from generally unactivated positions on the substrate. The utilization of this primary carbon radical in catalytic chemistry, however, also requires the RS enzymes to employ exquisite control and protection of the radical intermediate in order to avoid damaging side reactions. Recent insights into the structures of the RS enzymes, and how these structures relate to mechanism and control of reactivity, will be addressed in this review.

Structural insights into the radical SAM superfamily

Binding diverse substrates with a common fold

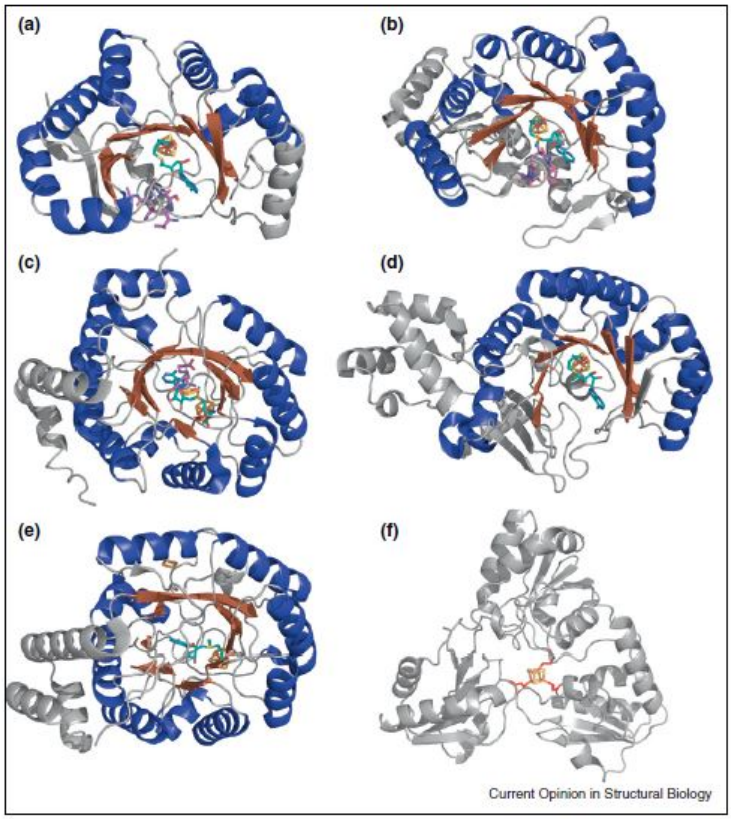
Several RS enzymes have been structurally characterized; these reveal a common fold consisting of a triosephosphate isomerase (TIM) barrel, which is a full $(\alpha/\beta)_8$ TIM barrel in some cases (e.g. biotin synthase (BioB) [8], HydE [9], and ThiC [10]) and a partial $(\alpha/\beta)_6$ TIM barrel in most other cases (Figure 2) [11,12$^{\bullet\bullet}$,13–17,18$^{\bullet\bullet}$]. The size of the TIM barrel inversely correlates with substrate size: enzymes that act on larger substrates tend to have less complete TIM barrels, thus making the barrel opening larger [4,5$^{\bullet\bullet}$]. The glycyl radical generating enzyme pyruvate formate lyase activating enzyme (PFL-AE), for example, is the smallest RS protein structurally characterized to date with little secondary structure outside the partial $(\alpha/\beta)_6$ TIM barrel (Figure 2a) [11]. The substrate for PFL-AE is among the largest RS substrates known: the 170 kDa homodimeric protein pyruvate formate lyase (PFL). On the basis of the evidence for direct H-atom abstraction from PFL G^{734} by the dAdo$^{\bullet}$ generated in the PFL-AE active site, it is clear that minimally the glycyl radical domain of PFL must bind

Figure 1



The reductive cleavage of SAM catalyzed by RS enzymes. SAM is coordinated via its amino and carboxyl moieties to the unique iron of a [4Fe–4S] cluster (left). The reduced $[4Fe–4S]^{+}$ cluster transfers an electron to SAM, thereby promoting homolytic cleavage to generate methionine and a 5′-deoxyadenosyl radical. The 5′-deoxyadenosyl radical abstracts a hydrogen atom from substrate (SH) to produce a substrate radical (S•), methionine, and 5′-deoxyadenosine (right).

Figure 2



Crystal structures of representative RS enzymes and Dph2. The Fe–S clusters are shown in rust for iron and yellow for sulfur. SAM molecules (teal carbons) and substrates (purple carbons) are also shown. **(a)** PFL-AE with SAM and the substrate PFL peptide (PDB ID: 3CB8). **(b)** SPL with SAM and substrate dinucleoside 5*R*-SP (PDB ID: 4FHD). **(c)** BioB with SAM, DTB substrate, and the additional [2Fe–2S] cluster (PDB ID: 1R30). **(d)** RlmN with SAM (PDB ID: 3RFA). **(e)** HydE with SAM and additional [2Fe–2S] cluster (PDB ID: 3IIZ). **(f)** Dph2 with the iron coordinating cysteines in red (PDB ID: 3LZD).

within this TIM barrel such that G^{734} is in close proximity to the [4Fe–4S] cluster and bound SAM in PFL-AE; this is consistent with the presence of an incomplete and splayed TIM barrel that provides a larger binding pocket for substrate [11,19•].

Spore photoproduct (SP) lyase (SPL) is another example of a RS enzyme that acts on a large substrate; in this case, the substrate is the SP (5-thyminyl-5,6-dihydrothymine) thymine dimer contained within double-stranded DNA (dsDNA). A recent structure of SPL reveals that, like PFL-AE, SPL contains a partial $(\alpha/\beta)_6$ TIM barrel with a wide lateral opening capable of binding large substrates (Figure 2b) [18••,20]. In contrast to PFL-AE and SPL, the RS enzyme BioB acts on a small-molecule substrate, dethiobiotin (DTB), and contains a full $(\alpha/\beta)_8$ TIM barrel; this full barrel still allows access of the small molecule substrate to the SAM-bound [4Fe–4S] cluster at the active site within the barrel, while also presumably shielding reactive radical intermediates from deleterious side reactions (Figure 2c) [8].

Positioning SAM and substrate for catalysis

In all RS structures to date, the catalytic [4Fe–4S] cluster bound to the characteristic RS cysteine motif resides at the C-terminal end of the TIM barrel, with the unique iron of the cluster pointing into the barrel. This unique iron is coordinated by the amino nitrogen and the carboxylate oxygen of SAM (Figure 1), an interaction first identified by electron nuclear double resonance (ENDOR) spectroscopic studies of PFL-AE [21,22] and subsequently observed in every RS crystal structure in which SAM is bound [5••]. This SAM–cluster interaction is unique to the RS enzymes and provides the key point of contact between the catalytic cluster and SAM for the production of dAdo•. Generally, in the crystal structures solved to date, the active site is exposed to solvent; however, upon binding of substrate, sections of the C-terminal region and the N-terminal region and/or the substrate itself provide a lid for the active site, subsequently blocking off solvent access to the active site [4,23•]. Such closure of the active site cavity during catalysis provides protection for the radical intermediates, including dAdo•, implicated in RS mechanisms. Without such shielding of reaction intermediates, the radicals involved in the catalytic mechanisms of these enzymes might not survive to react with their intended targets due to quenching by solvent. Further, exclusion of solvent would alter the dielectric of the active site, a factor that may be important in modulating the energetics of the catalytic steps [24•].

Similar to other RS enzymes, the [4Fe–4S] cluster in SPL is buried at the top of the barrel, in an environment rich in hydrophobic residues, with SAM bound through the amino and carboxylate groups [18••]. A structure with the dinucleoside 5*R*-SP bound shows that this substrate binds in proximity to SAM, accompanied by distinct conformational changes that appear to seal off the substrate binding pocket and provide a protected environment for subsequent radical chemistry (Figure 2b) [18••]. The conformational changes occur mainly in the catalytic pocket and the β-hairpin that resides just outside the catalytic pocket. Two residues (Arg304 and Tyr305) in the β-hairpin may help recognize and flip out the SP region from dsDNA through the insertion of the β-hairpin into dsDNA or through interactions with the DNA backbone [18••]. Other residues near the active site change their orientation to allow access of SP to the active site. Another interesting outcome of this structure is the revelation of the structural basis for the previously reported stereospecificity of SPL [20,25], which resides in the steric clashes that would occur when orienting the 5*S*-SP correctly for H-atom abstraction.

Similar to SPL, the crystal structures of PFL-AE in the presence and absence of a peptide analog of the PFL substrate reveal that binding of the peptide shields the active site from solvent and helps to stabilize and orient SAM in the active site (Figure 2a) [11]. The structures also reveal that binding of substrate induces a large conformational change in loop A of PFL-AE, wherein the loop swings up into the active site and interacts with the substrate to either stabilize and position it for H-atom abstraction or to induce conformational changes in the PFL substrate [11]. Given the evidence for direct H-atom abstraction from G^{734} of PFL by the dAdo• generated in the PFL-AE active site, together with the observation that G^{734} is buried in the interior of PFL in its crystal structures [19•,26], the involvement of significant conformational changes for PFL during activation has long been postulated. Recent biochemical and spectroscopic results support such a major conformational change in PFL upon interaction with PFL-AE. Peng *et al.* showed that in the presence of PFL-AE, PFL favors an open conformation in which the radical domain emerges from its buried position in the interior of PFL [19•]. PFL-AE thus appears to promote a conformational change in PFL that renders its glycyl radical domain accessible for binding in the PFL-AE active site [19•]. The elucidation of the details of this conformational change in PFL, and the detailed mechanism by which PFL-AE promotes this change to allow for glycyl radical formation, awaits further studies.

The SAM–cluster interaction and implications for mechanism

Uncoupled SAM cleavage, in which the dAdo• does not react with substrate but rather is quenched by protein or solvent, is a wasteful and potentially damaging reaction for RS enzymes. One method that RS enzymes use to prevent uncoupled cleavage of SAM is to take advantage of the large difference in redox potential between the [4Fe–4S] cluster and SAM. The reduction potential for

SAM is approximately −1.8 V, while the [4Fe–4S] cluster in RS enzymes is only about −450 mV, resulting in a barrier of about 1.4 V or 32 kcal mol^{-1} [4,27]. Wang and Frey have shown that binding of SAM and substrate to LAM lowers the energy barrier to 9 kcal mol^{-1}, resulting in more favorable conditions for the reductive cleavage of SAM [4,27]. Sulfur K-edge X-ray absorption spectroscopy and density functional theory calculations on PFL-AE have provided evidence for a back-bonding interaction between SAM and the cluster that is increased upon cluster reduction; this interaction is proposed to facilitate electron transfer from the $[4Fe–4S]^{+}$ cluster to SAM [24•]. Computational results also indicate that reductive cleavage of SAM is sensitive to the dielectric in the active site, and this sensitivity has been proposed to play a role in triggering inner-sphere electron transfer and subsequent SAM cleavage upon substrate binding [24•].

Novel chemistry for radical SAM enzymes

In the last several years, a number of newly characterized RS enzymes have been reported. These RS enzymes carry out novel chemistry and include the C-methyltransferase YtkT involved in the production of the antitumor agent yatakemycin [28], PqqE which is involved in the biosynthesis of pyrroloquinoline quinine (PQQ) [29], HpnP which is involved in the methylation of hopanoids [30], and the methylthiotransferase Cdkal1 [31] which was found to be linked to type 2 diabetes in mice [32]. Other newly identified RS enzymes discussed in more detail below play central roles in antiviral activity [33•,34,35], antibiotic production [36,37••], methylation reactions [12,38••,39,40] and metal cofactor biosynthesis [41–44]. These newly elucidated functions add to the already remarkably diverse chemistry known for the superfamily (see Refs. [2,3,5••,23•]).

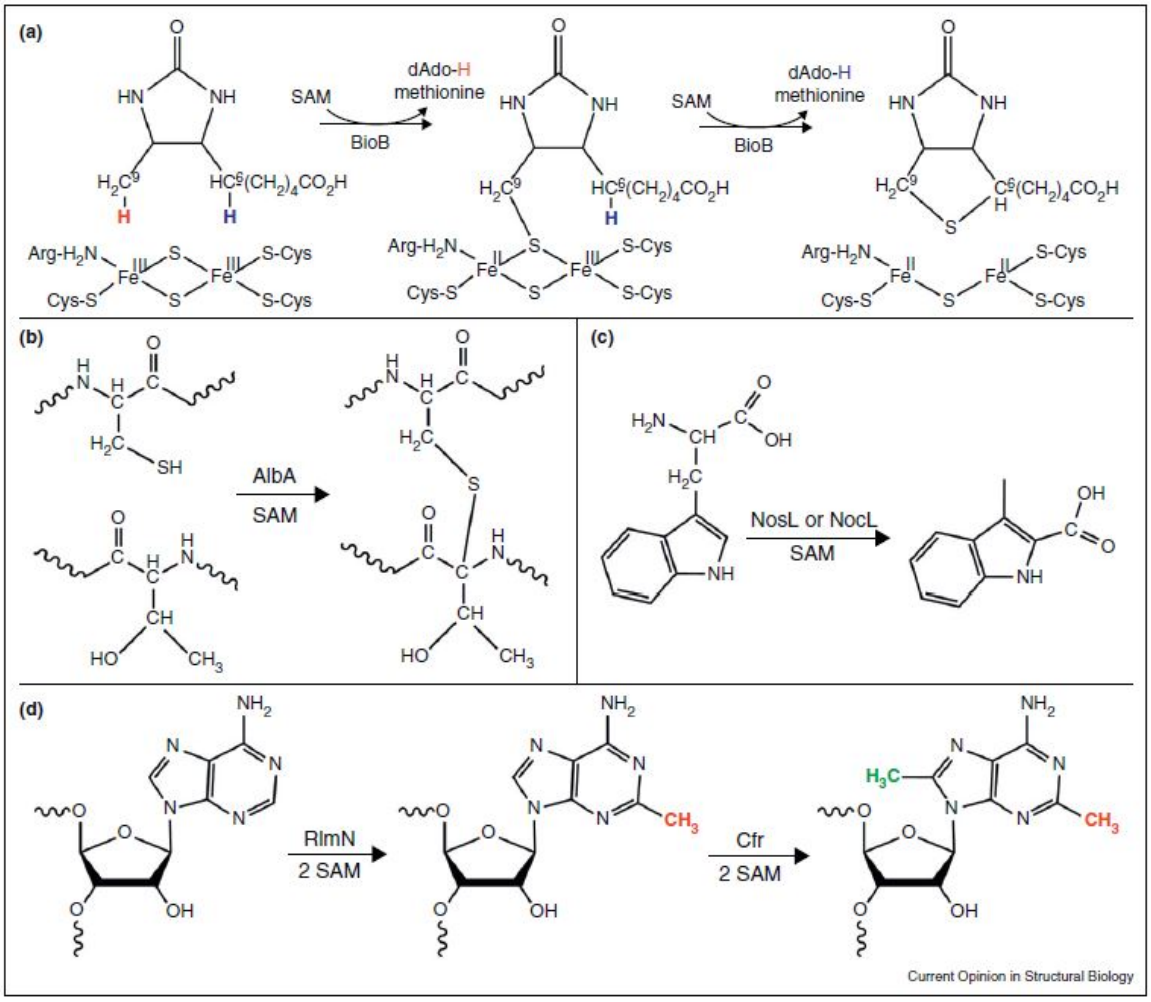
Viperin (*v*irus *i*nhibitory *p*rotein, *e*ndoplasmic *r*eticulum-associated, *in*terferon-inducible) is a mammalian protein that is upregulated in response to viral infections; however, the mechanism for its antiviral activity has yet to be determined [33•,34,35]. The proposed structure of viperin indicates a three-domain protein with a partial $(\alpha/\beta)_6$ TIM barrel RS domain, a leucine zipper domain possibly for protein folding and anchoring of the protein to the endoplasmic reticulum (ER), and a C-terminal domain which may be involved in substrate recognition or interactions with cofactors [45]. Viperin exhibits enhanced stability upon reconstitution with iron and sulfide [35,46], and UV–vis and electron paramagnetic resonance (EPR) spectroscopic analysis revealed the presence of a [4Fe–4S] cluster typical of the RS superfamily [33•]. Reductive cleavage of SAM was also observed, supporting the hypothesis that viperin is a RS enzyme [33•]. The mode by which RS chemistry aids in the antiviral response, however, is unknown. Viperin has been shown to interact with the enzyme farnesyl pyrophosphate synthase (FPPS) on the cytosolic face of the ER, decreasing its activity and disrupting the formation of lipid rafts, which are involved in budding of a number of viruses including HIV and influenza [33•,47]. While this interaction is an important observation, better understanding of the role of viperin in the antiviral response awaits identification of the reaction(s) it catalyzes.

Recent results demonstrate important roles for RS chemistry in antibiotic biosynthesis. AlbA is a RS enzyme involved in antimicrobial activity; it catalyzes the formation of three thioether bridges on the peptide SboA to produce subtilosin A, a sactibiotic (sulfur-to-α-carbon antibiotic) that has been shown to have antimicrobial activity against bacteria (Figure 3b) [48••,49]. The radical SAM protein NosL is involved in the production of the antibiotic thiopeptide nosiheptide (NOS) [37••]. Thiopeptides are sulfur rich, heterocyclic peptides with a macrocyclic core which includes a nitrogen-containing 6-membered ring central to multiple thiazoles and dehydroamino acids [37••,50]. In most polycylic thiopeptides, the functional side ring formation is independent of the precursor peptide and L-tryptophan provides the variable functional groups [37••]. NosL as well as NocL, which is 78% homologous to NosL and is involved in nocathiacin I (NOC-I) biosynthesis [36], are part of the MIA (3-methyl-2-indolic acid) synthase family that catalyze the conversion of L-tryptophan to MIA through an unusual fragmentation–recombination mechanism (Figure 3C).

Methylation of ribosomal RNA (rRNA) usually occurs via an S_N2 reaction with the donation of the methyl group from SAM. In the case of the RS enzymes RlmN and Cfr that methylate carbons 2 and 8, respectively, of adenosine 2503 of 23S rRNA, methylation occurs via radical subsequent to transfer of a methyl group to a non-cluster Cys (Figure 3d) [38••,39]. Two equivalents of SAM are needed: one for methylation of the Cys to form mCys, and one for dAdo• production necessary for H-atom abstraction from mCys [38••,39]. In the crystal structure of RlmN, the β7 loop moves to dip into the active site upon the addition of SAM, positioning the catalytic Cys^{355} closer to the active site for methyl transfer (Figure 2d) [12••]. This Cys^{355} residue was methylated in the structure, apparently by the first molecule of SAM, suggesting that the second molecule of SAM was bound, awaiting reductive cleavage to initiate H-atom abstraction [12••]. Unlike methylthiotransferases (MTTases) that utilize two [4Fe–4S] clusters for the insertion of a methylthio group into substrate, RlmN and Cfr contain only one [4Fe–4S] cluster bound to the typical RS CX_3CX_2C motif, and both SAM molecules presumably bind to this same [4Fe–4S] cluster at different steps in the catalytic cycle [12••,38••,39].

Another emerging function for RS enzymes is the biosynthesis of complex metal cofactors including the iron–molybdenum cofactor (FeMo-co) of nitrogenase and the

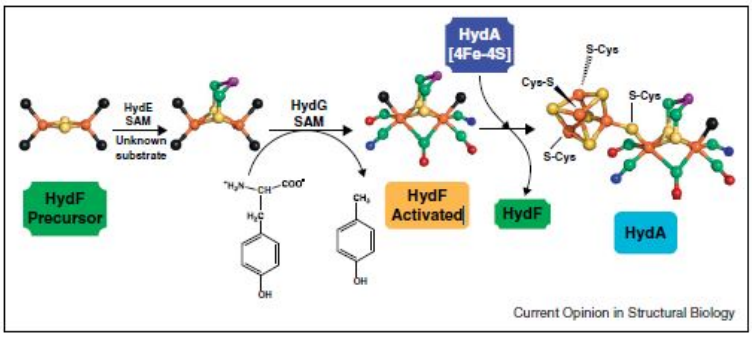
Figure 3



Representative radical SAM reactions. **(a)** BioB catalyzes the sequential abstraction of hydrogen atoms from C9 and C6 of DTB (left), with insertion of sulfur from the [2Fe–2S] cluster. **(b)** AlbA incorporates three thioether bonds between three cysteines and the α-C of two phenylalanines and one threonine during the maturation of subtilosin A. Shown is a representative reaction between one cysteine and threonine. **(c)** NosL and NocL catalyze a fragmentation–recombination reaction of L-Trp to MIA which is incorporated into NOS in the case of NosL or NOC-I in the case of NocL. **(d)** RlmN and Cfr catalyze the methylation of A2503 of the 23S rRNA utilizing two equivalents of SAM. The sequential methylations catalyzed by these two enzymes can occur in either order.

H-cluster of [Fe–Fe]-hydrogenase. NifB is a RS enzyme that inserts the central carbide in an essential step in FeMo-co maturation, with the carbide originating from the methyl group of SAM via novel chemistry [51]. The role of RS chemistry in H-cluster biosynthesis has been partially delineated in recent years [44]. The H-cluster consists of a [4Fe–4S] cluster bridged by a cysteine residue to a 2Fe cluster coordinated by three CO molecules, two CN^- ions, and a bridging dithiolate; this cluster is unique to [FeFe]-hydrogenase and is the site where protons are reduced to H_2 [42,52,53]. While the [4Fe–4S] cluster portion of the H-cluster is synthesized by the housekeeping Fe–S cluster assembly machinery, the 2Fe subcluster is assembled by three proteins, two of which (HydE and HydG) are RS enzymes [42,43]. HydG has been shown to synthesize the CO and CN^- ligands from tyrosine using RS chemistry (Figure 4) [54–56], and HydE is presumed to catalyze formation of the dithiolate

Figure 4



Proposed biosynthesis pathway for HydA H-cluster. HydE uses an unknown substrate to synthesize a dithiolate ligand on a [2Fe–2S] cluster of HydF. HydG catalyzes the decomposition of tyrosine to produce *p*-cresol, CO, and CN^-; the latter two diatomics bind to the H-cluster precursor 2Fe cluster on HydF. HydF then transfers the 2Fe H-cluster precursor to HydA to produce the complete H-cluster and the active hydrogenase. Colors of atoms are as follows: green, carbon; red, oxygen; blue, nitrogen; rust, iron; yellow, sulfur; purple, unknown bridging atom; black, unknown residue coordinating to protein.

ligand, although the substrate and reaction catalyzed remain a mystery. HydG and HydE deliver these synthesized ligands to the GTPase HydF where the 2Fe subcluster is assembled [41,57]. Once constructed, the 2Fe subcluster is transferred to hydrogenase already containing a [4Fe–4S] cluster in order to generate the H-cluster and the active enzyme [52,58,59].

Emerging themes in radical SAM chemistry

Multiple Fe–S clusters

All RS enzymes require a [4Fe–4S] cluster in the active site for the binding and reductive cleavage of SAM; however, an emerging theme in the RS field is the presence of a second Fe–S cluster in certain subclasses of RS enzymes. In some cases, the second cluster appears to be a source of sulfur that is inserted into substrate during catalysis, a role first proposed for biotin synthase (BioB) which catalyzes the conversion of DTB to biotin by a sulfur insertion reaction [8,60,61••,62]. BioB contains an additional [2Fe–2S] cluster positioned such that DTB is sandwiched in between SAM and the [2Fe–2S] cluster (Figure 2c) [8]. The [2Fe–2S] cluster was found to undergo reduction concomitant with the formation of a 9-mercaptodethiobiotin (9-MDTB) intermediate; such cluster reduction is consistent with sulfur donation from the cluster thus providing the most recent experimental evidence that the cluster serves as a sulfur source during biotin synthesis (Figure 3a) [60,62]. Lipoate synthase catalyzes a reaction that is quite similar to that of biotin synthase: the insertion of sulfur into an unactivated C–H bond (in this case the C6 and C8 of the octanoyl group) to form the lipoyl cofactor. Lipoate synthase contains two [4Fe–4S] clusters, one of which is the RS active cluster and the other appears to serve as the source of the two sulfides inserted during catalysis [63]. The methylthiotransferases such as RimO [64], MiaB [65], and MtaB [66] also require a sulfur source and contain a second Fe–S cluster; the implication is that the second cluster is the source of the sulfur required in catalysis, but direct biochemical evidence has yet to be reported.

Other potential purposes for auxiliary Fe–S clusters in RS enzymes have also been indicated, including such roles as electron acceptors or anchors for substrates. In the case of BtrN, Grove *et al.* found that the second [4Fe–4S] cluster cannot be reduced by chemical means, suggesting that this cluster is inaccessible to exogenous reductants [67]. During turnover, however, an EPR signal was observed that is proposed to arise as a result of the second cluster accepting an electron from the RS cluster during catalysis [67]. The second [4Fe–4S] cluster in MoaA binds its substrate 5′-GTP through the N1 of the purine ring to the unique Fe [68]. AlbA also contains a second [4Fe–4S] cluster that is proposed to be an electron acceptor during turnover [48••]. Anaerobic sulfatase-maturating enzymes (anSMEs), on the other hand, contain two additional [4Fe–4S] clusters that are thought to be involved with the reduction of the RS [4Fe–4S] cluster [69]. The anSMEs catalyze the oxidation of cysteine and serine residues of the sulfatase enzymes to produce C_α-formylglycine (FGly) [69]. Mutation studies to knock out the additional clusters resulted in loss of activity and it was proposed that either: first, one of the clusters binds substrate and acts as an electron acceptor while the second cluster transfers an electron from an external electron donor to the RS cluster [70]; or second, in a more recent hypothesis, both clusters act to transfer the electron to the RS cluster and neither cluster coordinates substrate [69].

The [FeFe]-hydrogenase maturation proteins HydE and HydG also contain additional Fe–S clusters. Although spectroscopic studies had indicated the presence of only [4Fe–4S] clusters in HydE, in the crystal structure of HydE there was a [2Fe–2S] cluster in addition to the RS [4Fe–4S] cluster (Figure 2e) [6,9,71]. The [2Fe–2S] cluster of HydE is bound in a site about 20 Å from the active site and on the exterior of the barrel separated from the active site by a water-filled cavity, quite different from the [2Fe–2S] cluster in biotin synthase, which was within the barrel and in close proximity to the active site [9]. Furthermore, the cysteine residues that coordinate the [2Fe–2S] cluster in HydE are not conserved across all HydE proteins, suggesting that this second cluster does not play an essential role in catalysis [9]. HydG contains two distinct [4Fe–4S] clusters upon reconstitution with iron and sulfide, and both of these clusters are coordinated by conserved cysteine motifs and have been shown to be essential for HydG activity [55••]. EPR spectroscopic characterization indicates that SAM binds to one of these clusters [55••]. Variants of HydG lacking the ligands for the second cluster were able to produce CN^- and *p*-cresol upon incubation under assay conditions with SAM and tyrosine; however, no CO production was observed, suggesting a role for the second cluster in CO production [53].

Unexpected cysteine motifs

One of the characteristic features of RS enzymes is the cluster-binding CX_3CX_2C triad motif; however, a number of variations of this cluster-binding motif have now been reported. A CX_2CX_4C motif was found in 4-amino-5-hydroxymethyl-2-methylpyrimidine phosphate (HMP-P) synthase (ThiC), a RS enzyme that converts 5-aminoimidazole ribonucleotide (AIR) into HMP-P during thiamine biosynthesis [10]. HmdB is a RS enzyme involved in the biosynthesis of the [Fe]-hydrogenase through an undetermined reaction, and exhibits a CX_5CX_2C motif [72]. Dph2, which is involved in diphthamide biosynthesis, has not been classified as a RS enzyme, although biochemical evidence strongly supports a catalytic mechanism in which a [4Fe–4S] cluster interacts with SAM to generate a 3-amino-3-carboxypropyl (ACP) radical intermediate; such chemistry is clearly analogous to RS reactions [73••,74]. Dph2 exhibits neither the cysteine triad motif nor the typical RS TIM barrel structure (Figure 2f); rather, each of the three cysteines coordinating the Fe–S cluster reside on a separate domain, with over one hundred amino acids separating each cysteine residue [73••,74]. The observation of non-canonical cluster binding motifs in RS enzymes, together with the characterization of RS-like chemistry in a protein that has neither the sequence nor the structural signatures of the superfamily, suggests the likelihood that many additional, as-yet unidentified proteins will ultimately be discovered which catalyze radical reactions using an Fe–S cluster and SAM.

Reductive cleavage of alternate C–S bonds of SAM

RS enzymes have been described as cleaving the S–5′C bond to form methionine and a dAdo• radical intermediate, where dAdo• abstracts a hydrogen from substrate, producing 5′-deoxyadenosine (dAdo) and a substrate radical (Figure 1). Recently, Dph2 and glycerol dehydratase activating enzyme (GDH-AE) were reported to produce alternatively 5′-deoxy-5′-methylthioadenosine (MTA) and a 3-amino-3-carboxypropyl (ACP) radical intermediate, thus implicating the reductive cleavage of an alternate S–C bond of SAM [73••,74,75]. Dph2, as stated previously, is not classified as a RS enzyme but yet it still catalyzes a radical reaction using SAM and an Fe–S cluster [73••]. GDH-AE, on the other hand, is a member of the RS superfamily and is predicted to contain a partial TIM barrel structure similar to PFL-AE [75]. It is unclear why these proteins cleave an alternate S–C bond of SAM although the regioselectivity of the reductive cleavage of SAM has been proposed to be a result of the orientation of SAM with respect to the [4Fe–4S] cluster and substrate [74,76•].

Concluding remarks

The RS superfamily contains an amazing variety of enzymes that carry out diverse and difficult radical reactions that are essential to the metabolic processes in all kingdoms of life. Despite the presence of little sequence homology among superfamily members, these enzymes exhibit a common TIM barrel fold, a common location of a catalytically essential [4Fe–4S] cluster within that barrel, and a mode of binding the [4Fe–4S] cluster through three cysteines to generate a site-differentiated Fe that can be coordinated by SAM. Functional and structural diversity is conferred in some cases by additional domains and by additional Fe–S clusters that can serve a variety of roles in catalysis. New insights into mechanism, as well as newly characterized functions, continue to emerge for this fascinating group of enzymes.

Acknowledgements

Research on RS enzymes in the Broderick Laboratory is supported by the National Institutes of Health (GM54608) and the Department of Energy (DE-FG02-10ER16194). The Astrobiology Biogeocatalysis Research Center is supported by NASA (NNA08C-N85A).

References and recommended reading

Papers of particular interest, published within the period of review, have been highlighted as:

- • of special interest
- •• of outstanding interest

1. Sofia HJ, Chen G, Hetzler BG, Reyes-Spindola JF, Miller NE: **Radical SAM, a novel protein superfamily linking unresolved steps in familiar biosynthetic pathways with radical mechanisms: functional characterization using new analysis and information visualization methods**. *Nucleic Acids Res* 2001, **29**:1097-1106.

2. Shepard EM, Broderick JB: **S-Adenosylmethionine and iron–sulfur clusters in biological radical reactions: the radical SAM**

superfamily. In *Comprehensive Natural Products. II. Chemistry and Biochemistry*, vol 8. Edited by Mander LN, Liu HW. Elsevier Press; 2010:625-662.

3. Frey PA, Hegeman AD, Ruzicka FJ: **The radical SAM superfamily**. *Crit Rev Biochem Mol Biol* 2008, **43**:63-88.

4. Duschene KS, Veneziano SE, Silver SC, Broderick JB: **Control of radical chemistry in the AdoMet radical enzymes**. *Curr Opin Chem Biol* 2009, **13**:74-83.

5. •• Vey JL, Drennan CL: **Structural insights into radical generation by the radical SAM superfamily**. *Chem Rev* 2011, **111**:2487-2506.
A review that focuses on the structures of radical SAM enzymes and how each enzyme utilizes their own structural architecture to carry out radical reactions on a wide array of substrates.

6. Nicolet Y, Amara P, Mouesca J-M, Fontecilla-Camps JC: **Unexpected electron transfer mechanism upon AdoMet cleavage in radical SAM proteins**. *Proc Natl Acad Sci U S A* 2009, **106**:14867-14871.

7. Hioe J, Zipse H: **Radicals in enzymatic catalysis — a thermodynamic perspective**. *Faraday Discuss* 2010, **145**:301-313.

8. Berkovitch F, Nicolet Y, Wan JT, Jarrett JT, Drennan CL: **Crystal structure of biotin synthase, an *S*-adenosylmethionine-dependent radical enzyme**. *Science* 2004, **303**:76-79.

9. Nicolet Y, Rubach JK, Posewitz MC, Amara P, Mathevon C, Atta M, Fontecave M, Fontecilla-Camps JC: **X-ray structure of the [FeFe]-hydrogenase maturase HydE from *Thermotoga maritima***. *J Biol Chem* 2008, **283**:18861-18872.

10. Chatterjee A, Li Y, Zhang Y, Grove TL, Lee M, Krebs C, Booker SJ, Begley TP, Ealick SE: **Reconstitution of ThiC in thiamine pyrimidine biosynthesis expands the radical SAM superfamily**. *Nat Chem Biol* 2008, **4**:758-765.

11. Vey JL, Yang J, Li M, Broderick WE, Broderick JB, Drennan CL: **Structural basis for glycyl radical formation by pyruvate formate-lyase activating enzyme**. *Proc Natl Acad Sci U S A* 2008, **105**:16137-16141.

12. •• Boal AK, Grove TL, McLaughlin MI, Yennawar NH, Booker SJ, Rosenzweig AC: **Structural basis for methyl transfer by a *radical SAM enzyme***. *Science 2011*, ***332***:*1089-1092*.
The authors reveal the first crystal structure of RlmN where they discovered a single molecule of SAM coordinates of the [4Fe–4S] cluster. The Cys^{355} residue is methylated and is located proximal to the SAM methyl group which suggests that both equivalents of SAM bind in the same site in the protein during the methylation of rRNA.

13. Arragain S, Garcia-Serres R, Blondin G, Douki T, Clemancey M, Latour J-M, Forouhar F, Neely H, Montelione GT, Hunt JF *et al.*: **Post-translational modification of ribosomal proteins: structural and functional characterization of RimO from *Thermotoga maritima*, a radical *S*-adenosylmethionine methylthiotransferase**. *J Biol Chem* 2010, **285**:5792-5801.

14. Hanzelmann P, Schindelin H: **Binding of 5′-GTP to the C-terminal FeS cluster of the radical *S*-adenosylmethionine enzyme MoaA provides insights into its mechanism**. *Proc Natl Acad Sci U S A* 2006, **103**:6829-6834.

15. Lepore BW, Ruzicka FJ, Frey PA, Ringe D: **The X-ray crystal structure of lysine-2,3-aminomutase from *Clostridium subterminale***. *Proc Natl Acad Sci U S A* 2005, **102**:13819-13824.

16. Layer G, Moser J, Heinz DW, Jahn D, Schubert W-D: **Crystal structure of coproporphyrinogen III oxidase reveals cofactor geometry of radical SAM enzymes**. *EMBO J* 2003, **22**: 6214-6224.

17. Goto-Ito S, Ishii R, Ito T, Shibata R, Fusatomi E, Sekine S-i, Bessho Y, Yokoyama S: **Structure of an archaeal TYW1, the enzyme catalyzing the second step of wye-base biosynthesis**. *Acta Crystallogr Sect D: Biol Crystallogr* 2007, **63**:1059-1068.

18. •• Benjdia A, Heil K, Barends TRM, Carell T, Schlichting I: **Structural insights into recognition and repair of UV-DNA damage by spore photoproduct lyase, a radical SAM enzyme**. *Nucleic Acids Res* 2012 http://dx.doi.org/10.1093/nar/gks603.
The authors provide the first description of the crystal structure of the radical SAM DNA repair enzyme spore photoproduct lyase, revealing important insights into mechanism.

19. • Peng Y, Veneziano SE, Gillispie GD, Broderick JB: **Pyruvate formate-lyase: evidence for an open conformation favored in the presence of its activating enzyme**. *J Biol Chem* 2010, **285**:27224-27231.
Using spectroscopic and biochemical approaches, the authors provided evidence that PFL has open and closed conformations that the distribution of the conformations is regulated by the presence of the radical SAM protein PFL-AE.

20. Heil K, Kneuttinger AC, Schneider S, Lischke U, Carell T: **Crystal structures and repair studies reveal the identity and the base-pairing properties of the UV-induced spore photoproduct DNA lesion**. *Chem Eur J* 2011, **17**:9651-9657.

21. Walsby CJ, Hong W, Broderick WE, Cheek J, Ortillo D, Broderick JB, Hoffman BM: **Electron-nuclear double resonance spectroscopic evidence that *S*-adenosylmethionine binds in contact with the catalytically active [4Fe–4S]$^{+}$ cluster of pyruvate formate-lyase activating enzyme**. *J Am Chem Soc* 2002, **124**:3143-3151.

22. Walsby CJ, Ortillo D, Broderick WE, Broderick JB, Hoffman BM: **An anchoring role for FeS clusters: chelation of the amino acid moiety of *S*-adenosylmethionine to the unique iron site of the [4Fe–4S] cluster of pyruvate formate-lyase activating enzyme**. *J Am Chem Soc* 2002, **124**:11270-11271.

23. • Dowling DP, Vey JL, Croft AK, Drennan CL: **Structural diversity in the AdoMet radical enzyme superfamily**. *Biochim Biophys Acta* 2012, **1824**:1178-1195.
This is a recent review of radical SAM enzymes that focuses on the structural aspects of radical SAM enzymes with an analysis of crystallographic data as well as biochemical, spectroscopic, and computational studies of specific radical SAM enzymes.

24. • Dey A, Peng Y, Broderick WE, Hedman B, Hodgson KO, Broderick JB, Solomon EI: **S K-edge XAS and DFT calculations on SAM dependent pyruvate formate-lyase activating enzyme: nature of interaction between the Fe4S4 cluster and SAM and its role in reactivity**. *J Am Chem Soc* 2011, **133**:18656-18662.
This paper provides evidence for backbonding interactions between the cluster and SAM that facilitate electron transfer from the cluster to SAM. The results also implicate the importance of the altered dielectric in the active site upon substrate binding as a trigger for the reductive cleavage of SAM.

25. Chandra T, Silver SC, Zilinskas E, Shepard EM, Broderick WE, Broderick JB: **Spore photoproduct lyase catalyzes specific repair of the 5*R* but not the 5*S* spore photoproduct**. *J Am Chem Soc* 2009, **131**:2420-2421.

26. Becker A, Fritz-Wolf K, Kabsch W, Knappe J, Schultz S, Volker Wagner AF: **Structure and mechanism of the glycyl radical enzyme pyruvate formate-lyase**. *Nat Struct Biol* 1999, **6**:969-975.

27. Wang SC, Frey PA: **Binding energy in the one-electron reductive cleavage of *S*-adenosylmethionine in lysine 2,3-aminomutase, a radical SAM enzyme**. *Biochemistry* 2007, **46**:12889-12895.

28. Huang W, Xu H, Li Y, Zhang F, Chen X-Y, He Q-L, Igarashi Y, Tang G-L: **Characterization of yatakemycin gene cluster revealing a radical *S*-adenosylmethionine dependent methyltransferase and highlighting spirocyclopropane biosynthesis**. *J Am Chem Soc* 2012, **134**:8831-8840.

29. Wecksler SR, Stoll S, Tran H, Magnusson OT, Wu S-p, King D, Britt RD, Klinman JP: **Pyrroloquinoline quinone biogenesis: demonstration that PqqE from *Klebsiella pneumoniae* is a radical *S*-adenosyl-L-methionine enzyme**. *Biochemistry* 2009, **48**:10151-10161.

30. Welander PV, Coleman ML, Sessions AL, Summons RE, Newman DK: **Identification of a methylase required for 2-methylhopanoid production and implications for the interpretation of sedimentary hopanes**. *Proc Natl Acad Sci U S A* 2010, **107**:8537-8542.

31. Arragain S, Handelman SK, Forouhar F, Wei F-Y, Tomizawa K, Hunt JF, Douki T, Fontecave M, Mulliez E, Atta M: **Identification of eukaryotic and prokaryotic methylthiotransferase for biosynthesis of 2-methylthio-N6-threonylcarbamoyladenosine in tRNA**. *J Biol Chem* 2010, **285**:28425-28433.

32. Wei F-Y, Suzuki T, Watanabe S, Kimura S, Kaitsuka T, Fujimura A, Matsui H, Atta M, Michiue H, Fontecave M *et al.*: **Deficit of tRNA(Lys) modification by Cdkal1 causes the development of type 2 diabetes in mice**. *J Clin Invest* 2011, **121**:3598-3608.

33. • Duschene KS, Broderick JB: **The antiviral protein viperin is a radical SAM enzyme**. *FEBS Lett* 2010, **584**:1263-1267.
This article provided the first evidence that viperin binds a [4Fe–4S] cluster and is capable of reductively cleaving SAM to produce 5′-deoxyadenosine, classifying it as a radical SAM enzyme.

34. Duschene KS, Broderick JB: **Viperin: a radical response to viral infection**. *BioMol Concepts* 2012, **3**:255-266.

35. Haldar S, Paul S, Joshi N, Dasgupta A, Chattopadhyay K: **The presence of the iron–sulfur motif is important for the conformational stability of the antiviral protein, viperin**. *PLoS One* 2012, **7**:e31797.

36. Zhang Q, Chen D, Lin J, Liao R, Tong W, Xu Z, Liu W: **Characterization of NocL involved in thiopeptide nocathiacin I biosynthesis: a [4Fe–4S] cluster and the catalysis of a radical *S*-adenosylmethionine enzyme**. *J Biol Chem* 2011, **286**:21287-21294.

37. •• Zhang Q, Li Y, Chen D, Yu Y, Duan L, Shen B, Liu W: **Radical-mediated enzymatic carbon chain fragmentation–recombination**. *Nat Chem Biol* 2011, **7**:154-160.
The authors reported that NosL is a radical SAM enzyme that catalyzes the conversion of L-Trp to MIA through the removal of the C_α-N unit and shifting the carboxylate to the indole ring. NosL works through an unusual fragmentation–recombination reaction that the authors proposed goes through a glycyl radical intermediate.

38. •• Grove TL, Benner JS, Radle MI, Ahlum JH, Landgraf BJ, Krebs C, Booker SJ: **A radically different mechanism for *S*-adenosylmethionine-dependent methyltransferases**. *Science* 2011, **332**:604-607.
Unlike most S_N2 reactions for the methylation of small molecules or macromolecules, the authors found that RlmN and Cfr utilize radical SAM chemistry. These enzymes use a ping–pong mechanism that involves methylation of a conserved Cys residue.

39. Grove TL, Radle MI, Krebs C, Booker SJ: **Cfr and RlmN contain a single [4Fe–4S] cluster, which directs two distinct reactivities for *S*-adenosylmethionine: methyl transfer by S(N)2 displacement and radical generation**. *J Am Chem Soc* 2011, **133**:19586-19589.

40. Yan F, LaMarre JM, Rohrich R, Wiesner J, Jomaa H, Mankin AS, Fujimori DG: **RlmN and Cfr are radical SAM enzymes involved in methylation of ribosomal RNA**. *J Am Chem Soc* 2010, **132**:3953-3964.

41. Shepard EM, Boyd ES, Broderick JB, Peters JW: **Biosynthesis of complex iron–sulfur enzymes**. *Curr Opin Chem Biol* 2011, **15**:319-327.

42. Swanson KD, Duffus BR, Beard TE, Peters JW, Broderick JB: **Cyanide and carbon monoxide ligand formation in hydrogenase biosynthesis**. *Eur J Inorg Chem* 2011, **2011**:935-947.

43. Duffus BR, Hamilton TL, Shepard EM, Boyd ES, Peters JW, Broderick JB: **Radical AdoMet enzymes in complex metal cluster biosynthesis**. *Biochim Biophys Acta* 2012, **1824**:1254-1263.

44. Peters JW, Broderick JB: **Emerging paradigms for complex iron–sulfur cofactor assembly and insertion**. *Annu Rev Biochem* 2012, **81**:429-450.

45. Jiang D, Guo HT, Xu CX, Chang JH, Gu BH, Wang LJ, Block TM, Guo J-T: **Identification of three interferon-inducible cellular enzymes that inhibit the replication of hepatitis C virus**. *J Virol* 2008, **82**:1665-1678.

46. Shaveta G, Shi J, Chow VTK, Song J: **Structural characterization reveals that viperin is a radical *S*-adenosyl-L-methionine (SAM) enzyme**. *Biochem Biophys Res Commun* 2010, **391**:1390-1395.

47. Wang X, Hinson ER, Cresswell P: **The interferon-inducible protein viperin inhibits influenza virus release by perturbing lipid rafts**. *Cell Host Microbe* 2007, **2**:96-105.

48. •• Fluhe L, Knappe TA, Gattner MJ, Schafer A, Burghaus O, Linne U, Marahiel MA: **The radical SAM enzyme AlbA catalyzes thioether bond formation in subtilosin A**. *Nat Chem Biol* 2012, **8**:350-357.
This article shows that AlbA catalyzes the formation of the three thioether bonds on the peptide SboA to produce subtilosin A through radical SAM chemistry, the first step during subtilosin A production. AlbA contains two clusters: one for SAM cleavage and one for generation of the thioether linkages.

49. Zhang Q, Yu Y: **Thioether crosslinkages created by a radical SAM enzyme**. *Chembiochem* 2012, **13**:1097-1099.

50. Yu Y, Duan L, Zhang Q, Liao R, Ding Y, Pan H, Wendt-Pienkowski E, Tang G, Shen B, Liu W: **Nosiheptide biosynthesis featuring a unique indole side ring formation on the characteristic thiopeptide framework**. *ACS Chem Biol* 2009, **4**:855-864.

51. Wiig JA, Hu Y, Lee CC, Ribbe MW: **Radical SAM-dependent carbon insertion into the nitrogenase M-cluster**. *Science* 2012, **337**:1672-1675.

52. Mulder David W, Shepard Eric M, Meuser Jonathan E, Joshi N, King Paul W, Posewitz Matthew C, Broderick Joan B, Peters John W: **Insights into [FeFe]-hydrogenase structure, mechanism, and maturation**. *Structure* 2011, **19**:1038-1052.

53. Nicolet Y, Martin L, Tron C, Fontecilla-Camps JC: **A glycyl free radical as the precursor in the synthesis of carbon monoxide and cyanide by the [FeFe]-hydrogenase maturase HydG**. *FEBS Lett* 2010, **584**:4197-4202.

54. Driesener RC, Challand MR, McGlynn SE, Shepard EM, Boyd ES, Broderick JB, Peters JW, Roach PL: **[FeFe]-hydrogenase cyanide ligands derived from *S*-adenosylmethionine-dependent cleavage of tyrosine**. *Angew Chem Int Ed Engl* 2010, **49**:1687-1690.

55. •• Shepard EM, Duffus BR, McGlynn SE, Challand MR, Swanson KD, Roach PL, Peters JW, Broderick JB: **[FeFe]-hydrogenase maturation: HydG-catalyzed synthesis of carbon monoxide**. *J Am Chem Soc* 2010, **132**:9247-9249.
The authors demonstrated that HydG catalyzes the synthesis of CO from tyrosine.

56. Kuchenreuther JM, George SJ, Grady-Smith CS, Cramer SP, Swartz JR: **Cell-free H-cluster synthesis and [FeFe] hydrogenase activation: all five CO and CN^- ligands derive from tyrosine**. *PLoS One* 2011, **6**:e20346.

57. Shepard EM, McGlynn SE, Bueling AL, Grady-Smith C, George SJ, Winslow MA, Cramer SP, Peters JW, Broderick JB: **Synthesis of the 2Fe-subcluster of the [FeFe]-hydrogenase H-cluster on the HydF scaffold**. *Proc Natl Acad Sci U S A* 2010, **107**:10448-10453.

58. Mulder DW, Boyd ES, Sarma R, Lange RK, Endrizzi JA, Broderick JB, Peters JW: **Stepwise [FeFe]-hydrogenase H-cluster assembly revealed in the structure of HydA(DeltaEFG)**. *Nature* 2010, **465**:248-251.

59. Mulder DW, Ortillo DO, Gardenghi DJ, Naumov AV, Ruebush SS, Szilagyi RK, Huynh B, Broderick JB, Peters JW: **Activation of HydA(Delta EFG) requires a preformed [4Fe–4S] cluster**. *Biochemistry* 2009, **48**:6240-6248.

60. Fugate CJ, Jarrett JT: **Biotin synthase: insights into radical-mediated carbon–sulfur bond formation**. *Biochim Biophys Acta* 2012, **1824**:1213-1222.

61. •• Fugate CJ, Stich TA, Kim EG, Myers WK, Britt RD, Jarrett JT: **9-Mercaptodethiobiotin is generated as a ligand to the [2Fe–2S](+) cluster during the reaction catalyzed by biotin synthase from *Escherichia coli***. *J Am Chem Soc* 2012, **134**:9042-9045.
The authors provide evidence that BioB catalyzes the production of dethiobiotin to biotin through a 9-mercaptodethiobitotin intermediate coordinated to a [2Fe–2S] cluster and that this cluster is the sulfur source for the production of biotin.

62. Taylor AM, Stoll S, Britt RD, Jarrett JT: **Reduction of the [2Fe–2S] cluster accompanies formation of the intermediate 9-mercaptodethiobiotin in Escherichia coli biotin synthase**. *Biochemistry* 2011, **50**:7953-7963.

63. Cicchillo RM, Lee K-H, Baleanu-Gogonea C, Nesbitt NM, Krebs C, Booker SJ: ***Escherichia coli* lipoyl synthase binds two distinct [4Fe–4S] clusters per polypeptide**. *Biochemistry* 2004, **43**:11770-11781.

64. Lee K-H, Saleh L, Anton BP, Madinger CL, Benner JS, Iwig DF, Roberts RJ, Krebs C, Booker SJ: **Characterization of RimO, a new member of the methylthiotransferase subclass of the radical SAM superfamily**. *Biochemistry* 2009, **48**: 10162-10174.

65. Pierrel F, Douki T, Fontecave M, Atta M: **MiaB protein is a bifunctional radical-*S*-adenosylmethionine enzyme involved in thiolation and methylation of tRNA**. *J Biol Chem* 2004, **279**:47555-47563.

66. Anton BP, Russell SP, Vertrees J, Kasif S, Raleigh EA, Limbach PA, Roberts RJ: **Functional characterization of the YmcB and YqeV tRNA methylthiotransferases of *Bacillus subtilis***. *Nucleic Acids Res* 2010, **38**:6195-6205.

67. Grove TL, Ahlum JH, Sharma P, Krebs C, Booker SJ: **A consensus mechanism for radical SAM-dependent dehydrogenation? BtrN contains two [4Fe–4S] clusters**. *Biochemistry* 2010, **49**:3783-3785.

68. Lees NS, Hanzelmann P, Hernandez HL, Subramanian S, Schindelin H, Johnson MK, Hoffman BM: **ENDOR spectroscopy shows that guanine N1 binds to [4Fe–4S] cluster II of the *S*-adenosylmethionine-dependent enzyme MoaA: mechanistic implications**. *J Am Chem Soc* 2009, **131**:9184-9185.

69. Benjdia A, Subramanian S, Leprince J, Vaudry H, Johnson MK, Berteau O: **Anaerobic sulfatase-maturating enzyme — a mechanistic link with glycyl radical-activating enzymes?** *FEBS J* 2010, **277**:1906-1920.

70. Grove TL, Lee K-h, St Clair J, Krebs C, Booker SJ: **In vitro characterization of AtsB, a radical SAM formylglycine-generating enzyme that contains three [4Fe–4S] clusters**. *Biochemistry* 2008, **47**:7523-7538.

71. Rubach JK, Brazzolotto X, Gaillard J, Fontecave M: **Biochemical characterization of the HydE and HydG iron-only hydrogenase maturation enzymes from *Thermotoga maritima***. *FEBS Lett* 2005, **579**:5055-5060.

72. McGlynn SE, Boyd ES, Shepard EM, Lange RK, Gerlach R, Broderick JB, Peters JW: **Identification and characterization of a novel member of the radical AdoMet enzyme superfamily and implications for the biosynthesis of the Hmd hydrogenase active site cofactor**. *J Bacteriol* 2010, **192**:595-598.

73. •• Zhang Y, Zhu X, Torelli AT, Lee M, Dzikovski B, Koralewski RM, Wang E, Freed J, Krebs C, Ealick SE *et al.*: **Diphthamide biosynthesis requires an organic radical generated by an iron–sulphur enzyme**. *Nature* 2010, **465**:891-896.
Dph2 is not classified as a radical SAM enzyme but contains a [4Fe–4S] cluster that is used to reductively cleave SAM. This article reveals that Dph2 catalyzes the first step of diphthamide biosynthesis through the unusual cleavage of the $C_{\gamma\text{-Met}}$–S bond to produce 5′-deoxy-5′-methylthioadenosine and the 3-amino-3-carboxypropyl radical.

74. Broderick JB: **A radically different enzyme**. *Nature* 2010, **465**:877-878.

75. Demick JM, Lanzilotta WN: **Radical SAM activation of the B12-independent glycerol dehydratase results in formation of 5′-deoxy-5′-(methylthio)adenosine and not 5′-deoxyadenosine**. *Biochemistry* 2011, **50**:440-442.

76. • Kampmeier JA: **Regioselectivity in the homolytic cleavage of *S*-adenosylmethionine**. *Biochemistry* 2010, **49**:10770-10772.
This article explores the differences in the cleavage of SAM by different radical SAM enzymes and suggests that the geometry of the SAM molecule with respect to the [4Fe–4S] cluster determines the cleavage site of SAM.

CHAPTER FIVE

GLYCYL RADICAL ACTIVATING ENZYMES: STRUCTURE, MECHANISMS AND SUBSTRATE INTERACTIONS

Contribution of Authors and Co-Authors

Manuscript(s) in Chapter(s) 4, 5, 6, 7, 9, 10

Author: Krista A Shisler

Contributions: Wrote manuscript and generated figures.

Co-Author: Joan B Broderick

Contributions: Aided in preparation of manuscript and figures.

Manuscript Information Page

Krista A Shisler and Joan B Broderick
Archives of Biochemistry and Biophysics
Status of Manuscript:
____ Prepared for submission to a peer-reviewed journal
____ Officially submitted to a peer-review journal
____ Accepted by a peer-reviewed journal
__X__ Published in a peer-reviewed journal

Published by Elsevier
Submitted November 1, 2013
Published online January 31, 2014
In Volume 546, 64-71 (2014)

Archives of Biochemistry and Biophysics 546 (2014) 64–71

Contents lists available at ScienceDirect

Archives of Biochemistry and Biophysics

journal homepage: www.elsevier.com/locate/yabbi

Review

Glycyl radical activating enzymes: Structure, mechanism, and substrate interactions ☆

Krista A. Shisler, Joan B. Broderick *

Department of Chemistry & Biochemistry and the Astrobiology Biogeocatalysis Research Center, Montana State University, Bozeman, MT 59717, United States

ARTICLE INFO

Article history:
Received 1 November 2013
and in revised form 20 January 2014
Available online 31 January 2014

Keywords:
Radical *S*-adenosylmethionine (SAM) enzyme
Glycyl radical enzyme activating enzyme (GRE–AE)
Glycyl radical enzyme (GRE)
Pyruvate formate lyase activating enzyme (PFL-AE)

ABSTRACT

The glycyl radical enzyme activating enzymes (GRE–AEs) are a group of enzymes that belong to the radical *S*-adenosylmethionine (SAM) superfamily and utilize a [4Fe–4S] cluster and SAM to catalyze H-atom abstraction from their substrate proteins. GRE–AEs activate homodimeric proteins known as glycyl radical enzymes (GREs) through the production of a glycyl radical. After activation, these GREs catalyze diverse reactions through the production of their own substrate radicals. The GRE–AE pyruvate formate lyase activating enzyme (PFL-AE) is extensively characterized and has provided insights into the active site structure of radical SAM enzymes including GRE–AEs, illustrating the nature of the interactions with their corresponding substrate GREs and external electron donors. This review will highlight research on PFL-AE and will also discuss a few GREs and their respective activating enzymes.

© 2014 Published by Elsevier Inc.

Introduction

Radical *S*-adenosylmethionine (SAM)[1] enzymes are a large superfamily of enzymes that utilize radical chemistry to catalyze diverse reactions through a similar mechanism for radical initiation. The radical SAM enzymes utilize a [4Fe–4S] cluster that is coordinated to the enzyme via a conserved cysteine motif, most commonly CX_3CX_2C, that coordinates three of the four irons of the cluster. The fourth iron of the cluster is then free to bind SAM through its amino and carboxylate moieties (Fig. 1). In the reduced state, the $[4Fe–4S]^+$ cluster transfers an electron to SAM, resulting in homolytic cleavage of SAM to produce methionine and the highly reactive 5′-deoxyadenosyl radical (dAdo$^\cdot$) intermediate. The dAdo$^\cdot$ abstracts a hydrogen atom from substrate to produce 5′-deoxyadenosine (dAdoH) and a substrate radical (Fig. 2, blue arrow) which can be the product of the reaction or can undergo further transformation [1–3]. In addition to a common mechanism, the radical SAM enzymes exhibit a conserved fold, with the [4Fe–4S] cluster bound within a partial $(\alpha/\beta)_6$ or full $(\alpha/\beta)_8$ triosephophate isomerase (TIM) barrel (Fig. 3) [1]. Other variations of the cluster binding motif [4,5] and enzyme fold [6,7] have been indentified in radical SAM enzymes or radical SAM-like enzymes. SAM has also been reported to undergo alternative cleavage reactions: in a radical SAM-like enzyme [6,7] as well as one GRE–AE [8], cleavage of the S—C(γ) bond has been reported (Fig. 2, green arrow), while the radical SAM enzyme TsrM cleaves the S—C(methyl) bond of SAM but in a non-radical mechanism [9]. This review will focus on the radical SAM enzyme pyruvate formate lyase activating enzyme (PFL-AE) as well as other radical SAM enzymes that utilize SAM to abstract a hydrogen atom from a protein glycine residue, placing them in a group known as glycyl radical enzyme activating enzymes (GRE–AEs).

The glycyl radical enzymes: substrates for the GRE–AEs

The GRE–AEs are a subclass of radical SAM enzymes which, after the production of the dAdo$^\cdot$, abstract a hydrogen atom from the alpha carbon of a highly conserved glycine residue in the

☆ This article was originally intended for publication in ABB Special Issue: Cofactor Assisted Enzymatic Catalysis. 544, (15 February 2014) http://www.sciencedirect.com/science/journal/00039861/544.

* Corresponding author. Address: Department of Chemistry & Biochemistry, 103 CBB, Montana State University, Bozeman, MT 59717, United States. Fax: +1 406 994 5407.
E-mail address: jbroderick@chemistry.montana.edu (J.B. Broderick).

[1] *Abbreviations used:* SAM, *S*-adenosylmethionine; dAdoH, 5′-deoxyadenosine; dAdo$^\cdot$, 5′-deoxyadenosyl radical; TIM, triosephophate isomerase; GRE–AE, glycyl radical enzyme activating enzyme; GRE, glycyl radical enzyme; PFL-AE, pyruvate formate lyase activating enzyme; PFL, pyruvate formate lyase; aRNR, anaerobic ribonucleotide reductase; Bss, benzylsuccinate synthase; Gdh, B_{12}-independent glycerol dehydratase; Hpd, 4-hydroxyphenylacetate decarboxylase; choline TMA-lyase, choline trimethylamine-lyase; aRNR-AE, anaerobic ribonucleotide reductase activating enzyme; Bss-AE, benzylsuccinate synthase activating enzyme; Gdh-AE, B_{12}-independent glycerol dehydratase activating enzyme; Hpd-AE, 4-hydroxyphenylacetate decarboxylase activating enzyme; *E. coli*, *Escherichia coli*; CoA, coenzyme A; MTA, 5′-deoxy-5′-methylthioadenosine; ACP, 3-amino-3-carboxylpropyl radical; ENDOR, electron nuclear double resonance; EPR, electron paramagnetic resonance; LAM, lysine 2,3-aminomutase; XAS, X-ray absorption spectroscopy; AMP, adenosine 5′-monophosphate; ADP, adenosine 5′-diphosphate; ATP, adenosine 5′-triphosphate.

0003-9861/$ - see front matter © 2014 Published by Elsevier Inc.
http://dx.doi.org/10.1016/j.abb.2014.01.020

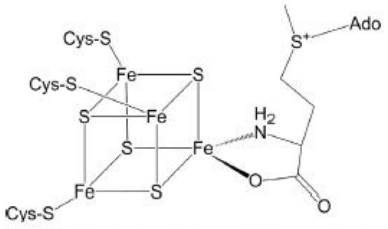


Fig. 1. SAM coordinated to the [4Fe–4S] cluster in radical SAM enzymes.

enzymes known as glycyl radical enzymes (GREs). The resulting glycyl radical is catalytically essential for the GRE, and during GRE catalysis, it abstracts an H-atom from a conserved cysteine residue to produce a thiyl radical followed by generation of a substrate radical (Fig. 4). The GREs include pyruvate formate lyase (PFL) [10–15], anaerobic ribonucleotide reductase (aRNR) [16–21], benzylsuccinate synthase (Bss) [22–26], B_{12}-independent glycerol dehydratase (Gdh) [27–29], 4-hydroxyphenylacetate decarboxylase (Hpd) [30–32], and CutC (more recently named choline trimethylamine-lyase or choline TMA-lyase) [33,34]. Each of these enzymes have a specific activating enzyme, and current results indicate no cross-reactivity between the GRE–AE and any non-partner GRE.

Although the GREs catalyze a diverse set of reactions, they share considerable sequence and structural homology. They are most commonly homodimeric proteins with a subunit size of 80–100 kDa, although Bss and Hpd contain additional subunits [25,35,36]. The core structure of a GRE monomer consists of a

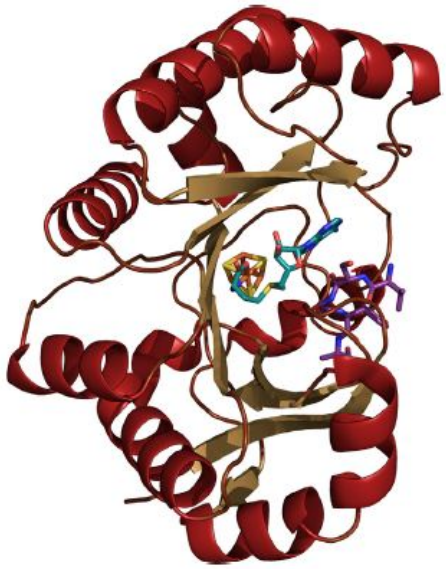


Fig. 3. Crystal structure of PFL-AE with the finger loop peptide of PFL (purple sticks) and SAM (teal sticks) (PDB ID: 3CB8).

10-stranded β-barrel surrounded by α-helices (Fig. 5) [10,11,20,28,30,37]. The GREs have half-site reactivity where only one monomer is activated by its activating enzyme with the

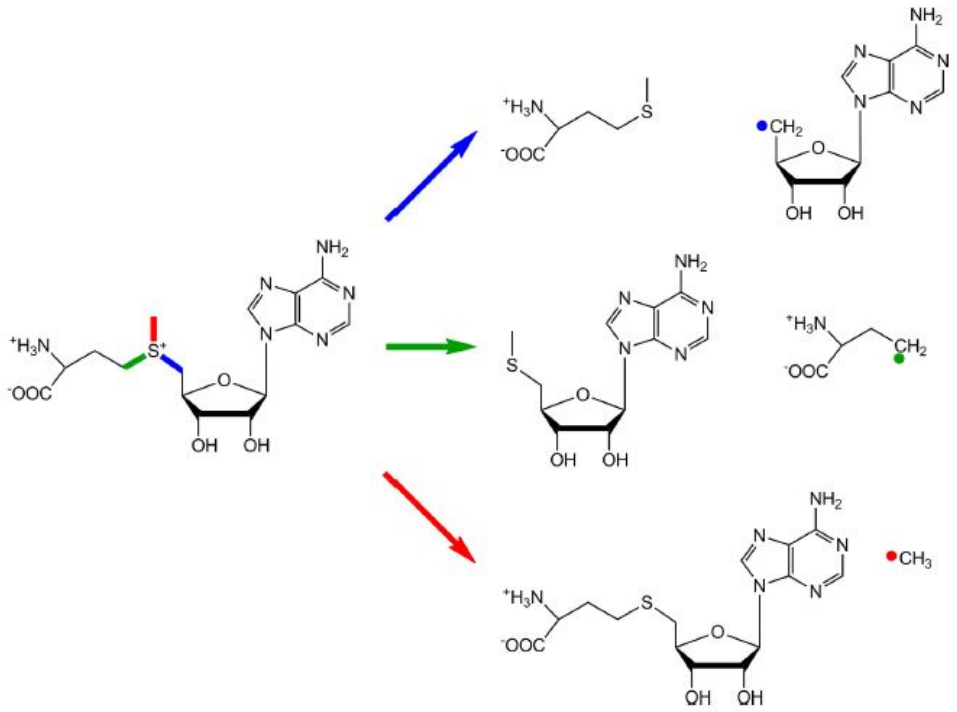


Fig. 2. SAM cleavage reactions. Blue: Traditional radical SAM cleavage to produce the 5′-deoxyadenosyl radical. Green: SAM cleavage to produce the proposed 3-amino-3-carboxylpropyl radical. Red: SAM cleavage to produce a methyl radical.

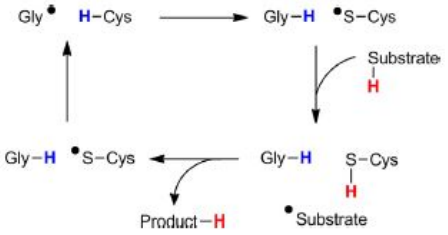


Fig. 4. General activation reaction for GREs involving the catalytic glycine and cysteine.

catalytic glycine residing on a finger loop with a highly conserved motif, RVXG[FWY]X_{6-8}[FL]X_4QX_2[IV]X_2R [36] and is in close proximity to the active site cysteine in the crystallized inactive state (Fig. 6). The glycyl radical produced during activation is highly stable under anaerobic conditions, with a half life of more than 24 h in the case of PFL [38,39]. The radical is then transferred to a conserved cysteine, or two cysteines sequentially in the case of PFL [13,40], whereupon this thiyl radical abstracts an H-atom from substrate to produce a substrate radical. Product is then formed through re-abstraction of an H-atom to reproduce the thiyl radical (Fig. 4). Further details on individual GREs and their cognate activating enzymes are provided in the following sections.

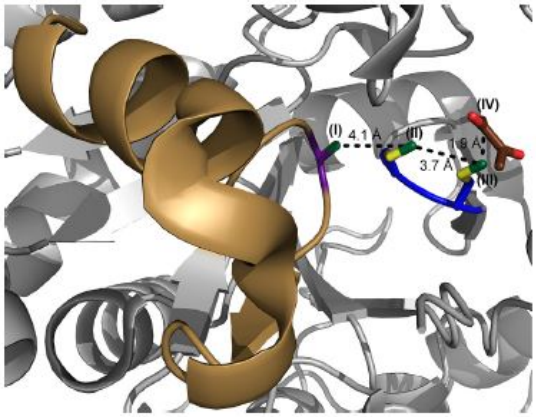


Fig. 6. Active site of PFL. The finger loop, shown in tan, contains the catalytic glycine (purple sticks) which resides next to the two catalytic cysteines (blue sticks) in the unactivated state. Also shown is the substrate pyruvate (brown sticks) which is located next to the catalytic cysteines. The distances between the abstracted hydrogens (green) and the substrate pyruvate oxygen (red) are shown in angstroms. The radical moves along the roman numerals from glycine (I) to pyruvate (IV) (PDB ID: 1H18).

Pyruvate formate lyase

PFL catalyzes the reaction of pyruvate and CoA to formate and acetyl-CoA (Fig. 7), providing the sole source of acetyl-CoA for cells under anaerobic conditions [12–15]. The glycyl radical abstracts an H-atom from a catalytic cysteine, and the resulting thiyl radical is then transferred to an adjacent cysteine residue. The second thiyl radical attacks the pyruvate carbonyl carbon, cleaving the carbon–carbon bond [10,11] to form a formate anion radical and the acetyl-S-Cys-enzyme. The formate anion radical abstracts a hydrogen from the catalytic glycine and the acetyl moiety reacts with CoA to form acetyl-CoA [13–15]. Each monomer in PFL is 85 kDa and composed of a 10-stranded β-barrel surrounded by α-helices, forming an α/β barrel with the active site located in the center (Fig. 5a) [10,11]. Upon oxygen exposure, PFL is irreversibly cleaved at the glycyl radical, forming two fragments of 82 kDa and 3 kDa in size. The 14 kDa *Escherichia coli* (*E. coli*) protein YfiD can restore full activity in O_2-damaged PFL, possibly by replacement of the C-terminal 3 kDa portion through complexation with PFL [41].

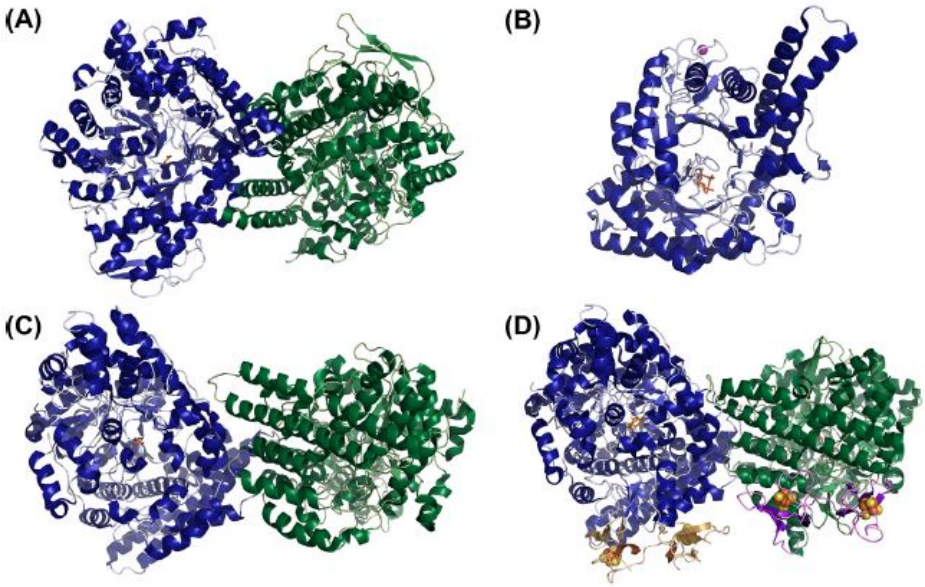


Fig. 5. Crystal structures of the GREs and their substrates (orange sticks). (A) PFL with pyruvate (PDB ID: 1H18); (B) aRNR with dGTP and Zn (purple sphere) (PDB ID: 1HK8); (C) Gdh with glycerol (PDB ID: 1R9D); (D) Hpd with HPA (PDB ID: 2YAJ).

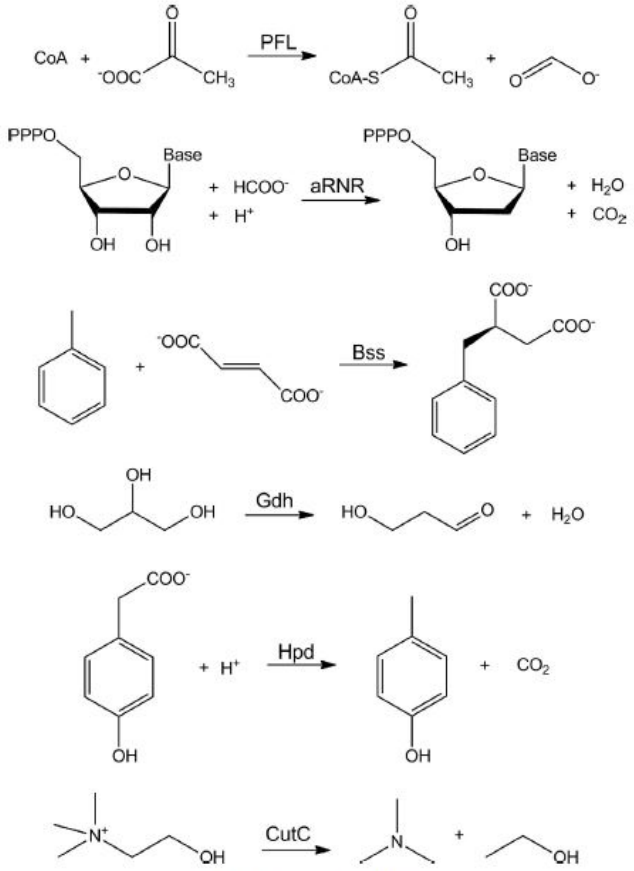


Fig. 7. Reactions catalyzed by GREs.

Anaerobic ribonucleotide reductase

The anaerobic ribonucleotide reductase (aRNR) catalyzes the conversion of ribonucleotides to their corresponding 2′-deoxyribonucleotides through the reduction of the C2′—OH bond in the ribonucleotide (Fig. 7) [16–19,42]. The reaction is initiated by H-atom abstraction of the ribonucleotide 3′-hydrogen by the catalytic cysteine (Cys290), generating a 3′-nucleotide radical. The 2′OH is protonated by another cysteine (Cys79) and then leaves as water, generating a 3′-keto-2′-deoxynucleotide radical. This radical is reduced by formate, producing CO_2. Two electron-coupled proton transfer steps generate the 3′-deoxynucleotide radical. This radical can abstract a hydrogen from the catalytic Cys290, generating product and a thiyl radical which regenerates the glycyl radical. [16,17,19,42,43]. The complete enzyme contains a large homodimer, α_2, with the catalytic glycine and a small homodimer, β_2, which contains the radical SAM [4Fe–4S] cluster [21]. The β_2 homodimer is tightly bound to the α_2 homodimer under normal conditions, but has been isolated and shown to function catalytically as an activating enzyme for α_2. Only the α_2 subunit has been crystallographically characterized, and it shows a strikingly similar topology to PFL with an α/β barrel and two opposing finger loops that meet to form the active site (Fig. 5b) [20,37]. The aRNR α_2 subunit was found to contain four conserved cysteines not needed for complexation with aRNR-AE (β_2) but are essential for glycyl radical activation of aRNR [44]. These cysteines coordinate one Zn ion per monomer which is thought to play a structural role [44,45].

Benzylsuccinate synthase

Benzylsuccinate synthase (Bss) catalyzes the formation of (*R*)-benzylsuccinate through the transfer of the methyl group of toluene to the double bond of fumarate through carbon–carbon bond formation (Fig. 7) [22,23,25,46]. The reaction proceeds through H-atom abstraction from toluene, generating a benzyl radical. This resulting benzyl radical then adds to fumarate, generating a benzylsuccinyl radical intermediate which regenerates the cysteine thiyl radical to produce (*R*)-benzylsuccinate [23,46]. Bss contains three subunits as an $\alpha_2\beta_2\gamma_2$ heterohexamer: the 98 kDa α_2 subunit has high similarity to other GREs and the 8.5 kDa β_2 and 6.5 kDa γ_2 subunits are homologous to those in other enzymes involved in activation of hydrocarbons such as xylenes, cresols, and alkanes to form succinate adducts [24,47]. The additional β_2 and γ_2 subunits contain two [4Fe–4S] clusters possibly coordinated by conserved cysteine residues and are necessary for the structural integrity of the complete complex [24,26].

In addition to Bss containing additional clusters, its activating enzyme, Bss-AE, contains two ferredoxin-like cysteine motifs in

addition to the radical SAM cluster binding site [25]. These auxiliary Fe–S clusters have become a rising theme in radical SAM enzymes [2]. These additional cluster(s) have been shown to facilitate sulfur insertion into product [48–50] or to assist in methylthiotransferase reactions as the sulfur source [51–53]. Other possible purposes for auxiliary Fe–S clusters include reducing the radical SAM [4Fe–4S] cluster [54], acting as an electron acceptor during catalysis [55], or substrate coordination [56].

B_{12}-independent glycerol dehydratase

B_{12}-independent glycerol dehydratase (Gdh) is the GRE involved in the microbial dehydration of glycerol to 3-hydroxylpropionaldehyde, which is ultimately converted to 1,3-propanediol (Fig. 7) [27–29]. The reaction was originally proposed to involve the transfer of the hydroxyl group from the central carbon to a terminal carbon where the diol intermediate cleaves to produce water and 3-hydroxylpropionaldehyde [28]. A recent study suggests that the active site of Gdh does not facilitate this migration of the hydroxyl group [27]. Instead, surrounding amino acids act as proton donors and acceptors where a histidine residue donates a proton to the central hydroxyl group, releasing water. Glutamate accepts a proton, forming a carbonyl group at C-1 on glycerol followed by H-atom abstraction from cysteine by the substrate to reproduce the thiyl radical [27]. This reaction takes place in a 10-stranded β-barrel surrounded by α-helices similar to PFL and aRNR with no additional subunits (Fig. 5c) [28].

The activating enzyme for Gdh, Gdh-AE, has been reported to cleave SAM not through the C5′-S bond to produce dAdo· and methionine but rather through an alternative bond to form 5′-deoxy-5′-methylthioadenosine (MTA) and a proposed 3-amino-3-carboxylpropyl radical (ACP) (Fig. 2) [8]. Dph2, termed a radical SAM-like enzyme because it lacks the sequence and structural characteristics of the superfamily (including the CX_3CX_2C the TIM barrel fold) but still utilizes a [4Fe–4S] cluster to carry out SAM radical chemistry, also cleaves the S—C(γ) bond of SAM to produce MTA and the proposed ACP radical [6,7]. How radical SAM enzymes control the regioselectivity of SAM cleavage is unclear but the orientation of SAM with respect to the [4Fe–4S] cluster likely plays a role [7,57]. In addition to the radical SAM cysteine binding motif, Gdh-AE contains two additional cysteine-rich domains, CX_2CX_2-CX_3C, which are ferredoxin-like [4Fe–4S] cluster binding domains [8,29]. It was proposed that these auxiliary clusters may contribute to the altered site of SAM cleavage but this possibility is still under investigation.

4-Hydroxyphenylacetate decarboxylase

4-Hydroxyphenylacetate decarboxylase (Hpd) catalyzes the last step in the fermentation pathway of tyrosine through the decarboxylation of 4-hydroxyphenylacetate (HPA) to *p*-cresol (Fig. 7) [30–32,58,59]. From the crystal structure and substrate binding, a Kolbe-type decarboxylation reaction was proposed for Hpd [30]. The reaction is initiated through a radical transfer between the catalytic cysteine and the substrate carboxylic group and a proton transfer from the hydroxyl group of the substrate to a glutamate residue. Decarboxylation is then coupled with proton transfer from a glutamate residue (Glu637) to the phenolic hydroxyl group, producing a *p*-hydroxybenzyl radical. Glu505 transfers a proton to the catalytic cysteine which is abstracted to produce the product *p*-cresol [59]. Hpd is a heterotetramer ($\beta_4\gamma_4$) with a 100 kDa β_4 subunit containing the catalytic glycine and cysteine and a 9.5 kDa γ_4 subunit which binds two [4Fe–4S] clusters (Fig. 5d). This smaller subunit has been proposed to be involved in the regulation of the oligomeric state and the activity of the enzyme [30,32]. The N-terminal cluster is coordinated by three cysteines and a histidine while the C-terminal cluster is coordinated by four cysteines buried in the $\beta_4\gamma_4$ heterodimer interface.

Like Bss-AE and Gdh-AE, the activating enzyme for Hpd, Hpd-AE, contains two cysteine rich motifs in addition to the radical SAM [4Fe–4S] cluster which are thought to bind auxiliary Fe–S clusters. Chemically reconstituted Hpd-AE contained about 8 Fe per protein [32] and more recently 12 Fe per protein after as-isolated protein was treated with iron–sulfur cluster (ISC) assembly proteins followed by chemical reconstitution [58]. The functional roles for these additional clusters in Hpd-AE are still under investigation.

CutC

A newly characterized GRE, CutC or choline TMA-lyase, catalyzes the conversion of choline to trimethylamine (TMA) (Fig. 7) [33,34]. The reaction involves breaking a C—N bond, which is unusual for glycyl radical enzymes. CutC shows active site similarity to Gdh [34]. Little characterization has been conducted on CutC or its activating enzyme, CutD, but two mechanisms for CutC catalysis have been proposed. Both involve abstraction of an H-atom from C1 of choline by a thiyl radical generated by the glycyl radical, followed by migration of the trimethylamino group at C2 to C1 to produce a carbinolamine radical; the mechanistic proposals differ in the details of this migration and the release of TMA [33,34]. Further biochemical and mechanistic studies need to be conducted to establish a mechanism and structure of this novel GRE.

PFL-AE as a model for the GRE–AEs

Most of the GRE–AEs have proven difficult to study due to instability, difficulty in overexpression, lability of the iron-sulfur cluster, or other reasons. PFL-AE is the exception, and after the initial discovery of the iron–sulfur cluster in this enzyme [60], considerable understanding of radical SAM enzymes in general, and GRE–AEs in particular, has come about via detailed studies of this enzyme.

Interaction of PFL-AE and PFL

Initial work on PFL suggested that an activase, later identified as PFL-AE, was required for catalysis [61,62]. It was later shown that the pro-*S* hydrogen of the PFL Gly734 was abstracted by a SAM-derived dAdo· during PFL activation [12]. The catalytic glycine residue in PFL, as in the other GREs, is located on a finger loop which is buried in the interior of PFL [10]. In the unactivated state of PFL characterized by crystallography, the catalytic glycine on the finger loop is positioned near an opposing loop housing the two catalytic cysteines involved in the conversion of pyruvate and CoA to formate and acetyl-CoA; we have referred to this state of PFL as the "closed state" (Fig. 6) [10,11,63]. In the "open state" of PFL, the finger loop is flipped out to interact with PFL-AE [63]. The structure of PFL-AE crystallized with a peptide portion of this finger loop of PFL showed that the finger loop is located next to SAM and the [4Fe–4S] cluster inside the partial TIM barrel of PFL-AE (Fig. 3) [64]. The catalytic glycine is positioned near SAM in preparation for H-atom abstraction. The dynamics of the open and closed state are regulated by the presence or absence of PFL-AE, with more PFL in the open state at higher concentrations of PFL-AE [63]. This conformational change is proposed to be similar in other GREs due both to their sequence and structural similarities and to their need to undergo direct H-atom abstraction in the GRE–AE active site.

Nature of the iron–sulfur cluster in PFL-AE and its interaction with SAM

The initiation of catalysis in all radical SAM enzymes is thought to occur though a common mechanism where a $[4Fe–4S]^{2+}$ cluster is reduced by an external electron donor and the electron is then transferred from the cluster to SAM through inner-sphere electron transfer, whereupon SAM is cleaved and abstracts a hydrogen atom from substrate to produce a substrate radical. The unique coordination mode of SAM, in which the amino and carboxylate moieties of SAM chelate the unique iron of the [4Fe–4S] cluster, was first demonstrated via spectroscopic studies of PFL-AE [65–67] and was further substantiated by X-ray crystal structures of PFL-AE and other radical SAM enzymes [4,64,68–76].

Using UV–vis absorption, resonance Raman, electron paramagnetic resonance (EPR), and Mössbauer spectroscopy, PFL-AE was initially found to contain a [4Fe–4S] cluster in its active site [60,77,78]. Mössbauer studies demonstrated that the unique Fe coordination changes upon addition of SAM, and an increase in coordination number with a ligand other than sulfur was proposed [65]. EPR experiments further emphasized SAM binding to the cluster: the cluster signal converted from a rhombic to a nearly axial signal in the presence of SAM [66]. Electron nuclear double resonance (ENDOR) spectroscopic studies of PFL-AE bound to a series of SAMs containing NMR-active nuclei introduced at specific positions (e.g. the methyl carbon and hydrogens, the carboxylate oxygen, or the amino nitrogen) revealed coupling between the paramagnetic $[4Fe–4S]^{+}$ cluster and these nuclei, demonstrating that SAM coordinates to the cluster through the amino and a carboxyl oxygen of SAM (Fig. 1) [67] and is in direct orbital overlap with the cluster [66]. This coordination allows for the sulfonium ion to orient itself close to the unique iron in preparation for electron transfer.

In order to control uncoupled SAM cleavage, radical SAM enzymes utilize the large redox barrier between [4Fe–4S] clusters (−450 mV) and SAM (−1.8 V). This barrier of about 1.4 V or 32 kcal mol^{-1} is lowered to more favorable SAM cleavage conditions through binding of SAM to the cluster, contributing to a 19 kcal mol^{-1} decrease, and the binding of substrate, contributing to a 4 kcal mol^{-1} decrease in the case of lysine 2,3-aminomutase (LAM) [79,80]. The reduction is largely attributed to the coordination of SAM to the [4Fe–4S] cluster. Upon electron transfer, the unique iron transforms from a pentacoordinate state in the $[4Fe–4S]^{+}$ cluster to the more favorable hexacoordinate state in the $[4Fe–4S]^{2+}$ cluster. The sulfur of SAM is also within van der Waals contact of the Fe, facilitating inner-sphere electron transfer [79]. To investigate the interaction between SAM and the [4Fe–4S] cluster, sulfur K-edge X-ray absorption spectroscopy (XAS) and DFT calculations were utilized [81]. An increase in the intensity of the pre-edge feature with the presence of SAM was detected, which is indicative of decreased covalency of the Fe–S bonds of the cluster. The orientation of the C—S σ^* orbital in relation to the unique iron may contribute, possibly in conjunction with the polarity of the medium, to decreasing the large reduction potential barrier for the cleavage of SAM through the backbonding interactions. Control of the dielectric conditions, which are lowered upon substrate binding, could also aid in the decrease of uncoupled SAM cleavage in the absence of substrate [81]. Another contributing factor may be proximity of the sulfonium ion of SAM and the unique Fe as enzymes with a shorter $Fe–S_{SAM}$ distance show an increase in the rate of uncouple SAM cleavage.

The state of the iron–sulfur cluster in vivo

Previously, PFL-AE had been shown to purify with a mixture of [2Fe–2S], [3Fe–4S], and [4Fe–4S] clusters [77,78] with the conversion to [4Fe–4S] clusters under reducing conditions [60,78]. In order to probe PFL-AE *in vivo*, Yang et al. investigated the clusters in *E. coli* whole cells overexpressing PFL-AE under aerobic and anaerobic conditions [82]. Under aerobic conditions, the cells contained mixed iron states in the form of [4Fe–4S] clusters, [2Fe–2S] clusters, high spin Fe^{III}, and high spin Fe^{II}, but after anaerobic incubation, the only clusters observed were [4Fe–4S] with some free Fe^{II} species. When converting back to aerobic conditions, [2Fe–2S] clusters reappeared with a decrease in [4Fe–4S] clusters [82].

While investigating the cluster conversion in whole cells, Yang et al. surprisingly found that the [4Fe–4S] clusters in the cells under anaerobic conditions where in a valence localized state [82]. Typically [4Fe–4S] clusters contain two delocalized $Fe^{II}Fe^{III}$ pairs; no other radical SAM enzymes have shown this valence localization event and only one other case of protein-bound [4Fe–4S] clusters in this state has been found [83]. For the [4Fe–4S] cluster of PFL-AE in whole cells, three quadrupole doublets were observed in the Mössbauer spectrum that correspond to a delocalized Fe^{II}-Fe^{III} pair, a high spin Fe^{II}, and a Fe^{III} site in a 2:1:1 ratio, indicating that 100% of the [4Fe–4S] clusters were in this valence-localized state [82]. The valence localized state observed in PFL-AE in whole cells is likely to arise from altered coordination at the unique iron site of the cluster; that 100% of the cluster is in this state indicates that whatever binds to the cluster to induce valence localization is likely an abundant small molecule. In order to explore possible inducers of valence localization, a series of small molecules including SAM degradation products (MTA, dAdoH, methionine, adenine, and ribose), molecules associated with PFL (pyruvate, CoA, and acetyl-CoA), and cellular metabolites (ATP, ADP, and AMP) were added to purified PFL-AE and the Mössbauer spectra were recorded [82]. Upon addition of MTA, dAdoH, AMP, and ADP, partial valence localization in the purified protein was observed; AMP was proposed as the most likely candidate to induce valence localization in whole cells due to it highest abundance in *E. coli* cells [82]. When SAM was added to PFL-AE containing the small molecules, complete conversion to SAM-bound clusters was observed, demonstrating that SAM is able to displace these small molecules in preparation for catalysis [82].

The reason for valence localization is still under investigation but protecting the cluster from oxidative damage and/or reactivity control are possibilities. The Fe–S clusters in radical SAM enzymes are generally highly oxygen sensitive, degrading to [3Fe–4S] and [2Fe–2S] clusters upon oxygen exposure, as discussed previously. Under aerobic conditions, these small molecules could protect the unique iron site, maintaining the [4Fe–4S] cluster which was observed after purified protein was exposed to air for 30 min [82].

Interaction with in vivo electron donors

In vitro studies have shown that flavodoxins can be used as external electron donors to reduce the [4Fe–4S] clusters in radical SAM enzymes and is thought to be one of the electron donors *in vivo* [84–86]. In order for flavodoxin to donate an electron to PFL-AE, flavodoxin must contain its flavin mononucleotide cofactor (FMN); even the interaction between flavodoxin and PFL-AE requires FMN, which was shown using surface plasmon resonance (SPR) experiments [87]. Using the crystal structure of PFL-AE, docking studies of PFL-AE with flavodoxin showed possible sites of interaction and essential amino acids for electron transfer. A tryptophan residue, W57, in PFL-AE is thought to facilitate the electron transfer from flavodoxin to the [4Fe–4S] cluster [87]. Sequence alignments show that other radical SAM enzymes have similar conserved regions as PFL-AE and are thought to be electron donor binding sites.

Conclusions

The GRE–AE enzymes are a unique class of radical SAM enzymes, activating a much larger protein. One of the most prominent GRE–AEs, PFL-AE, was one of the first radical SAM enzymes characterized and has provided considerable insights into the SAM-cluster interactions for this superfamily. PFL-AE has also shown unusual active site electronic structure *in vivo* that can be replicated in the presence of small molecules *in vitro*, and may provide insights into control of reactivity in the GRE–AEs. Recent studies have provided insight into how PFL-AE catalyzes direct H-atom abstraction on a buried glycine residue of PFL, and similar complex protein–protein interactions are also likely for the structurally related GRE–AE/GRE pairs described herein. It is likely that additional GREs and their cognate activating enzymes will continue to be discovered, and the understanding of PFL and PFL-AE will provide an important foundation for elucidating their structures, mechanisms, and interactions.

Acknowledgments

Research on radical SAM activating enzymes in the Broderick laboratory is supported by the National Institutes of Health (GM54608).

References

[1] J.L. Vey, C.L. Drennan, Chem. Rev. 111 (2011) 2487–2506.
[2] N.D. Lanz, S.J. Booker, Biochim. Biophys. Acta 1824 (2012) 1196–1212.
[3] K.A. Shisler, J.B. Broderick, Curr. Opin. Struct. Biol. 22 (2012) 701–710.
[4] A. Chatterjee, Y. Li, Y. Zhang, T.L. Grove, M. Lee, C. Krebs, S.J. Booker, T.P. Begley, S.E. Ealick, Nat. Chem. Biol. 4 (2008) 758–765.
[5] S.E. McGlynn, E.S. Boyd, E.M. Shepard, R.K. Lange, R. Gerlach, J.B. Broderick, J.W. Peters, J. Bacteriol. 192 (2010) 595–598.
[6] Y. Zhang, X. Zhu, A.T. Torelli, M. Lee, B. Dzikovski, R.M. Koralewski, E. Wang, J. Freed, C. Krebs, S.E. Ealick, H. Lin, Nature 465 (2010) 891–896.
[7] J.B. Broderick, Nature 465 (2010) 877–878.
[8] J.M. Demick, W.N. Lanzilotta, Biochemistry 50 (2011) 440–442.
[9] S. Pierre, A. Guillot, A. Benjdia, C. Sandstrom, P. Langella, O. Berteau, Nat. Chem. Biol. 8 (2012) 957–959.
[10] A. Becker, K. Fritz-Wolf, W. Kabsch, J. Knappe, S. Schultz, A.F. Volker, Nat. Struct. Biol. 6 (1999) 969–975.
[11] A. Becker, W. Kabsch, J. Biol. Chem. 277 (2002) 40036–40042.
[12] M. Frey, M. Rothe, A.F. Wagner, J. Knappe, J. Biol. Chem. 269 (1994) 12432–12437.
[13] C.V. Parast, K.K. Wong, S.A. Lewisch, J.W. Kozarich, J. Peisach, R.S. Magliozzo, Biochemistry 34 (1995) 2393–2399.
[14] W. Plaga, R. Frank, J. Knappe, Eur. J. Biochem. 178 (1988) 445–450.
[15] W. Plaga, G. Vielhaber, J. Wallach, J. Knappe, FEBS Lett. 466 (2000) 45–48.
[16] K.B. Cho, F. Himo, A. Gräslund, P.E.M. Siegbahn, J. Phys. Chem. B 105 (2001) 6445–6452.
[17] M. Fontecave, E. Mulliez, D.T. Logan, Prog. Nucleic Acid Res. Mol. Biol. 72 (2002) 95–127.
[18] A. Jordan, P. Reichard, Annu. Rev. Biochem. 67 (1998) 71–98.
[19] M. Kolberg, K.R. Strand, P. Graff, K.K. Andersson, Biochim. Biophys. Acta 1699 (2004) 1–34.
[20] K.M. Larsson, J. Andersson, B.M. Sjoberg, P. Nordlund, D.T. Logan, Structure 9 (2001) 739–750.
[21] S. Ollagnier, E. Mulliez, J. Gaillard, R. Eliasson, M. Fontecave, P. Reichard, J. Biol. Chem. 271 (1996) 9410–9416.
[22] H.R. Beller, A.M. Spormann, FEMS Microbiol. Lett. 178 (1999) 147–153.
[23] V.S. Bharadwaj, A.M. Dean, C.M. Maupin, J. Am. Chem. Soc. 135 (2013) 12279–12288.
[24] M. Hilberg, A.J. Pierik, E. Bill, T. Friedrich, M.L. Lippert, J. Heider, Inorg. Chem. 17 (2012) 49–56.
[25] B. Leuthner, C. Leutwein, H. Schulz, P. Horth, W. Haehnel, E. Schiltz, H. Schagger, J. Heider, Mol. Microbiol. 28 (1998) 615–628.
[26] L. Li, D.P. Patterson, C.C. Fox, B. Lin, P.W. Coschigano, E.N. Marsh, Biochemistry 48 (2009) 1284–1292.
[27] M. Feliks, G.M. Ullmann, J. Phys. Chem. B 116 (2012) 7076–7087.
[28] J.R. O'Brien, C. Raynaud, C. Croux, L. Girbal, P. Soucaille, W.N. Lanzilotta, Biochemistry 43 (2004) 4635–4645.
[29] C. Raynaud, P. Sarçabal, I. Meynial-Salles, C. Croux, P. Soucaille, Proc. Natl. Acad. Sci. USA 100 (2003) 5010–5015.
[30] B.M. Martins, M. Blaser, M. Feliks, G.M. Ullmann, W. Buckel, T. Selmer, J. Am. Chem. Soc. 133 (2011) 14666–14674.
[31] T. Selmer, P.I. Andrei, Eur. J. Biochem. 268 (2001) 1363–1372.
[32] L. Yu, M. Blaser, P.I. Andrei, A.J. Pierik, T. Selmer, Biochemistry 45 (2006) 9584–9592.
[33] S. Craciun, E.P. Balskus, Proc. Natl. Acad. Sci. USA 109 (2012) 21307–21312.
[34] C.J. Thibodeaux, W.A. van der Donk, Proc. Natl. Acad. Sci. USA 109 (2012) 21184–21185.
[35] P.I. Andrei, A.J. Pierik, S. Zauner, L.C. Andrei-Selmer, T. Selmer, Eur. J. Biochem. 271 (2004) 2225–2230.
[36] T. Selmer, A.J. Pierik, J. Heider, Biol. Chem. 386 (2005) 981–988.
[37] D.T. Logan, J. Andersson, B.M. Sjoberg, P. Nordlund, Science 283 (1999) 1499–1504.
[38] M.R. Nnyepi, Y. Peng, J.B. Broderick, Arch. Biochem. Biophys. 459 (2007) 1–9.
[39] C.J. Walsby, D. Ortillo, J. Yang, M.R. Nnyepi, W.E. Broderick, B.M. Hoffman, J.B. Broderick, Inorg. Chem. 44 (2005) 727–741.
[40] J. Knappe, S. Elbert, M. Frey, A.F. Wagner, Biochem. Soc. Trans. 21 (Pt 3) (1993) 731–734.
[41] A.F. Wagner, S. Schultz, J. Bomke, T. Pils, W.D. Lehmann, J. Knappe, Biochem. Biophys. Res. Commun. 285 (2001) 456–462.
[42] H. Eklund, M. Fontecave, Structure 7 (1999) R257–262.
[43] J. Stubbe, J. Ge, C.S. Yee, Trends Biochem. Sci. 26 (2001) 93–99.
[44] D.T. Logan, E. Mulliez, K.M. Larsson, S. Bodevin, M. Atta, P.E. Garnaud, B.M. Sjoberg, M. Fontecave, Proc. Natl. Acad. Sci. USA 100 (2003) 3826–3831.
[45] F. Luttringer, E. Mulliez, B. Dublet, D. Lemaire, M. Fontecave, Inorg. Chem. 14 (2009) 923–933.
[46] C.J. Krieger, W. Roseboom, S.P. Albracht, A.M. Spormann, J. Biol. Chem. 276 (2001) 12924–12927.
[47] J. Heider, Curr. Opin. Chem. Biol. 11 (2007) 188–194.
[48] R.M. Cicchillo, K.H. Lee, C. Baleanu-Gogonea, N.M. Nesbitt, C. Krebs, S.J. Booker, Biochemistry 43 (2004) 11770–11781.
[49] C.J. Fugate, J.T. Jarrett, Biochim. Biophys. Acta 1824 (2012) 1213–1222.
[50] A.M. Taylor, S. Stoll, R.D. Britt, J.T. Jarrett, Biochemistry 50 (2011) 7953–7963.
[51] B.P. Anton, S.P. Russell, J. Vertrees, S. Kasif, E.A. Raleigh, P.A. Limbach, R.J. Roberts, Nucleic Acids Res. 38 (2010) 6195–6205.
[52] K.H. Lee, L. Saleh, B.P. Anton, C.L. Madinger, J.S. Benner, D.F. Iwig, R.J. Roberts, C. Krebs, S.J. Booker, Biochemistry 48 (2009) 10162–10174.
[53] F. Pierrel, T. Douki, M. Fontecave, M. Atta, J. Biol. Chem. 279 (2004) 47555–47563.
[54] A. Benjdia, S. Subramanian, J. Leprince, H. Vaudry, M.K. Johnson, O. Berteau, FEBS J. 277 (2010) 1906–1920.
[55] T.L. Grove, J.H. Ahlum, P. Sharma, C. Krebs, S.J. Booker, Biochemistry 49 (2010) 3783–3785.
[56] N.S. Lees, P. Hanzelmann, H.L. Hernandez, S. Subramanian, H. Schindelin, M.K. Johnson, B.M. Hoffman, J. Am. Chem. Soc. 131 (2009) 9184–9185.
[57] J.A. Kampmeier, Biochemistry 49 (2010) 10770–10772.
[58] B. Selvaraj, A.J. Pierik, E. Bill, B.M. Martins, J. Bio, Inorg. Chem. (2013) 1–11.
[59] M. Feliks, B.M. Martins, G.M. Ullmann, J. Am. Chem. Soc. 135 (2013) 14574–14585.
[60] J.B. Broderick, R.E. Duderstadt, D.C. Fernandez, K. Wojtuszewski, T.F. Henshaw, M.K. Johnson, J. Am. Chem. Soc. 119 (1997) 7396–7397.
[61] J. Knappe, F.A. Neugebauer, H.P. Blaschkowski, M. Ganzler, Proc. Natl. Acad. Sci. USA 81 (1984) 1332–1335.
[62] J. Knappe, T. Schmitt, Biochem. Biophys. Res. Commun. 71 (1976) 1110–1117.
[63] Y. Peng, S.E. Veneziano, G.D. Gillispie, J.B. Broderick, J. Biol. Chem. 285 (2010) 27224–27231.
[64] J.L. Vey, J. Yang, M. Li, W.E. Broderick, J.B. Broderick, C.L. Drennan, Proc. Natl. Acad. Sci. USA 105 (2008) 16137–16141.
[65] C. Krebs, W.E. Broderick, T.F. Henshaw, J.B. Broderick, B. Huynh, J. Am. Chem. Soc. 124 (2002) 912–913.
[66] C.J. Walsby, W. Hong, W.E. Broderick, J. Cheek, D. Ortillo, J.B. Broderick, B.M. Hoffman, J. Am. Chem. Soc. 124 (2002) 3143–3151.
[67] C.J. Walsby, D. Ortillo, W.E. Broderick, J.B. Broderick, B.M. Hoffman, J. Am. Chem. Soc. 124 (2002) 11270–11271.
[68] S. Arragain, R. Garcia-Serres, G. Blondin, T. Douki, M. Clemancey, J.M. Latour, F. Forouhar, H. Neely, G.T. Montelione, J.F. Hunt, E. Mulliez, M. Fontecave, M. Atta, J. Biol. Chem. 285 (2010) 5792–5801.
[69] A. Benjdia, K. Heil, T.R. Barends, T. Carell, I. Schlichting, Nucleic Acids Res. 40 (2012) 9308–9318.
[70] F. Berkovitch, Y. Nicolet, J.T. Wan, J.T. Jarrett, C.L. Drennan, Science 303 (2004) 76–79.
[71] A.K. Boal, T.L. Grove, M.I. McLaughlin, N.H. Yennawar, S.J. Booker, A.C. Rosenzweig, Science 332 (2011) 1089–1092.
[72] S. Goto-Ito, R. Ishii, T. Ito, R. Shibata, E. Fusatomi, S.I. Sekine, Y. Bessho, S. Yokoyama, Acta Crystallogr. D Biol. Crystallogr. 63 (2007) 1059–1068.
[73] P. Hanzelmann, H. Schindelin, Proc. Natl. Acad. Sci. USA 103 (2006) 6829–6834.
[74] G. Layer, J. Moser, D.W. Heinz, D. Jahn, W.D. Schubert, EMBO J. 22 (2003) 6214–6224.
[75] B.W. Lepore, F.J. Ruzicka, P.A. Frey, D. Ringe, Proc. Natl. Acad. Sci. USA 102 (2005) 13819–13824.
[76] Y. Nicolet, J.K. Rubach, M.C. Posewitz, P. Amara, C. Mathevon, M. Atta, M. Fontecave, J.C. Fontecilla-Camps, J. Biol. Chem. 283 (2008) 18861–18872.
[77] J.B. Broderick, T.F. Henshaw, J. Cheek, K. Wojtuszewski, S.R. Smith, M.R. Trojan, R.M. McGhan, A. Kopf, M. Kibbey, W.E. Broderick, Biochem. Biophys. Res. Commun. 269 (2000) 451–456.
[78] C. Krebs, T.F. Henshaw, J. Cheek, B. Huynh, J.B. Broderick, J. Am. Chem. Soc. 122 (2000) 12497–12506.
[79] S.C. Wang, P.A. Frey, Biochemistry 46 (2007) 12889–12895.

CHAPTER SIX

EPR AND ENDOR ANALYSIS OF SMALL MOLECULES INDUCING VALENCE LOCALIZATION IN PFL-AE

Contribution of Authors and Co-Authors

Manuscript(s) in Chapter(s) 4, 5, 6, 7, 9, 10

Author: Krista A Shisler

Contributions: Prepared, collected, and analyzed EPR samples. Prepared ENDOR samples. Wrote manuscript and generated figures.

Co-Author: Masaki Horitani

Contributions: Collected and analyzed ENDOR results at Northwestern University, wrote sections related to ENDOR analysis and instrumentation, and prepared ENDOR figures.

Co-Author: Brian M. Hoffman

Contributions: Provided insights into ENDOR analysis and aided in preparation of manuscript and figures.

Co-Author: Joan B Broderick

Contributions: Provided interpretation of the EPR and ENDOR results, provided insight into the preparation of samples, and aided in preparation of manuscript and figures.

Manuscript Information Page

Krista A Shisler, Masaki Horitani, Brian M Hoffman, and Joan B Broderick
Journal of the American Chemical Society
Status of Manuscript:
__X__ Prepared for submission to a peer-reviewed journal
____ Officially submitted to a peer-review journal
____ Accepted by a peer-reviewed journal
____ Published in a peer-reviewed journal

Publisher ACS Publications

CHAPTER 6

EPR AND ENDOR ANALYSIS OF SMALL MOLECULES INDUCING VALENCE LOCALIZATION IN PFL-AE

Introduction

Fe-S cluster are some of the most versatile and ubiquitous prosthetic groups found in biological systems [1,2]. They carry out roles such as electron transfer, substrate binding, storage, or structural roles. The basic structure of Fe-S clusters is a Fe_2S_2 rhomb which can be combined to form [2Fe-2S], [3Fe-4S], [4Fe-4S] clusters and even more complex structures and thus, the Fe_2S_2 rhombs can be considered the building blocks of assembly. For example, the cubane [4Fe-4S] clusters can be assembled from two [2Fe-2S] units whereas the [3Fe-4S] clusters are formed from the loss of one Fe from the [4Fe-4S] cluster [1,2].

A [4Fe-4S] cluster sits at the core of radical *S*-adenosyl-L-methionine (SAM) enzymes. The [4Fe-4S] cluster is ligated to the protein via a $CX_3CX\Phi C$ motif, where Φ is an aromatic residue, and this three-cysteine motif creates a unique Fe site in the [4Fe-4S] cluster to which SAM coordinates through its amino and carboxyl moieties [3,4]. Upon one electron reduction of a $[4Fe\text{-}4S]^{2+}$ cluster to a $[4Fe\text{-}4S]^{+}$ cluster, inner sphere electron transfer to SAM occurs, reductively cleaving the S–5'-C bond, generating the highly reactive 5'-deoxyadenosyl radical (5'-dAdo•) and methionine (Figure 6.1). Once 5'-dAdo• is generated, these radical SAM enzymes can carry out diverse reactions such as activating a protein through radical generation, DNA repair, sulfur insertion, and

isomerization [3]. The reactions of radical SAM enzymes are highly controlled within the active site [5] which resides at the terminus of a partial $(\alpha/\beta)_6$ TIM barrel in most cases or a complete $(\alpha/\beta)_8$ TIM barrel in other cases [4]. Pyruvate formate lyase activating enzyme (PFL-AE) is a well-characterized radical SAM enzyme that activates the homodimeric pyruvate formate lyase (PFL) protein. PFL-AE abstracts the pro-*S* hydrogen from a glycine residue of PFL (G734), producing a stable glycyl radical (Figure 6.1). Once activated, PFL catalyzes the first step in anaerobic glucose metabolism through the generation of formate and acetyl-CoA from pyruvate and coenzyme A (CoA) [6-8].

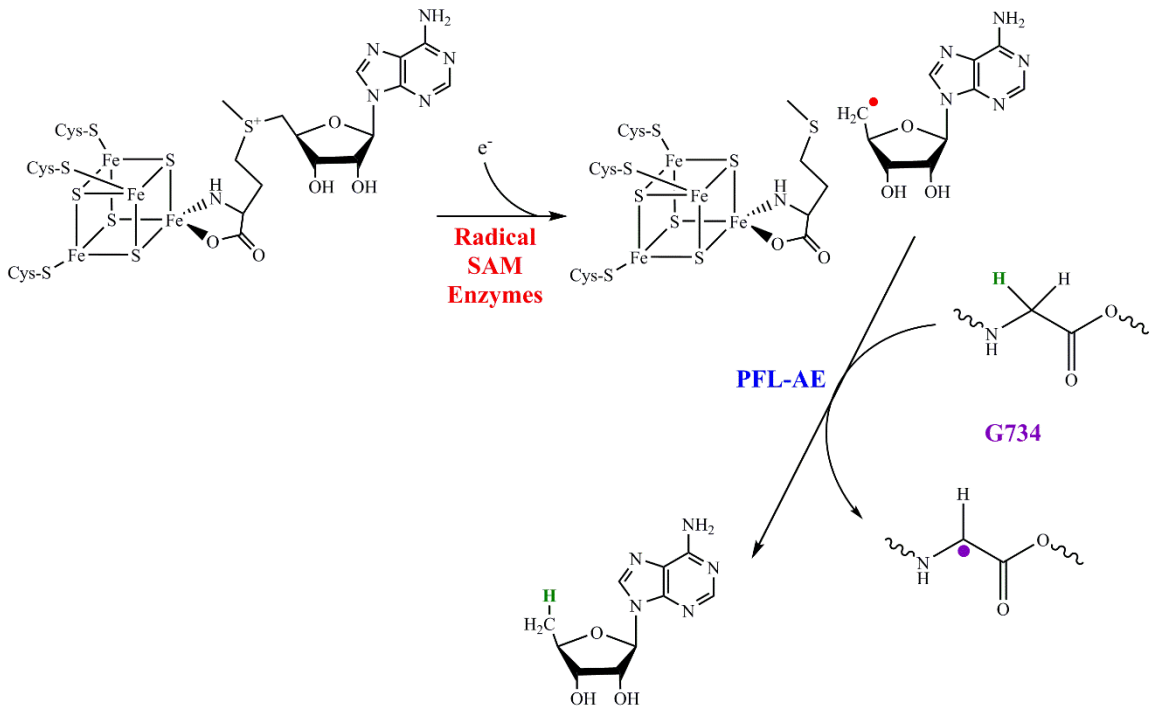


Figure 6.1. Reaction of the reductive cleavage of SAM by radical SAM enzymes and the activation of PFL by the radical SAM enzyme PFL-AE. After reduction of the cluster, SAM is cleaved to produce the 5'-dAdo• radical (red) and methionine. In PFL-AE, 5'-dAdo• abstracts a hydrogen (green) from G734 on PFL to produce a glycyl radical (purple) and 5'-dAdo, thus activating PFL.

A typical $[4Fe\text{-}4S]^{2+}$ cluster contains two valence delocalized $Fe^{2.5+}$-$Fe^{2.5+}$ pairs (Figure 6.2a) while in the reduced $[4Fe\text{-}4S]^{+}$ state, a $Fe^{2.5+}$-$Fe^{2.5+}$ pair and a Fe^{2+}-Fe^{2+} pair is present [1]. PFL-AE in whole cells was found to contain an unprecedented valence-localized $[4Fe\text{-}4S]^{2+}$ cluster containing one Fe^{2+}-Fe^{3+} pair and one $Fe^{2.5+}$-$Fe^{2.5+}$ pair (Figure 6.2b), based on Mössbauer spectroscopic studies conducted on *E. coli* cells overexpressing PFL-AE [9]. While Mössbauer spectroscopic studies of purified PFL-AE

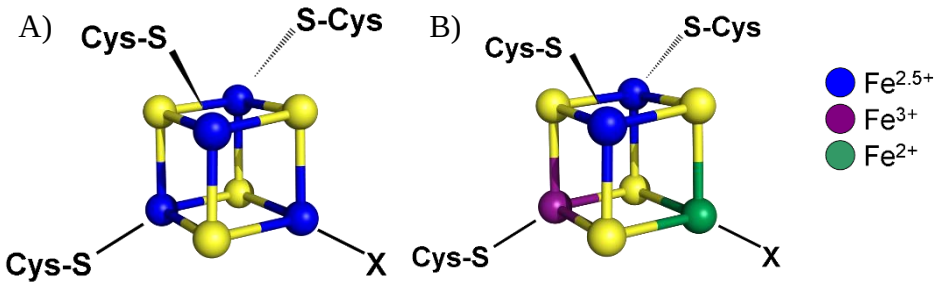


Figure 6.2. Representations of (a) a valence delocalized $[4Fe\text{-}4S]^{2+}$ cluster with two $Fe^{2.5+}$-$Fe^{2.5+}$ pairs (blue spheres) and (b) a valence localized $[4Fe\text{-}4S]^{2+}$ cluster with a $Fe^{2.5+}$-$Fe^{2.5+}$ and a Fe^{3+}-Fe^{2+} (purple and green, respectively) pair.

had previously shown it to contain a typical valence-delocalized cluster [10], partial valence localization was shown to be achieved upon the addition of 5'-deoxyadeonsine (5'-dAdo), 5'-deoxy-5'-(methylthio)adenosine (MTA), adenosine 5'-monophosphate (AMP), and adenosine 5'-diphosphate (ADP) [9]. The only previous report of a valence-localized $[4Fe\text{-}4S]^{2+}$ cluster in a protein is in the two-electron reduced form of ferredoxin:thioredoxin reductase (FTR) where a free thiol (C87) is within van der Waals contact of an Fe and a bound cysteine (C55) [11]. A strong H-bonding interaction is formed between the protonated C87 and the S atom of C55, promoting a charge buildup on the Fe to produce a valence localized Fe^{2+}-Fe^{3+} pair while still retaining a delocalized

$Fe^{2.5+}$-$Fe^{2.5+}$ pair [11]. In this case, valance localization is thought to be a means to prime the active site for one-electron reduction and cleavage of the disulfide of thioredoxin.

The work described in this paper explores the valence localized phenomenon with electron paramagnetic resonance (EPR) and electron nuclear double resonance (ENDOR) spectroscopies to investigate the reduced, paramagnetic $[4Fe\text{-}4S]^{+}$ cluster of PFL-AE in order to understand how small molecules (notably AMP, MTA, 5'-dAdo, and adenosine) interact with the cluster to induce valence localization.

Materials and Methods

Materials

All materials and chemicals were purchased from commercial sources and were of the highest purity. Isotopically labeled [ribose-$^{13}C_5$]-adenosine was purchased from Cambridge Isotope Laboratories, Inc. and [U-$^{13}C_{10}$,$^{15}N_5$]-AMP was purchased from Aldrich.

Expression of PFL-AE

The *Escherichia coli* (*E. coli*) gene *pflA* (PFL-AE) was transformed into *E. coli* BL21(DE3)pLysS (Stratagene) cells, as previously described. A 50 mL LB and 50 μg/mL ampicillin starter culture grown overnight was used to inoculate 10 L of minimal media in a bench-top fermentor (New Brunswick) containing 50 μg/mL ampicillin, a solution of glucose and vitamins. The minimal media consists of 100 g Casamino acids, 84.2 g MOPS, 8.0 g Tricine, 14.7 g NaCl, 16.0 g KOH, 5.1 g NH_4Cl in 9.8 L of water. The glucose solution was sterile filtered prior to addition to the fermentor and contained

the following: 50 g of glucose in 200 mL water; 25 mL of "O" solution (0.1 g $FeCl_2$•$4H_2O$ dissolved in 10 mL of 12 M HCl, 2.68 g $MgCl_2$•$6H_2O$, and 1 mL "T" solution [18.4 mg $CaCl_2$•$2H_2O$, 64 mg H_3BO_3, 40 mg $MnCl_2$•$4H_2O$, 18 mg $CoCl_2$•$6H_2O$, 4 mg $CuCl_2$•$2H_2O$, 340 mg $ZnCl_2$, and 605 mg Na_2MoO_4•$2H_2O$ diluted to 100 mL with H_2O] and the "O" was brought up to a final volume of 50 mL with H_2O; 25mL of 1 M KH_2PO_4; 12.5 mL of 276 mM K_2SO_4; and 62.5mL of 0.1 M $CaCl_2$. Additionally, 10 mg of the vitamins biotin, pantothenic acid, vitamin B_{12}, thiamine, folic acid, riboflavin, niacinamide, thioctic acid, and pyridoxine were added to the fermentor. The growth was incubated at 37°C with agitation and a flow of 5 L/min of compressed air. Once the cells reached an OD_{600} of ~0.5, isopropyl-β-D-thiogalactopyranoside (IPTG) was added to a final concentration of 0.5 mM and 0.75 g of $Fe(NH_4)_2(SO_4)_2$•$6H_2O$ was added. After ~2 hours, the cells were cooled and put under anaerobic conditions by purging the cells with N_2 once the culture was ~ 30°C followed by another addition of 0.75 g of $Fe(NH_4)_2(SO_4)_2$•$6H_2O$ once the culture was ~20°C. The culture was purged with N_2 overnight in a 4°C fridge. The cells were harvested and stored in a -80°C freezer until purification.

PFL-AE Purification

PFL-AE was purified in an anaerobic Coy chamber. The cell pellets were lysed in a 50 mM Tris, pH 7.5, buffer containing 200 mM NaCl, 5% w/v glycerol, 1% w/v Triton X-100, and 10 mM $MgCl_2$. To 100 mL of this buffer, 18 mg of PMSF, 78 mg of DTT, 16 mg of lysozyme, and trace amounts of DNase and RNase were added. Approximately 2 mL of this lysis buffer per 1 g of cell pellet was added to the cells and

allowed to lyse, with stirring, for ~1 hour upon which the lysate was centrifuged at 18,000 rpm for 30 minutes. The supernatant was decanted and applied to a Superdex-75 resin. The gel filtration buffer, 50 mM Tris, pH 7.5 with 200 mM NaCl and 1 mM DTT was run over the column and the dark brown fractions were pooled and concentrated using a 10K MWCO Millipore Amicon Ultra centrifugal concentrator. The protein was run over the column a second time and the fractions with the highest 426/280 nm ratio were pooled and concentrated. Cutoff ratios depended on the purification but a typical 426/280 nm ratio for the best protein was >0.160. The Bradford method was used and a correction factor determined by acid hydrolysis [12] was applied to determine the PFL-AE concentration. The iron number was determined by the method of Beinert [13]. The average iron content for purified PFL-AE was between 3.5 and 3.8 Fe/protein.

PFL-AE Variants

Generation of PFL-AE variants was carried out using the QuikChange site-directed mutagenesis kit from Stratagene and plasmids containing the mutant genes were transformed into BL21(DE3)pLysS cells. The mutagenesis primers (IDT) were specifically designed for the H37A site (GCT GCC TGT ATT GT**G C**TA ACC GCG ACA), the H202A site (GCT TCT CCC CTA C**GC** CGA GCT GGG CA), the Y201A site (CGA GCT TCT CCC C**GC** CCA CGA GCT G), the R166A site (ATG TGA AGG TGT GGA TC**G C**CT ACG TTG TTG TCC CAG), and the D104A site (CAT TCA TAC CTG TCT GG**C** CAC CAA CGG TTT TGT TC). The expression and purification procedure was identical to that described above for WT PFL-AE, and the resulting

purified proteins had Fe content of 2.8 for H37A, 1.3 for H202A, 3.0 for Y201A, 3.9 for R166A, and 4.2 Fe/protein for D104A.

Synthesis of [Ribose-$^{13}C_5$]-AMP

The synthesis of [ribose-$^{13}C_5$]-AMP from [ribose-$^{13}C_5$]-adenosine was performed in a 25 mM Pipes, pH 7.0 buffer with 1.25 mM $MgCl_2$•$6H_2O$, and 0.01% w/v BSA. Labeled adenosine was added to a final concentration 3 mM. Purified adenosine kinase (1.5 mL) was added. A stock solution of 100 mM ATP was added slowly (over 3 hours) to a final concentration of 3 mM. The pH of the solution was monitored and adjusted after each addition of reactant. The reaction was stirred overnight at ambient temperature. The reaction was spun down to remove particulates and purified on a DEAE sephacel column with a linear gradient from Buffer A (H_2O) to 100% Buffer B (0.5 M NH_4HCO_3 pH 8.0). Fractions containing AMP (checked by HPLC) were roto-vapped to solid.

Preparation of EPR Samples

EPR samples were prepared in an anaerobic Unilab MBraun box with $\leq$1 ppm O_2. All solutions were degassed on a Schlenk line and brought into the MBraun box prior to sample preparation. For EPR samples, PFL-AE (WT or variant) was photoreduced in a 150 mM Tris, pH 7.6 buffer with 100 µM 5-deazariboflavin, 200 mM KCl (or NaCl), and 5 mM DTT. The solution was illuminated using a 300 W halogen lamp in an ice bath for ~1 hour in a shortened NMR tube. After photoreduction, PFL-AE was aliquoted into Eppendorf tubes. Small molecules (5'-dAdo, AMP, ADP, ATP, MTA, NAD^+, NADH,

CoA, ribose, adenine, adenosine, oxamate, or buffer for a negative control) were added to the Eppendorf tube at a final concentration of 2 mM for each small molecule and a 200 μM final concentration of PFL-AE for a total volume of 250 μL. Stock solutions of the small molecules were prepared in a Tris, pH 7.5 buffer. Due to the low solubility of MTA in aqueous solvents, MTA was dissolved in DMSO prior to addition to PFL-AE. PFL-AE in the presence of each the small molecule (250 μL) was loaded into separate X-band EPR tubes. Capped EPR tubes were taken out of the MBraun chamber and flash frozen in liquid N_2.

Preparation of ENDOR Samples

ENDOR samples were prepared in a similar fashion to EPR samples in an anaerobic Unilab MBraun box with $\leq$1 ppm O_2 and all solutions were degassed on a Schlenk line prior to sample preparation. PFL-AE was photoreduced in a 150 mM Tris, pH 7.5 buffer with 200 μM 5-deazariboflavin, 200 mM KCl, and 1 mM DTT in a shortened NRM tube. After ~1 hour photoreduction, PFL-AE was aliquoted into Eppendorf tubes and mixed with unlabeled AMP, [U-$^{13}C_{10}$,$^{15}N_5$]-AMP, adenosine, [ribose-$^{13}C_5$]-adenosine, or [ribose-$^{13}C_5$]-AMP to a final concentration of 5 mM for the small molecules and 500 μM or 250 μM PFL-AE at a total volume of 100 μL. Samples were then loaded into Q-band tubes by a Pasteur pipette, capped, and frozen in liquid N_2 upon removal from the MBraun chamber.

For ENDOR samples prepared in D_2O, PFL-AE was buffer exchanged into a Tris-D_2O, pD 7.5 buffer containing 200 mM KCl using a 10K MWCO Millipore Micron Ultracel centrifugal filter. The Tris-D_2O buffer was prepared in H_2O with 200 mM KCl

and the pH was adjusted to 7.5. The buffer was then lyophilized on a Schlenk line, brought into the MBraun chamber where the appropriate amount of D_2O was added. The D_2O buffer was then added to PFL-AE with about a 5 fold excess of buffer, concentrated by centrifugation in a centrifugal filter. This process was repeated about 8 times. Small molecules were brought into the MBraun and dissolved in Tris-D_2O buffer prior to addition to reduced PFL-AE. [U-$^{13}C_{10}$,$^{15}N_5$]-AMP was first lyophilized on a Schlenk line and then dissolved in the Tris-D_2O buffer. Photoreduction and sample preparation was identical to that described in the previous paragraph.

EPR and ENDOR Spectroscopy

EPR spectra were recorded on a Bruker EMX X-band spectrometer equipped with a liquid helium cryostat and temperature controller from Oxford Instruments. Typical experimental parameters were T = 12 K, 9.37 GHz with 1.0 mW microwave power, 100 kHz modulation frequency, 10 G modulation amplitude, and an average of four scans. Q-band pulsed EPR/ENDOR spectra were collected on a spectrometer described earlier [14] equipped with a helium immersion dewar for measurements at 2 K. ENDOR measurements employed the Mims pulse sequence (π/2-τ-π/2-T-π/2-τ-echo, RF applied during interval T) for small hyperfine couplings or the Davies pulse sequence (π-T -π/2-τ-π-τ-echo) for large hyperfine couplings [15]. For nuclei (N) of spin I = ½ (^{13}C, ^{1}H) interacting with a S = 1/2 paramagnetic center, the first-order ENDOR spectrum for a single molecular orientation is a doublet with frequencies (ν_+/ν_-):

$$\nu_{\pm} = |\nu_N \pm \frac{A}{2}| \quad (1)$$

where ν_N is the Larmor frequency and *A* is the orientation-dependent hyperfine constant. For a nucleus with hyperfine coupling, *A*, Mims pulsed ENDOR has a response *R* that depends on the product, $A\tau$, according to the equation:

$$R \approx [1 - cos\theta(2\pi A\tau)] \quad (2)$$

This function has zeros, corresponding to minima in the ENDOR response (hyperfine "suppression holes"), at $A\tau = n$; n = 0, 1, …, and a maxima at $A\tau = (2n + 1)/2$; n = 0, 1, … [15]. The "holes" at $A = n/\tau$, n = 1, 2, 3, … can be adjusted by varying τ. However, the "central", n = 0 hole at $\nu = \nu_N$ persists regardless. This can be of significance in distinguishing a tensor that is dominated by anisotropic interactions from one that is dominated by isotropic ones. The latter would never lead to ENDOR intensity near ν_N; the former does so for certain orientations, but the ν = 0 Mims hole tends to diminish the differences between the two cases.

Docking Studies

Docking of AMP into the active site of PFL-AE (PDB ID 3CB8) was performed with the AutoDock Vina program [16]. Placement of polar hydrogens on AMP was performed using Avogadro. Input files containing a flexible AMP ligand and a rigid PFL-AE receptor were prepared using AutoDockTools 1.5.6. Polar hydrogens were added to the protein and Gasteiger chargers were calculated with AutoDockTools. A receptor grid large enough to encompass the cluster and any possible AMP binding sites within the active site was used with the grid point dimensions of 22 x 20 x 20 Å with a grid-point spacing of 1 Å. The binding modes of AMP were analyzed with PyMOL [17]. The process for docking of AMP into NosL crystallized with tryptophan and *S*-adenosyl-

L-homocysteine (PDB ID 4R33) was identical to PFL-AE except a receptor grid with the dimensions of 24 x 24 x 24 Å was used.

Results

EPR Spectroscopy of WT PFL-AE

After the detection of a valence localized cluster in PFL-AE *in vivo* and *in vitro* using Mössbauer spectroscopy, we wanted to further investigate how these small molecules are interacting with the cluster using magnetic resonance techniques. Although the Mössbauer experiments were conducted on the oxidized, $[4Fe\text{-}4S]^{2+}$ state in the report by Yang *et al.* [9], EPR spectroscopy must be conducted in the paramagnetic $[4Fe\text{-}4S]^{+}$ state. EPR samples were prepared with reduced PFL-AE in the presence of a variety of adenosyl-moiety containing molecules including SAM degradation products (MTA, 5'-dAdo, adenine, ribose), substrates and substrate analogs of PFL (CoA and oxamate), and cellular metabolites (ATP, ADP, AMP, NAD^{+} and NADH).

The EPR spectrum of the $[4Fe\text{-}4S]^{+}$ in PFL-AE was perturbed in the presence of AMP, MTA, 5'-dAdo, and adenine (Figure 6.3), consistent with the Yang *et al.* [9] results which showed that AMP, MTA, and 5'-dAdo induce valence localization in purified PFL-AE. With the addition of MTA and 5'-dAdo, the most significant changes in the EPR spectra were observed. The signal exhibited a shift to lower g values in both $g_{\|}$ and $g_{\perp}$ with a change to a more rhombic signal and an intensification of the signal. These changes do not correspond to changes in the EPR spectrum in the presence of SAM; however, since the EPR spectrum is perturbed in the presence of small molecules,

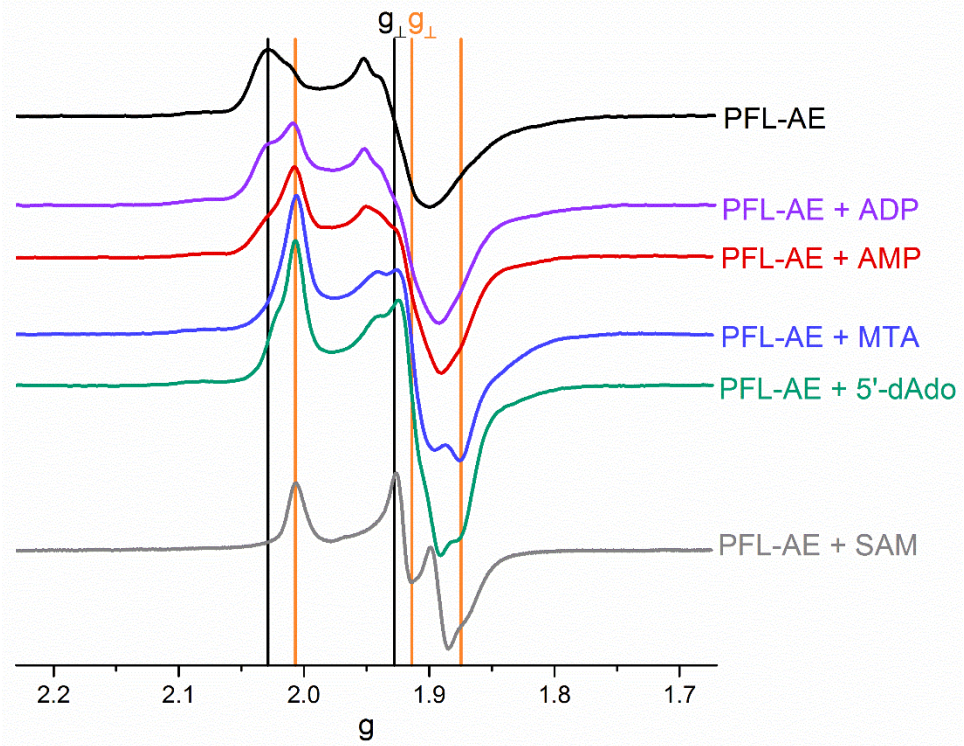


Figure 6.3. EPR spectra of PFL-AE in the presence of ADP (purple), AMP (red), MTA (blue), 5'-dAdo (green), SAM (gray), or in the absence of small molecule (black). Vertical black lines correspond to $g_{\parallel}$ and $g_{\perp}$ of PFL-AE alone (conformation A) and vertical orange lines correspond to conformation B with the shifts in g values in the presence of the small molecules that induce valence localization.

it is possible that these small molecules are directly interacting with the cluster. The EPR spectra of PFL-AE in the absence or presence of small molecules or SAM can be described as arising from three difference conformations: PFL-AE alone (conformation "A"); PFL-AE with bound small molecules giving rise to a more rhombic signal (conformation "B"); and PFL-AE with bound SAM (conformation "C"). The EPR spectrum of conformations B and C have different shifts in their g values compared to PFL-AE without any molecule (conformation A). Consistent with Mössbauer results where the extent of valence localization in purified PFL-AE was dependent on the small molecule and did not constitute 100% of purified protein, the EPR spectra in the presence

of small molecules contains a mixture of the A and B conformations. With the addition of MTA and 5'-dAdo, the EPR spectrum has the least amount of the A conformation while in the presence of AMP, the EPR spectrum retained more of the A conformation.

PFL-AE contains a cation binding site in its active site and the enzyme activity and EPR spectral properties are both dependent on the identity of this cation (manuscript in preparation). The most significant changes in the EPR spectral properties are seen in the presence of KCl and NaCl, where the EPR signal is nearly axial in the absence of SAM. In the presence of SAM, the KCl signal becomes more rhombic while the NaCl signal is still nearly axial but with a shift in the g values (manuscript in preparation). In the presence of either MTA or 5'-dAdo, the EPR spectrum of PFL-AE was almost identical regardless of whether NaCl or KCl was present in the buffer, suggesting that cation binding is not important in these small molecule complexes or that cation identity does not have appreciable effect on small molecule binding conformation (SI Figure 6.1).

Consistent with the Mössbauer results [9], the EPR spectra for PFL-AE were not significantly perturbed in the presence of ATP, CoA, oxamate, ribose, NAD^+, nor NADH (Figure 6.4), suggesting these molecules do not interact with the cluster. They are possibly too large to enter the active site or they lack the adenosyl-moiety which is thought to hold these small molecules in the active site.

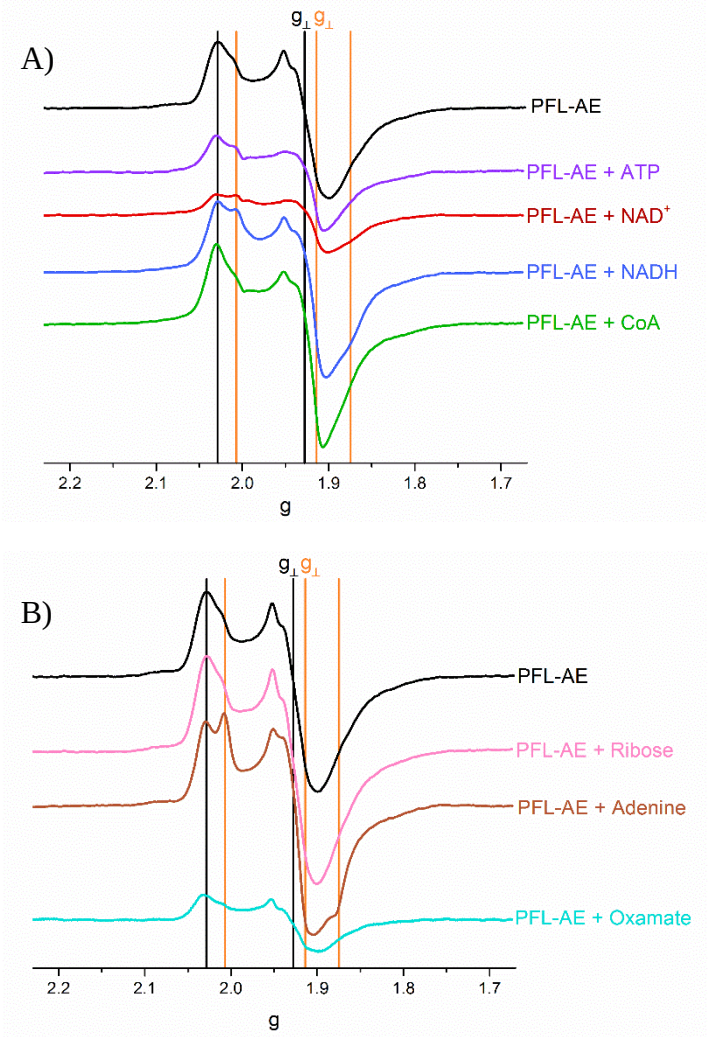


Figure 6.4. (A) EPR spectra of PFL-AE in the absence of small molecules (black) or presence of ATP (purple), NAD^+ (red), NADH (blue), or CoA (green). The EPR spectrum in the presence of these small molecules are identical to conformation A, or PFL-AE in the absence of small molecules. (B) EPR spectra of PFL-AE in the presence of ribose (pink), adenine (brown), or oxamate (cyan). Vertical black lines correspond to the g values for conformation A and vertical orange lines correspond to changes to conformation B in the presence of small molecules that bind and effect the EPR spectrum of PFL-AE, as observed in Figure 6.3.

EPR Spectroscopy of Variant PFL-AE

Analysis of the crystal structure of PFL-AE revealed possible binding sites of these small molecules. Since all the molecules in which valence localization has been

observed contain an adenosyl-moiety, these small molecules may interact with PFL-AE in the same fashion as SAM. Of particular interest are the side chains of H37 and H202 (Figure 6.5) which are oriented parallel to the purine ring of SAM with a distance of about 3.0-3.5 Å.

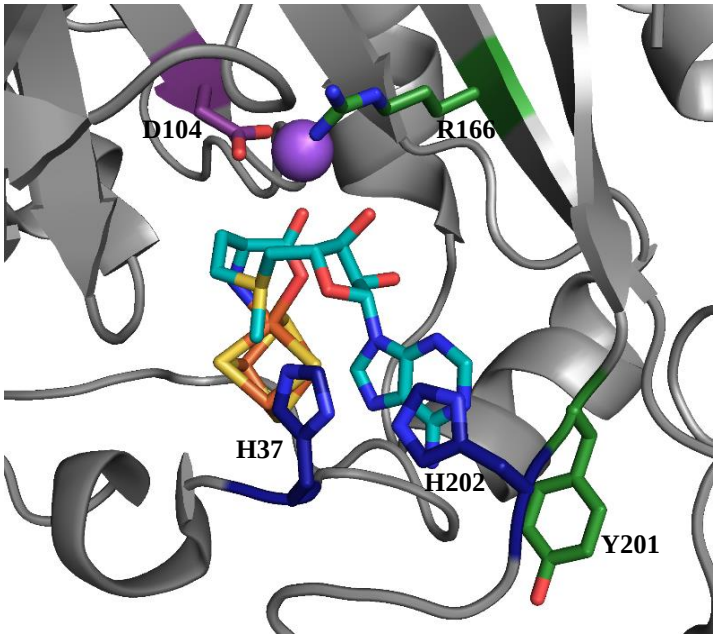


Figure 6.5. The PFL-AE active site with amino acids involved in SAM (teal carbons) binding. H37 and H202 (blue carbons) were of special interest for small molecule coordination due to their proximity to the adenine portion of SAM. D104 (purple carbons), was previously found to be involved in cation binding (purple sphere). R166 and Y201 (green carbons), are also thought to help coordinate SAM in the active site.

To probe a possible small molecule binding site, both histidines were changed to alanine separately (H37A and H202A). First, activity assays were conducted to determine if these mutations were detrimental to activity. Both H37A and H202A had similar activities that were higher in activity than WT after accounting for Fe number (SI Table 6.1). Next, to probe whether small molecules were able to bind in the active site, EPR spectroscopy was conducted on the two variants in the presence of both NaCl and

KCl. In the absence of small molecules, each variant have similar EPR signals as WT (SI Figure 6.2) and have a slightly different spectrum in the presence of NaCl or KCl, consistent with WT PFL-AE (manuscript in preparation). Presumably, if either histidine is essential for small molecule binding, no EPR shift to conformation B will be observed. These variants differed in the extent of shifting to conformation B with the addition of small molecules which will be discussed below.

The PFL-AE H37A Variant. EPR spectroscopy of the H37A variant showed only a slight shift in the $g_{\perp}$ value to conformation B in samples prepared in NaCl and in the presence of AMP, MTA, and 5'-dAdo (Figure 6.6) compared to PFL-AE H37A in the absence of small molecule. On the other hand, in the presence of KCl, 5'-dAdo and MTA samples had a shift in both $g_{\parallel}$ and $g_{\perp}$ to conformation B and the 5'-dAdo sample has some splitting in $g_{\parallel}$ (Figure 6.6) compared to PFL-AE H37A in the absence of small molecule. The less drastic shift to conformation B with small molecule bound compared to WT could be attributed to the requirement for interaction between H37 and small molecule. How H37 interacts with the small molecule still needs to be determined.

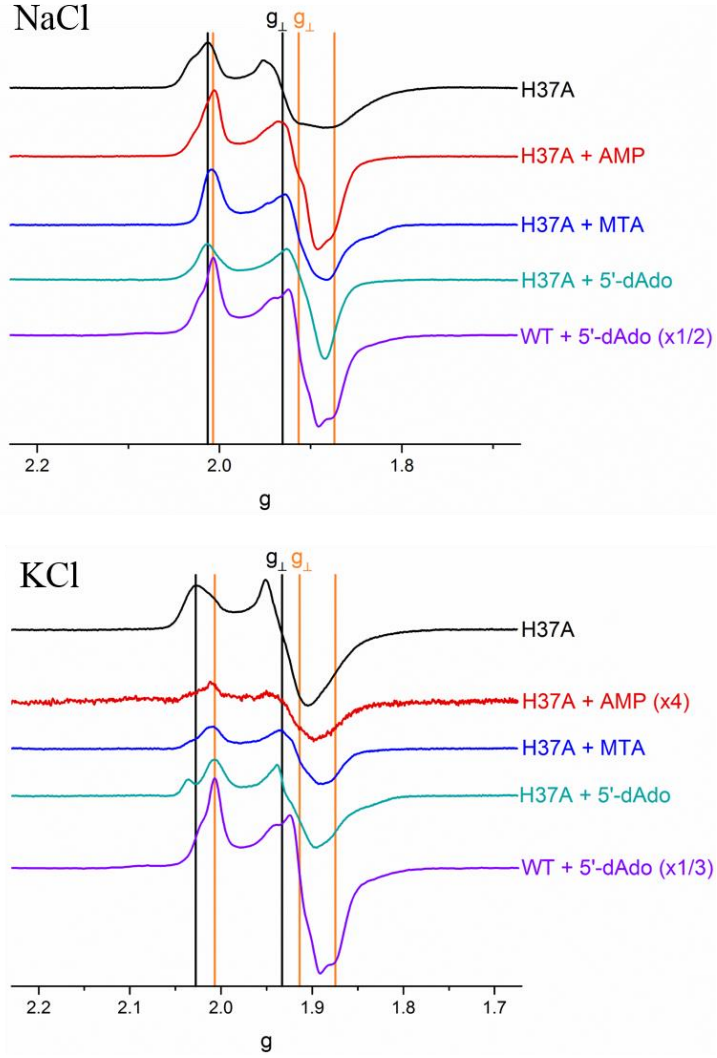


Figure 6.6. EPR spectra of the H37A PFL-AE variant (black) in the presence of AMP (red), MTA (blue), or 5'-dAdo (green) prepared with NaCl (top) or KCl (bottom) compared to WT in the presence of 5'-dAdo (purple). Vertical black lines correspond to g values of conformation A of H37A in the absence of small molecules and vertical orange lines correspond to conformation B of WT in the presence of 5'-dAdo. The variant has a slightly different signal in the presence of KCl and NaCl, which is also observed in WT. This causes the vertical black lines to differ in each case.

The PFL-AE H202A Variant. EPR spectroscopy of the H202A variant in the presence of AMP showed very little difference in the presence of both NaCl and KCl compared to PFL-AE H202A in the absence of small molecule, which is similar to WT

(Figure 6.7). In the presence of NaCl, addition of either MTA or 5'-dAdo results in spectral changes to conformation B with the addition of 5'-dAdo having slightly more conformation A than MTA (Figure 6.7). In the presence KCl, addition of MTA showed

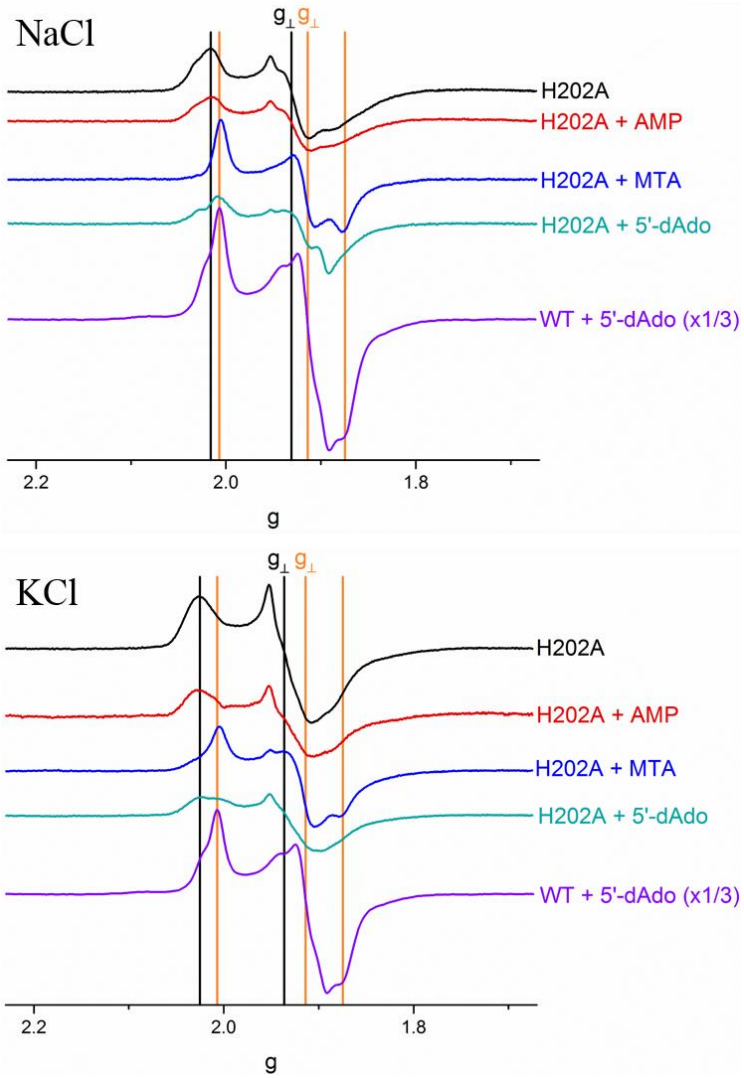


Figure 6.7. EPR spectra of the H202A PFL-AE variant (black) in the presence of AMP (red), MTA (blue), or 5'-dAdo (green) prepared with NaCl (top) or KCl (bottom) compared to WT in the presence of 5'-dAdo (purple). Vertical black lines correspond to g values of conformation A of H202A and vertical orange lines correspond to conformation B of WT in the presence of 5'-dAdo. Similar to H37A, the H202A variant has a slightly different signal in the presence of KCl and NaCl, which is also observed in WT. This causes the vertical black line to differ in each case.

spectral changes while in the presence of 5'-dAdo, the EPR spectrum only exhibits slight changes compared to H202A in the absence of small molecule. This EPR data suggests that H202 is not required for small molecule interactions.

Additional PFL-AE Variants. Other amino acid residues, chosen for their proposed interactions with SAM and thus possible interactions with small molecules which cause valence localization, were changed to alanine and small molecule interactions were analyzed via EPR spectroscopy (SI Figure 6.3). These variants included D104A, Y201A, and R166A and had varying activities (SI Table 6.1). Neither the D104 nor the R166 residues directly interact with SAM but are completely conserved and are in close proximity to the 5'-C of SAM. D104 was discovered to be involved with cation binding (manuscript in preparation) and without this residue, the cation cannot bind as efficiently. The aromatic side chain in Y201 sits parallel to SAM but shifted to a distance of about 4.1 Å away from the adenine ring. All these variants show EPR spectral changes in the presence of small molecules with AMP having the least amount of g shift (SI Figure 6.3), consistent with WT. Since all these variants still contain spectral changes to conformation B in the presence of small molecules, it is concluded that these amino acids are not required for small molecule binding.

ENDOR Spectroscopy of Isotopically Labeled Small Molecules

In order to investigate how these small molecules interact with the cluster, ENDOR spectroscopy was employed to probe interactions between the paramagnetic $[4Fe\text{-}4S]^{+}$ cluster and isotopically labeled [U-$^{13}C_{10}$,$^{15}N_5$]-AMP, [ribose-$^{13}C_5$]-Ado, and

[ribose-$^{13}C_5$]-AMP (Figure 6.8). Labeled AMP was chosen because, *in vivo,* it was proposed to be interacting with the cluster [9]. Mössbauer experiments showed that 5'-dAdo had the greatest effect on valence localization [9] and EPR analysis reported here revealed significant spectral changes in the presence of 5'-dAdo. Thus, labeled adenosine (Ado) was also chosen for ENDOR experiments. Due to the limited availability of isotopically labeled molecules, Ado not 5'-dAdo was purchased.

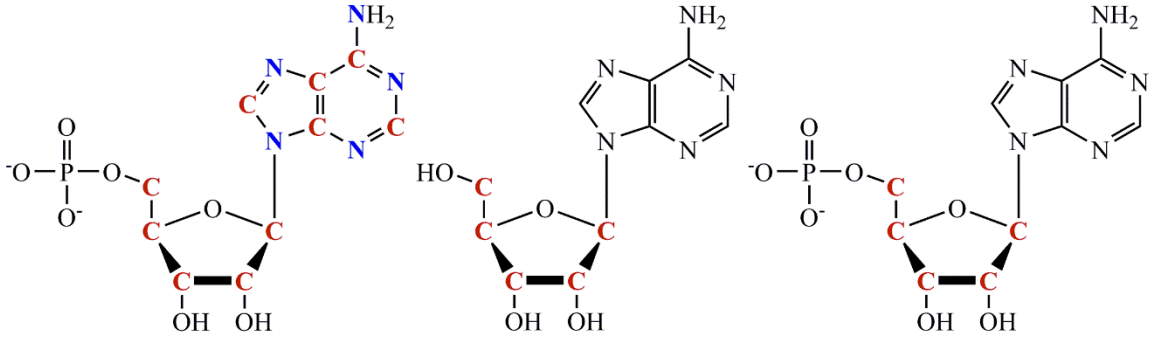


Figure 6.8. Isotopically labeled molecules used in this study including [U-$^{13}C_{10}$,$^{15}N_5$]-AMP (left), [ribose-$^{13}C_5$]-Ado (center), and [ribose-$^{13}C_5$]-AMP (right) with the ^{13}C colored red and ^{15}N colored blue.

^{31}P ENDOR. Since EPR spectral changes are observed in the presence of small molecules, it was proposed that these small molecules are directly coordinating to the unique Fe to cause a charge build-up on the cluster. One plausible site of coordination for AMP is through the phosphate group. Pulsed and continuous wave (CW) techniques were performed on samples containing AMP to observe any ^{31}P coupling with the cluster; however, no ^{31}P signal was observed (SI Figure 6.4), suggesting that the phosphate group is not directly interacting with the cluster.

^{13}C and ^{15}N ENDOR. Mims ^{13}C ENDOR, a pulsed ENDOR technique optimized for observation of weaker coupled centers, was used to analyze coupling between [U-$^{13}C_{10}$,$^{15}N_5$]-AMP, [ribose-$^{13}C_5$]-Ado, and [ribose-$^{13}C_5$]-AMP and the paramagnetic cluster. The spectrum of [U-$^{13}C_{10}$,$^{15}N_5$]-AMP bound to reduced [4Fe-4S]$^{+}$-PFL-AE reveals two doublets: one with A(^{13}C) = 0.72 MHz and one with A(^{13}C) = 0.15 MHz (Figure 6.9) coupling. The weaker coupled feature was also observed in the sample prepared with [ribose-$^{13}C_5$]-Ado (Figure 6.9), suggesting that the adenine portion of AMP is closer to the [4Fe-4S] cluster of PFL-AE and giving rise to the stronger-coupled signal. A very small feature with A(^{13}C) = 0.72 MHz coupling appears in the [ribose-$^{13}C_5$]-Ado sample which we attribute to naturally abundant ^{13}C. Simulations of the spectrum reveal a ^{13}C distance to the [4Fe-4S] cluster of approximately 3.5 Å for the stronger coupled carbon in the adenine while a distance of approximately 5.0 Å was calculated for a weakly coupled carbon in the ribose ring. Surprisingly, however, no ^{15}N ENDOR signal was observed for the sample made with [U-$^{13}C_{10}$,$^{15}N_5$]-AMP, despite the strongly-coupled carbon in the adenine portion of AMP suggesting coordination through a base nitrogen (SI Figure 6.4).

In order to investigate whether the differences observed in Figure 6.9 were not due to the absence of the phosphate moiety in Ado (although no ^{31}P coupling was observed in AMP), [ribose-$^{13}C_5$]-AMP was synthesized from [ribose-$^{13}C_5$]-Ado. The EPR signal and the subsequent ENDOR signal were very weak but in the presence of [ribose-$^{13}C_5$]-AMP, the signal displayed only one doublet with weak coupling at A(^{13}C) ~ 0.2 MHz (Figure 6.9) similar to the [ribose-$^{13}C_5$]-Ado containing samples; the conclusion

from these results is that AMP and adenosine are oriented similarly relative to the cluster, with the stronger coupled carbon arising from the adenine and the weaker coupled carbon on the ribose.

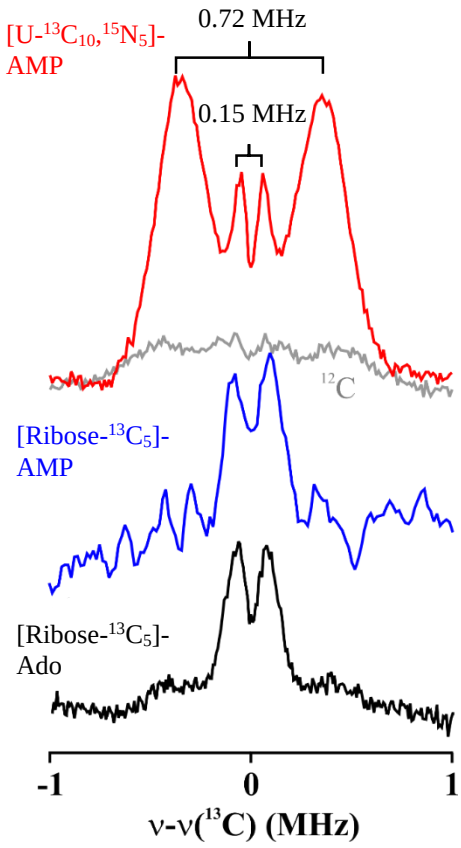


Figure 6.9. Mims ^{13}C ENDOR spectra of PFL-AE in the presence of [U-$^{13}C_{10}$,$^{15}N_5$]-AMP (red), and [ribose-$^{13}C_5$]-AMP (blue), [ribose-$^{13}C_5$]-Ado (black), and unlabeled AMP (grey). Only the $A(^{13}C)$ = 0.15 MHz coupling is observed in the [ribose-$^{13}C_5$]-Ado and [ribose-$^{13}C_5$]-AMP samples. Parameters include 34.628 GHz with 8.0 dB, rf = 14 dB, tau = 500 ns and rep = 200 ms.

^{1}H ENDOR. To analyze the paramagnetic site further, samples of reduced PFL-AE in the presence and absence of [U-$^{13}C_{10}$,$^{15}N_5$]-AMP and [ribose-$^{13}C_5$]-Ado were prepared in ^1H_2O and ^2H_2O. The ^{1}H ENDOR spectrum at g = 1.88 revealed coupling of

$A(^1H)$ = ~6 MHz, which matches with the breadth of ^2H Mims ENDOR signal from ^2H_2O samples (Figure 6.10). This ^1H coupling is similar to that observed for the ^1H ENDOR from H_2O bound to the unique iron of aconitase ($A(^1H)$ = 6-10 MHz) in the absence and presence of substrate [18]. These results suggest that the unique iron of PFL-AE is directly coordinated by H_xO both in the absence and presence of AMP or Ado.

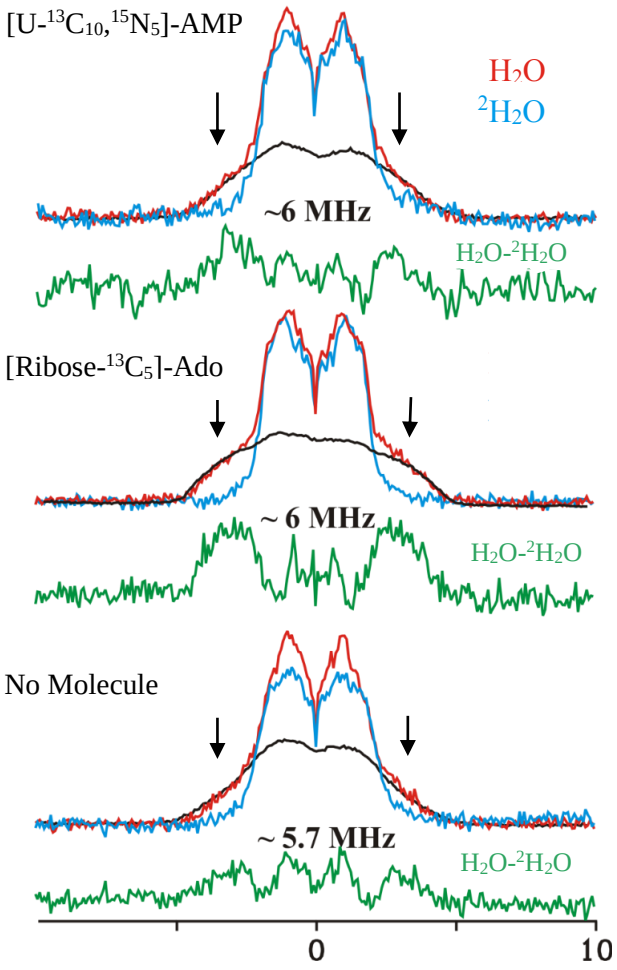


Figure 6.10. ^1H soft Davies ENDOR spectra at g = 1.88 of PFL-AE in H_2O (red) or ^2H_2O (blue) with the H_2O and ^2H_2O difference (green) in the presence of [U-$^{13}C_{10}$,$^{15}N_5$]-AMP (top), [ribose-$^{13}C_5$]-Ado (center), and absence of small molecule (bottom). The ^2H Mims ENDOR is also shown (black). The feature (black arrows) disappears in when samples were prepared in ^2H_2O.

Docking AMP into the Active Site of PFL-AE

The ENDOR results suggest that AMP may not be oriented in the active site in a manner similar to SAM, because the SAM-type binding mode would place the ribose ring closer to the cluster than the adenine. Docking was performed to find an orientation of AMP that is consistent with the ENDOR results, with ~3.5 Å for a C in the adenine ring and ~5 Å for a C in the ribose ring. Three different structures that agree at least partially with the ENDOR results were obtained and discussed in detail below.

A SAM-Like Binding Model. The first AMP docking, termed a SAM-like model, utilizes the inherent adenine binding pocket involving π-stacking with H37 and H202 which are involved in SAM coordination. Due to the flexibility of the phosphate group, three different possibilities were observed (Figure 6.11). Each had minimal movement for the adenosine position but placement of the phosphate group varied from a solvent exposed position (1), to alignment with the sulfonium of SAM (2), to placement between the unique Fe where the oxygens could interact with cation (3) (Figure 6.11). These three binding affinities were very close: -9.2, -9.1, and -8.9 kcal/mol for 1, 2, and 3, respectively. Models 2 and 3 do place the phosphate about 3.2 and 3.5 Å from the unique Fe which would be detectable by ENDOR spectroscopy, while model 1 places the phosphate at a distance of about 6.6 Å. Only model 1 permits an H_xO species to bind the unique Fe of the cluster. In all 3 models, only one carbon of the adenine ring is within coupling distance of the cluster: about 3.8 Å from the closest sulfur of the cluster. Each of the five carbons in the ribose ring have varying distances (SI Table 6.2). For each case, the 2'-C carbon is the closest to the S of the cluster at a distance between 3.8 and

4.1 Å, with the exception of model 3 in which the 5'-C is 3.5 Å of the cluster. Each mode places the nitrogens of the adenine ring over 4.5 Å from the cluster, consistent with the lack of ENDOR nitrogen coupling; however, none of these three models satisfies the estimated ENDOR carbon distances.

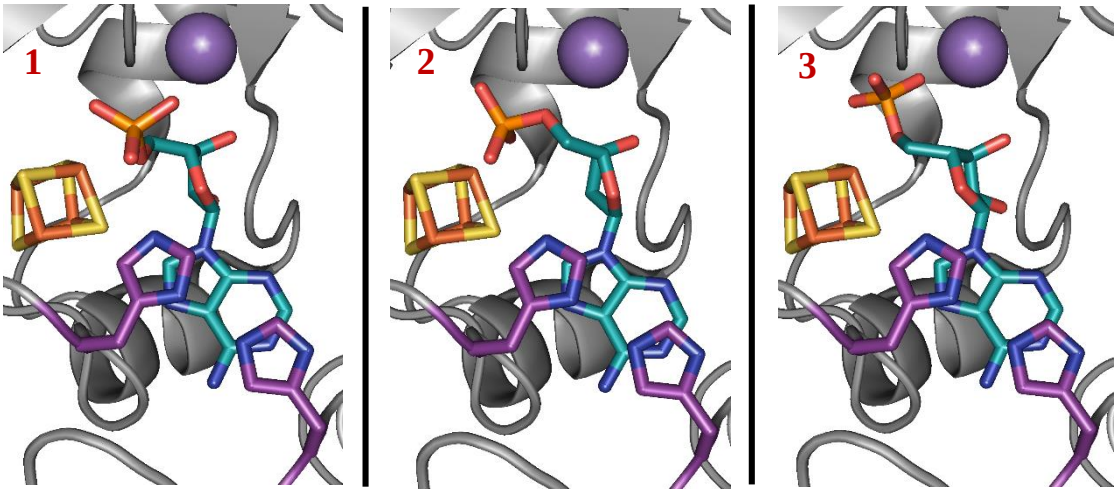


Figure 6.11. SAM-like docking of AMP (teal carbons) into the active site of PFL-AE with different phosphate positions. In (1), the phosphate is more substrate exposed while (2) positions phosphate near the sulfonium of SAM (SAM not shown) and (3) places the phosphate between the unique Fe and the monovalent cation. The two histidines (H37 and H202, purple carbons) that interact with the adenine ring of SAM are also shown. These histidines are in position to interact with the adenine portion of AMP.

A π-Cation Binding Model. The localization event *in vivo* is very unusual and one might expect an unusual binding of these small molecules in the active site to induce valence localization. A second model revealed a very unusual π-cation binding mode that places the adenine ring between the unique Fe and the cation, and gives distances of 3.6 Å and 4.6 Å from the cluster to the closest carbon of the adenine ring and the ribose, respectively (Figure 6.12). The binding affinity for this first docking mode was -8.1 kcal/mol, which is slightly less favorable compared to the -9.2 kcal/mol in the SAM-like

model. Three of the adenine carbons are 3.6 Å away from the unique Fe while two are 3.4 Å, in agreement with ENDOR results. The 1'-C of the ribose ring is 4.9 Å from the unique Fe, in agreement with ENDOR analysis. The phosphate group is located on the surface of the binding pocket and is within hydrogen bonding distances of the residues N38 and H37. Two significant problems arise with this docking mode, however. First, this binding mode gives a close proximity of the adenine ring nitrogens to the cluster, and therefore we would expect to see ^{15}N coupling from the uniformly-labeled AMP; however, no ^{15}N coupling is observed. Second, this docking mode leaves insufficient room for coordination of solvent to the unique iron of the cluster, and is therefore inconsistent with the ^{1}H ENDOR results presented in Figure 6.10.

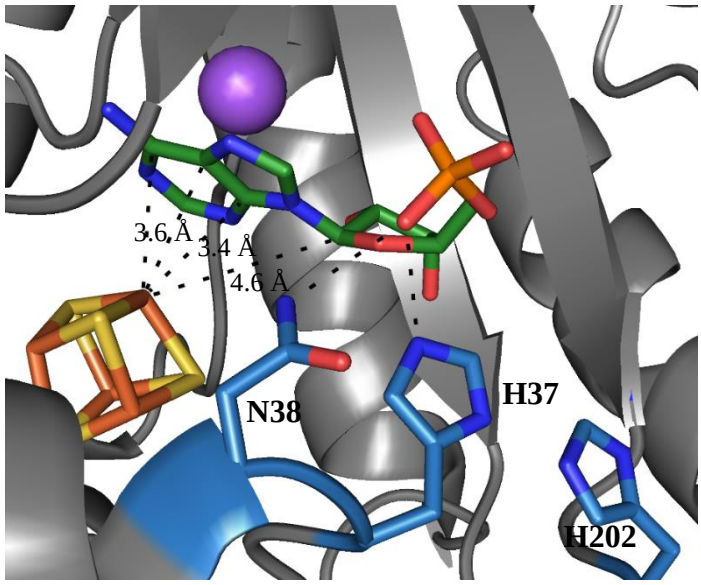


Figure 6.12. The π-cation docking model with AMP (green carbons) sandwiched between the cluster and the monovalent cation (purple sphere). The adenine ring is within 3.4 Å and 3.6 Å of the unique Fe while the closest carbon of the ribose ring is at a distance of 4.6 Å of the unique iron. The phosphate group is oriented next to N38 and H37 (light blue carbons).

A Rotated SAM-Like Model. A third AMP docking model was also obtained when an OH species was simulated onto the unique Fe site prior to docking studies (Figure 6.13). The docking model revealed a rotated SAM-like docking mode where the adenine ring of AMP is in a similar position as SAM but it has rotated, placing the purine ring of AMP in the place of the imidazole ring of SAM (Figure 6.13b). The binding affinity for this model is slightly less favorable than the two previous models with a calculated value of -7.9 kcal mol^{-1}. However, this docking model agrees with the ENDOR results and allows space for an H_xO bound to the unique Fe.

Compared to the SAM-like model, this rotated SAM-like model places the ribose ring further away from the cluster. Unlike the π-cation mode, a larger N-cluster distance was obtained. In this model, one carbon from the adenine ring is located 3.5 Å from a cluster S while the 2'-C of the ribose ring is 5.0 Å away from the cluster S (Figure 6.13c), consistent with ENDOR analysis. The nearest N is about 4 Å from a cluster S, which is at a distance that can be more difficult to observe in ENDOR experiments. An oxygen of the phosphate group is oriented within ~3 Å of the simulated OH while another is oriented within ~3 Å of an asparagine residue (N38) and a serine residue (S76), in position for a possible H-bonding network. Of the three docking models, this rotated SAM-like model utilizes the inherent SAM binding nature of PFL-AE and agrees with the ENDOR calculations, representing the most plausible docking mode.

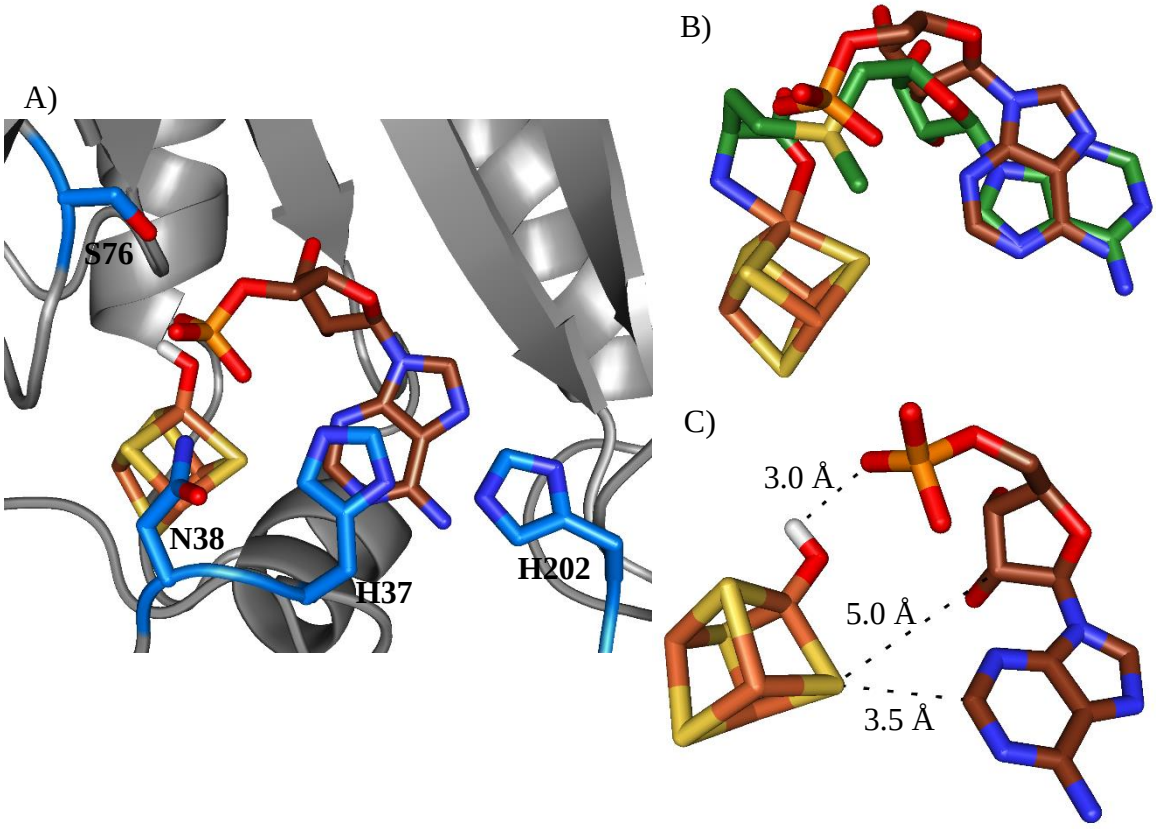


Figure 6.13. A) Rotated SAM-like docking of AMP (brown carbons). For this model, an OH was simulated on the unique Fe of the cluster (oxygens colored red, hydrogens colored white). The histidine residues (H37 and H202) that interact with SAM are shown in blue. A serine (S76) and an asparagine (N38) residue that can interact with the phosphate group of AMP are shown in blue. B) Comparison of the rotated SAM-like docking modeling of AMP (brown carbons) to coordinated SAM (green carbons). C) The distances from the 2'-C (5.0 Å) and a C of the adenine ring (3.5 Å) to a cluster S and the distance from a phosphate oxygen to the simulated OH (3.0 Å) are shown and are in agreement with ENDOR results. The closest N is about 4.0 Å from a cluster S.

Discussion

Small molecules previously shown to induce valence localization in the oxidized $[4Fe\text{-}4S]^{2+}$ state of PFL-AE are shown here to perturb the reduced $[4Fe\text{-}4S]^{+}$ cluster as well, based on the EPR spectra of PFL-AE in the presence of 5'-dAdo, MTA, AMP, and adenine. These molecules must be interacting with the cluster, presumably with the

unique Fe, to promote a charge localization. In the presence of MTA and 5'-dAdo, the EPR signal of the $[4Fe\text{-}4S]^{+}$ intensifies and sharpens, an effect similar to that observed in the presence of SAM. SAM, however, does not induce valence localization, and 5'-dAdo, MTA, AMP, and adenine do not contain the moieties of SAM that are responsible for coordination to the unique iron; it is clear, therefore, that the interactions of these small molecules are different from the well-characterized interaction of SAM with the cluster.

In order to investigate the structure of these small molecules with respect to the cluster, ENDOR spectroscopy was employed. ENDOR, like EPR spectroscopy, requires the paramagnetic reduced cluster, while the previous Mössbauer studies were carried out on the diamagnetic oxidized cluster. It is assumed that these small molecules interact with the cluster identically in the reduced and oxidized state, as identical binding in the two oxidation states has been found for SAM [19-21]. The oxidized structure was observed by cyroreduction of the $[4Fe\text{-}4S]^{2+}$/SAM complex to maintain the oxidized cluster/SAM geometry but in an EPR observable state. Identical ENDOR coupling was observed for cyroreduced and the photoreduced cluster/SAM samples, suggesting SAM binds in the same manner in both the oxidized and reduced states [19].

ENDOR analysis of PFL-AE in the presence of isotopically labeled AMP and Ado revealed that these molecules are indeed interacting with the cluster but not through a direct bond to the unique Fe. Instead, an H_xO species is bound to the cluster, similar to the case for aconitase [18], and therefore, while these small molecules are in close proximity to the unique Fe, they are not coordinated. The ^{13}C coupling in the

[U-$^{13}C_{10}$,$^{15}N_5$]-AMP and [ribose-$^{13}C_5$]-Ado samples suggests that the adenine ring is interacting with the unique Fe with a carbon at a distance of ~ 3.5 Å and a carbon of the ribose ring at a distance of ~ 5.0 Å. No N coupling was observed in ENDOR experiments however, which is very puzzling since an adenine carbon is 3.5 Å from the cluster. The [ribose-$^{13}C_5$]-AMP ENDOR results were consistent with the [ribose-$^{13}C_5$]-Ado results, suggesting that adenosine and AMP might be interacting with the cluster in a similar fashion. Other molecules, such as isotopically labeled MTA, could confirm whether this binding mode is similar for each molecule that induces valence localization. Further ENDOR analysis on other small molecules and more specific labeling needs to be conducted to identify more direct interactions between this H_xO bound cluster and these small molecules.

Since a valence localized cluster $[4Fe\text{-}4S]^{2+}$ is rare in proteins, it is likely that the binding mode of the valence-localizing molecules is unusual, while still occupying the same general binding pocket as SAM. Docking of AMP into the active site of PFL-AE revealed three different binding modes for AMP: one is a SAM-like orientation, another is a π-cation binding mode with the adenine ring sandwiched between the unique Fe and the cation, while a third places AMP in a rotated position with respect to SAM. The rotated SAM-like docking mode is the most plausible as it satisfies the ENDOR results with respect the estimated carbon distances. The π-cation docking mode, however, is intriguing because it is very similar to binding of pyridine diphosphate inhibitors in the [4Fe-4S] cluster containing IspH enzyme [22]. The crystal structure of IspH in the presence of the most effective inhibitor, (pyridine-3-yl)methyl diphosphate, revealed a

distance of 2.3 Å between the nearest C and N of the pyrimidine ring to the site differentiated Fe. Continuous electron density was observed between the unique Fe and the N of the ring, suggesting a direct bond between the two [22]. However, no ^{14}N coupling was observed between the cluster and labeled AMP in PFL-AE and further analysis of PFL-AE needs to be conducted to determine the actual binding mode of these small molecules.

Currently, no other radical SAM enzyme has been found to exhibit this unusual valence localization of the [4Fe-4S] cluster *in vivo* nor *in vitro*. Out of the radical SAM enzymes with known crystal structures in the presence of SAM or SAM-like molecules such as *S*-adenosyl-L-homocysteine (SAH) or 5'-dAdo, NosL was the only enzyme to contain an aromatic residue, F364, oriented parallel to the adenine portion of SAH. Upon alignment of the crystal structures of PFL-AE and NosL, this phenylalanine residue in NosL aligns with H37 in PFL-AE and may interact with a small molecule to induce valence localization in NosL. Docking of AMP into the active site of NosL was performed on the solved structure crystalized in the presence of SAH and substrate tryptophan. The SAM-like model and the π-cation model observed in PFL-AE was also observed in NosL (Figure 6.14). NosL does not appear to have a cation binding site; however, the observed π-cation docking model in NosL placed the adenine carbons at a distance of 3.5 Å, 3.5 Å, and 4.7 Å and a ribose carbon 5.1 Å from the unique Fe (Figure 6.14), very similar to PFL-AE. Comparable to PFL-AE, only the SAM-like model could facilitate an H_xO species at the unique Fe. Further analysis needs to be conducted on other radical SAM enzymes to verify if valence localization is unique to PFL-AE.

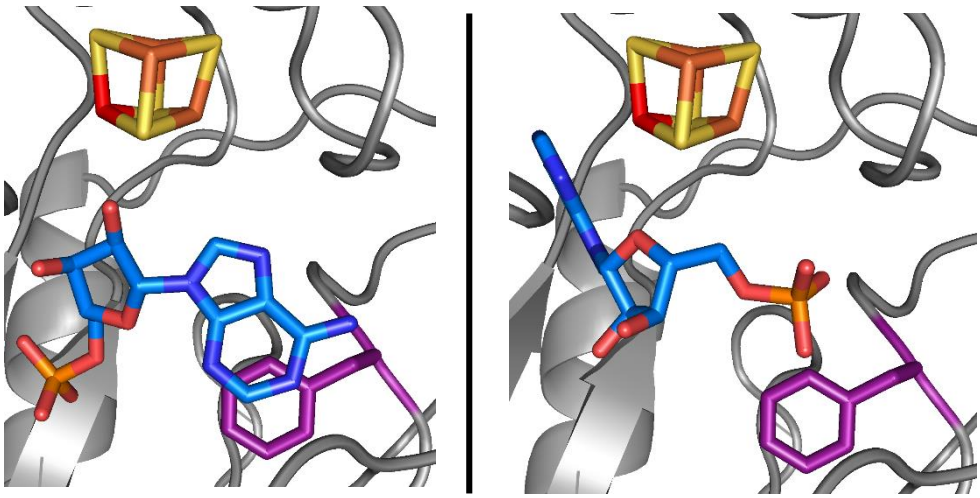


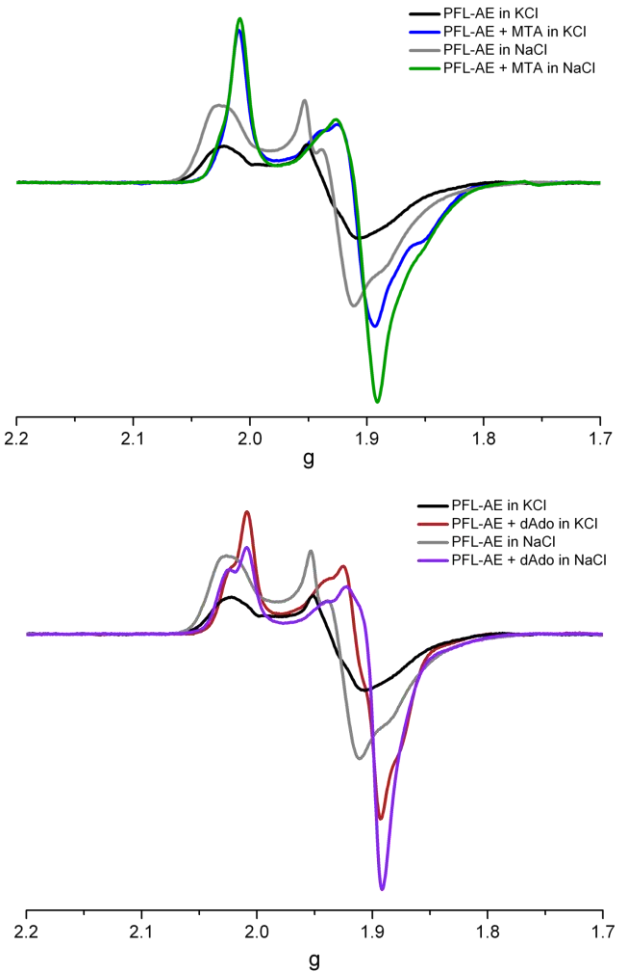
Figure 6.14. Active site of the radical SAM enzyme NosL docked with AMP (blue carbons). The unique iron is colored bright red, while the other three irons are pale red. The F364 that can interact with the adenine ring of AMP is colored purple. The model on the left is similar to the SAM-like docking obtained in PFL-AE while the model on the right is similar to the π-cation docking in PFL-AE.

The purpose for the valence localized state in PFL-AE is still not understood. Small molecules may help to stabilize the active site and provide a means to protect the cluster from oxidative degradation. Upon prolonged exposure to oxygen, the [4Fe-4S] cluster degrades to [3Fe-4S] and ultimately [2Fe-2S] clusters. Previous results demonstrated that overexpressed PFL-AE in whole cells are stable against oxidative damage after 30 minutes of exposure to air with no change in cluster state [9]. Another possible function for valence localization is for redox control of the cluster in the absence of SAM and substrate. A delocalized metal cluster would be expected to exhibit higher rates of electron transfer due to the lower reorganization energy involved. Electron transfer from a more localized state, in contrast, would involve greater reorganization energy and thus would be expected to be slower. Valence localization could therefore be a mechanism by which electron transfer from reduced flavodoxin, an *in vivo* electron

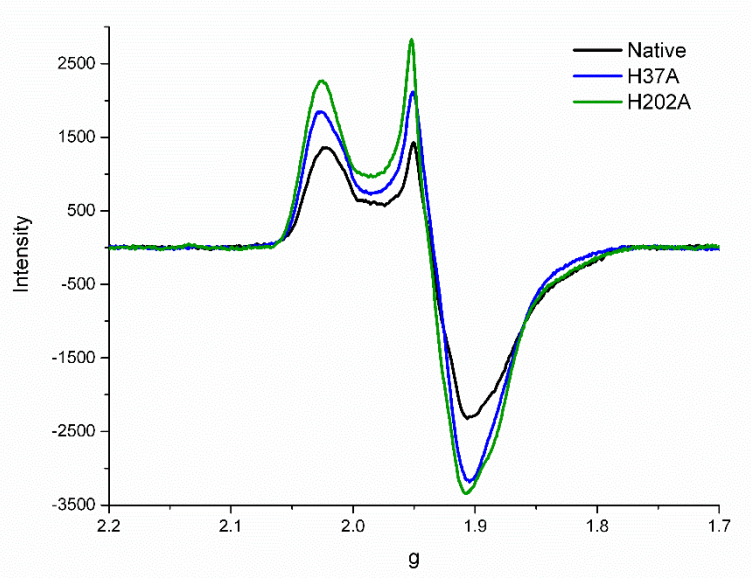
donor, to the cluster or from the cluster to SAM would be switched off, thereby avoiding the production of radicals when they are not needed to catalyze reactions. Valence delocalization brought about by loss of a valence-localizing small molecule could then serve as a trigger to initiate the key electron transfer steps in a radical SAM reaction.

Supplementary Information

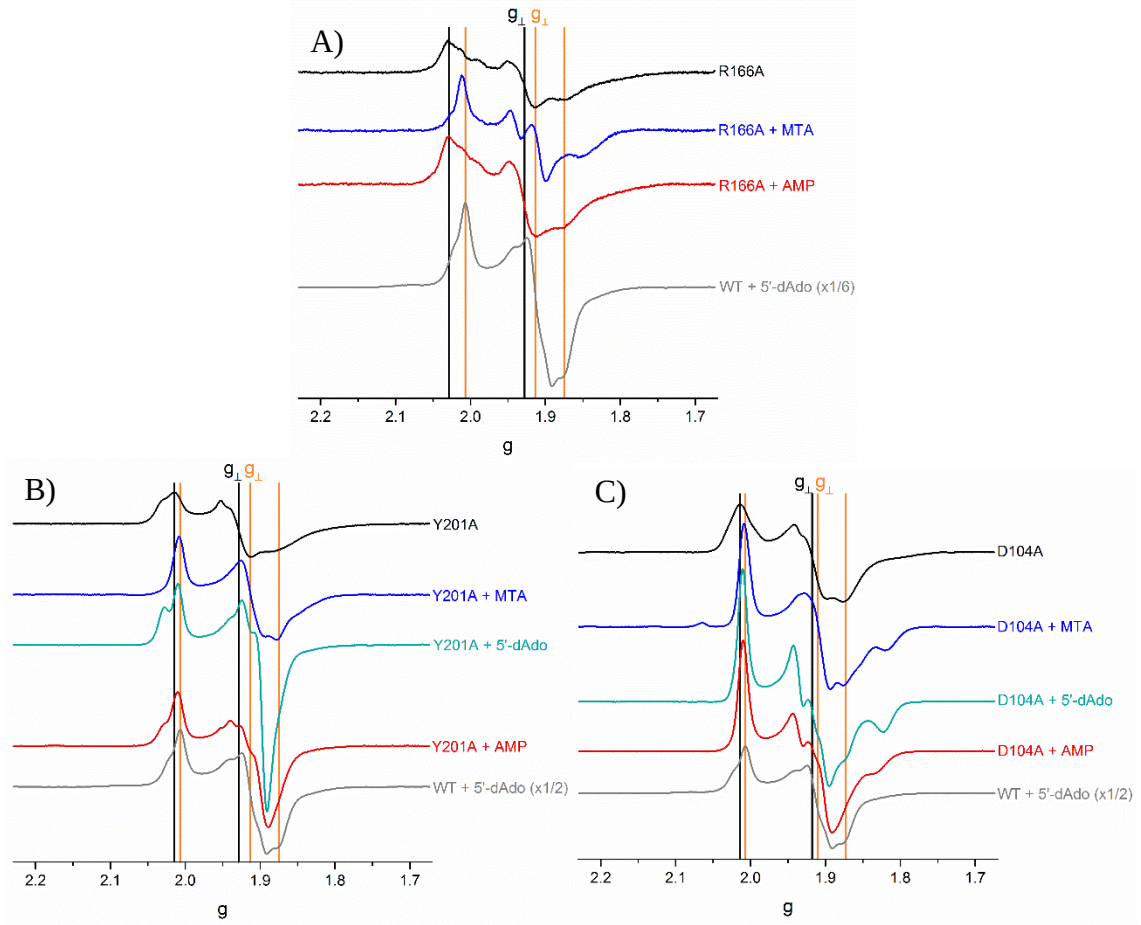
SI Figures



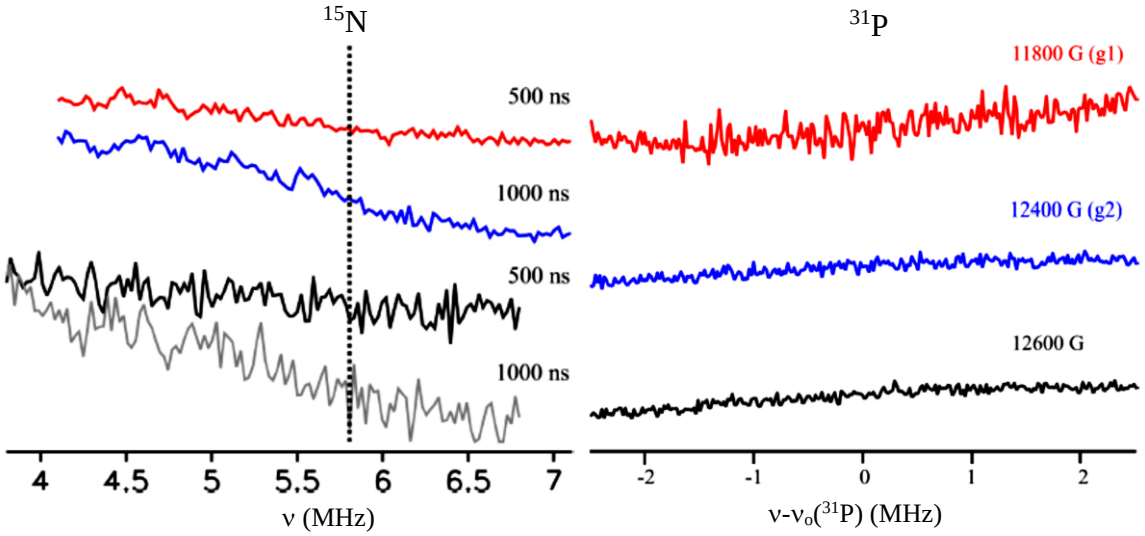
SI Figure 6.1. Top: EPR spectra of PFL-AE in the presence of MTA and KCl (blue) or NaCl (green). Bottom: PFL-AE in the presence of 5'-dAdo and KCl (red) or NaCl (purple). PFL-AE in the absence of small molecule but in the presence of KCl (black) or NaCl (grey) are shown for reference. The EPR spectrum of PFL-AE in the presence of MTA and 5'-dAdo do differ significantly in the presence of either KCl or NaCl.



SI Figure 6.2. EPR spectra comparing native PFL-AE (black) to the variants H37A (blue) and H202A (green).



SI Figure 6.3. EPR spectra of the PFL-AE variants R166A (A), Y201A (B), and D104A (C) in the presence of MTA (blue), 5'-dAdo (teal), or AMP (red). WT PFL-AE in the presence of 5'-dAdo (grey) is also shown. Black vertical lines correspond to features in conformation A (dependent on each variant) while vertical orange lines correspond to conformation B of WT in the presence of 5'-dAdo. All samples were prepared in 100 mM NaCl. R166A in the presence of 5'-dAdo had cluster degradation and the spectrum was omitted.



SI Figure 6.4. Mims ENDOR spectra of ^{15}N (left) and ^{31}P (right) of PFL-AE in the presence of [U-$^{13}C_{10}$,$^{15}N_5$]-AMP. No signal was obtained for either at different tau values (^{15}N, colored lines) or g values (^{31}P, colored lines). Vertical dotted line is the ^{15}N Larmor frequency. Parameters for ^{31}P include 34.788 GHz at 8.0 dB, RF = 14dB, tau = 500 ns with 200 ms rep.

SI Table 6.1. Specific Activity (SA, in U/mg) of WT PFL-AE and PFL-AE variants including the amount of Fe per protein (Fe #) and the specific activity normalized for the amount of Fe per protein. All activity assays were performed in 100 mM KCl.

	SA	Fe #	SA Normalized for Fe #
WT	41.23	2.7	15.27
H37A	60.32	2.8	21.54
H202A	26.32	1.3	20.25
D104A	5.47	4.2	1.30
Y201A	73.91	3	24.64
R166A	65.07	3.9	16.68

SI Table 6.2. Distances (in Å) for the ribose carbons to the nearest cluster S, or the unique Fe (where indicated), for the three different SAM-like docking models of AMP into the active site of PFL-AE.

Structure	1'-C	2'-C	3'-C	4'-C	5'-C
1	4.7	3.8	4.6	5.1	4.5 (Fe)
2	5.0	4.1	5.1	5.7	5.5 (Fe)
3	4.6	4.0	4.6	4.5 (Fe)	3.5 (Fe)

References

1. Beinert, H.; Holm, R. H.; Munck, E. *Science* **1997**, *277*, 653-659.

2. Johnson, D. C.; Dean, D. R.; Smith, A. D.; Johnson, M. K. *Annu. Rev. Biochem.* **2005**, *74*, 247-281.

3. Broderick, J. B.; Duffus, B. R.; Duschene, K. S.; Shepard, E. M. *Chem. Rev.* **2014**, *114*, 4229-4317.

4. Vey, J. L.; Drennan, C. L. *Chem. Rev.* **2011**, *111*, 2487-2506.

5. Horitani, M.; Byer, A. S.; Shisler, K. A.; Chandra, T.; Broderick, J. B.; Hoffman, B. M. *J. Am. Chem. Soc.* **2015**, *137*, 7111-7121.

6. Frey, M.; Rothe, M.; Wagner, A. F.; Knappe, J. *J. Biol. Chem.* **1994**, *269*, 12432-12437.

7. Plaga, W.; Frank, R.; Knappe, J. *Eur. J. Biochem.* **1988**, *178*, 445-450.

8. Shisler, K. A.; Broderick, J. B. *Arch. Biochem. Biophys.* **2014**, *546*, 64-71.

9. Yang, J.; Naik, S. G.; Ortillo, D. O.; Garcia-Serres, R.; Li, M.; Broderick, W. E.; Huynh, B. H.; Broderick, J. B. *Biochemistry* **2009**, *48*, 9234-9241.

10. Krebs, C.; Henshaw, T. F.; Cheek, J.; Huynh, B.; Broderick, J. B. *J. Am. Chem. Soc.* **2000**, *122*, 12497-12506.

11. Walters, E. M.; Garcia-Serres, R.; Jameson, G. N.; Glauser, D. A.; Bourquin, F.; Manieri, W.; Schurmann, P.; Johnson, M. K.; Huynh, B. H. *J. Am. Chem. Soc.* **2005**, *127*, 9612-9624.

12. Broderick, J. B.; Henshaw, T. F.; Cheek, J.; Wojtuszewski, K.; Smith, S. R.; Trojan, M. R.; McGhan, R. M.; Kopf, A.; Kibbey, M.; Broderick, W. E. *Biochem. Biophys. Res. Commun.* **2000**, *269*, 451-456.

13. Beinert, H. *Methods Enzymol.* **1978**, *54*, 435-445.

14. Davoust, C. E.; Doan, P. E.; Hoffman, B. M. *J. Magn. Reson.* **1996**, *A119*, 38-44.

15. Doan, P. E.; Hoffman, B. M. *Chem. Phys. Lett.* **1997**, *269*, 208-214.

16. Trott, O.; Olson, A. J. *J Comput Chem* **2010**, *31*, 455-461.

17. *PyMOL Molecular Graphics System*; 1.7.4 ed.; Schrodinger, LLC.

18. Werst, M. M.; Kennedy, M. C.; Beinert, H.; Hoffman, B. M. *Biochemistry* **1990**, *29*, 10526-10532.

19. Walsby, C. J.; Hong, W.; Broderick, W. E.; Cheek, J.; Ortillo, D.; Broderick, J. B.; Hoffman, B. M. *J. Am. Chem. Soc.* **2002**, *124*, 3143-3151.

20. Walsby, C. J.; Ortillo, D.; Broderick, W. E.; Broderick, J. B.; Hoffman, B. M. *J. Am. Chem. Soc.* **2002**, *124*, 11270-11271.

21. Walsby, C. J.; Ortillo, D.; Yang, J.; Nnyepi, M. R.; Broderick, W. E.; Hoffman, B. M.; Broderick, J. B. *Inorg. Chem.* **2005**, *44*, 727-741.

22. Span, I.; Wang, K.; Eisenreich, W.; Bacher, A.; Zhang, Y.; Oldfield, E.; Groll, M. *J. Am. Chem. Soc.* **2014**, *136*, 7926-7932.

CHAPTER SEVEN

THE ACTIVATION OF THE RADICAL SAM ENZYME PYRUVATE FORMATE LYASE ACTIVATING ENZYME IS STIMULATED BY POTASSIUM

Contribution of Authors and Co-Authors

Manuscript(s) in Chapter(s) 4, 5, 6, 7, 9, 10

Author: Krista A Shisler

Contributions: Conducted activity assays in different monovalent and divalent cations with M^+-free PFL-AE. Prepared and collected EPR spectra in addition to analysis and simulation of EPR results of PFL-AE in various monovalent and divalent cations. Prepared, collected, and analyzed CD spectra of PFL-AE in various monovalent cations. Generated and purified PFL-AE variants and conducted EPR on these variants. Wrote manuscript and generated figures for manuscript.

Co-Author: Rachel U Hutcheson

Contributions: Conducted the initial activity assays in monovalent cations with PFL-AE, prepared the initial EPR samples in monovalent cations, and helped write manuscript and generate figures.

Co-Author: Kaitlin S Duschene

Contributions: Aided in data collection of activity assays in monovalent cations and helped collect EPR spectra of PFL-AE.

Co-Author: Adam V Crain

Contributions: Performed activity assays in the presence of choline chloride.

Co-Author: Ashley Rasmussen

Contributions: Aided in data collection for the activity assay in monovalent cations.

Contribution of Authors and Co-Authors Continued

Co-Author: Jian Yang

Contributions: Conducted initial EPR experiments in different monovalent cations.

Co-Author: Jessica L Vey

Contributions: Collected x-ray crystal data and solved the two structures of PFL-AE in the presence of SAM and in the presence of SAM and a 7-mer peptide of PFL. Refined the cation site in PFL-AE by modeling different monovalent and divalent cations into the active site of PFL-AE.

Co-Author: Joan B Broderick

Contributions: Provided interpretation of results including activity assays, EPR and CD spectra. Provided insights into the preparation of samples and assisted in preparation of manuscript and figures.

Manuscript Information Page

Krista A Shisler, Rachel U Hutcheson, Kaitlin S Duschene, Adam V Crain, Ashley Rasmussen, Jian Yang, Jessica L Vey, and Joan B Broderick
Biochemistry
Status of Manuscript:
__X__ Prepared for submission to a peer-reviewed journal
____ Officially submitted to a peer-review journal
____ Accepted by a peer-reviewed journal
____ Published in a peer-reviewed journal

Publisher ACS Publications

CHAPTER SEVEN

THE ACTIVATION OF THE RADICAL SAM ENZYME PYRUVATE FORMATE-LYASE ACTIVATING ENZYME BY POTASSIUM ION

Krista A. Shisler, Rachel U. Hutcheson, Kaitlin S. Duschene, Adam V. Crain, Ashley Rasmussen, Jian Yang, Jessica L. Vey, and Joan B. Broderick

Department of Chemistry and Biochemistry, Montana State University, Bozeman, MT 59717, and the Departments of Chemistry and Biology, Massachusetts Institute of Technology, Cambridge, MA 02139

Keywords

radical *S*-adenosyl-L-methionine, iron-sulfur cluster, glycyl radical, monovalent cation stimulation

Abstract

Pyruvate formate-lyase activating enzyme (PFL-AE), which activates pyruvate formate-lyase (PFL) through generation of a catalytically essential glycyl radical on PFL, is one of the earliest known members of the radical SAM superfamily. Enzymes in this superfamily utilize a [4Fe-4S] cluster to reductively cleave SAM (*S*-adenosyl-L-methionine) to produce a 5'-deoxyadenosyl radical (5'-dAdo•) intermediate that subsequently abstracts a hydrogen atom from substrate to initiate a radical reaction. These enzymes share a common structural core composed of either a full $(\alpha/\beta)_8$, or partial

$(\alpha/\beta)_6$, TIM barrel fold. Here we refine the crystal structure of PFL-AE with alternative species in a putative metal site in the enzyme active site, providing evidence for the binding of sodium ion in this site. The significance of this cation in PFL-AE function has been explored through activity assays as well as EPR spectroscopic studies of PFL-AE with and without SAM bound. Of the six monovalent cations tested (Na^+, K^+, NH_4^+, Rb^+, Cs^+, and Li^+), potassium ion provided the highest activity, with a strong correlation of activity with cation size across this series. PFL-AE purified and assayed in the absence of any simple monovalent cation exhibited very little activity, indicating that the monovalent cation is important for enzyme activity. Several divalent cations (Ca^{2+}, Mg^{2+}, and Zn^{2+}) were shown to inhibit PFL-AE activity. The concentration dependence of the cation activation of PFL-AE was tested for K^+, and the enzyme activity was found to be maximal above a potassium ion concentration of approximately 100 mM, with half-maximal activation obtained at $[K^+] = 44 \pm 10.5$ mM. The presence of monovalent cation affects both the EPR and CD spectral properties of PFL-AE, particularly in the presence of SAM, consistent with the cation's close proximity to the iron-sulfur cluster and its intimate interaction with SAM. The likely roles for this monovalent cation in enzyme catalysis are discussed.

Introduction

Pyruvate formate-lyase activating enzyme (PFL-AE) is a member of the large and diverse radical *S*-adenosyl-L-methionine (SAM) superfamily, members of which use an iron-sulfur cluster and SAM to initiate difficult radical transformations in all kingdoms of

life [1-3]. Radical SAM enzymes share a common CX_3CX_2C motif or variation thereof, and the conserved cysteines coordinate three irons of a [4Fe-4S] cluster, while SAM coordinates the fourth iron through its amino and carboxylate moieties [4,5]. Radical SAM catalysis is initiated by electron transfer from the reduced $[4Fe\text{-}4S]^+$ cluster to the sulfonium of SAM, inducing S-C(5') bond cleavage to give methionine and a 5'-deoxyadensyl radical (5'-dAdo•) intermediate that abstracts a hydrogen atom from substrate. In the case of PFL-AE, the 5'-dAdo• radical abstracts a hydrogen atom from glycine 734 of pyruvate formate-lyase (PFL), a central metabolic enzyme catalyzing the conversion of pyruvate and coenzyme A (CoA) to formate and acetyl-CoA under anaerobic conditions [6,7]. Although 5'-dAdo• has never been experimentally observed, the PFL-AE/PFL system allowed quantitative determination of the product of H-atom abstraction, the stable glycyl radical on PFL, demonstrating the 1:1 stoichiometry between electron loss from the $[4Fe\text{-}4S]^+$ cluster and product formation on PFL [8].

Two crystal structures of PFL-AE have been solved: one with PFL-AE in complex with SAM and another with PFL-AE in complex with SAM and a 7-mer PFL peptide substrate analog containing the target glycine residue (Figure 7.1) [9]. The structures reveal a partial $(\alpha/\beta)_6$ triosephosphate isomerase (TIM) barrel with a wide opening able to accommodate the large substrate PFL, a domain of which is proposed to bind in the active site of PFL-AE [9]. SAM is bound through the amino and carboxylate moieties to the unique iron of the cluster, a binding mode first revealed by electron nuclear double resonance (ENDOR) spectroscopy [5]. Two motifs conserved in the radical SAM superfamily show interactions with SAM: the GGE motif (PFL-AE residues

G77, G78, and E79) directly binds the methionine portion of SAM, while the GXIXGXXE motif (X = V168, V170, G172, and E175 in PFL-AE) stabilizes the adenine moiety binding site. The PFL peptide substrate is bound across the lateral opening of the partial TIM barrel primarily by peptide backbone to PFL-AE side chain contacts. One of these interactions involves the highly conserved DGXGXR motif located on PFL-AE loop A (residues 10-20), and upon peptide binding, this loop undergoes a large conformational change by swinging up into the active site to establish these interactions. The movement of this loop is thought to be essential to the activation of PFL, possibly by orienting the glycine loop of PFL in the active site [9].

PFL is a homodimer wherein each monomer consists of a 10-stranded α/β barrel with the active site located at the center (Figure 7.2) [10,11]. Within the active site are two catalytically essential cysteine residues, C418 and C419, as well as the site of the glycyl radical, G734. This active site is buried 8 Å from the surface of the protein; however, G734 must be directly accessed by the active site of PFL-AE in order for the stereospecific H-atom abstraction, and thus PFL activation, to occur. Taken together, the structures of PFL and PFL-AE thereby suggest that a significant PFL conformational change is required for the glycine-containing loop to be accessible to the active site of PFL-AE. Experimental evidence for such a conformational change has been provided by a study utilizing fluorescence and electron paramagnetic resonance (EPR) spectroscopies and activity assays that together point to an open conformation of PFL in the presence of PFL-AE [12]. In the proposed open conformation of PFL, the radical domain containing G734 flips out of the protein and becomes accessible to PFL-AE [12].

Subsequent to our report of the PFL-AE structure, further analysis of the structure solutions revealed the presence of a bound monovalent cation in the active site (Figure 7.1 and Figure 7.3). This was an intriguing observation given that we had also observed dramatic alterations in EPR spectral properties for reduced PFL-AE depending on whether Na^+ or K^+-containing buffers were used in sample preparation. In order to further probe the nature of the cation binding site, the identity of the likely *in vivo* metal occupying that site, and the potential functional relevance of the monovalent cation, we carried out detailed structural refinement and analysis, as well as EPR and CD spectroscopic studies and enzyme activity assays as a function of the presence and identity of simple monovalent and divalent cations. The results together point to an important role in catalysis for the monovalent ion bound in the active site of PFL-AE.

Materials and Methods

All chemicals were obtained from commercial sources and were of the highest purity commercially available. The enzymes citrate synthase and malic dehydrogenase were purchased from Sigma.

Refinement of Alternative Species in the Putative Metal Site

PFL-AE was originally crystallized in conditions consisting of 100 mM HEPES, 3.5 M sodium formate and 0.2 mM 2,6-dimethyl-4-heptyl-beta-d-maltopyranoside, pH 6.8 [13]. The original peptide-PFL-AE model was refined in CNS [14]. Density located near the carbonyl group of SAM originally attributed to a bound water molecule was

modeled and refined as a sodium ion based on the geometry of the surrounding atoms, comparisons of the water/sodium ion's B-factors to those of the surrounding atoms (Table 7.1), and F_o-F_c electron density maps (Figure 7.4) [13]. Here, ten additional cycles of refinement of the deposited structure (PDB entry 3CB8) were carried out in parallel in REFMAC5 [15] in the CCP4i program suite [16] with the site modeled as a water molecule, sodium ion, magnesium ion, potassium ion or calcium ion (note that other than water, of these ions, only sodium was known to be present in the crystallization conditions). Additionally, a round of refinement was carried out in CNS using the same starting model with water, sodium, magnesium, potassium or calcium modeled in the metal site, this time, refining the occupancy of metal site with the site's B-factor set to 76.00 (the average B-factor of the surrounding atoms). The B-factors, R-factors (Table 7.2), occupancies (Table 7.3), distances to nearby atoms (Table 7.4 and Table 7.5), and difference density maps (Figure 7.4) of the resulting models were examined to judge likelihood of each atom type's presence in the site in question.

Expression and Purification of PFL and PFL-AE and Generation of Variants

PFL-AE wild-type and variants were expressed and purified as previously described [5,17-19] with modifications. The pCAL-n-EK plasmid containing the PFL-AE gene was transformed into *E. coli* BL21(DE3)pLysS (Stratagene) cells for overexpression. Mutagenesis was carried out using the QuikChange site-directed mutagenesis kit from Stratagene and plasmids containing the variant genes were transformed into BL21(DE3)pLysS cells. Mutagenesis primers to introduce the D104A

change (CAT TCA TAC CTG TCT GGC CAC CAA CGG TTT TGT TC) and the D129A change (CGT TCA TCT GTT TGA GAG CGA GCA TTA CCA GGT C) were synthesized by Integrated DNA Technologies. Expression and purification of WT and variant PFL-AE were carried out under identical conditions. A 50 mL LB and 50 μg/mL ampicillin starter culture grown overnight was used to inoculate 10 L of minimal media in a bench-top fermentor (New Brunswick) containing 50 μg/mL ampicillin and a solution of glucose and vitamins. The minimal media consists of 100 g Casamino acids, 84.2 g MOPS, 8.0 g Tricine, 14.7 g NaCl, 16.0 g KOH, 5.1 g NH_4Cl in 9.8 L of water. The glucose solution was sterile filtered prior to addition to the fermentor and contained the following: 50 g of glucose in 200 mL water; 25 mL of "O" solution (0.1 g $FeCl_2 \cdot 4H_2O$ dissolved in 10 mL of 12 M HCl, 2.68 g $MgCl_2 \cdot 6H_2O$, and 1 mL "T" solution [18.4 mg $CaCl_2 \cdot 2H_2O$, 64 mg H_3BO_3, 40 mg $MnCl_2 \cdot 4H_2O$, 18 mg $CoCl_2 \cdot 6H_2O$, 4 mg $CuCl_2 \cdot 2H_2O$, 340 mg $ZnCl_2$, and 605 mg $Na_2MoO_4 \cdot 2H_2O$ diluted to 100 mL with H_2O] and the "O" was brought up to a final volume of 50 mL with H_2O; 25 mL of 1 M KH_2PO_4; 12.5 mL of 276 mM K_2SO_4; and 62.5 mL of 0.1 M $CaCl_2$. Additionally, 10 mg of the vitamins biotin, pantothenic acid, vitamin B_{12}, thiamine, folic acid, riboflavin, niacinamide, thioctic acid, and pyridoxine were added to the fermentor. The growth was incubated at 37°C with 250 rpm agitation and a flow of 5 L/min of compressed air. Once the cells reached an OD_{600} of ~0.5, isopropyl-β-D-thiogalactopyranoside (IPTG) was added to a final concentration of 0.5 mM and 0.75 g of $Fe(NH_4)_2(SO_4)_2 \cdot 6H_2O$ was added. After ~2 hours, the cells were cooled and put under anaerobic conditions by purging the cells with N_2 once the culture was ~ 30°C, followed by another addition of 0.75 g of

$Fe(NH_4)_2(SO_4)_2 \cdot 6H_2O$ once the culture was ~20°C. The culture was purged with N_2 overnight in a 4°C fridge. The cells were harvested and stored in a -80°C freezer until purification.

PFL-AE was purified from cell pellets in an anaerobic Coy chamber. To obtain protein lacking a bound monovalent cation, all lysis and purification buffers were made without any monatomic monovalent cation. The cell pellets were lysed in a 50 mM Tris, pH 7.5 buffer containing 5% w/v glycerol, 1% w/v Triton X-100, and 10 mM $MgCl_2$. To 100 mL of lysis buffer, 18 mg of PMSF, 78 mg of DTT, 16 mg of lysozyme, and trace amounts of DNase and RNase were added. Approximately 2 mL of lysis buffer per 1 g of cell pellet was added to the cells and allowed to lyse on ice for ~1 hour, with stirring, after which the lysate was centrifuged. The supernatant was applied to a Superdex-75 resin. The gel filtration buffer, 50 mM Tris, pH 7.5 and 1 mM DTT was washed over the column and the dark brown fractions were pooled and concentrated using a 10K MWCO Millipore Amicon Ultra centrifugal concentrator. The concentrated protein was run over the column a second time and the fractions with the highest 426/280 nm ratio were pooled and concentrated. Typically, a 426/280 nm ratio greater than 0.16 were pooled and concentrated. Protein concentrations were determined using the method of Bradford [20] using dye reagent from Biorad. A correction factor determined by acid hydrolysis was utilized in the final calculations of PFL-AE concentration [17]. Iron content was determined using atomic absorption spectroscopy. PFL-AE contained between 3.0 and 3.8 Fe per protein for the following experiments.

PFL was purified from BL21(DE3)pLysS/pKK-PFL cells that were grown aerobically in a benchtop fermentor containing 10 L of LB as previously described [17]. A 50 mL LB and 50 μg/mL ampicillin starter culture was grown overnight and used to inoculate 10 L of LB and 50 μg/mL ampicillin. Cell pellets were lysed aerobically in a 20 mM Tris, pH 7.2 buffer containing 5% w/v glycerol, 1% w/v Triton X-100, and 10 mM $MgCl_2$. Again, 18 mg of PMSF, 16 mg of lysozyme, and trace amounts of DNase and RNase were added. Approximately 2 mL of lysis buffer per 1 g of cell pellet was added to the cells which incubated on ice for ~1 hour, with stirring, after which the lysate was centrifuged. The supernatant was applied to a Waters AP-5, 300 mm column containing Accell Plus QMA resin with Buffer A (20 mM Tris, pH 7.2 and 1 mM DTT). The column was washed with 300 mL of Buffer A followed by a 900 mL linear gradient to 100% Buffer B (20 mM Tris, pH 7.2 with 500 mM NaCl and 1 mM DTT), and ending with 300 mL of 100% Buffer B. PFL eluted around 50% Buffer B and fractions were collected and analyzed via SDS-PAGE. Most abundant and the purest fractions were then pooled and buffer exchanged into a high salt buffer (10 mM Tris, pH 7.2 with 1 M $(NH_4)_2SO_4$ and 1 mM DTT) and loaded onto a HighLoad High Performance 16/10 phenyl sepharose column. The column was washed with 50 mL of the high salt buffer followed by a 50 mL linear gradient to 100% Buffer A (20 mM Tris, pH 7.2 and 1 mM DTT) and ended with a 50 mL wash of Buffer A. PFL eluted at 100% Buffer A, and again was analyzed via SDS-PAGE. PFL was buffer exchanged into a 20 mM Tris, pH 7.2 buffer to remove excess M^+ from purification and then degassed on a Schlenk line, aliquoted into tubes, and stored at -80°C.

PFL-AE Activity Assays

PFL-AE activity was assayed in a Unilab MBraun anaerobic chamber containing ≤ 1 ppm O_2 using a modified version of the coupled enzyme assays previously published [17,21,22]. For assaying the effect of each metal ion on activity, a 100 mM Tris pH 7.6 buffer containing 100 mM of monovalent cation salt (NaCl, KCl, NH_4Cl, RbCl, CsCl, or LiCl) or 1 mM of divalent cation salt ($CaCl_2$, $MgCl_2$, or $Zn(NO_3)_2$) was used. A control lacking any salt addition was also conducted with each assay. To carry out the assay, 450 µL of activation solution was mixed containing a final concentration of 0.05 µM PFL-AE purified in the absence of M^+, 5 µM PFL, 0.1 mM SAM, 10 mM oxamate (or 10 mM pyruvate for assays conducted with $CaCl_2$), 8 mM DTT and 25 µM 5-deazariboflavin (added last in the dark) in a 100 mM Tris, pH 7.6 buffer containing different cations as described above (all concentrations given as final concentrations). This mixture was added to a shortened NMR tube and PFL-AE was photoreduced by illumination with a 300 W halogen lamp and the protein was kept in a 30°C ± 2°C water bath for 5 minutes and then covered with foil to prevent further reduction. To assay the activity, 5 µL of the resulting activation solution was placed on a lid of an anaerobic cuvette containing 895 µL of coupling solution (3 mM NAD^+, 55 µM CoA, 0.05 mg/mL BSA, 10 mM pyruvate, 10 mM malate, 2 U/mL citrate synthase, 30 U/mL malic dehydrogenase, and10 mM DTT in a 100 mM Tris, pH 8.1 buffer) prior to sealing the cuvette and removing it from the chamber. The two solutions were mixed by inverting the cuvette just prior to placing in a thermostatted (at 30°C) Cary 60 UV-Vis spectrophotometer. The production of NADH was monitored at 340 nm for 90 seconds. Rates were calculated from the slope of

absorbance vs. time from 18 seconds to 90 seconds, when the slopes stabilized and were the most linear. One unit of PFL activity corresponds to the production of one μmole of pyruvate per minute, and 35 units of PFL is equivalent to 1 nmole of PFL active sites [23]. The definition of one unit of PFL-AE activity is the amount that catalyzes the production of 1 nmole of active PFL per minute [17]. All assays were conducted in triplicate.

To minimize any cation contamination, separate NMR tubes were used for each cation and were acid washed before switching to different cations. Acid-free substances were purchased, when available. Pyruvate was only available as the sodium salt but was only added to the coupling solution. Once PFL-AE comes into contact with the coupling solution, presumably all PFL has been activated and any trace sodium would not stimulate PFL-AE activity.

To examine the dependence of PFL-AE activity on the concentration of K^+, PFL-AE was assayed with 500 mM, 300 mM, 200 mM, 100 mM, 75 mM, 50 mM, 25 mM, 10 mM, or 0 mM KCl in a 100 mM Tris, pH 7.6 buffer with 1 mM DTT. The ionic strength was maintained at a constant value by adding choline chloride for those with less than 100 mM KCl and activity was monitored.

EPR Sample Preparation and Spectroscopy

In an Mbruan anaerobic chamber with ≤1 ppm O_2, 300 μM PFL-AE, 100 μM 5-deazariboflavin (added last in the dark), 5 mM DTT in a 100 mM Tris, pH 7.6 buffer containing either no cation, 100 mM of NaCl, KCl, NH_4Cl, RbCl, CsCl, or LiCl or 1 mM of $CaCl_2$, $MgCl_2$, or $Zn(NO_3)_2$ was placed in an EPR tube. Photoreduction was

accomplished by illumination with a 300 W halogen lamp in an ice bath for one hour, and samples were either frozen as-is or SAM was added to a final concentration of 2 mM and incubated for ~5 minutes before freezing in liquid nitrogen.

EPR spectra were recorded on a Bruker EMX X-band spectrometer equipped with a liquid helium cryostat and temperature controller from Oxford Instruments. Typical experimental parameters were 12 K and 9.37 GHz, with 1.0 mW microwave power, 100 kHz modulation frequency, and 10 G modulation amplitude. Each spectrum is the average of four scans. The EPR spectra in the presence of SAM were simulated using Easy Spin version 4.5.5 [24].

Circular Dichroism

CD experiments were conducted under anaerobic conditions using a Jasco-710 spectropolarimeter at room temperature. Measurements were collected in a 1 cm path length cuvette from 300-800 nm with a sensitivity of 100 millidegrees, 0.1 nm data pitch, continuous scan mode with a speed of 100 nm/min, a response time of 1 s, 1.0 nm band width, and accumulation of 3 scans. PFL-AE was added to an anaerobic cuvette in an MBraun anaerobic chamber to a final concentration of 50 μM containing 1 mM DTT in a 100 mM Tris, pH 7.6 buffer and either no cation or 100 mM of NaCl, KCl, NH_4Cl, RbCl, CsCl, or LiCl. After initial scans without SAM were conducted, SAM was added to a final concentration of 500 μM. For determination of the K_D for K^+, a final concentration of 50 μM PFL-AE and 500 μM SAM was used prior to KCl addition. KCl was titrated to final concentrations of 0 mM, 2 mM, 3 mM, 6 mM, 12 mM, 21 mM, 35 mM, 49 mM, 101 mM, and 177 mM, 301 mM, and 500 mM.

Results

Refinement of Alternative Species in the Putative Metal Site

The two most likely biologically relevant cations are Na^+ and K^+, but determining the cation's identity in a crystal structure, and *in vivo,* can be difficult; Na^+ has the same number of electrons as a water molecule and K^+ has an ionic radius almost identical to a water molecule [25]. However, some insight can be gained from the distances between M^+ and the atoms with which it interacts: an average distance of ~2.4 Å for Na^+ and ~2.8 Å for K^+ is generally observed [26]. The putative metal site in PFL-AE is located near the active site and involves one of the SAM carboxylate oxygen atoms (Figure 7.1 and Figure 7.3). In total, five oxygen atoms are located within 3 Å this site, which assumes distorted trigonal bipyramidal geometry (Figure 7.3). The locations and B-factors of these four oxygen ligands do not change significantly after refinement in REFMAC, regardless of whether water, sodium or calcium was modeled into the site (Figure 7.4), though small shifts do occur to accommodate the different atoms' radius (for example, compare the distances listed in (Table 7.4 and Table 7.5)). To examine whether the presence of water or a metal ion provides better agreement with the crystallographic data, we set the occupancies of these ions/molecule to 100%, and compared the B-factors for each following refinement. If the resulting B-factor is lower than the average of the surrounding area, that indicates that the ions/molecule has too little scattering to account for the density, whereas if the B-factor is higher, that is an indication of too much scattering. The best fit is the ion/molecule with a B-factor that is most similar to the

average in that area. We find that water has a significantly lower than the average B-factor compared to the surrounding atoms, calcium and potassium are significantly higher, and sodium is the closest to average (Table 7.2). Magnesium would also be a good fit to the crystallographic data (Table 7.2), but as far as we know, no magnesium was present in the sample. In addition, more extensive positive F_o-F_c electron density is present in this site when modeled with water than when modeled with sodium (Figure 7.4a,b), and negative F_o-F_c electron density appears when the site is modeled as calcium (Table 7.4e). These observations are consistent with presence of sodium in this site.

Next, we set the B-factor of the ions/molecule to the average of the surrounding area, allowed the occupancies to refine, and compared the resulting occupancies (Table 7.3). A resulting occupancy value of higher than 100% would indicate that the modeled species has too little scattering, whereas a lower occupancy would reflect that the modeled species has too much scattering power. Whereas water had too high an occupancy, the other ligands had occupancies of less than 100%. As expected, sodium and magnesium had the most reasonable occupancy values. Again, these observations are consistent with presence of sodium or magnesium in this site, with sodium more likely because it was known to be present in our crystals.

We also considered coordination geometry and the average distance of the oxygen ligands (Table 7.4 and Table 7.5) in our assignment of the likely ion/molecule to occupy this site. Based on these criteria, water is not a good candidate, as it would not be capable of forming so many interactions and the geometry (distorted trigonal bipyramidal) of the interactions is also incorrect for water coordination. In contrast,

trigonal bipyramidal is a common geometry for metal ions. The average metal-oxygen distance (2.5 Å) is also exactly what one would expect based on both protein structures with sodium bound as well as the Cambridge Structural Database [27]. Potassium-oxygen distances tend to be longer (2.8 Å), so one would expect a slight rearrangement for potassium to occupy this site.

Effect of Cations on PFL-AE Activity

To examine whether the monovalent cation affected PFL-AE enzymatic activity, coupled enzyme activity assays were carried out in the presence of each of six monovalent cations (Na^+, K^+, NH_4^+, Rb^+, Cs^+, and Li^+) and three divalent cations (Ca^{2+}, Mg^{2+}, and Zn^{2+}). The activity of PFL-AE reaches a maximum after approximately 5 minutes of photoreduction (unpublished data) under the conditions we used, and so 5 minutes was chosen as the uniform time for photoreduction of PFL-AE. This photoreduction puts PFL-AE into its catalytically active $[4Fe\text{-}4S]^+$ state, which is then assayed for its ability to activate PFL. These PFL-AE activity assays showed that K^+ (54.2 ± 1.5 U/mg) gave the highest specific activity (Figure 7.5 and Table 7.6). PFL-AE was also activated by NH_4^+ (45.8 ± 3.9 U/mg) and Na^+ (38.0 ± 2.8 U/mg) although to a lesser extent than K^+. Rb^+ (14.6 ± 4.2 U/mg), Cs^+ (4.9 ± 2.2 U/mg), and Li^+ (12.2 ± 2.4 U/mg) provided yet lower activity. All of these monovalent cations with the exception of Cs^+, however, stimulated PFL-AE activity above that for enzyme lacking any simple monovalent cation (M^+-free PFL-AE, 5.1 ± 1.0 U/mg). Divalent cations (Ca^{2+}, Mg^{2+}, Zn^{2+}) proved to be inhibitory, with PFL-AE activities being below the very low activity observed for M^+-free PFL-AE (Figure 7.5 and Table 7.6).

In order to provide insight into the affinity of the monovalent cation for its site in the PFL-AE active site, we assayed PFL-AE in a range of potassium ion concentrations. The PFL-AE specific activity increased with increasing K^+ concentrations up to 100 mM. The PFL-AE activity plateaued at 100 mM K^+ and then began to decline at concentrations greater than 200 mM (Figure 7.6). These results provided a K_m of 44.0 $\pm$ 10.5 mM for K^+. *In vivo* K^+ concentrations in *E. coli* have been determined to be between 77 mM and 115 mM [28-30] with the ion content increasing during the cell cycle [29]. Maximal activity in PFL-AE falls within this range.

Effect of Cations on the Electronic Structure of PFL-AE

The proximity of the monovalent cation site to the [4Fe-4S] cluster suggests the cation can affect the electronic structure of the active site of PFL-AE. This perturbation was investigated using electron paramagnetic resonance (EPR) spectroscopy of PFL-AE in the presence of the monovalent and divalent cations used in the activity assays, and with and without SAM. The presence and identity of the cation alters the g-values and line shapes of the signal arising from the $[4Fe\text{-}4S]^+$ cluster in the absence of SAM (Figure SI.7.1). The most significant changes are seen in the presence of Na^+ and NH_4^+, whereas the other monovalent cations have features similar to the M^+-free samples albeit with some line broadening.

As has been previously shown [8,31], the addition of SAM to PFL-AE causes a change in line shape, a shift in g values, and an intensification of the $[4Fe\text{-}4S]^+$ EPR signal. The effects of the monovalent cation on the EPR signal are more prominent in the

presence of SAM as well (Figure 7.7). The EPR signals for M^+-free PFL-AE in the absence of SAM and for all the PFL-AE samples in the presence of different monovalent cations and SAM were simulated using two different spin systems. The g values obtained for one spin system of the PFL-AE samples in the presence of different monovalent cations and SAM (Table 7.7) are similar to the previously reported g values (g = 2.01, 1.89, and 1.88) [8,31]. The second spin system has different g values (Table 7.7) than those previously reported. In general, the g values for the samples prepared with each monovalent cation (and lack of cation) are similar to each other with variability in the percent of the two spin systems.

EPR spectra of PFL-AE in the presence of the Ca^{2+}, Mg^{2+}, and Zn^{2+} were essentially identical to those for the M^+-free PFL-AE (Figure SI.7.2). Even with the addition of SAM, the spectra look almost identical to the M^+-free signal with SAM (Figure SI.7.3), suggesting the divalent cations do not affect SAM binding with the [4Fe-4S] cluster.

To further analyze how different cations affect the active site in PFL-AE, circular dichroism (CD) spectroscopy in the visible region was performed on the M^+-free purified protein in the presence and absence of different monovalent cations and SAM. CD spectroscopy in the visible region is used to analyze d-d transitions of metals in chiral environments such as the [4Fe-4S] clusters in PFL-AE. In the absence of SAM, the CD spectrum of each monovalent cation looks similar to the M^+-free spectrum (Figure SI.7.4). On the other hand, when SAM is present, new spectral features appear in the

presence of K^+, NH_4^+, Rb^+, and Na^+ (Figure 7.8). The most prominent features emerge at approximately 400 nm and 500 nm.

Because there was a change observed at 400 nm and 500 nm with the addition of SAM and these monovalent cations, K^+ was titrated into a solution containing PFL-AE and SAM. The features at approximately 355 nm, 400 nm, and 500 nm grew in with the addition of K^+ (Figure 7.9). These features plateaued after 50 mM KCl and then the intensity dropped off drastically after approximately 177 mM KCl. Using the results up to 177 mM (before inhibition was observed), a K_D was determined to be 7.6 $\pm$ 1.2 mM at 407 nm (Figure 7.9).

Altering the Cation Binding Site

To further investigate the cation binding site in PFL-AE, the two conserved aspartate (D104 and D129) residues were changed to alanine (D104A and D129A, respectively). Activity assays in the presence of 100 mM KCl revealed that the D104A PFL-AE variant had very low activity (5.5 $\pm$ 0.2 U/mg), similar to M^+-free PFL-AE. The D129A PFL-AE, on the other hand, had significant enzymatic activity (42.7 $\pm$ 3.4 U/mg), albeit with lower activity than wild type PFL-AE in the presence of K^+.

EPR analysis of these two variants suggests D104A is required for cation binding. The presence of any of the monovalent cations had little effect on the EPR signals for $[4Fe\text{-}4S]^+$-PFL-AE or $[4Fe\text{-}4S]^+$-PFL-AE-SAM, with the EPR spectra in all cases looking very similar to the buffer exchanged M^+-free D104A variant (Figure 7.10). The lack of any effect due to addition of cation for the D104A variant was supported by the results of simulations of these EPR signals: similar g-values for M^+-free D104A and M^+-free WT in

all cases (Table 7.8 and Table 7.9). The slight differences between these variant spectra and those of WT are most likely due to minor active site alterations due to changing the highly conserved amino acid. The EPR signal observed for D104A in the presence of SAM is similar to D104A M^+-free in the absence of SAM, suggesting SAM is not binding appreciably in this variant (Table 7.9).

The D129A PFL-AE, on the other hand, shows significant perturbations of the $[4Fe\text{-}4S]^+$ signal in the presence of K^+ and Na^+ compared to M^+-free D129A (Figure 7.11a). The spectra were best simulated by including a third component that might be attributed to an alternate positioning of the cation when this aspartate is absent (Table 7.8). In the presence of SAM, the D129A variants show cation-dependent EPR spectra that are similar to those of WT (Figure 7.11b). The EPR g-values for D129A with SAM are also very similar to those of WT in the presence of each of the monovalent cations (Table 7.9).

Discussion

PFL-AE contains a monovalent cation in its active site which is in close proximity to 5 oxygens: two carboxylate oxygens from conserved aspartate residues (D104 and D129), two backbone carbonyls from T105 and M127, and one carboxyl oxygen of SAM. In the crystal structure of PFL-AE, the cation binding site is located at the back of the active site against the barrel. While M^+ sites usually occur where there is no secondary structure, all four of the residues mentioned above are part of the beta strands forming the inside of the TIM barrel. The interactions of the monovalent cation with amino acid

residues and SAM may help the protein to achieve a conformation not available in aqueous solutions alone, and/or to orient SAM into a more favorable position in preparation for homolytic cleavage.

The proximity of the monovalent cation to the cluster and SAM suggests that its presence and identity would have an effect on PFL-AE activity. When coupled enzyme activity assays were performed on PFL-AE in the presence of different monovalent and divalent cations, it was discovered that PFL-AE activity was highest in the presence of the K^+ ion. Like most enzymes that have higher activity with K^+, activity decreased in the presence of smaller cations such as Li^+ and Na^+ and had slightly lower activity in the presence of the larger cation NH_4^+. The largest cations tested, Cs^+ and Rb^+, resulted in a much lower activity.

Since K^+ exhibited the highest activity of the monovalent cations tested, we analyzed its concentration dependence on PFL-AE activity. Many K^+ activated enzymes reach their maximum activity around 100 mM K^+ or lower concentrations [32,33]. In this study, PFL-AE activity was monitored between 0 and 500 mM KCl. PFL-AE activity was found to increase with increasing concentration of K^+ up to 100 mM, after which activity gradually decreased. An earlier study carried out by Wong *et al*. found K^+-dependence on PFL-AE activity, however their low iron content (~1 Fe per protein) and high concentrations of KCl (100 – 160 mM) used likely obscured the effects we report here [34]. Potassium is generally the most prominent monovalent cation *in vivo* with concentrations ranging from approximately 77-115 mM in the *E. coli* cells, where PFL-AE is naturally found [28-30]. Given that K^+ provides the highest PFL-AE activity

and is also present at significant concentrations in bacterial cells, we propose that K^+ is the dominant activating cation in PFL-AE *in vivo*.

Activity was inhibited in the presence of the divalent cations Ca^{2+}, Mg^{2+}, and Zn^{2+}. For Ca^{2+}, slight activity was observed but it was still lower than M^+-free activity. This small amount of activity could be due to the presence of sodium pyruvate instead of oxamate. In the activity assays, oxamate (a pyruvate analogue) is added to the activation mix to allow for glycyl radical formation on PFL. Oxamate is insoluble in the presence of calcium and thus sodium pyruvate was substituted during PFL-AE activation. The small amount of sodium (10 mM sodium pyruvate) may have caused the apparent activity in the presence of Ca^{2+}. However, the nature of the divalent cation inhibitor effect is still not understood. EPR results of PFL-AE in the presence of these divalent cations are identical to the M^+-free protein suggesting the divalent cation cannot enter the cation site; however, the Zn^{2+} and Mg^{2+} ions have ionic radii similar to that of Li^+. In the presence of Li^+, PFL-AE exhibited very little spectral changes in the presence and absence of SAM. From the EPR results, we cannot conclude whether these divalent cations can occupy the cation site. The divalent cations presumably do not alter SAM binding since the EPR spectrum in the presence of divalent cation and SAM is identical to M^+-free PFL-AE with SAM.

Mutation of the two aspartate ligands to alanine resulted in a dramatic reduction of activity for the D104A variant while only a modest decrease in activity for the D129A variant was observed. The EPR analysis of the two aspartate variants suggest that D104 is required for cation binding while D129 plays a less critical role. The D104A variant

shows little perturbation of the EPR signal in the presence of different cations and, unlike WT, the signal does not intensify or have significant changes in the presence of SAM, suggesting that in the absence of cation, SAM cannot bind as effectively. In contrast, EPR spectral studies of the D129A variant indicate that the monovalent cations bind, and SAM coordinates in a manner similar to that of the WT.

Given the location of the cation within the active site, it is plausible that the identity of the cation would influence the electronic structure of the [4Fe-4S] cluster. The perturbation of the EPR signals observed in the presence of the different monovalent cations suggests that the identity of the monovalent cation does have an effect on the active site. Changes in the signal can be seen with each monovalent cation with the most significant changes observed in the presence of SAM. These differences in the EPR signal are presumably a result of the slightly different conformation of the active site adopted by PFL-AE due to slight conformational changes in the protein amino acids and SAM to accommodate the change in ionic radius of the monovalent cation.

Simulations of both the EPR signal of PFL-AE/SAM in the presence of the monovalent cations and that of M^+-free PFL-AE in the absence of SAM revealed that the signals contain two spin systems. The two spins for the "no SAM" sample are most likely due to some population of PFL-AE having water bound to the unique Fe (as seen previously in PFL-AE [8,31]) and some having no water bound and perhaps DTT bound to the cluster. For the samples containing SAM, the two spin systems are very similar for the different monovalent cations with only the percentage of each spin system changing. Spin system one has different g values than the "no SAM" signal while spin system two

has very similar g values (g_2 and g_3) to the spin system two of the "no SAM," M^+-free signal (Table 7.7). The two systems for the "+ SAM" simulation could be due to some of the PFL-AE population with SAM bound to the cluster and some without SAM bound. This is supported by the second spin system's similarities to the M^+-free, no SAM sample.

In the presence of SAM, the CD results revealed the most spectral changes when PFL-AE is prepared in K^+, NH_4^+, Rb^+, and Na^+ compared to M^+-free conditions. Since the monovalent cations induce little change in the CD spectra in the absence of SAM, CD results support that the binding of these cations is stabilized by SAM. The CD results correlate with specific activity: the greatest change in the CD spectrum is in the presence of K^+ and NH_4^+ which give the highest specific activity, followed by Rb^+, which stimulates activity in PFL-AE but to a lesser extent than K^+.

Activation of an enzyme by M^+ is not accomplished through regulation, as concentrations of Na^+ and K^+ are both tightly controlled within a cell [35]. Instead, the M^+ cation assists in catalysis by altering the energies of the ground and/or transition states [25]. This can occur when the M^+ ion is used to directly interact with the substrate or when M^+ binding to the enzyme triggers conformation changes. These two different effects are used to separate enzymes activated by M^+ (such as Na^+ or K^+) into two types, cofactor-like (type I) and allosteric (type II) [25]. In type I enzymes, the M^+ is absolutely required for enzyme activity, and helps to anchor the substrate in the active site, often acting in tandem with a divalent cation. In type II enzymes, no direct M^+ to substrate binding occurs and conformational changes are elicited which enhance enzyme activity;

in this case the M^+ is not absolutely required for activity or substrate binding. For example, in the type I enzyme diol dehydratase, a coenzyme B_{12}-dependent enzyme, the catalytically essential K^+ [36] is coordinated by five protein ligands, draws in the substrate through interactions with two of its hydroxyl oxygens, and as such is essential to substrate binding [37]. Aminoimidazole riboside kinase is a type II activated enzyme and the binding of K^+ is proposed to alter the conformation of the backbone residues 252-255 [38]. The alteration would position the catalytic D255 in a manner that would allow it to interact with the phosphate moiety of the nucleotide, thus enabling phosphorylation of the substrate aminoimidazole riboside [38]. For K^+ activated enzymes, NH_4^+ and Rb^+ can also generally activate as well, but the smaller Na^+ and Li^+ cations or the larger Cs^+ cations are not effective activators. In contrast, Na^+ activated enzymes are not activated as well by any of the larger cations (K^+, Rb^+, and Cs^+) nor the smaller Li^+ cation [39]. In this work, we show that PFL-AE activity is activated by K^+ and to a lesser extent by NH_4^+ and Na^+, while other monovalent cations provide very little activity enhancement. From the evidence presented here it is difficult to categorize PFL-AE as a type I or II M^+-activated enzyme. The location of the monovalent cation in the active site (Figure 7.12) and its interaction with SAM would suggest that PFL-AE is a type I M^+ activated enzyme. However, the cation has no interactions with PFL, the other substrate of PFL-AE, and PFL-AE still shows slight activity when purified in the absence of a monovalent cation, indicating that the cation is not absolutely required for activity but instead only acts to stimulate activity. Both of these observations would place PFL-AE in the type II M^+ category. Although, this conclusion is under the assumption that the assay is

completely salt free. Precautions were performed to eliminate any M^+ contamination. Glassware was acid washed to remove any M^+ prior to use. If available, acid-free substances were purchased; however, pyruvic acid is only available as a sodium salt. Pyruvate is only added to the coupling solution containing the substrates for PFL and presumably when the activation solution, containing PFL-AE and activated PFL, is mixed with the coupling solution, all the PFL has been activated. Any trace amounts of sodium in the coupling solution should not have an effect on the ability of PFL-AE to activate PFL. Although PFL-AE cannot be classified at this point, the experimental data presented here show the large impact that a monovalent cation has on PFL-AE catalysis.

With the cation positioned in the active site in such close proximity to the Fe-S cluster and with an interaction between itself and an oxygen of SAM, it is not surprising that the activity is affected by the identity and concentration of the cation, nor is it unexpected that the cation also affects the electronic structure of the active site. How the cation is able to accomplish this is still not completely understood. It does appear to bring some stability to PFL-AE. After multiple freeze-thaw cycles, the activity for the M^+-free PFL-AE decreases, possibly suggesting loss of structure or loss of its [4Fe-4S] cluster (data not shown). Normal purification methods in our laboratory involve the presence of NaCl, and under these conditions, PFL-AE is more stable and can undergo multiple freeze-thaw events. The interaction of the cation with SAM may also be relevant to the activity perhaps by correctly positioning SAM in the active site. The cation is only about 2.4 Å from the carboxyl moiety of SAM which could help stabilize SAM in the active site.

Of the radical SAM enzymes structurally characterized to date, PFL-AE is the only one that has been observed to contain a monovalent cation in its active site; it is also the only one for which the effect of the monovalent cation on activity has been explored. Recently, the activity for the radical SAM enzyme 7-carboxy-7-deazaguanine synthase (QueE) was found to have dependence on Mg^{2+} and a crystal structure was solved with Mg^{2+} in the active site [40,41]. In the presence of Mg^{2+}, QueE had about an 11-fold increase in activity compared to absence of cation [41]. The Mg^{2+} site could be replaced via crystal soaks with either Na^{+} or Mn^{2+}, however neither stimulated activity [40]. Unlike PFL-AE, the metal ion coordination site in QueE does not involve four amino acids and SAM; rather, the Mg^{2+} is pseudo-octahedral with coordination by three water molecules, substrate carbonyl and carboxylate oxygens, and a hydroxyl of a threonine amino acid. Upon substitution with Na^{+}, the carbonyl coordination is lost. With substitution by Mn^{2+}, a water ligand is lost and replaced with a nitrogen ligand of substrate [40]. These three crystal structures of QueE could shed some light on the differences in activity and EPR signal in PFL-AE. In the presence of Na^{+}, the substrate carbonyl moves about 0.5 Å away from the cation site in comparison to the Mg^{2+} structure. In the Na^{+} structure, a movement of ~45º is found in the C4a-N5-C6-C angle when compared to the Mg^{2+} and Mn^{2+} structures. This could be due to the larger size of Na^{+} (102 pm for Na^{+} versus 72 pm for Mg^{2+} and 67 pm for Mn^{2+}) pushing the substrate away. In PFL-AE, substitution to a smaller cation could pull SAM away from the cluster while the larger cations could be pushing SAM closer to the cluster thereby affecting activity and its EPR signal.

Although no monovalent cation has been shown to cause an effect on the activity of other radical SAM enzymes, alignment of PFL-AE with other radical SAM enzymes including other activating enzymes and other enzymes with differing substrate size, revealed possible cation sites only in other activating enzymes (Figure 7.13). The other glycyl radical enzyme activating enzymes (GRE-AE) contain a highly conserved motif similar to the $DTX_{21}MXD$ binding motif in PFL-AE with a varying stretch of X = 18-21 in the other activating enzymes and replacement of a glutamate for D104. RNR-AE has a larger stretch with X = 26 but both aspartates are conserved in RNR-AE. The methionine and threonine in PFL-AE interact with the cation through backbone carbonyls, so variability can be expected. Interestingly, all of the activating enzymes (except RNR-AE) contain a threonine in the same position as the threonine in PFL-AE. Since no crystal structure has been solved for other activating enzymes, we can only speculate that the conserved residues are involved in cation binding. Further analysis of these radical SAM enzymes will conclude whether the cation site is unique to PFL-AE. Whether a monovalent cation site is unique to PFL-AE, the enhancement of a monovalent cation on the activity of PFL-AE and its effects on the electronics of the cluster is very remarkable for a radical SAM enzyme.

Acknowledgements

The authors would like the thank Eric Shepard for help obtaining and providing valuable insight into EPR data. Research on PFL-AE is supported by the National Institutes of Health grant GM54608.

Figures

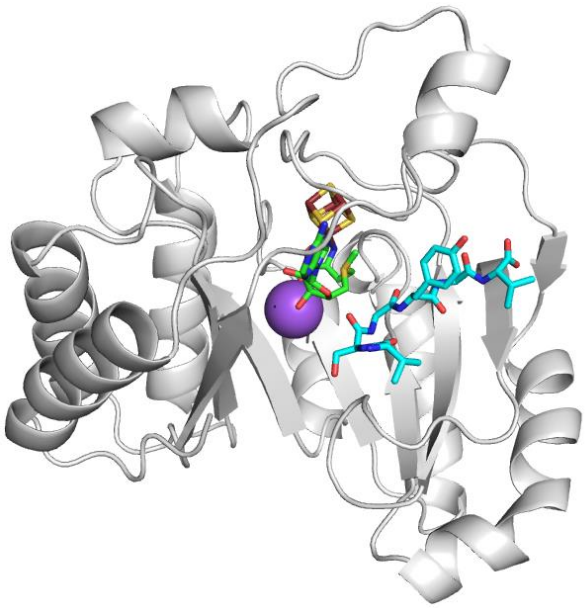


Figure 7.1. Location of the putative metal site in the peptide-bound PFL-AE model. The protein chain is shown in grey cartoon representation with the [4Fe-4S] cluster, SAM and peptide substrate mimic displayed as sticks. The modeled sodium ion is shown in sphere representation. Atom types are colored as follows: oxygen, red; nitrogen, blue; sulfur, yellow; iron, ruby; sodium, purple; SAM carbons, green; 7-mer peptide of PFL carbons, teal.

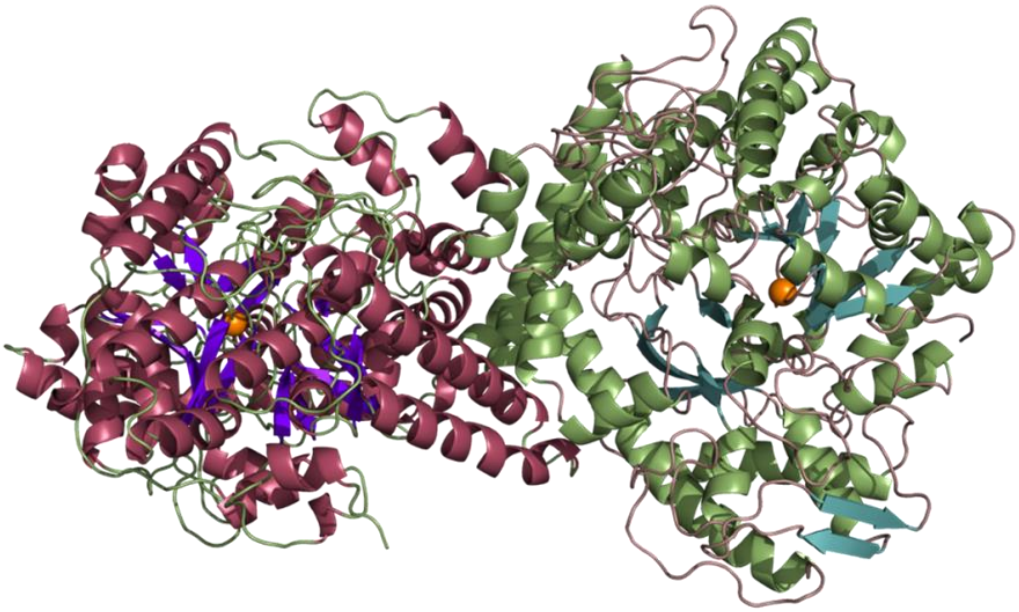


Figure 7.2. The PFL crystal structure with one monomer shown in purple and the other in green. Glycine 734, which harbors the glycyl radical, is shown as an orange sphere and is buried within the active site near the center of the 10 stranded α/β barrel. Also in the active site near Gly734 on an opposing finger loop are the two catalytic cysteine residues, Cys418 and Cys419. The distance between Gly734 Cα and Cys419 Sγ is 3.7 Å.

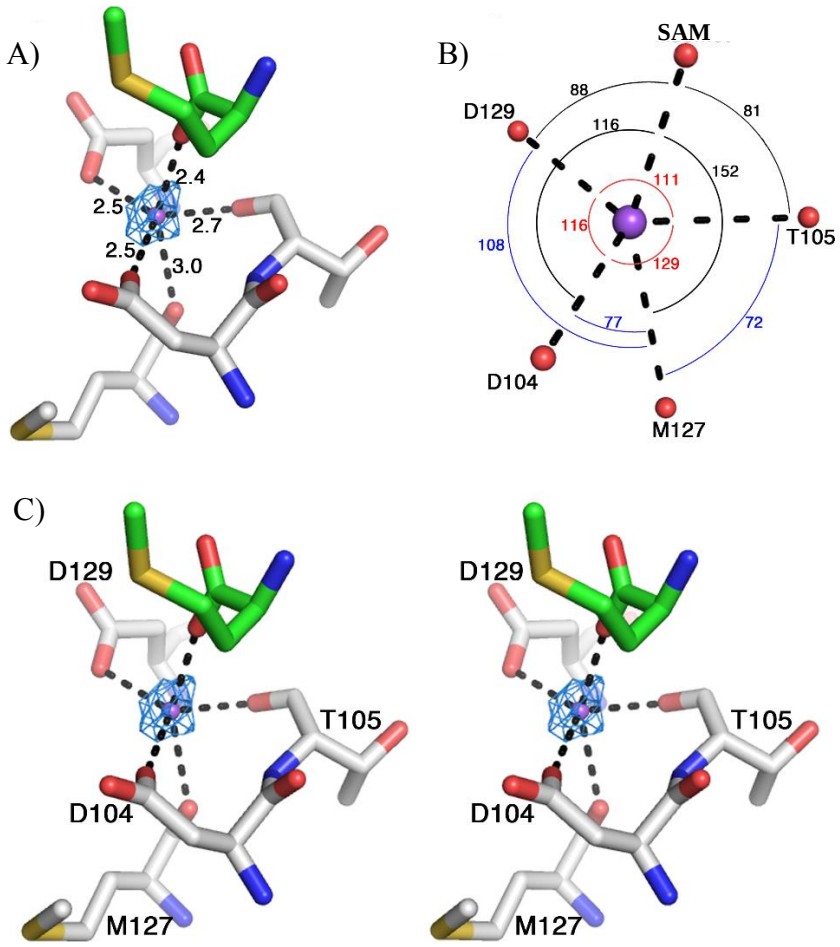


Figure 7.3. Putative metal site with sodium modeled (purple sphere). Protein amino acids are shown in grey while a portion of SAM is shown in green. (A) Refined distances to sodium. (B) Angles between metal ligands. (C) Stereoview of the putative metal site with sodium modeled. The site is displayed in the same orientation and as described in Figure 7.. A $2F_o$-F_c electron density map is shown in panels (A) and (C) contoured at 0.75 σ and displayed as a blue mesh within 2 Å of the sodium ion.

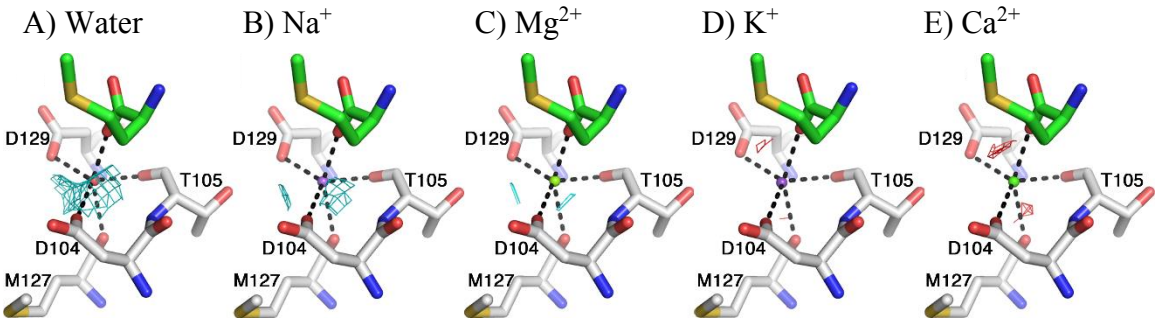


Figure 7.4. Refinement of different ions/molecules in the putative metal site. The site is shown with nearby protein residues (grey carbons) and a portion of SAM (green carbons) shown in stick representation with water (a) or a modeled sodium (b), magnesium (c), potassium (d), or calcium (e), which are shown as a sphere. The F_o-F_c difference electron density maps are shown contoured at 1.5 σ within 2 Å of the metal site. The map is shown as a mesh, with positive difference density in teal and negative difference density in red. Distances between the water or cation and the surrounding oxygen atoms are highlighted with dashed black lines.

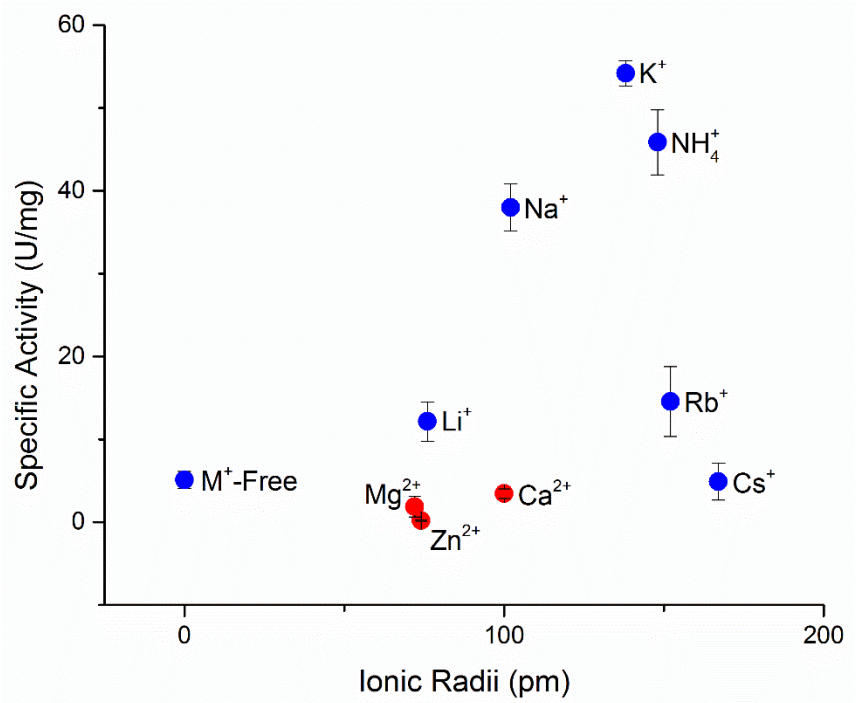


Figure 7.3. PFL-AE specific activity (U/mg) is influenced by the ionic radius of the cation present in the activity assay and thus the active site. Activity for monovalent cations (blue) stimulates PFL-AE activity while divalent cations (red) inhibit PFL-AE activity. For these assays, a concentration of 5 µM PFL, 0.05 µM PFL-AE, and 0.1 mM SAM in the presence of 100 mM of the specified monovalent cation or 1 mM of divalent cation was used. Data is the average of at least three different trials with each trial done in triplicate on one day. M^+-free is PFL-AE purified protein in the absence of any cation and no cation is added to the assay.

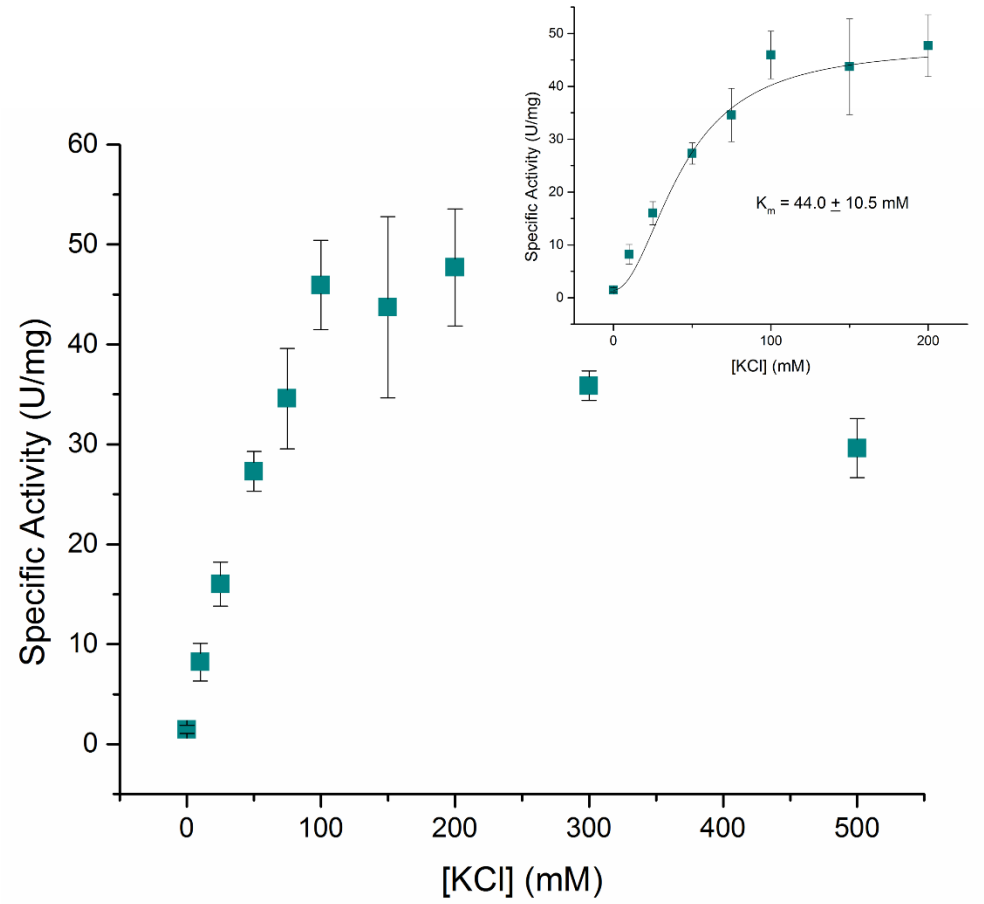


Figure 7.4. The effect of [K^+] on PFL-AE activity reported as specific activity (U/mg). The activity of PFL-AE increases with the increase in KCl concentration. A K_M of 44.0 ± 10.5 mM was calculated for KCl concentrations up to 200 mM. After 200 mM KCl, activity was inhibited and these values were not used for the calculations. For these assays, a concentration of 5 µM PFL, 0.05 µM PFL-AE, and 0.1 mM SAM was used. The ionic strength for each assay was maintained at 100 mM through the addition of choline chloride for conditions with 100 mM KCl or lower.

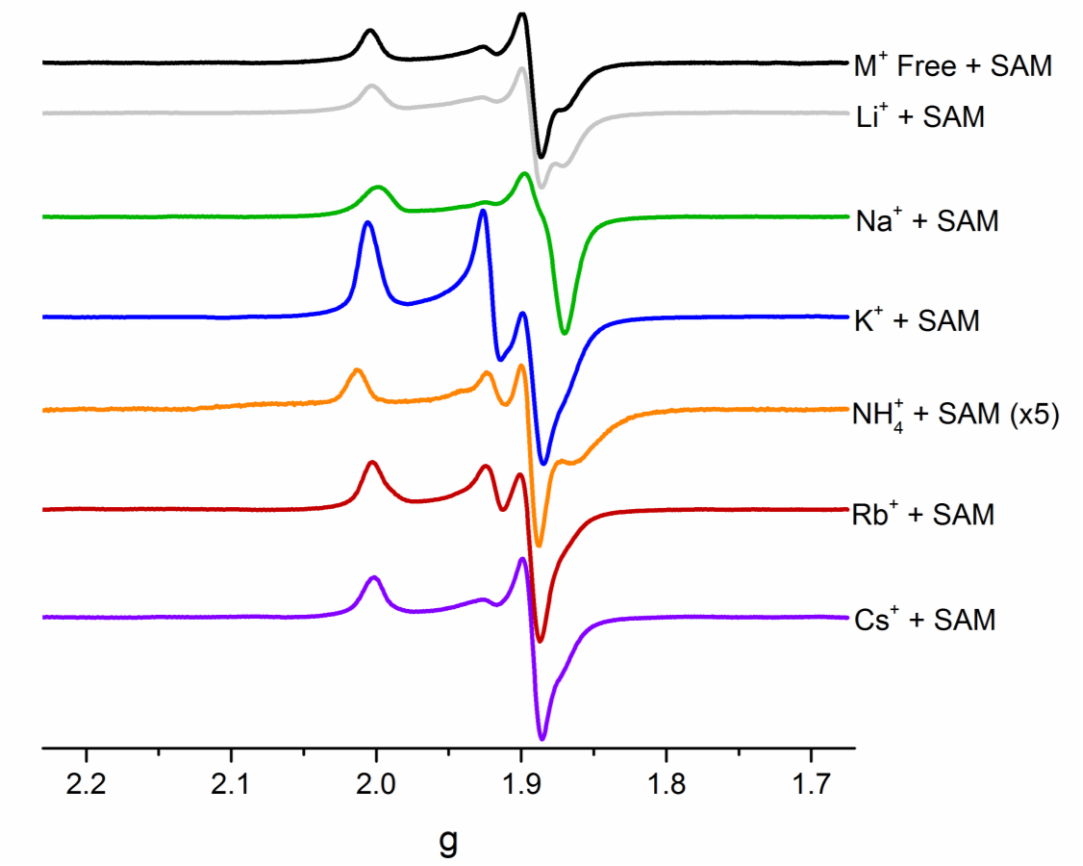


Figure 7.5. EPR spectra of PFL-AE in the presence of SAM and in the absence of M^+ (black) and in the presence of the different monovalent cations Li^+ (grey), Na^+ (green), K^+ (blue), NH_4^+ (orange), Rb^+ (red), and Cs^+(purple). Each sample contained 300 µM PFL-AE in the presence of 100 mM of the cation indicated and 2 mM SAM. EPR parameters: 12 K, 9.37 GHz, 1.0 mW.

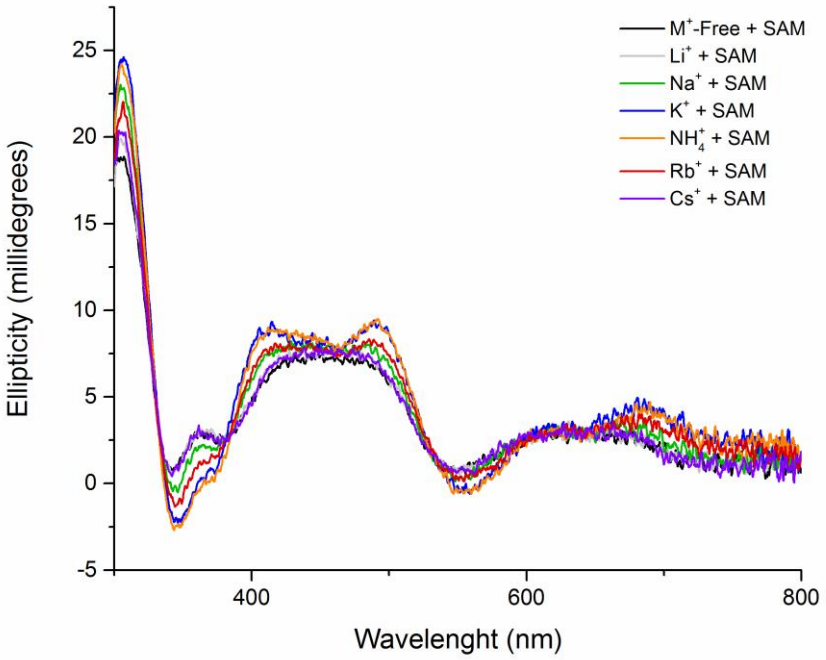


Figure 7.6. CD spectra of PFL-AE in the presence of different monovalent cations and SAM. Each sample contained 50 μM PFL-AE, 500 μM SAM, and 100 mM of the indicated cation: M^+-free (black), Li^+ (grey), Na^+ (green), K^+ (blue), NH_4^+ (orange), Rb^+ (red), and Cs^+ (purple).

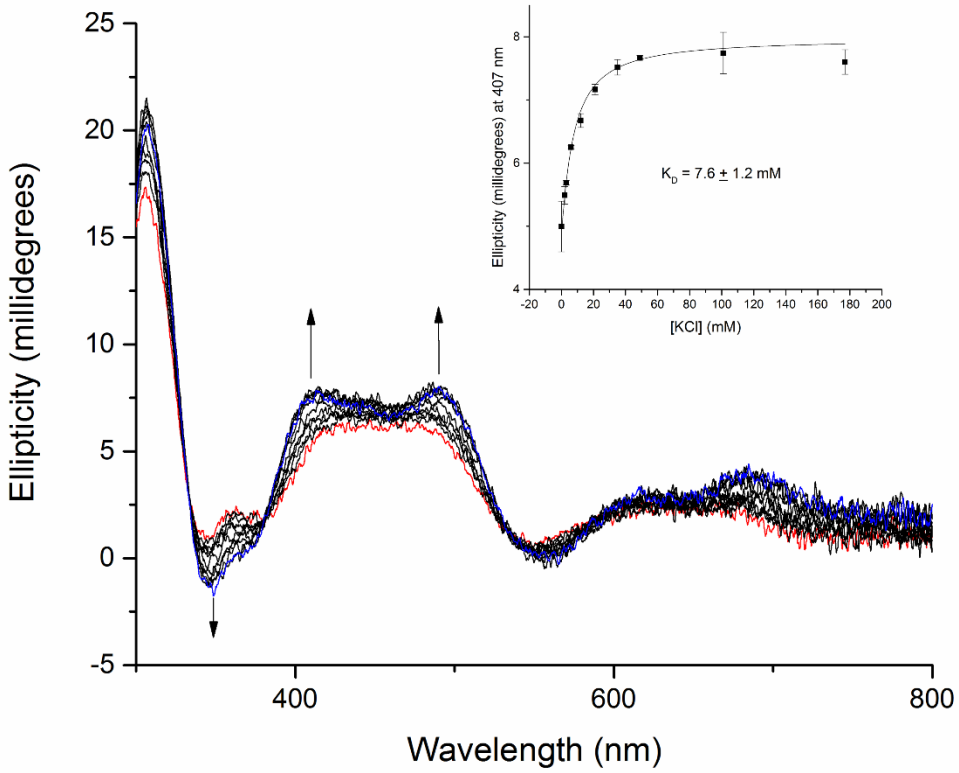


Figure 7.7. CD spectra of PFL-AE in the presence of SAM with KCl additions. KCl was titrated into 50 μM PFL-AE and 500 μM SAM from 0 mM KCl to 500 mM KCl final concentration. After 177 mM, the ellipticity sharply decreased and only the 0 mM KCl (red) to 177 mM KCl (blue) is shown for clarity and these values were used for a K_D determination of 7.6 ± 1.2 mM.

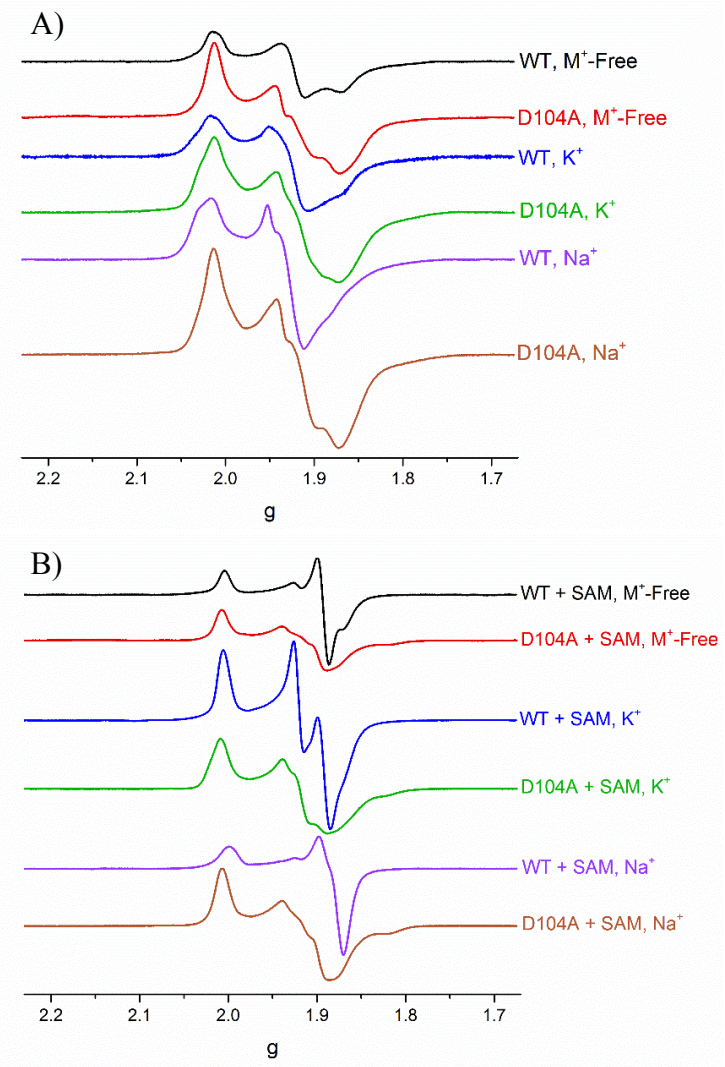


Figure 7.8. EPR spectra of the PFL-AE variant D104A and wild type (WT) PFL-AE in the absence (A) or presence (B) of SAM. WT and variant PFL-AE are shown in the absence of monovalent cation (M^+-free) or in the presence of K^+ or Na^+.

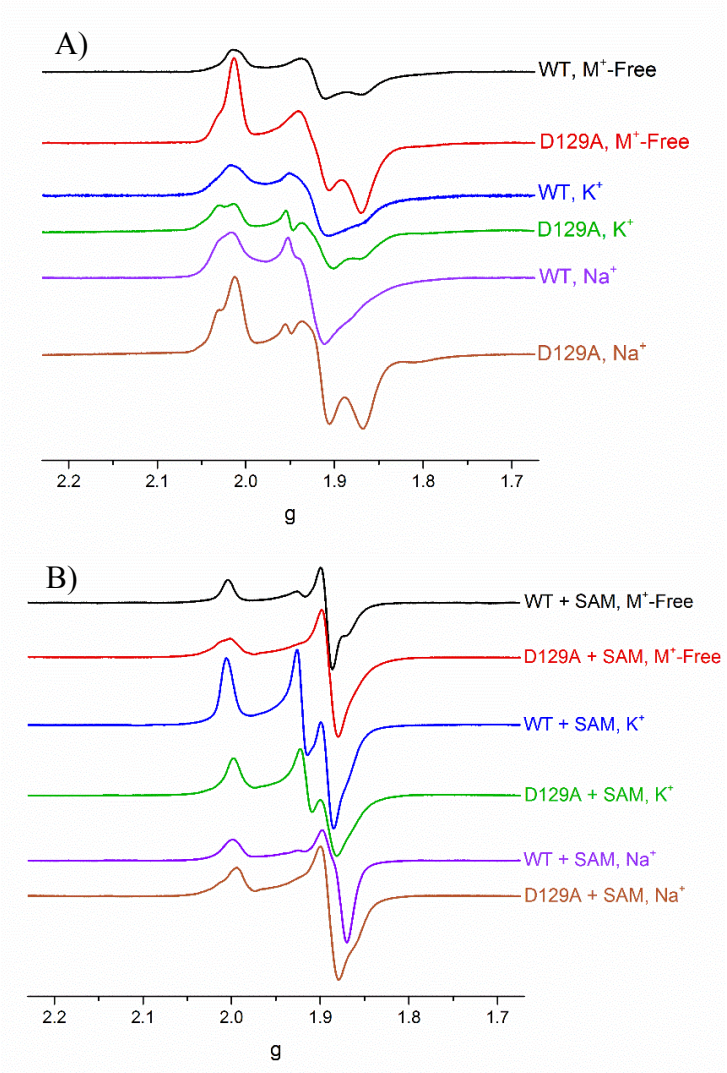


Figure 7.9. EPR spectra of the PFL-AE variant D129A and wild type (WT) PFL-AE in the absence (A) or presence (B) of SAM. WT and variant PFL-AE are shown in the absence of monovalent cation (M^+-free) or in the presence of K^+ or Na^+.

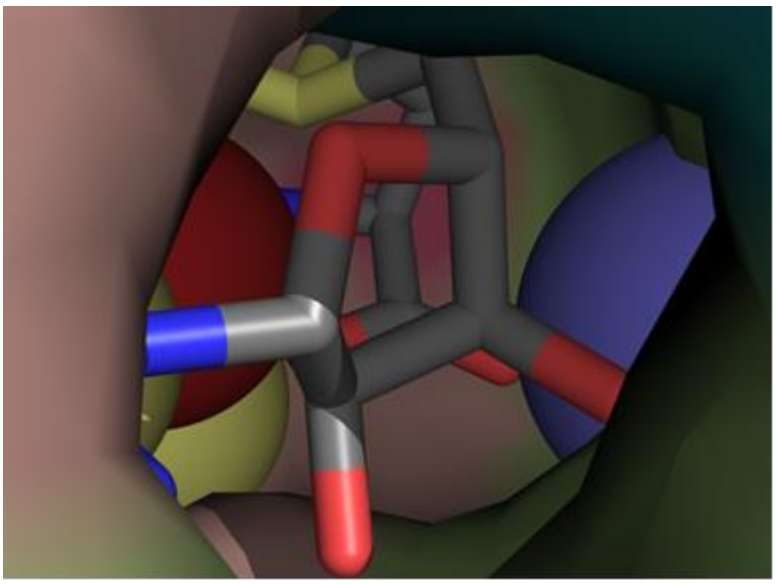


Figure 7.10. A surface representation of the PFL-AE active site as seen from the active site opening with the monovalent cation (shown as a purple sphere) projecting into the active site. Also shown is the interaction between the cation and the unbound carboxyl oxygen (red) of SAM (grey carbons) and the presence of the [4Fe-4S] cluster (red and yellow spheres).

```
PFL-AE        GGVTASGGE-AIL--------QAEFVR------DWFRACKKEGI-----HTCLDTNGFVR 111
RNR-AE        QGISLSGGD-PLH--------PQNVPDILKLVKRIRAECPDKDI-----AECPDKDIWVW 109
Bss-AE        GGVTISGGD-PLY--------FPDFTR------QLASELHARGV-----HVAIETSCFPK 171
Hpd-AE        GGVTFSGGE-PLL--------QHEFLH------EVLLKCHEVNI-----HTAIETSACVS 176
GD-AE         GGITLSGGE-VLL--------QPDFAV------ELLKECKSYGW-----HTAIETAMYVN 168
anSMEcpe      CSFAFQGGE-PTL--------AGL-EFFEK----LMELQRKHNYKNLKIYNSLQTNGTLI 104
MoaA          KKIRITGGE-PLM--------RRDLDVL------IAKLNQIDGIED----IGLTTNGLLL 108
RlmN          NVVMMGMGE-PLL--------NLNNVVP-----AMEIMLDDFGFGLSKRRVTLSTSGVVP 217
LAM           RDVLLSGGD-ALL--------VSDETLEYII--AKLREIPHVEIV----RIGSRTPVVLP 208
HydE          KTIVLQSGE-DPY-------------YMPDVISDIVKEIKKMGVA-----VTL-SLGEWP 141
HydG          TRILLVMGE-EPE--------DKTLSYLEEIIPAIYSEVDIRRIN-------V-NIAPLT 189
BtrN          I-SFHFYGE-PLLCKNLDLFVGMTTEYIPRARPIIYTNGDFL-----------------T 117
BioB          TRFCMGAAWKNPH--------ERDMPYLEQ----MVQGVKAMGLE-----ACM-TLGTLS 158
SPL           --------YINER--------APEITRFE---------------A-----AC-------- 167
viperin       EKINFSGGE-PFL--------QDRGEYLGK----LVRFCKV---ELRLPSVSIVSNGSLI 161

PFL-AE        R-YDPVIDE-LLEVTDLV---MLDLKQMNDEIHQN--LVG--V----SNHRTLE---FAK 156
RNR-AE        TGYKLDDLNAAQMQVVDLINVLVDGKFVQDLKDPSLIWRG--S----SNQVV-H---HLR 154
Bss-AE        Q--GKVVES-MIGIVDLF---IVDLKTLDAHKHLD--VIG--W----PLAPILA---NLE 215
Hpd-AE        N---EVFNK-IFKDIDFA---FIDIKHMDREKHKE--QTG--V----YNDLILE---NIS 219
GD-AE         S---ESVKK-VIPYIDLA---MIDIKSMNDEIHRK--FTG--V----SNEIILQ---NIK 211
anSMEcpe      D---ESWAKFLSENKFLV---GLSMDGPK--EIH---NLNRKD---CCGLDTFS---KVE 148
MoaA          K---KHGQKLYDAGLRRI---NVSLDAIDDTLFQ---SINNRN---IKATTILE---QID 154
RlmN          A-----LDK-LGDMIDVA--LAISLHAPNDEIRDEIVPINKKYNIETFLAAVRR---YLE 267
LAM           Q---RITPE-LVNM--------------LKKYHP--VWLNTHF--NHPNEITEESTRACQ 247
HydE          REYYEKWKE---AGADRY---LLRHETAN-------------------------------- 164
HydG          LKGYERLKK---LKIGTY---QLFQESYN-------------------------------- 212
BtrN          EKRLQTLTE---LGIQKF---IVTQHAGA-------------------------------- 140
BioB          ESQAQRLAN---AGLDYY---NHNLDTSP-----E--FYGNIIT-----T---------- 190
SPL           -----TSDI---VGIDHL---THSLKKAI-----E--FIGATDYGRLRFVTKYE---HVD 207
viperin       R---ERWFQNYGEYLDIL---AISCDSFDEEVNV---LIGRGQ----GKKNHVE---NLQ 206
```

Figure 7.11. Sequence alignment of PFL-AE and other activating enzymes and radical SAM enzymes. The $DTX_{21}MXD$ in PFL-AE is highlighted in green along with the other conserved residues in this motif. Conserved changes are highlighted in cyan. Alignments were done using Clustal Omega.

Tables

Table 7.1. B-factor comparison after previous refinement in CNS.

	Species modeled in the site	
	Water	**Sodium**
R_{work} / R_{free} values	22.96/25.53	22.91/25.42
B-factors (Å^2)*		
Species modeled	51.35	62.54
D104 carboxylate O	74.88	75.28
T105 carbonyl O	66.10	66.12
D129 carboxylate O	71.20	71.50
SAM carboxylate O	65.59	65.36
Average of nearby atoms	69.44	69.57

*When occupancies are set at 100%.

Table 7.2. B-factor comparison after refinement in REFMAC.

	Species modeled in the site				
	Water	**Sodium**	**Magnesium**	**Potassium**	**Calcium**
R_{work} / R_{free} values	19.46/25.15	19.47/25.14	19.45/25.10	19.45/25.13	19.46/25.22
B-factors (Å^2)*					
Species modeled	54.46	68.83	70.7	93.78	95.36
D104 carboxylate O	78.22	78.51	78.43	76.34	76.92
T105 carbonyl O	74.81	74.94	74.87	74.67	74.80
D129 carboxylate O	78.58	78.79	78.91	78.15	78.73
SAM carboxylate O	71.09	71.63	72.18	72.78	73.06
Average of nearby atoms	75.58	75.97	76.10	75.485	75.88

*When occupancies are set at 100%.

Table 7.3. B-factor and occupancy comparison after occupancy refinement in CNS.

Atom	Water	Sodium	Magnesium	Potassium	Calcium
B factor	78.74	78.66	78.68	78.74	78.75
Occupancy (%)	118	88	86	51	1.0

Table 7.4. Distances between sodium and nearby atoms.

Atom	Distance (Å)	Angle (to D104)	Angle (to T105)	Angle (to D129)	Angle (to SAM)	Angle (to T105N)	Angle (to M127)
D104 carboxylate O	2.5	n/a	129.42	116.12	116.42	72.58	77.03
T105 carbonyl O	2.7	129.42	n/a	111.42	81.15	57.40	72.62
D129 carboxylate O	2.5	116.12	111.42	n/a	87.52	165.07	108.29
SAM carboxylate O	2.4	116.42	81.15	87.52	n/a	99.51	152.84
T105 amine N	3.2	72.58	57.40	165.07	99.51	n/a	60.41
M127 carbonyl O	3.0	77.03	72.62	108.29	152.84	60.41	n/a

Table 7.5. Distances between modeled potassium and nearby atoms.

Atom	Distance (Å)	Angle (to D104)	Angle (to T105)	Angle (to D129)	Angle (to SAM)	Angle (to T105N)	Angle (to M127)
D104 carboxylate O	2.6	n/a	128.92	120.34	117.57	73.38	78.67
T105 carbonyl O	2.9	128.92	n/a	108.90	77.74	55.96	71.39
D129 carboxylate O	2.7	120.34	108.90	n/a	84.772	163.56	111.330
SAM carboxylate O	2.6	117.57	77.74	84.772	n/a	96.90	148.39
T105 amine N	3.3	73.38	55.96	163.56	96.90	n/a	60.09
M127 carbonyl O	3.1	78.67	71.39	111.330	148.39	60.09	n/a

Table 7.6. Specific activities of PFL-AE in the presence or absence of different monovalent and divalent cations.

Cation Present	Specific Activity (U/mg)
M^+-Free	5.1 ± 1.0
Li^+	12.2 ± 2.4
Na^+	38.0 ± 2.8
K^+	54.2 ± 1.5
NH_4^+	45.8 ± 3.9
Rb^+	14.6 ± 4.2
Cs^+	4.9 ± 2.2
Ca^{2+}	3.4 ± 0.6
Mg^{2+}	1.9 ± 1.2
Zn^{2+}	0.2 ± 0.1

Table 7.7. Simulated g values of PFL-AE in the absence of monovalent cation (M^+-free), absence of SAM (– SAM), presence of SAM (+ SAM), and the presence of different monovalent cations. The percentage of each spin system is given as a whole number.

Monovalent Cation Present	Spin 1				Spin 2				Spin 3			
	g_1	g_2	g_3	%	g_1	g_2	g_3	%	g_1	g_2	g_3	%
M^+-free - SAM	2.01	1.88	1.88	52	2.01	1.91	1.91	48				
M^+-free + SAM	2.00	1.89	1.87	69	2.00	1.91	1.89	31				
Li^+ + SAM	2.00	1.89	1.87	73	2.00	1.91	1.89	27				
Na^+ + SAM	2.00	1.88	1.87	86	2.00	1.91	1.89	14				
K^+ + SAM	2.00	1.89	1.88	68	2.00	1.91	1.90	32				
NH_4^+ + SAM	2.01	1.89	1.86	60	2.01	1.91	1.89	16	2.07	1.92	1.89	24
Rb^+ + SAM	2.00	1.89	1.88	79	2.00	1.91	1.91	21				
Cs^+ + SAM	2.00	1.89	1.88	82	2.00	1.91	1.92	18				

Table 7.8. Simulated g values of the WT PFL-AE (purple rows) and the D104A and D129A variants in the absence of a monovalent cation (M^+-free), presence of different monovalent cations, and absence of SAM.

	Spin 1				Spin 2				Spin 3			
	g_1	g_2	g_3	%	g_1	g_2	g_3	%	g_1	g_2	g_3	%
WT M^+-Free	2.01	1.88	1.88	52	2.01	1.92	1.91	48				
D104A M^+-Free	2.01	1.91	1.87	40	2.01	1.93	1.86	60				
D104A K^+	2.01	1.91	1.87	36	2.01	1.93	1.86	64				
D104A Na^+	2.01	1.91	1.87	44	2.01	1.93	1.86	56				
D129A M^+-Free	2.01	1.88	1.88	56	2.01	1.92	1.91	44				
D129A K^+	2.01	1.88	1.88	41	2.03	1.91	1.91	41	2.03	1.95	1.8	18
D129A Na^+	2.01	1.88	1.88	50	2.03	1.91	1.91	30	2.03	1.95	1.80	20

Table 7.9. Simulated g values of the WT PFL-AE (purple rows) and the D104A and D129A variants in the absence of a monovalent cation (M^+-free), presence of different monovalent cations and SAM.

	Spin 1				Spin 2			
	g_1	g_2	g_3	%	g_1	g_2	g_3	%
WT M^+-Free + SAM	2.00	1.89	1.87	69	2.00	1.92	1.89	31
D104A M^+-Free + SAM	2.01	1.89	1.89	47	2.00	1.93	1.82	53
D129A M^+-Free + SAM	2.00	1.89	1.86	74	2.02	1.90	1.88	26
WT K^+ + SAM	2.00	1.89	1.88	68	2.00	1.92	1.90	32
D104A K^+ + SAM	2.01	1.91	1.83	42	2.01	1.93	1.88	58
D129A K^+ + SAM	2.00	1.89	1.87	80	2.02	1.91	1.91	20
WT Na^+ + SAM	2.00	1.88	1.87	86	2.00	1.92	1.89	14
D104A Na^+ + SAM	2.01	1.91	1.87	58	2.01	1.93	1.86	42
D129A Na^+ + SAM	2.00	1.89	1.86	84	1.99	1.90	1.87	16

Supplementary Information

SI Figures

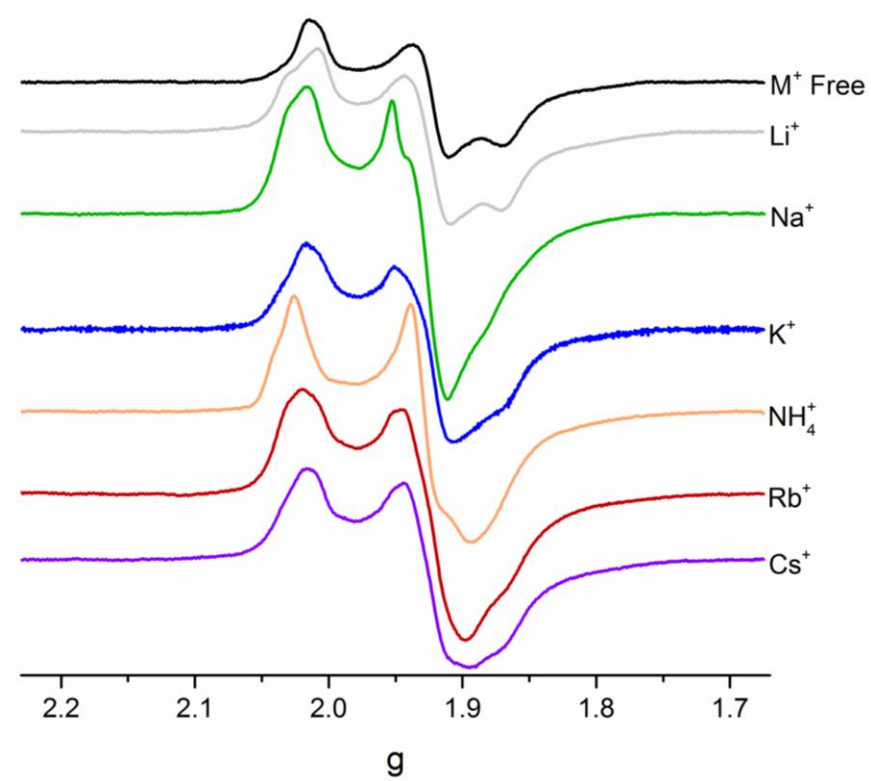


Figure SI.7.1. EPR spectra of PFL-AE in the absence (black) or presence of the different monovalent cations: Li^+ (grey), Na^+ (green), K^+ (blue), NH_4^+ (orange), Rb^+ (red), and Cs^+(purple). PFL-AE concentration is 300 μM and cation concentration is 100 mM. EPR parameters: 12 K, 9.37 GHz, 1.0 mW.

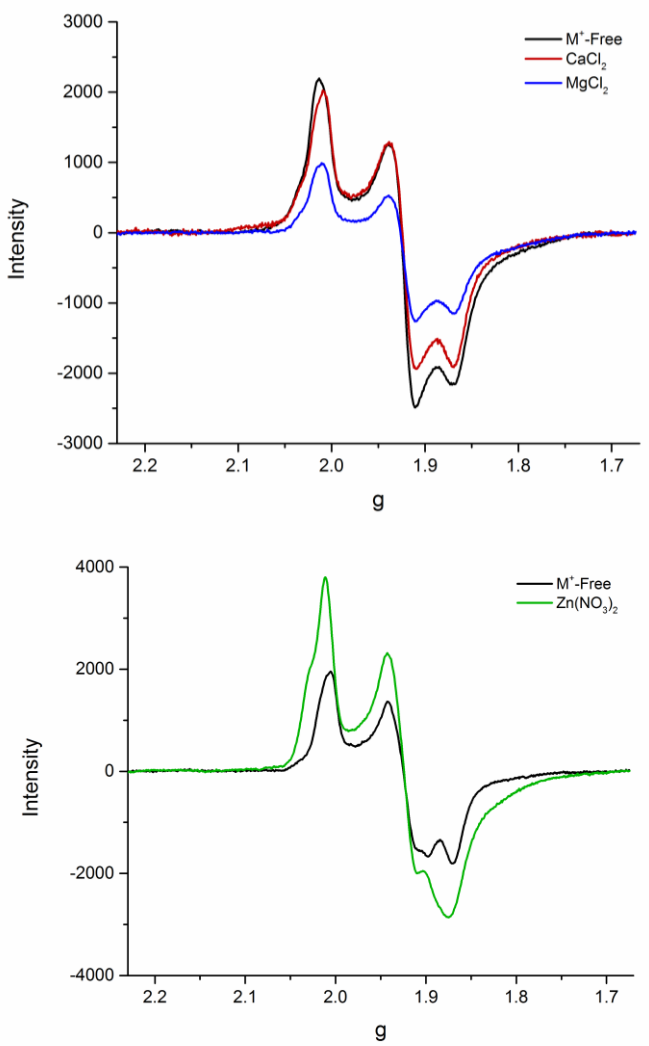


Figure SI.7.2. EPR spectra of PFL-AE (300 µM) in the absence of cation (black) and in the presence of 1 mM Ca^{2+} (red), Mg^{2+} (blue), or Zn^{2+} (green). Spectrum of PFL-AE in the presence of Zn^{2+} was conducted with a different stock protein (below) but still has similar features as the M^{+}-free PFL-AE. EPR parameters: 12 K, 9.37 GHz, 1.0 mW.

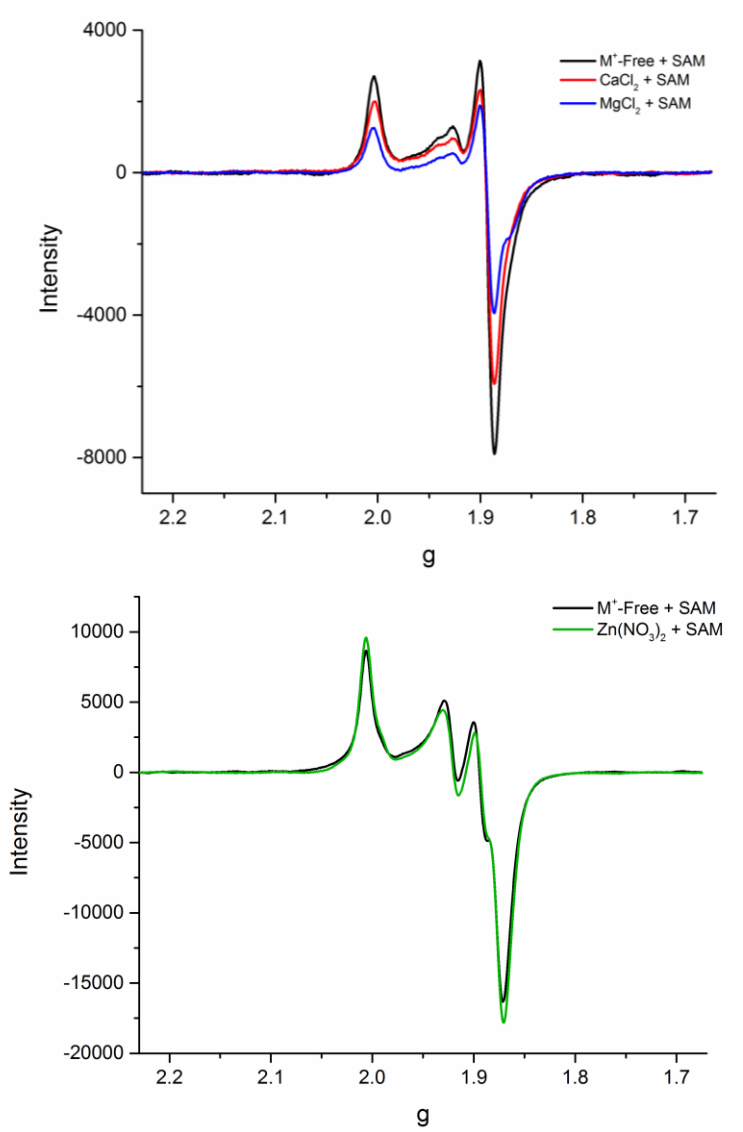


Figure SI.7.3. EPR spectra of PFL-AE (300 μM) in the absence of cation (black) and in the presence of 1 mM Ca^{2+} (red), Mg^{2+} (blue), or Zn^{2+}(green) and in the presence of 2 mM SAM. Spectra of PFL-AE in the presence of Zn^{2+} were conducted with a different stock protein (bottom) but still has similar features as the M^{+}-free PFL-AE + SAM. EPR parameters: 12 K, 9.37 GHz, 1.0 mW.

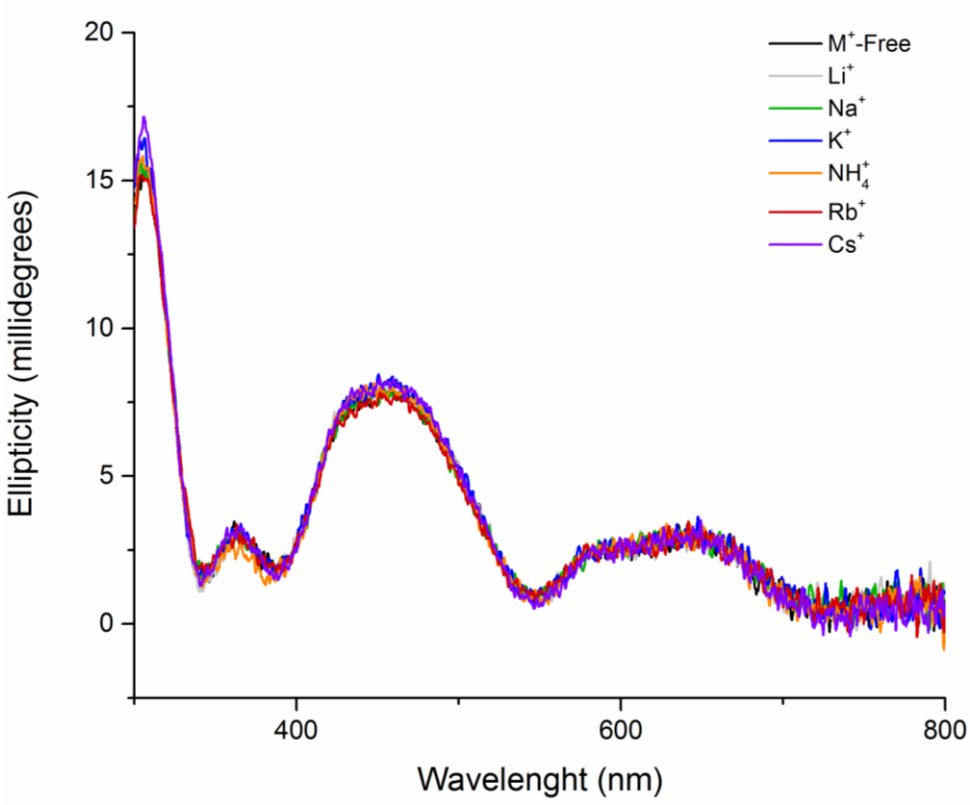


Figure SI.7.4. CD spectra of M^+-free PFL-AE in the absence (black) presence of different monovalent cations. Each sample contained 50 μM PFL-AE and 100 mM of the indicated cation: M^+-free (black), Li^+ (grey), Na^+ (green), K^+ (blue), NH_4^+ (orange), Rb^+ (red), and Cs^+ (purple).

References

1. Sofia, H. J.; Chen, G.; Hetzler, B. G.; Reyes-Spindola, J. F.; Miller, N. E. *Nucleic Acids Res.* **2001**, *29*, 1097-1106.

2. Frey, P. A.; Hegeman, A. D.; Ruzicka, F. J. *Crit. Rev. Biochem. Mol. Biol.* **2008**, *43*, 63-88.

3. Broderick, J. B.; Duffus, B. R.; Duschene, K. S.; Shepard, E. M. *Chem. Rev.* **2014**, *114*, 4229-4317.

4. Krebs, C.; Broderick, W. E.; Henshaw, T. F.; Broderick, J. B.; Huynh, B. *J. Am. Chem. Soc.* **2002**, *124*, 912-913.

5. Walsby, C. J.; Ortillo, D.; Broderick, W. E.; Broderick, J. B.; Hoffman, B. M. *J. Am. Chem. Soc.* **2002**, *124*, 11270-11271.

6. Knappe, J.; Neugebauer, F. A.; Blaschkowski, H. P.; Ganzler, M. *Proc. Natl. Acad. Sci. USA* **1984**, *81*, 1332-1335.

7. Wagner, A. F.; Frey, M.; Neugebauer, F. A.; Schafer, W.; Knappe, J. *Proc. Natl. Acad. Sci. USA* **1992**, *89*, 996-1000.

8. Henshaw, T. F.; Cheek, J.; Broderick, J. B. *J. Am. Chem. Soc.* **2000**, *122*, 8331-8332.

9. Vey, J. L.; Yang, J.; Li, M.; Broderick, W. E.; Broderick, J. B.; Drennan, C. L. *Proc. Natl. Acad. Sci. USA* **2008**, *105*, 16137-16141.

10. Becker, A.; Fritz-Wolf, K.; Kabsch, W.; Knappe, J.; Schultz, S.; Volker Wagner, A. F. *Nature structural biology* **1999**, *6*, 969-975.

11. Becker, A.; Kabsch, W. *J. Biol. Chem.* **2002**, *277*, 40036-40042.

12. Peng, Y.; Veneziano, S. E.; Gillispie, G. D.; Broderick, J. B. *J. Biol. Chem.* **2010**, *285*, 27224-27231.

13. Vey, J. L.; Yang, J.; Li, M.; Broderick, W. E.; Broderick, J. B.; Drennan, C. L. *Proceedings of the National Academy of Sciences of the United States of America* **2008**, *105*, 16137-16141.

14. Brünger, A. T.; Adams, P. D.; Clore, G. M.; DeLano, W. L.; Gros, P.; Grosse-Kunstleve, R. W.; Jiang, J. S.; Kuszewski, J.; Nilges, M.; Pannu, N. S.; Read, R.

J.; Rice, L. M.; Simonson, T.; Warren, G. L. *Acta. Crystallogr. D Biol. Crystallogr.* **1998**, *54*, 905-921.

15. Murshudov, G. N.; Skubák, P.; Lebedev, A. A.; Pannu, N. S.; Steiner, R. A.; Nicholls, R. A.; Winn, M. D.; Long, F.; Vagin, A. A. *Acta Crystallogr. D Biol. Crystallogr.* **2011**, *67*, 355-367.

16. Potterton, E.; Briggs, P.; Turkenburg, M.; Dodson, E. *Acta Crystallogr. D Biol. Crystallogr.* **2003**, *59*, 1131-1137.

17. Broderick, J. B.; Henshaw, T. F.; Cheek, J.; Wojtuszewski, K.; Smith, S. R.; Trojan, M. R.; McGhan, R. M.; Kopf, A.; Kibbey, M.; Broderick, W. E. *Biochem. Biophys. Res. Commun.* **2000**, *269*, 451-456.

18. Nnyepi, M. R.; Peng, Y.; Broderick, J. B. *Arch. Biochem. Biophys.* **2007**, *459*, 1-9.

19. Walsby, C. J.; Hong, W.; Broderick, W. E.; Cheek, J.; Ortillo, D.; Broderick, J. B.; Hoffman, B. M. *J. Am. Chem. Soc.* **2002**, *124*, 3143-3151.

20. Bradford, M. M. *Anal. Biochem.* **1976**, *72*, 248-254.

21. Conradt, H.; Hohmann-Berger, M.; Hohmann, H. P.; Blaschkowski, H. P.; Knappe, J. *Arch. Biochem. Biophys.* **1984**, *228*, 133-142.

22. Brush, E. J.; Lipsett, K. A.; Kozarich, J. W. *Biochemistry* **1988**, *27*, 2217-2222.

23. Kulzer, R.; Pils, T.; Kappl, R.; Huttermann, J.; Knappe, J. *J. Biol. Chem.* **1998**, *273*, 4897-4903.

24. Stoll, S.; Schweiger, A. *J. Magn. Reson.* **2006**, *178*, 42-55.

25. Page, M. J.; Di Cera, E. *Physiol. Rev.* **2006**, *86*, 1049-1092.

26. Harding, M. M. *Acta Crystallogr. D Biol. Crystallogr.* **2002**, *58*, 872-874.

27. Zheng, H.; Chruszcz, M.; Lasota, P.; Lebioda, L.; Minor, W. *J. Inorg. Biochem.* **2008**, *102*, 1765-1776.

28. Epstein, W.; Schultz, S. G. *J. Gen. Physiol.* **1965**, *49*, 221-234.

29. Kung, F. C.; Raymond, J.; Glaser, D. A. *J. Bacteriol.* **1976**, *126*, 1089-1095.

30. Lusk, J. E.; Williams, R. J. P.; Kennedy, E. P. *J. Biol. Chem.* **1968**, *243*, 2618-2624.

31. Walsby, C. J.; Ortillo, D.; Yang, J.; Nnyepi, M. R.; Broderick, W. E.; Hoffman, B. M.; Broderick, J. B. *Inorg. Chem.* **2005**, *44*, 727-741.

32. Evans, H. J.; Wildes, R. A. In *Potassium in Biochemistry and Physiology*; International Potash Institute: Berne, Switzerland, 1971.

33. Wilson, R. H.; Evans, H. J. In *The Role of Potassium in Agriculture*; Kilmer, V. J., Younts, S. E., Brady, N. C., Eds.; ASA, CSSA, SSSA: Madison, WI, 1968, p 189-202.

34. Wong, K. K.; Murray, B. W.; Lewisch, S. A.; Baxter, M. K.; Ridky, T. W.; Ulissi-DeMario, L.; Kozarich, J. W. *Biochemistry* **1993**, *32*, 14102-14110.

35. Burdette, S. C.; Lippard, S. J. *Proc. Natl. Acad. Sci. U.S.A.* **2003**, *100*, 3605-3610.

36. Toraya, T.; Sugimoto, Y.; Tamao, Y.; Shimizu, S.; Fukui, S. *Biochemistry* **1971**, *10*, 3475-3484.

37. Shibata, N.; Masuda, J.; Tobimatsu, T.; Toraya, T.; Suto, K.; Morimoto, Y.; Yasuoka, N. *Structure* **1999**, *7*, 997-1008.

38. Zhang, Y.; Dougherty, M.; Downs, D. M.; Ealick, S. E. *Structure* **2004**, *12*, 1809-1821.

39. Rana, S.; Pozzi, N.; Pelc, L. A.; Di Cera, E. *Proc. Natl. Acad. Sci. USA* **2011**, *108*, 5221-5225.

40. Dowling, D. P.; Bruender, N. A.; Young, A. P.; McCarty, R. M.; Bandarian, V.; Drennan, C. L. *Nat. Chem. Biol.* **2014**, *10*, 106-112.

41. McCarty, R. M.; Krebs, C.; Bandarian, V. *Biochemistry* **2013**, *52*, 188-198.

CHAPTER EIGHT

AN EPR AND ENDOR INVESTIGATION OF THE CATION SITE IN PFL-AE

Introduction

Pyruvate kinase was the first enzyme identified to absolutely require K^+ for catalysis, [1,2] and since then the requirement of a monovalent cation (M^+) for optimal activity has been discovered in a range of enzymes [2,3]. The effect of a M^+ on enzyme activity can be classified as either cofactor-like (type I) or allosteric (type II); the M^+ is absolutely required for type I while requirement is not absolute for type II although the cation stimulates catalytic activity. M^+ dependence has exquisite specificity, with K^+ and Na^+ as the preferred M^+, consistent with their higher availability *in vivo*. Since the concentrations of M^+ in the cell are highly regulated, the preference for K^+ vs. Na^+ can be attributed to enzyme location: K^+ dependent enzymes reside in intracellular locations while Na^+ enzymes reside in extracellular locations [2,3]. In general, enzymes requiring K^+ are still active with slightly larger M^+ like Rb^+ and NH_4^+, albeit with lower activity in most cases, but are significantly less active or inactive with smaller M^+ like Li^+ and Na^+, and with the significantly larger cation Cs^+. Enzymes requiring Na^+, are more selective and are not activated as well by Li^+ or the larger K^+, Rb^+, and Cs^+ cations [2,3].

Recently, the radical *S*-adenosylmethionine (SAM) enzyme pyruvate formate lyase (PFL-AE) was reported to contain a M^+ site identified in the crystal structure, with occupancy affecting both EPR spectroscopic properties and enzyme activity (manuscript

in preparation). Radical SAM enzymes are a large superfamily that catalyze diverse chemical reactions through intermediate radical species. Catalysis is initiated through the one electron reduction of a site-differentiated $[4Fe\text{-}4S]^{2+}$ cluster coordinated through three of its four iron atoms via a CX_3CX_2C tricysteine motif [4,5]. The fourth, unique Fe is coordinated by SAM through its amino N and a carboxyl O in a manner that allows for inner sphere electron transfer and homolytic cleave of SAM to produce the highly reactive 5'-deoxyadenosyl (5'-dAdo•) radical. This radical can then abstract a hydrogen from substrate, producing a substrate radical which can undergo further radical mediated chemistry. Radical SAM active sites are nestled inside a triosephosphate isomerase (TIM) barrel which is a partial $(\alpha/\beta)_6$ TIM barrel in most cases but a full $(\alpha/\beta)_8$ TIM barrel in a few other cases [4-6]. The substrates for radical SAM enzymes range from small molecules to large biomolecules and proteins. Pyruvate formate lyase activating enzymes (PFL-AE) is one of the smallest radical SAM enzymes with a partial $(\alpha/\beta)_6$ TIM barrel that reflects its need to accommodate its large homodimeric protein substrate pyruvate formate lyase (PFL). During catalysis, PFL-AE abstracts a hydrogen atom from a glycine residue (G734) on PFL, thus activating it to convert pyruvate and coenzyme A (CoA) to formate and acetyl-CoA [7,8].

The cation in PFL-AE was assigned as a Na^+ in the crystal structure but K^+ had the largest stimulatory effect on activity and thus was proposed to be the *in vivo* M^+ of choice for PFL-AE (manuscript in preparation). Activity was tested in the presence of five other monovalent cations, Na^+, NH_4^+, Rb^+, Cs^+, and Li^+, all of which had decreased activity compared to that in the presence of K^+, while addition of the three divalent

cations, Ca^{2+}, Mg^{2+}, and Zn^{2+}, inhibited activity. PFL-AE still had slight activity in the absence of M^+, suggesting that a cation wasn't absolutely required. The M^+ has 5-coordinate ligation to the protein via two Asp side chain oxygen atoms, two backbone oxygen atoms from a Thr and a Met, and the free carboxyl oxygen of SAM (Figure 8.1). The M^+ identity also affected the electronic structure of the [4Fe-4S] cluster causing electron paramagnetic resonance (EPR) and circular dichroism (CD) spectral changes in

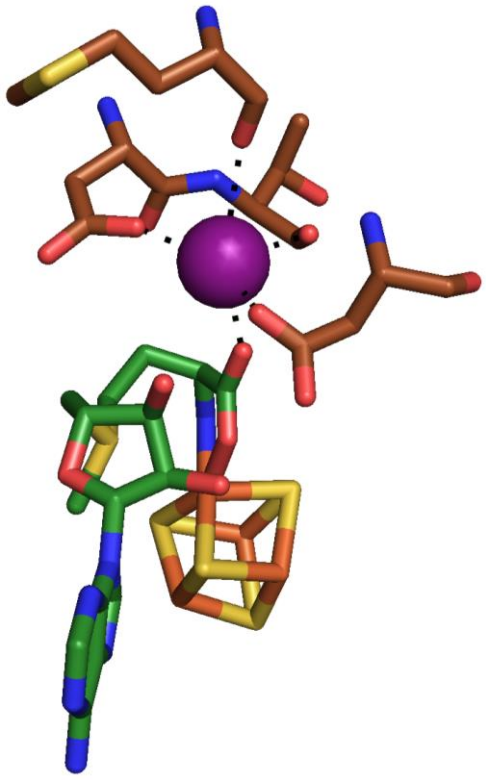


Figure 8.1. The cation site in PFL-AE. The cation, identified as Na^+ in the crystal structure (purple sphere), has 5-coordinate oxygen geometry with 2 aspartate side chains oxygens (Asp104 and Asp 129 at a distance of 2.5 Å from the cation), a methionine (3.0 Å) and threonine (2.7 Å) backbone oxygents, and the unbound carboxyl oxygen of SAM (2.4 Å) in a distorted trigonal bipyramidal geometry. The coordinating amino acids are colored with brown carbons and SAM is colored with green carbons.

the presence of different cations which was more apparent in the presence of SAM. It was proposed that the change in the M^+ size would push or pull the carboxyl oxygen of SAM and only in the presence of K^+ was SAM in the appropriate position for optimal activity (manuscript in preparation). Currently, no other radical SAM enzyme has been found to contain a monovalent cation site but QueE was recently shown to have divalent cation dependence with Mg^{2+} increasing activity [9,10]. The Mg^{2+} coordination sphere does not include SAM but Mg^{2+} was directly ligated to substrate [9].

To further investigate the M^+ site of PFL-AE, we have used electron nuclear double resonance (ENDOR) spectroscopy of PFL-AE in the presence of K^+, Na^+, and Tl^+. ENDOR spectroscopy probes the coupling (hyperfine interactions) between a paramagnetic species, such as a reduced $[4Fe\text{-}4S]^+$ cluster, and a nucleus with a nuclear spin ($I \geq ½$), and provides insight into geometric and electronic structures of such systems. K^+ and Na^+ both have $I = 3/2$ nuclear spin and Tl^+ has an $I = ½$ nuclear spin. Both ^{203}Tl and ^{205}Tl have a larger isotropic hyperfine couplings (~6500 mT), compared to ^{39}K (8 mT) and ^{23}Na (32 mT) [11]. If the cation binding site is sufficiently close to the cluster, it is expected that Tl^+ coupling would be easily observed. Tl^+ (ionic radius 150 pm) can replace K^+ (ionic radius 138 pm) in many enzymes activated by K^+ with only ~20% decrease of in activity but with higher affinity than other M^+ [12]. In this study, ENDOR spectroscopy was used to analyze coupling between the M^+ and the cluster in order to determine distances between the cluster and different monovalent cations in addition to revealing any variability in SAM coordination with different M^+ to provide insight into the role of the monovalent cation in enzyme activity.

Materials and Methods

Materials

All chemicals were obtained from commercial sources and were of the highest purity commercially available. [Methyl-^{13}C]-methionine was purchased from Cambridge Isotope Laboratories and was used to synthesize SAM as previously described [13,14].

Expression and Purification of PFL-AE

PFL-AE was expressed and purified as previously described (manuscript in preparation) in the absence of M^+. In brief, overexpression was conducted with *E. coli* cells under anaerobic conditions. Enzymatic lysis and purification by size exclusion with a 50 mM Tris, pH 7.5 and 1 mM DTT buffer were conducted in an anaerobic Coy chamber. Fractions with the highest 426/280 nm ratio were pooled. PFL-AE concentration was determined using the method of Bradford [15] using dye reagent from Biorad. A correction factor was utilized in the final calculations of PFL-AE concentration [16]. Iron content was determined using atomic absorption spectroscopy and PFL-AE contained between 3.5 and 3.8 Fe per protein for the following experiments.

PFL-AE Activity Assays

Activity assays of PFL-AE were conducted as previously described (manuscript in preparation) in the absence of M^+ (M^+-free), and presence of 1 mM Tl^+, 100 mM K^+, or 100 mM Na^+, all in a 100 mM Tris, pH 7.5 buffer. In short, 450 µL of an activation solution containing 0.05 µM PFL-AE purified in the absence of M^+, 5 µM PFL, 0.1 mM SAM, 10 mM oxamate, 8 mM DTT, and 25 µM 5-deazariboflavin (added last in the

dark) were added to a 100 mM Tris, pH 7.6 buffer containing different cations as described above (all concentrations given are final concentrations). This solution was photoreduced by illumination with a 300 W halogen lamp in a 30 ± 2°C water bath for 5 minutes. To assay the activity, 5 µL of the resulting activation solution was placed on the lid of an anaerobic cuvette containing 895 µL of coupling solution (3 mM NAD+, 55 µM CoA, 0.05 mg/mL BSA, 10 mM pyruvate, 10 mM malate, 2 U/mL citrate synthase, 30 U/mL malic dehydrogenase and 10 mM DTT in a 100 mM Tris, pH 8.1 buffer (concentrations given as a final concentration after mixing of both solutions with a final volume of 900 µL)). The two solutions were mixed by inverting the cuvette just prior to UV-vis analysis in a Cary 60 UV-Vis spectrophotometer. The production of NADH was monitored at 340 nm for 90 seconds. One unit of PFL activity corresponds to the production of one µmole of pyruvate per minute, and 35 units of PFL is equivalent to 1 nmole of PFL active sites [17]. One unit of PFL-AE activity is defined as the production of 1 nmole of active PFL per minute [16]. All assays were conducted in triplicate.

EPR and ENDOR Sample Preparation

EPR samples were prepared as previously described (manuscript in preparation). In an anaerobic MBraun glovebox with < 1 ppm O_2, 300 µM PFL-AE (final concentration post photoreduction and SAM addition) was added to a 100 mM Tris, pH 7.5 buffer with 1 mM DTT which contained either 100 mM KCl, 100 mM NaCl, 1 mM TlCl or 1 mM $TlNO_3$ (which both produced identical results), or no M^+ (M^+-free). A final concentration of 100 µM 5-deazariboflavin was added last. The mixture was photoreduced for about one hour after which SAM or buffer was added to a final

concentration of 300 μM PFL-AE and 2 mM SAM. Samples were loaded into an X-band tube, capped, and flash frozen in liquid nitrogen upon removal from the MBraun chamber. EPR spectra were recorded on a Bruker EMX X-band spectrometer equipped with a liquid helium cryostat and temperature controller from Oxford Instruments. Typical experimental parameters were 12 K and 9.37 GHz, with 1.0 mW microwave power, 100 kHz modulation frequency, and 10 G modulation amplitude. Each spectrum is the average of four scans.

ENDOR samples were also prepared in MBraun glovebox with < 1 ppm O_2 as previously described (manuscript in preparation). PFL-AE (300 μM final concentration post photoreduction and SAM addition) was added to a 100 mM Tris, pH 7.5 buffer containing 1 mM DTT and either 100 mM KCl, 100 mM NaCl, or 1 mM TlCl or 1 mM $TlNO_3$ (which both produced identical results) followed by addition of 100 μM 5-deazariboflavin (final concentration). The mixture was photoreduced for about one hour after which SAM (unlabeled or [methyl-^{13}C]-SAM) or buffer was added to a final concentration of 300 μM PFL-AE and 3 mM unlabeled SAM or 2 mM [methyl-^{13}C]-SAM. Samples were loaded into an Q-band tube, capped, and flash frozen in liquid nitrogen. Q-band EPR and pulsed ENDOR spectroscopy at Q-band were conducted at 2 K as previously described [18]. Calculations and simulations of ENDOR experimentation of SAM binding were conducted as previously described [13,18].

Results

Specific Activity of PFL-AE in the Presence of K^+, Na^+, and Tl^+

Activity assays were previously reported in the presence of six monovalent cations (K^+, Na^+, NH_4^+, Rb^+, Cs^+, and Li^+) and three divalent cations (Ca^{2+}, Zn^{2+}, and Mg^+) with K^+ having the greatest stimulatory effect and the divalent cations inhibiting activity (manuscript in preparation). These assays were repeated in the presence of Tl^+ (Figure 8.2), and analyzed against the activity of PFL-AE in the presence of K^+, Na^+, and

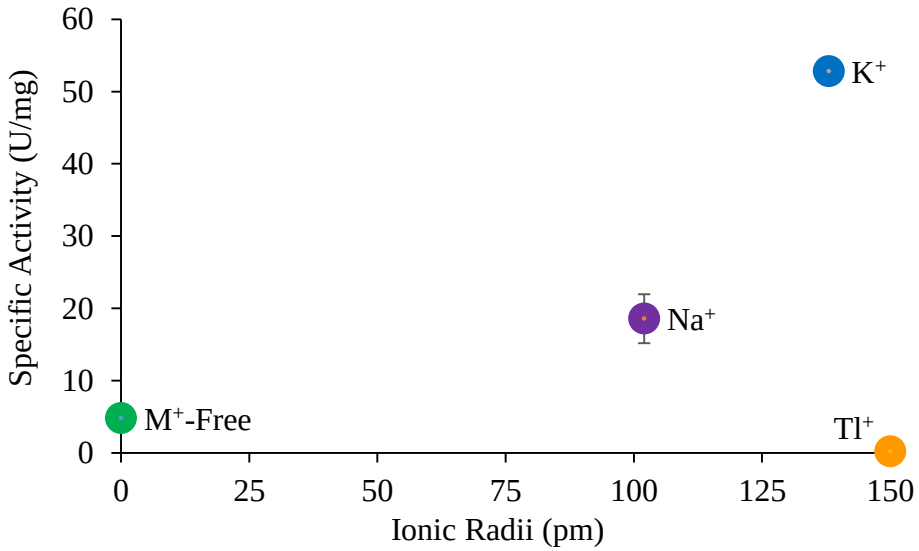


Figure 8.2. Specific activity (U/mg) of PFL-AE in the presence of Na^+, K^+, or Tl^+ or in the absence of cation (M^+-free). Trials were done in triplicate.

in the absence of cation (M^+-free). In the presence of Tl^+, activity was inhibited with a specific activity lower than that of M^+-free protein. The ionic radii for Tl^+ is similar to that of K^+ and many other enzymes activated by K^+ can also be activated by Tl^+ [12] and it's surprising that Tl^+ inhibits PFL-AE. To determine whether this was due to a lack of a

Tl^+ cation in the active site or other unknown effects, we wanted to conduct EPR and ENDOR experiments.

EPR Spectroscopy of
PFL-AE in the Presence of Tl^+

Previously, we reported that the EPR spectral properties of the $[4Fe\text{-}4S]^+$ cluster of PFL-AE were affected by the monovalent cations K^+, Na^+, Rb^+, Cs^+, NH_4^+, and Li^+ (manuscript in preparation). The most significant M^+-dependent changes were observed in the presence of SAM, and given the coordination of SAM to M^+ seen in the crystal structure, we proposed that the cation helps stabilize SAM in the active site. In order to further understand the cation site and its relation to the [4Fe-4S] cluster, we substituted Tl^+ into the cation site in an attempt to probe hyperfine interactions. The EPR spectrum of reduced PFL-AE in the presence of Tl^+ is almost identical to PFL-AE in the presence of K^+, with some similarities to M^+-free and fewer similarities to the sample with Na^+ (Figure 8.3). The ionic radius of Tl^+ (150 pm) is very similar to that of K^+ (138 pm), while Na^+ (102 pm) is much smaller; Tl^+ is therefore expected to behave similarly to K^+. In the presence of SAM and Tl^+, however, the X-band EPR spectrum is unlike any signal previously observed for PFL-AE (Figure 8.3). There is an intensification of the signal, which is typical for PFL-AE in the presence of SAM, but there are also significant changes in the line shape and g-values of the signal. Both the $g_{\|}$ and $g_{\perp}$ have shifted up-field with respect to the signals observed for PFL-AE in the presence of the other cations (K^+, Na^+, or M^+-free) and there appears to be hyperfine splitting in both the $g_{\|}$ and $g_{\perp}$ components.

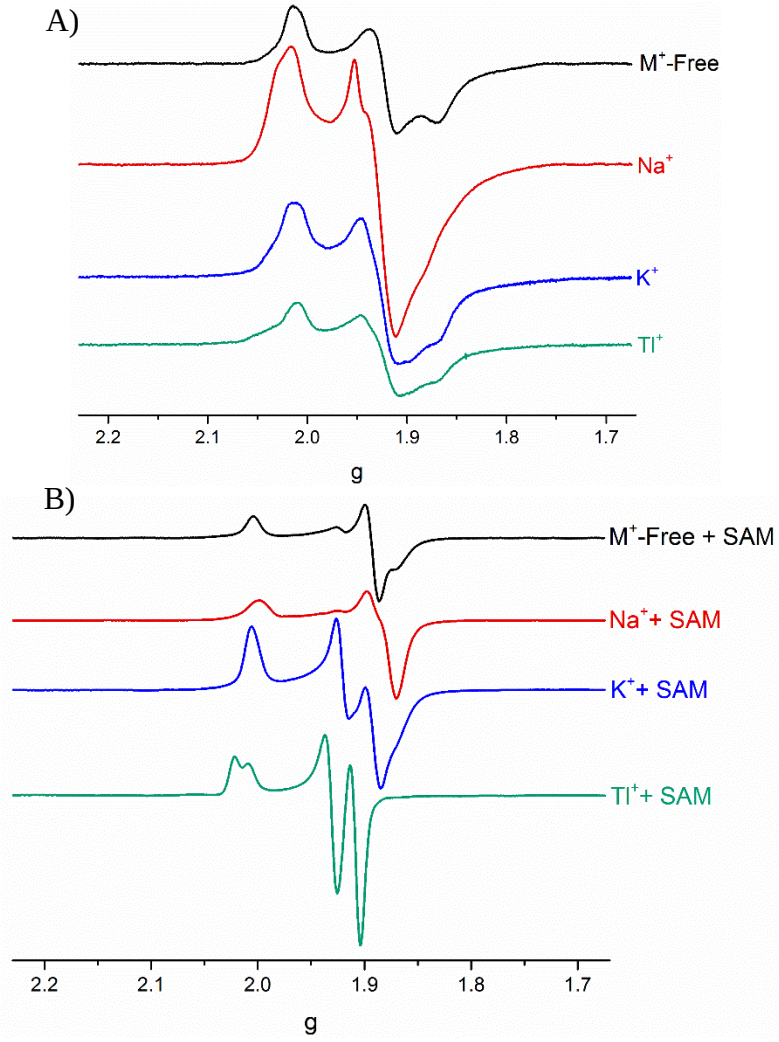


Figure 8.3. X-band EPR spectra of PFL-AE in the absence of cation (M^+-free, black), or in the presence of Na^+ (red), K^+ (blue), or Tl^+ (green) and in the absence (left) or presence of SAM (right).

Surprisingly, the splitting at both $g_{\|}$ and $g_{\perp}$ at X-band is not observed at Q-band (35 GHz) under rapid-passage conditions, which raises the question of whether the splitting observed at X-band is truly hyperfine coupling or two different conformations (Figure 8.4 a). Usually, initial Q-band continuous wave (CW) scans results in rapid-passage conditions due to the extremely low temperatures and high microwave power.

Under these conditions, the spin cannot relax between scans. Without adequate relaxation, broadening and loss of features occurs. In order to shift to non-rapid passage conditions, although this causes more noise to occur in the spectrum, the power was decreased and the modulation amplitude was increased. At a 50 dB power, a splitting of the $g_{\perp}$ feature appears after 5 G modulation (Figure 8.4b). The splitting at $g_{\parallel}$ is approximately 20 G at X-band and increases to 80 G at Q-band under non-rapid passage conditions while the splitting at $g_{\perp}$ is approximately 35 G at X-band and increases to 130 G at Q-band (SI Figure 8.1).

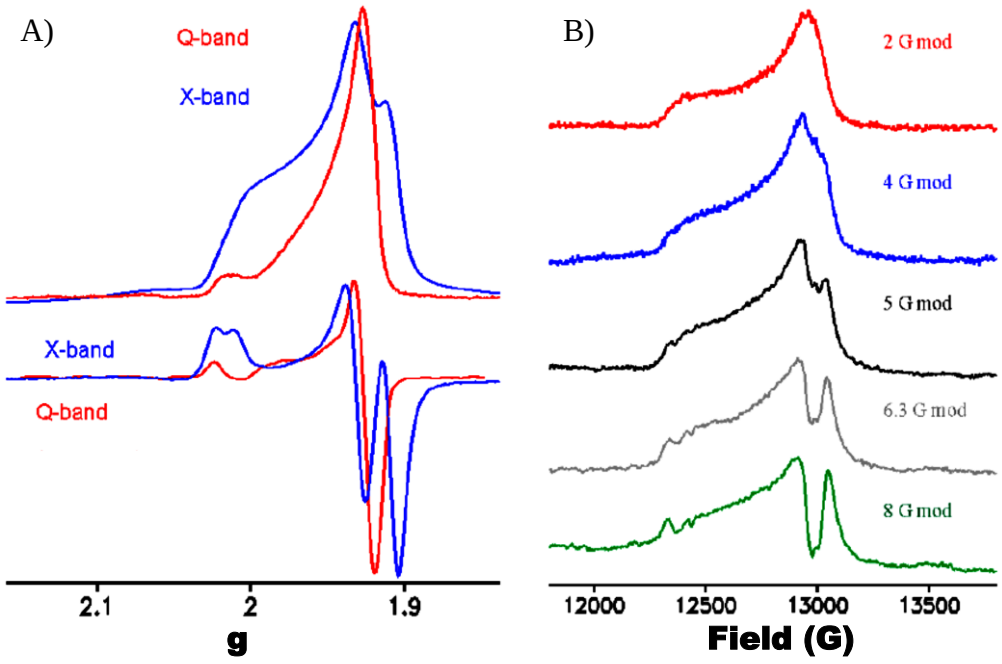


Figure 8.4. EPR spectrum of PFL-AE in the presence of 1 mM Tl^{+} and 2 mM SAM. A) Comparison of the X-band (blue) and Q-band (red) EPR specturm showing the absorbance spectrum (top) and the derivate (bottom). B) Q-band EPR spectra at 50 dB and 2 K with differing modulation amplitudes (2 G to 8 G modulation) to induce non-passage conditions. After 6.3 G modulation, splitting appears at $g_{\perp}$ (at ~13,000 G).

The splitting increases by a factor of ~3.7 upon the 9 GHz → 35 GHz shift which is consistent with the ratio of X-band and Q-band microwave quantum energy. If the splitting were hyperfine, one would expect ~35.7 G (100 MHz) splitting at Q-band. Taken together, the relaxation properties at Q-band and the larger splitting than expected only observed under non-passage conditions suggests that two different conformations give rise to the unique EPR spectrum in the presence of Tl^+.

ENDOR Spectroscopy of the Cation Site

Although the strong hyperfine splitting in the X-band EPR spectrum is indeed not due to strong hyperfine coupling between the cluster and Tl^+, weak coupling was in fact observed between the two centers using ENDOR spectroscopy. Mims ENDOR spectroscopy at $g_\perp$ and continuous wave (CW) ENDOR of PFL-AE in the presence of Tl^+ at varying g values reveals a weak $A_{2,3}$ ~ 1.1 MHz and A_1 ~ 2 MHz coupling, corresponding to a distance of > 5.5 Å (Figure 8.5) between the reduced cluster and the Tl^+ nucleus. The peaks in the ENDOR spectrum were asymmetric due to the natural isotopic distribution of Tl^+: ~30% ^{203}Tl and ~70 ^{205}Tl with Larmor frequencies of 31.93 MHz and 32.23 MHz at 12910 G, respectively. The Mims ^{23}Na ENDOR spectrum of PFL-AE in the presence of Na^+ revealed an A_2 ~ 0.14 MHz coupling at g_2 (g = 1.87) centered at the Larmor frequency, corresponding to a distance of ~5-6 Å between the cation and the cluster (Figure 8.6). Both of these distances are consistent with the 6.5 Å distance to the center of the cation to the unique Fe of the cluster in the crystal structure of PFL-AE. Thus, the decrease in activity in the presence of Tl^+ is not due to an absence of monovalent cation. No K^+ coupling to the cluster was observed via ENDOR

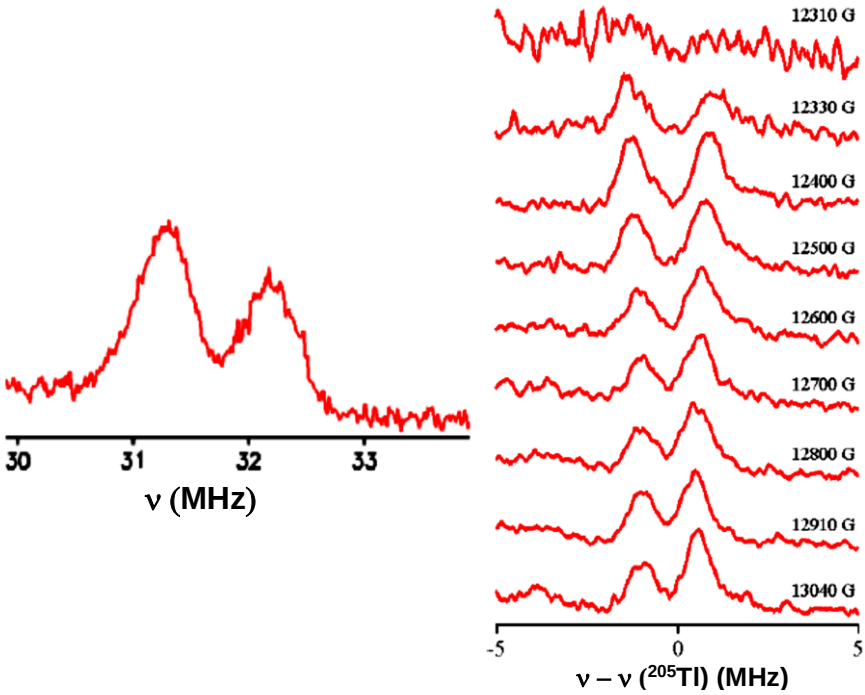


Figure 8.5. Mims $^{203}Tl/^{205}Tl$ ENDOR spectrum at $g_{\perp}$ (left) and the 2-D pattern of CW Tl ENDOR (right) at various g values (in Gauss). The CW ENDOR is not symmetric because Tl^{+} has two naturally abundant isotopes with two slightly different Larmor frequencies. The CW ENDOR spectrum is center at the Larmor frequency of the ^{205}Tl (70% abundance) isotope. The $A_1 \sim 2$ MHz and $A_{2,3} \sim 1.1$ MHz splitting calculates to a Tl^{+} distance > 5.5 Å from the cluster.

spectroscopy which is probably due to its weaker hyperfine coupling constant (only 8 mT versus 32 mT for Na^{+}).

Interestingly, the ^{23}Na ENDOR signal was overlooked in a previous ENDOR analysis to determine the SAM orientation in PFL-AE in the presence of Na^{+} and [methyl-^{13}C]-SAM [13]. Weak coupling at approximately 14.6 MHz was assigned to naturally abundant ^{57}Fe in the cluster; however, this signal is absent in a more recent ^{57}Fe ENDOR spectrum of an ^{57}Fe labeled [4^{57}Fe-4S] cluster prepared in K^{+} (SI Figure 8.2).

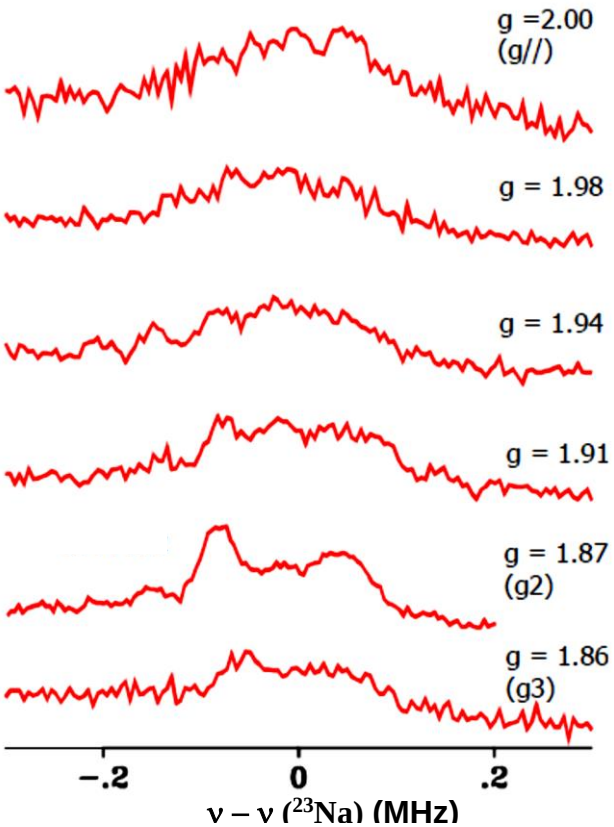


Figure 8.6. The 2-D Mims ^{23}Na ENDOR pattern of PFL-AE in the presence of Na^+ centered at the Larmor frequency of ^{23}Na. At g_2 (g = 1.87), the A = ~1.4 MHz coupling gives rise to a Na^+ distance of about 5-6 Å from the cluster.

SAM Coordination Differences
Observed by ENDOR Spectroscopy

The crystal structure of PFL-AE showed that the free carboxyl O of SAM is a fifth ligand to the monovalent cation (M^+), and due to the close proximity of the cation, it is proposed that M^+ size will affect the orientation of SAM with respect to the cluster (manuscript in preparation). Any difference in geometry of SAM may explain the differences in specific activity and the spectral properties of PFL-AE in the presence of different monovalent cations. The amino N, the carboxyl group, and the α-C form a ring, ligating SAM to the unique Fe (Figure 8.7). If changing the monovalent metal ion, and

thus the size of the M^+, results in movement of the carboxyl O of SAM, the N orientation relative to the unique Fe should change and this may be observable via ENDOR spectroscopy. Here we report the ENDOR spectral changes of the amino N and methyl-C.

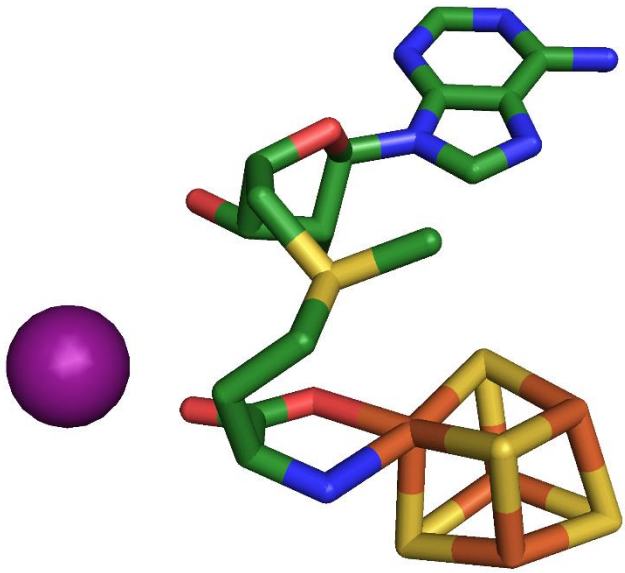


Figure 8.7. View of the methionine bidentate ring structure of SAM bound to the [4Fe-4S] cluster. The cation (purple sphere) interacts with the free carboxyl oxygen of SAM.

The Davies ^{14}N ENDOR spectrum of SAM bound to PFL-AE revealed slight variations in the coordination of SAM to the $[4Fe\text{-}4S]^+$ cluster of PFL-AE in the presence of Tl^+, K^+, and Na^+ (Figure 8.8a). The M^+-free prepped PFL-AE in the presence of Na^+ is almost identical to the PFL-AE purified in Na^+ (results from [14]) (Figure 8.8a). Like the study published by Walsby *et al.* [14], only the ν_+ peak is visible in the ^{14}N ENDOR spectrum for all cations tested. How exactly SAM coordination differs in the presence of these three different cations is unclear; however, it does appear that the coupling between

the cluster and the amino N of SAM is affected by the size of the monovalent cation present in the active site of PFL-AE.

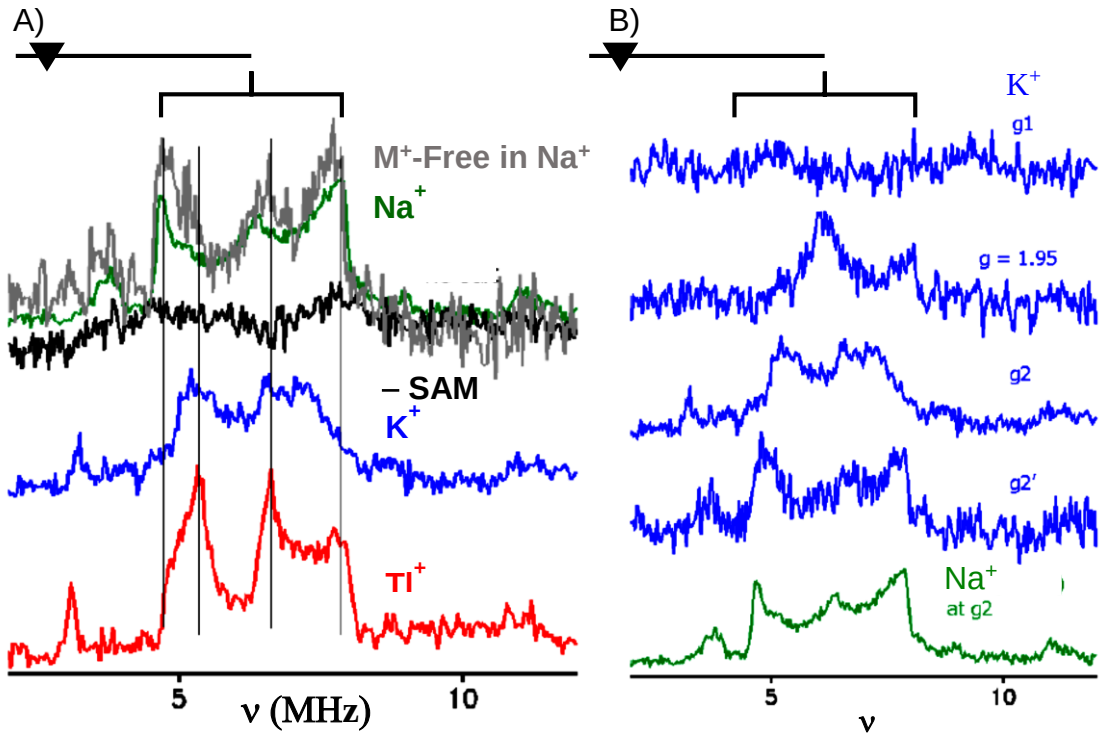


Figure 8.8. A) The ^{14}N Davies ENDOR spectra of SAM bound to PFL-AE at $g_\perp$ in the presence of different monovalent cations. PFL-AE was purified in the absence of cation followed by addition of Na^+ (M^+-free in Na^+, grey), K^+ (blue), or Tl^+ (red) or absence of SAM and M^+ (black). Protein purified in Na^+ (green) is from [13]. Spectra are at different fields due to variability of $g_\perp$ for each cation. B) The Davies ^{14}N ENDOR 2-D pattern of SAM bound to PFL-AE prepared in K^+ (blue) compared to the $g_\perp$ of Na^+ (green). The g_2' (g = 1.87) of the K^+ containing sample is very similar to the $g_\perp$ (g = 1.87) of the Na^+ containing sample.

To further explore the extent of amino N coupling to the cluster at varying g values, ^{14}N ENDOR spectrum of SAM was conducted at different g values in the presence of K^+ resulting in what is termed a 2-D pattern (Figure 8.8b). The 2-D ^{14}N ENDOR pattern of the amino N in the presence of K^+ has different ^{14}N coupling contributions at each g

value with one signal almost identical to that observed in the presence of Na^+. This result is very perplexing and suggests that SAM may have two conformations in the presence of K^+, one of which is similar to PFL-AE in the presence of Na^+. More analysis of the ^{14}N ENDOR spectrum of SAM is underway to understand how SAM orientation is modulated by the presence of these and other cations.

Mims ^{13}C ENDOR spectroscopy was used to compare the [methyl-^{13}C]-SAM coupling to the cluster in the presence of K^+, Na^+, and Tl^+ and compared with the previous results of Mims ^{13}C ENDOR of PFL-AE which was prepared in the presence of Na^+ [13]. Slight changes were observed in the 2-D ^{13}C ENDOR pattern in the presence of these monovalent cations (Figure 8.9) with the most significant difference associated with the contribution from $g_{\|}$ ($g = 2.00$) with the Na^+ sample having the strongest coupling. Since there is a difference in the contributions of the ^{13}C nucleus to the cluster in these three monovalent cations at different g values, it can be concluded that the methyl-C orientation is changing with cation size. Also, the ENDOR line widths in the presence K^+ are smaller/sharper than those in the presence of Na^+ and Tl^+, suggesting a more well-defined structure in the presence of K+. With a more stabilized methyl-C portion of SAM when K^+ is present could explain why K^+ has the greatest stimulatory effect on PFL-AE activity.

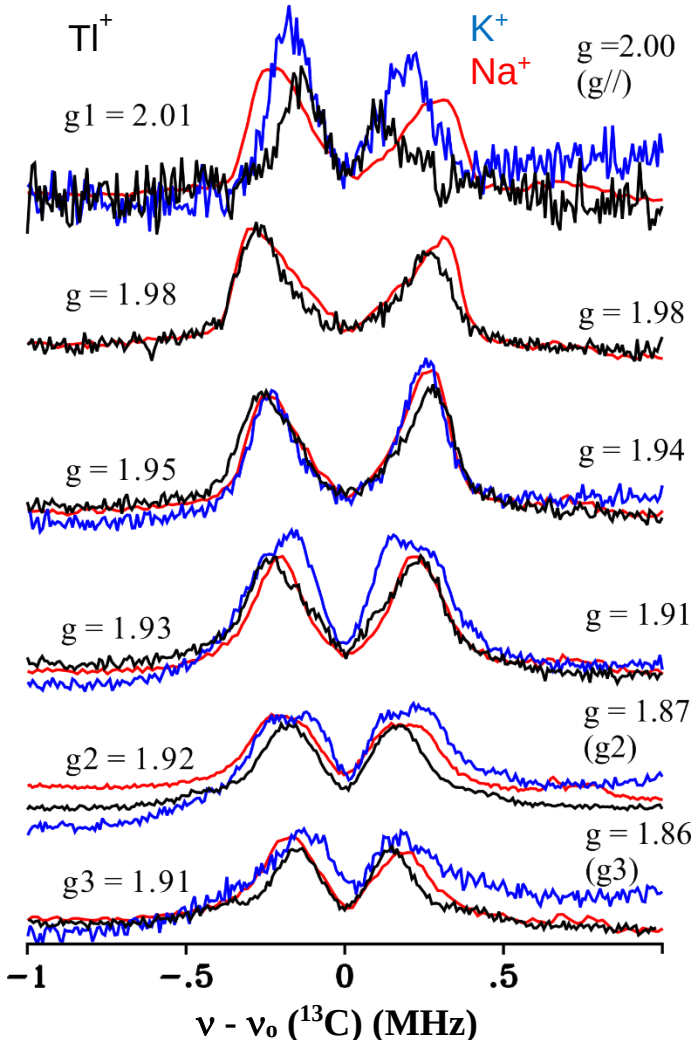


Figure 8.9. The 2-D Mims ^{13}C ENDOR pattern of [methyl-^{13}C]-SAM bound to PFL-AE in the presence of K^+ (blue), Na^+ (red), and Tl^+ (black) centered at the Larmor frequency of ^{13}C.

Discussion

PFL-AE activity has a stimulatory affect in the presence of a monovalent cation, with a maximal activity observed in the presence of K^+. To explore how this M^+ is interacting with the cluster and SAM and affecting activity, EPR and ENDOR studies were conducted to probe structural differences influenced by M^+ identity. The nuclear

spin and large hyperfine coupling constant of Tl^+ was initially exploited to probe the cation site. Although PFL-AE in the presence of Tl^+ exhibited unusual splitting in X-band EPR, there was no hyperfine splitting in rapid passage Q-band conditions and only a weak Tl^+ coupling to cluster was observed by ENDOR spectroscopy. EPR splitting at Q-band could be resolved upon a decrease in power and an increase in modulation amplitude to induce non-rapid passage conditions. The size of the splitting under non-rapid passage conditions was larger than expected for hyperfine splitting and suggests two different conformations of the active site give rise to the unique EPR signal. The origin of these two conformations is still unknown. The coupling between Tl^+ and the cluster observed during ENDOR experiments produced a distance consistent with that observed for Na^+, suggesting Na^+ and Tl^+ occupy the same binding pocket in the active site observed in the crystal structure. Since Tl^+ is present in the cation site, the decrease in activity is not due to an absence of M^+.

The ^{14}N and ^{13}C ENDOR signals arising from the coupling of the amino-N and the methyl-C of SAM with the reduced cluster are altered in the presence of K^+, Na^+, and Tl^+, suggesting cation size affects SAM orientation. The amino N, carboxyl C and O, and the C_α of methionine form a 5-member chelate ring at the unique Fe (Figure 8.7) and presumably, if the O is pushed or pulled in the presence of larger or smaller cations, this would in turn affect the amino N of SAM. The ^{14}N ENDOR results reveal changes in the ^{14}N signal in the presence of K^+, Na^+, and Tl^+. How the orientation differs in the presence of these different monovalent cations still needs further investigation. The ^{14}N ENDOR data in the presence of K^+ revealed two possible conformations of SAM with

one of these being identical to that in the presence of Na^+. However, the ENDOR results for PFL-AE in the presence of [methyl-^{13}C]-SAM suggests that SAM is in a better-defined structure in the presence of K^+, compared to addition of Na^+, and thus contradicts the proposal of two conformations. The source of the discrepancy in these results is not yet clear. Perhaps the flexibility in SAM ligation to the cluster via its amino N with a more well-defined methyl-C orientation in the presence of K^+ could be required to obtain an intermediate discovered during rapid freeze quench (RFQ) experiments. Unpublished results of an intermediate signal observed after a 500 ms quench has been assigned as an organometallic Fe-C bond with the 5'-C of adenosine bound to the unique Fe of the cluster post SAM cleavage (manuscript in preparation). It is proposed that SAM is cleaved, and after the addition of two electrons to SAM from the cluster (exact mechanism still under debate), the 5'-C binds to the unique Fe of a paramagnetic $[4Fe\text{-}4S]^{3+}$ cluster. During the process, the amino N and carboxyl O in methionine are thought to dissociate before the 5'-C binds the cluster in this intermediate due to an absence of ^{14}N coupling to the $[4Fe\text{-}4S]^{3+}$. It is possible that the M^+ is involved with methionine interactions post cleavage. If the amino N of SAM is more flexible in the presence of K^+, dissociation of methionine from the cluster might be more favorable. Two crystal structures for PFL-AE have been solved: one in the presence of disordered SAM and one in the presence of SAM and a PFL 7-mer peptide [19]. The peptide bound structure contains a complete SAM molecule and a cation. The SAM-only structure contains a disorder SAM and only a portion of the methionine of SAM is visible. Although no cation was observed in this structure, superposition of the two structures

revealed that the amino N and a carboxyl O of the disorder SAM are orientated towards the cation site with a distance of ~3.8 Å (Figure 8.10). This distance is further than the structure with a complete SAM molecule with an oxygen-cation distance of 2.4 Å. Although the disordered SAM has not been catalytically cleaved in the crystal structure, it's possible that a similar orientation could occur post SAM cleavage to move the methionine portion away from the cluster to allow for the 5'-C to bind the unique Fe.

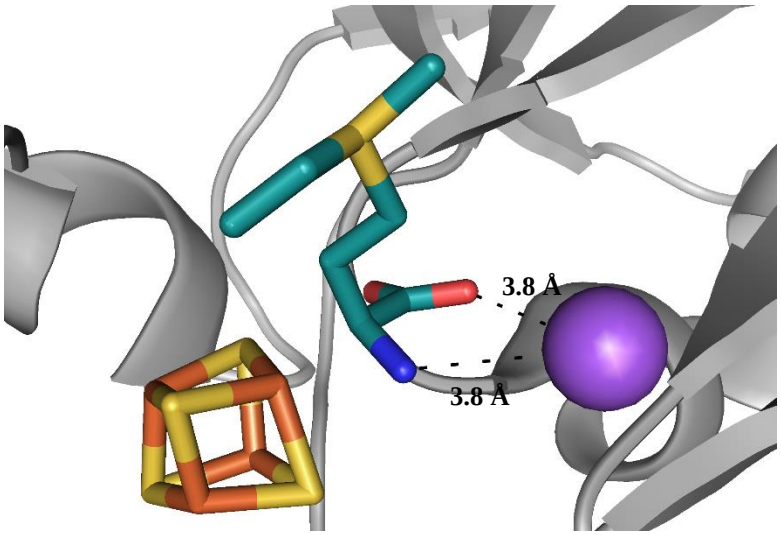
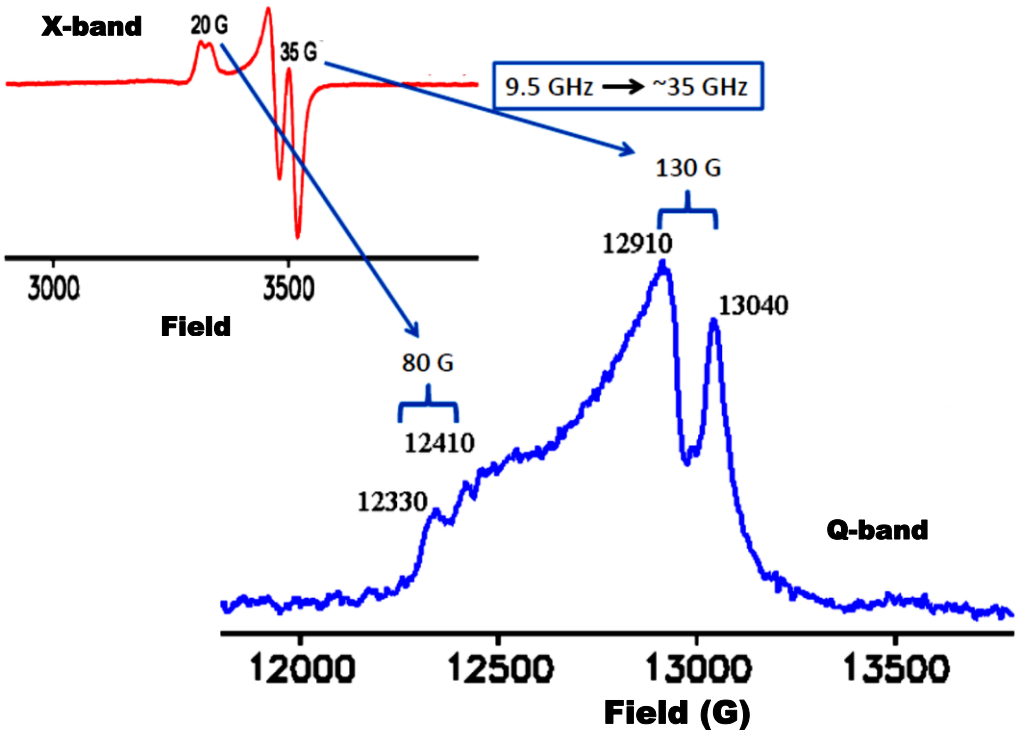


Figure 8.10. Superposition of the PFL-AE structure in the presence of disordered SAM (methionine portion shown in teal carbons) and the PFL-AE structure with the 7-mer peptide (not shown) and cation (purple sphere). The carboxyl O and amino N are 3.8 Å from the cation.

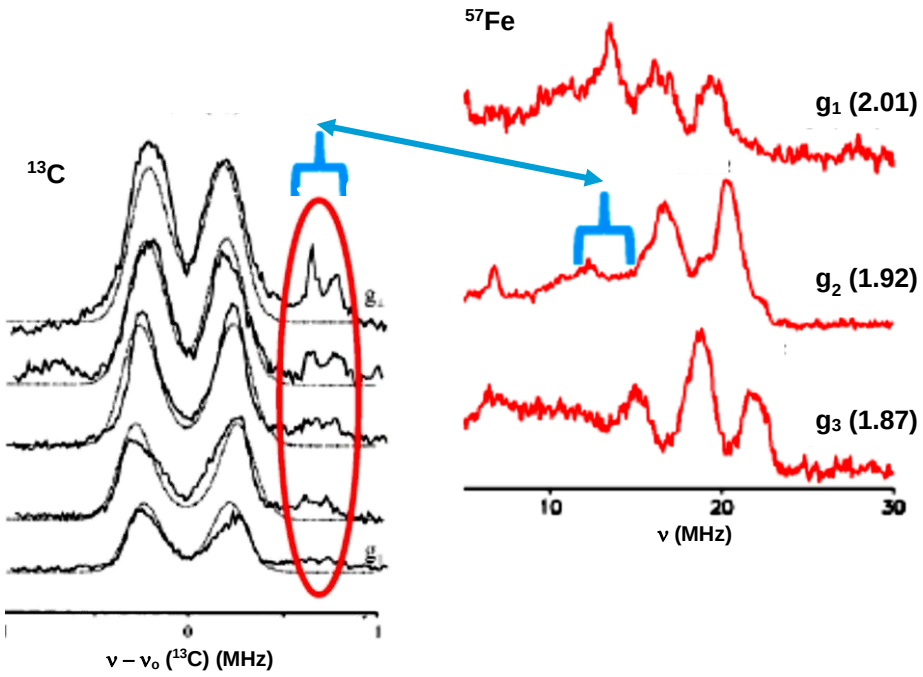
Exactly how the SAM orientation changes with different M^+ needs further investigation and crystallography may expose these key differences. For example, replacement of K^+ for Na^+ in M^+ requiring enzymes can either have no effect on the crystal structure as in pyruvate kinase [2,20] or significant changes in the coordination geometry of the active site as observed in the case of Hsc70 where the residues involved

in substrate and cofactor binding were significantly perturbed [2,21,22]. Crystallography of PFL-AE could determine whether the coordination environment of the M^+ changes or how SAM moves with these different monovalent cations and give insights into the changes in activity and its spectroscopic signals.

Supplementary Figures



SI Figure 8.1. Splitting values in the X-band (red) EPR and Q-band (blue) EPR spectrum of PFL-AE in the presence of Tl^+ and SAM. Upon the 9.5 GHz to ~35 GHz transition, the splitting increases by approximately 3.7 times. This is consistent with the ratio of X- and Q-band microwave quantum energies. This further supports that the apparent splitting in the X-band EPR spectrum is due to two distinct conformations of PFL-AE and not hyperfine interactions.



SI Figure 8.2. Comparison of the Mims ^{13}C 2-D ENDOR pattern of [methyl-^{13}C]-SAM bound to PFL-AE in the presence of Na^+ from Walsby *et al.* [13] (left) with the CW ^{57}Fe 2-D ENDOR pattern of PFL-AE with a [4^{57}Fe-4S] labeled cluster in the presence of K^+ (right). The pattern on the left is in the reverse order, going from g_2 (top) to g_1 (bottom) while the pattern on the right goes from g1 (top) to g_3 (bottom) The signal at ~14.6 MHz (red circled region in the ^{13}C ENDOR spectra) was previously assigned to a naturally abundant ^{57}Fe signal. This signal is absent in the ^{57}Fe ENDOR signal (bracketed region) when the samples were prepared in the presence of K^+. This signal has been assigned to Na^+ coupling to the cluster.

References

1. Kachmar, J. F.; Boyer, P. D. *J. Biol. Chem.* **1953**, *200*, 669-682.

2. Page, M. J.; Di Cera, E. *Physiol. Rev.* **2006**, *86*, 1049-1092.

3. Di Cera, E. *J. Biol. Chem.* **2006**, *281*, 1305-1308.

4. Broderick, J. B.; Duffus, B. R.; Duschene, K. S.; Shepard, E. M. *Chem. Rev.* **2014**, *114*, 4229-4317.

5. Vey, J. L.; Drennan, C. L. *Chem. Rev.* **2011**, *111*, 2487-2506.

6. Shisler, K. A.; Broderick, J. B. *Curr. Opin. Struct. Biol.* **2012**, *22*, 701-710.

7. Frey, M.; Rothe, M.; Wagner, A. F.; Knappe, J. *J. Biol. Chem.* **1994**, *269*, 12432-12437.

8. Shisler, K. A.; Broderick, J. B. *Arch. Biochem. Biophys.* **2014**, *546*, 64-71.

9. Dowling, D. P.; Bruender, N. A.; Young, A. P.; McCarty, R. M.; Bandarian, V.; Drennan, C. L. *Nat. Chem. Biol.* **2014**, *10*, 106-112.

10. McCarty, R. M.; Krebs, C.; Bandarian, V. *Biochemistry* **2013**, *52*, 188-198.

11. Weil, J. A.; Bolton, J. R. *Electron Paramagnetic Resonance: Elementary Theory and Practical Applications*; 2 ed.; Wiley-Interscience, 2007.

12. Markham, G. D.; Leyh, T. S. *J. Am. Chem. Soc.* **1987**, *109*, 599-600.

13. Walsby, C. J.; Hong, W.; Broderick, W. E.; Cheek, J.; Ortillo, D.; Broderick, J. B.; Hoffman, B. M. *J. Am. Chem. Soc.* **2002**, *124*, 3143-3151.

14. Walsby, C. J.; Ortillo, D.; Broderick, W. E.; Broderick, J. B.; Hoffman, B. M. *J. Am. Chem. Soc.* **2002**, *124*, 11270-11271.

15. Bradford, M. M. *Anal. Biochem.* **1976**, *72*, 248-254.

16. Broderick, J. B.; Henshaw, T. F.; Cheek, J.; Wojtuszewski, K.; Smith, S. R.; Trojan, M. R.; McGhan, R. M.; Kopf, A.; Kibbey, M.; Broderick, W. E. *Biochem. Biophys. Res. Commun.* **2000**, *269*, 451-456.

17. Kulzer, R.; Pils, T.; Kappl, R.; Huttermann, J.; Knappe, J. *J. Biol. Chem.* **1998**, *273*, 4897-4903.

18. Horitani, M.; Byer, A. S.; Shisler, K. A.; Chandra, T.; Broderick, J. B.; Hoffman, B. M. *J. Am. Chem. Soc.* **2015**, *137*, 7111-7121.

19. Vey, J. L.; Yang, J.; Li, M.; Broderick, W. E.; Broderick, J. B.; Drennan, C. L. *Proc. Natl. Acad. Sci. USA* **2008**, *105*, 16137-16141.

20. Larsen, T. M.; Benning, M. M.; Rayment, I.; Reed, G. H. *Biochemistry* **1998**, *37*, 6247-6255.

21. Flaherty, K. M.; DeLuca-Flaherty, C.; McKay, D. B. *Nature* **1990**, *346*, 623-628.

22. Wilbanks, S. M.; McKay, D. B. *J. Biol. Chem.* **1995**, *270*, 2251-2257.

CHAPTER NINE

WHY NATURE USES RADICAL *S*-ADENOSYL-L-METHIONINE ENZYMES SO WIDELY: ELECTRON NUCLEAR DOUBLE RESOANCE STUDIES OF LYSINE 2,3-AMINOMUTASE SHOW THE 5'-DADO• "FREE RADICAL" IS NEVER FREE

Contribution of Authors and Co-Authors

Manuscript(s) in Chapter(s) 4, 5, 6, 7, 9, 10

Author: Masaki Horitani

Contributions: Collected and analyzed EPR and ENDOR results at Northwestern University, prepared manuscript, and generated figures.

Co-Author: Amanda S Byer

Contributions: Synthesized anSAM, prepared ENDOR samples of LAM with labeled lysine and anSAM, prepared ENDOR samples of LAM with lysine and labeled anSAM. Assisted in manuscript preparation and generation of figures.

Co-Author: Krista A Shisler

Contributions: Prepared ENDOR samples of LAM with labeled lysine and anSAM, prepared ENDOR samples of LAM with lysine and labeled anSAM. Purchased different lysine labels for ENDOR analysis. Assisted in development of new ENDOR sample preparations. Assisted in manuscript editing.

Co-Author: Tilak Chandra

Contributions: Assisted in the syntheses of anSAM through the synthesis of anhydroadenosine triphosphate (anATP).

Co-Author: Joan B Broderick

Contributions: Provided interpretation of the ENDOR results, provided insights into the preparation of anSAM and ENDOR samples, and aided in preparation of manuscript and figures.

Contribution of Authors and Co-Authors Continued

Co-Author: Brian M Hoffman

Contributions: Provided interpretation of the ENDOR results, and aided in preparation of manuscript and figures.

Manuscript Information Page

Masaki Horitani, Amanda S Byer, Krista A Shisler, Tilak Chandra, Joan B Broderick, Brian M Hoffman
Journal of the American Chemical Society
Status of Manuscript:
____ Prepared for submission to a peer-reviewed journal
____ Officially submitted to a peer-review journal
____ Accepted by a peer-reviewed journal
__X__ Published in a peer-reviewed journal

Publisher ACS Publications
Submitted January 15, 2015
Published April 29, 2015
In Volume 137, 7111-7121 (2015)

JACS
JOURNAL OF THE AMERICAN CHEMICAL SOCIETY
Article
pubs.acs.org/JACS

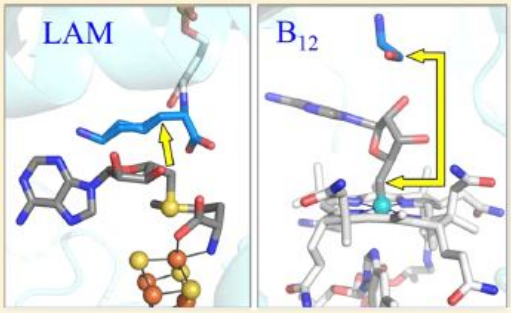
Why Nature Uses Radical SAM Enzymes so Widely: Electron Nuclear Double Resonance Studies of Lysine 2,3-Aminomutase Show the 5′-dAdo• "Free Radical" Is Never Free

Masaki Horitani,[†,§] Amanda S. Byer,[‡,§] Krista A. Shisler,[‡] Tilak Chandra,[‡] Joan B. Broderick,*[,‡] and Brian M. Hoffman*[,†]

[†]Department of Chemistry, Northwestern University, Evanston, Illinois 60208, United States
[‡]Department of Chemistry and Biochemistry, Montana State University, Bozeman, Montana 59717, United States

Supporting Information

ABSTRACT: Lysine 2,3-aminomutase (LAM) is a radical *S*-adenosyl-L-methionine (SAM) enzyme and, like other members of this superfamily, LAM utilizes radical-generating machinery comprising SAM anchored to the unique Fe of a [4Fe-4S] cluster via a classical five-membered N,O chelate ring. Catalysis is initiated by reductive cleavage of the SAM S−C5′ bond, which creates the highly reactive 5′-deoxyadenosyl radical (5′-dAdo•), the same radical generated by homolytic Co−C bond cleavage in B_{12} radical enzymes. The SAM surrogate *S*-3′,4′-anhydroadenosyl-L-methionine (anSAM) can replace SAM as a cofactor in the isomerization of L-α-lysine to L-β-lysine by LAM, via the stable allylic anhydroadenosyl radical (anAdo•). Here electron nuclear double resonance (ENDOR) spectroscopy of the anAdo• radical in the presence of ^{13}C, ^{2}H, and ^{15}N-labeled lysine completes the picture of how the active site of LAM from *Clostridium subterminale* SB4 "tames" the 5′-dAdo• radical, preventing it from carrying out harmful side reactions: this "free radical" in LAM is never free. The low steric demands of the radical-generating [4Fe-4S]/SAM construct allow the substrate target to bind adjacent to the S−C5′ bond, thereby enabling the 5′-dAdo• radical created by cleavage of this bond to react with its partners by undergoing small motions, ~0.6 Å toward the target and ~1.5 Å overall, that are controlled by tight van der Waals contact with its partners. We suggest that the accessibility to substrate and ready control of the reactive C5′ radical, with "van der Waals control" of small motions throughout the catalytic cycle, is common within the radical SAM enzyme superfamily and is a major reason why these enzymes are the preferred means of initiating radical reactions in nature.

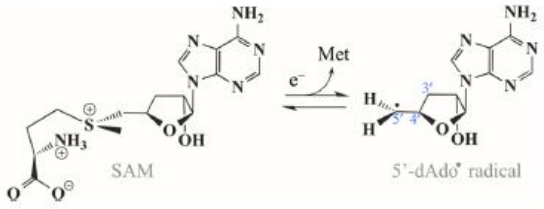


INTRODUCTION

Lysine 2,3-aminomutase (LAM) is a member of the radical *S*-adenosyl-L-methionine (SAM) enzyme superfamily,[1,2] whose reactions are initiated by radical-generating machinery comprising SAM anchored to the unique Fe of a [4Fe-4S] cluster via a classical five-membered N,O chelate ring formed by the methionine.[3] This novel structural motif for radical generation was discovered by electron nuclear double resonance (ENDOR) spectroscopy of pyruvate formate-lyase activating enzyme (PFL-AE)[4−6] and LAM,[7] and subsequently visualized by X-ray structure determination of these two enzymes as well as other superfamily members.[1,8−10] Electron transfer from the $[4Fe4S]^{1+}$ cluster initiates radical SAM reactions by reductive cleavage of the S−C5′ bond to create the highly reactive 5′-deoxyadenosyl radical (5′-dAdo•) (Scheme 1).[1]

The 5′-dAdo• radical is common to both radical SAM and B_{12}-dependent enzymes, with the latter generating this radical through homolytic cleavage of the Co−C5′ bond of the B_{12} coenzyme.[11]

Scheme 1



LAM utilizes the radical-SAM machinery to isomerize L-α-lysine to L-β-lysine (Scheme 2) in a reaction directly analogous to the B_{12}-dependent isomerases.[11−13]

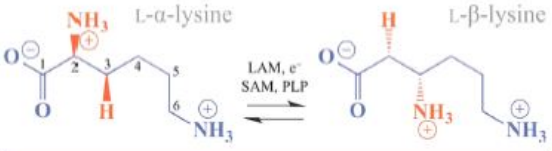
The reactive 5′-dAdo• radical formed by reductive cleavage of SAM (Figure 1, state **2**)[1] abstracts an H atom from substrate

Received: January 15, 2015
Published: April 29, 2015

ACS Publications © 2015 American Chemical Society

DOI: 10.1021/jacs.5b00498
J. Am. Chem. Soc. 2015, 137, 7111−7121

Scheme 2



bound to pyridoxal 5′-phosphate (PLP) to form 5′-deoxyadenosine (5′-dAdoH) and the α-Lys• radical (Lys•) (state **3**). This radical isomerizes to the β-Lys• radical (state **4**), which then abstracts an H atom from 5′-dAdoH to form β-Lys and 5′-dAdo• radical (state **5**); the latter then regenerates SAM. A schematic representation of these states is provided in Figure 1, with individual states numbered for easy reference throughout this paper.

Multinuclear ENDOR spectroscopy (^{13}C, ^{1,2}H, ^{31}P, and ^{14}N) led us to propose that inner sphere electron transfer from the reduced $[4Fe\text{-}4S]^{+}$ cluster cleaves the S−C5′ bond of SAM to form the 5′-dAdo• radical, while the sulfur of methionine becomes the sixth ligand to the unique iron.[7] This approach also was used to characterize the active site of LAM in intermediate states that contain the isomeric substrate radicals or analogues.[14] With L-α-lysine as substrate, the β-Lys• radical (state **4**) produced by H atom abstraction and rearrangement was monitored. In parallel, state **3** was probed through use of two substrate analogues (*trans*-4,5-dehydro-L-lysine and 4-thia-L-lysine), which generate stable analogues of the α-Lys• radical. This study provided a first glimpse of the motions of active site components during catalytic turnover, and suggested a possible major movement of PLP during catalysis. The principal focus of that work, however, was on the relative positions of the carbons involved in H atom transfer. By use of ENDOR to study hyperfine couplings to the substrate radicals it was concluded that the active site facilitates hydrogen atom transfer by enforcing van der Waals contact between radicals and their reacting partners, and that this constraint "tames" the highly reactive 5′-dAdo• radical, enabling the enzyme to minimize and even eliminate side reactions of this highly reactive species.

Noticeably absent from this or *any* study of radical SAM enzymes was any direct examination of the central event in the catalytic cycle of a radical SAM enzyme: the creation of the 5′-dAdo• radical by reductive S−C5′ bond cleavage, and its subsequent migration to the site of H atom abstraction from substrate (state **2**). Of all steps in the cycle, one would presume this must be the most tightly controlled, so as to occur without side reaction of the 5′-dAdo• radical with the environment. The intermediate 5′-dAdo• radical, however, is so reactive that it has never been observed, either in radical SAM or B_{12}-dependent enzymes, precluding characterization of this step.

To overcome this obstacle, Frey, Reed, and co-workers developed the SAM surrogate, *S*-3′,4′-anhydroadenosyl-L-methionine (anSAM).[15,16] The compound is a true cofactor for LAM, catalyzing the isomerization shown in Scheme 2 with a specific activity of 0.10 ± 0.02 IU/mg, compared to 35−40 IU/mg for the natural cofactor SAM.[15] However, when the $[4Fe\text{-}4S]^{1+}$ donates an electron to anSAM, cleaving the S−C5′ bond, this forms the stable allylic anhydroadenosyl radical (anAdo•) (Scheme 3) which can be used to investigate active site rearrangements through use of ENDOR spectroscopy. Once the catalytically competent 5′-dAdo• *or* anAdo• radicals are "born", the active site must than *precisely* shepherd the radical to the substrate site of H atom abstraction, so as to avoid side reactions, a process that has been incisively studied with B_{12}-dependent enzymes.[17−25] We here probe this rearrangement in

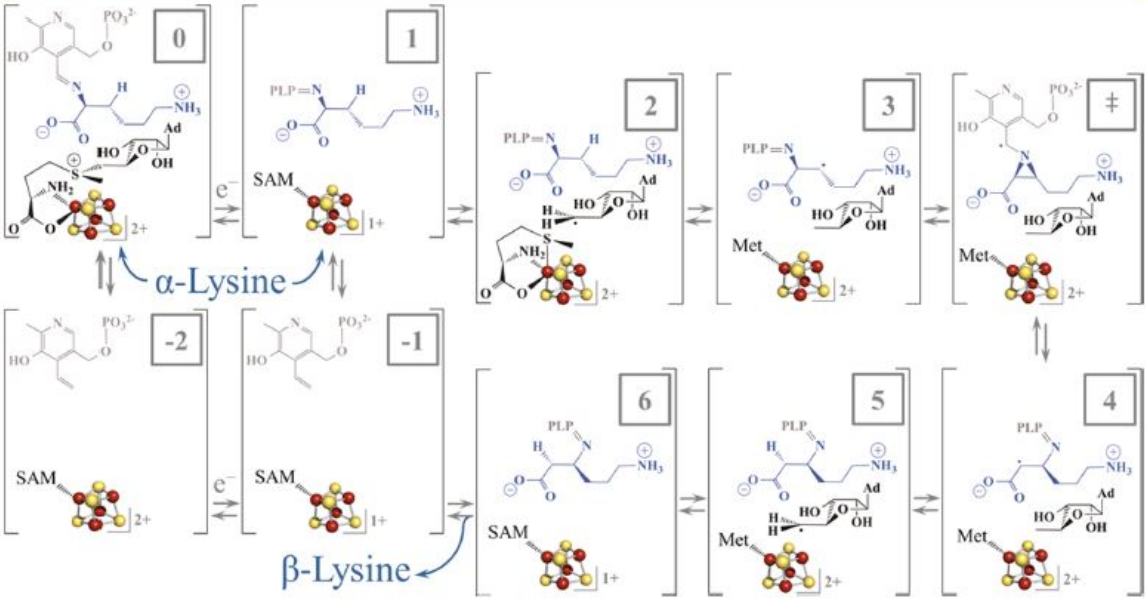
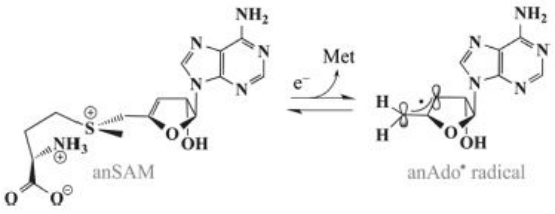


Figure 1. Steps in the reaction catalyzed by LAM. State **0** is the oxidized $[4Fe\text{-}4S]^{2+}$ state with SAM coordinated to the unique iron of the cluster and substrate Lys present as a Schiff base. One-electron reduction of the cluster provides state **1**, which initiates reductive cleavage of SAM to generate the 5′-dAdo• in state **2**. States **3**−**6** represent the radical rearrangement of α-lysine to β-lysine, abstraction of H• from 5′-dAdoH, and reformation of SAM. PLP is depicted in grey, while lysine is in blue.

DOI: 10.1021/jacs.5b00498
J. Am. Chem. Soc. 2015, 137, 7111−7121

Scheme 3



LAM through the use of $^{13}C/^{1,2}H/^{15}N$ ENDOR to monitor the distances and interactions between the anAdo• radical and multiple sites of isotopically labeled Lys substrate, especially the site of H atom abstraction. We also probe the distance to the $-S^{13}CH_3$ of the methionine formed by SAM cleavage.

Comparison of these ENDOR results for state **2** with the X-ray crystal structure of state **0**, both of enzyme from *C. subterminale*, reveals how the active site of LAM "tames" the 5′-dAdo• radical: this "free radical" is never free. Substrate binds with the 3-C atom of Lys, from which the target H is abstracted, adjacent to the S–C5′ bond of SAM, Figure 2(A), an arrangement similar to that

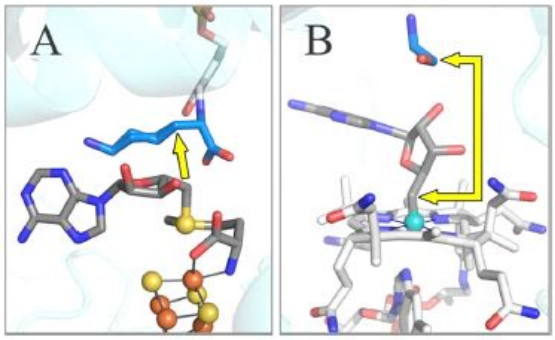


Figure 2. Active site structure of LAM (A) and ethanolamine ammonia-lyase (EAL) (B). The illustration of EAL contains the B_{12} cofactor as modeled from the crystal structure of EAL with the analogue adeninylpentylcobalamin. The yellow arrows show the distance from C5′ prior to S–C5′ or Co–C5′ bond cleavage, to target carbon atom in the substrate. PDB IDs are 2A5H (LAM) and 3ABS (ethanolamine ammonia-lyase). Carbon atoms are colored as: blue for substrate, dark grey for adenosine and SAM, and light grey for cobalamin and PLP.

found in all other structures of radical SAM enzymes with bound substrate.[10] As a result, upon cleavage of the S–C5′ bond only minimal motions of the 5′-dAdo• radical are needed for it to carry out H atom abstraction from substrate, during which the radical is chaperoned by van der Waals contact with its reaction partners. Integration of this study with our previous study[14] of states **3** and **4** completes a picture in which side reactions of the 5′-dAdo• radical are eliminated both at the beginning and the end of the catalytic cycle because this radical undergoes only small motions, which are controlled by "van der Waals constraints".

We suggest that the accessibility of the C5′ radical to highly diverse substrates is a major reason why evolution spread the use of this construct across all of the kingdoms of life. In contrast, for B_{12} enzymes, the steric demands of the cofactor force the substrate target to bind farther from the nascent radical at C5′, Figure 2(B), and C5′ must therefore migrate larger distances to reach the target.[17−23] The high steric constraints of the coenzyme B_{12} thus may explain why evolution has found so few uses for this radical generating machinery, which is limited to a few reactions involving small molecules, and to the animal kingdom.[11,13,26−30]

■ MATERIALS AND METHODS

Materials. Adenosine triphosphate (ATP), L-methionine, L-cysteine, L-lysine, pyridoxal 5′-phosphate (PLP), adenylate kinase, phosphocreatine kinase, and phosphocreatine were purchased from Sigma. Uniformly labeled ^{13}C and ^{15}N L-lysine were purchased from Cambridge Isotope Laboratories. D,L-lysine-1,2-^{13}C and D,L-lysine-2-^{13}C were purchased from Aldrich. L-Lysine-2,6,6-^{2}H, L-lysine-3,3,4,4,5,5,6,6-^{2}H and D,L-lysine-2-^{15}N were purchased from CDN Isotopes. Sodium dithionite was purchased from Acros Organics and ammonium iron(II) sulfate was purchased from Fisher Chemicals. L-[Methyl-^{13}C]-methionine was purchased from Cambridge Isotope Laboratories. All labeled substrates had a minimum of 99 atom % labeling. L-[U-^{14}C] lysine was obtained from NEN Life Sciences Products. SAM and anSAM were prepared in our laboratory as described in the following sections. All other chemicals and reagents were of the highest purity and used as supplied.

Preparation of LAM. All experiments described herein utilized LAM from *Clostridium subterminale* SB4. Genetic constructs containing the LAM gene from *C. subterminale* SB4 (a gift from Perry Frey) were appended with a C-terminal 6-histidine tag by ligation into pET-23a and then transformed into *Escherichia coli* BL21(DE3)pLysS (Stratagene) cells for protein overexpression. The transformation was plated on LB agar plates containing 50 μg/mL of ampicillin. A single colony was used to inoculate 50 mL of LB media containing ampicillin in a 37 °C incubator shaker at 250 rpm. The overnight growth was then transferred to a New Brunswick Bioflo 110 anaerobic fermentor (10 L) with nutrient enriched LB/ampicillin, and grown with shaking at 250 rpm to an optical density (OD) of ∼0.5 at 600 nm. Once the desired OD was reached, protein expression was induced with IPTG (1 mM final concentration) and supplemented with ferrous ammonium sulfate and zinc sulfate. Cells were then allowed to grow with shaking for an additional 2 h, then they were cooled to approximately 30 °C and additional ferrous ammonium sulfate was added. The culture was ultimately cooled to 4 °C and purged with nitrogen for an additional 15 h. The cells were then centrifuged and the resulting cell pellets were stored at −80 °C until further use.

Cell lysis and protein purification were carried out under anaerobic conditions in a Coy chamber. Cell pellets were thawed and resuspended in a lysis buffer containing 50 mM EPPS, 300 mM KCl, 0.1 mM lysine, 10 μM PLP, pH 8.0, 1% Triton X-100, 10 mg PMSF, 9 mg lysozyme, ∼1 mg RNase A and DNase I per 50 mL, respectively. The lysis mixture was stirred for ∼1 h and then the lysate was centrifuged in gastight bottles at 18 000 rpm for 30 min. The resulting supernatant was loaded onto a HisTrap Ni^{2+} affinity column (GE healthcare) equilibrated with 50 mM EPPS, 300 mM KCl, 0.1 mM L-lysine, 10 μM PLP, 10 mM imidazole, pH 8.0 (buffer A). Buffer A was utilized for column equilibration and washing. The protein elution was accomplished by increasing the imidazole concentration in a stepwise manner from 10 to 20 to 50 to 75 to 100% using buffer B (50 mM EPPS, 300 mM KCl, 0.1 mM L-lysine, 10 μM PLP, pH 8.0, 500 mM imidazole). Eluted protein (20 and 50% B) was concentrated using a Millipore (13−14 kDa MWCO) spin concentrator. After purification and concentration, the protein was flash frozen in liquid N_2 and stored at −80 °C or in liquid N_2 until further use. The concentrated protein was dialyzed in 50 mM EPPS, 1 mM dithiothrietol, 0.1 mM L-lysine, 10 μM PLP, pH 8.0 prior to reconstitution. The concentration of the protein was determined by the Bradford[31] method, and the iron analysis was done by the colorimetric iron assay described by Fish.[32]

A reconstitution was performed after protein centrifugation and incubation with dithiothreitol (5 mM) similar to that previously described.[33] Sodium sulfide nonahydrate and ferrous ammonium sulfate were added incrementally over 1−2 h, with gentle stirring, to a final concentration of 6× the protein concentration. The solution was incubated for 6 h at 4 °C before being centrifuged, concentrated and

DOI: 10.1021/jacs.5b00498
J. Am. Chem. Soc. 2015, 137, 7111−7121

passed over a desalting G25 column in buffer (50 mM EPPS, 1 mM DTT, 10 μM PLP, pH 8.0). The protein sample was then concentrated further. All purification was performed in an anaerobic coy chamber.

Preparation of anSAM. The synthesis of (3′,*A*′)-anhydroadenosine and subsequent preparation of anSAM was similar to that described by Magnusson and Frey,[16] but with alterations as described herein. The enzymatic reaction implemented to phosphorylate (3′,)-anhydroadenosine requires adenylate kinase, adenosine kinase, and phosphocreatine kinase. The adenylate kinase and the phosphocreatine kinase were obtained from commercial sources and dialyzed into the assay buffer. The adenosine kinase was prepared in our lab with methods similar to those described previously,[34] with the following adjustments. Human T cell cDNA (Molt 14) was a generous gift of the Jutila lab at MSU, and was used for amplification of the adenosine kinase gene with the following promoters:

Forward: 5′ CGG GCA GCA TAT GAC GTC AGT CAG AGA AA 3′.

Reverse: 5′ GCG TTC GGA TCC ATC AGT GGA AGT CTG G 3′.

The amplified DNA was ligated into the T7 based expression vector, pET-14b (Novagen), which also introduces a polyhistidine tag for protein purification. The plasmid with insert was transformed into XL1 Blue supercompetent cells for plasmid amplification, and the purified plasmid was then transformed into BL21(DE3)pLysS for protein expression. Successful expression of this protein required culture temperatures near 22 °C due to formation of inclusion bodies at higher temperatures. Protein expression was induced by addition of IPTG at OD_{600nm} of approximately 0.5; the growth was supplemented with glucose (2 mg/mL) ~5 h after induction and harvested 22 h after induction. The cells were lysed in Tris pH 7.5 buffer (10 mL/g of cells) containing lysozyme (0.2 mg/mL), PMSF (0.5 mg/mL), DNase I (10 μg/mL), RNase A (10 μg/mL), $MgSO_4$ (1 mM), and dithiothreitol (1 mM), by sequentially freezing and thawing the suspension three times. The clarified lysate was fractionated by ammonium sulfate precipitation, and the adenosine kinase precipitated in the 65% to 100% ammonium sulfate cut. The precipitated adenosine kinase was dissolved in 10 mM Tris-HCl/1 mM DTT pH 7.5 and dialyzed against the same buffer before applying it to a HisTrap column equilibrated with 20 mM Tris-HCl/100 mM KCl/10 mM imidazole (pH 7.5). The protein was eluted using a gradient to 20 mM Tris-HCl/100 mM KCl/500 mM imidazole (pH 7.5), eluting at ~182 mM imidazole. After buffer exchange into Tris-HCl (10 mM, pH 7.5) with dithiothreitol (1 mM), the AdoK was loaded onto an HR16/10 DEAE Sephacel column equilibrated with the same buffer. AdoK was eluted with a linear gradient of 0−100 mM KCl in the same buffer, eluting at ~40 mM KCl. The AdoK was then exchanged into PIPES (25 mM), $MgCl_2$ (1.25 mM), pH 7.5.

In order to convert anhydroadenosine to anhydroATP, PIPES (25 mM), $MgCl_2$ (1.25 mM), BSA (0.01% w/v), anhydroadenosine (3 mM), phosphocreatine (20 mM), adenosine kinase (1000 IU), adenylate kinase (2000 IU), and phosphocreatine kinase (2000 IU) were combined while maintaining pH at approximately 7.0; GTP (0.6 mM) was added to initiate the phosphorylation. The reaction was monitored by TLC and quantified by HPLC. Upon completion of the phosphorylation reactions, the anhydroadenosine triphosphate (anATP) was purified using a HR10/30 DEAE Sephadex A_{25} column with a linear gradient of NH_4HCO_3 (10−500 mM); the anATP elutes around 350 mM ammonium bicarbonate. The anATP was then rotovapped or lyophilized to a solid.

SAM synthetase was expressed and purified as described by Markham et al.,[17] with some minor modifications.[4] In a reaction similar to that described by Park et al.[35] and modified by us previously[4] and further modified herein, we utilized SAM synthetase to enzymatically transform anhydroadenosine triphosphate into anhydro-*S*-adenosyl-L-methionine (anSAM) in EPPS buffer (50 mM, pH 8.0). The anSAM was then purified on a Source 15S cation exchange column with a linear gradient of 0 to 1 M HCl, as confirmed by NMR (Bruker Cryomagnet BZH 500/51; 64.2A, 11.70 T) and LC−MS (Agilent HPLC 1100 with Bruker MicroTOF). AnSAM containing ^{13}C in the methyl group was synthesized from ATP and L-[methyl-^{13}C]-methionine by use of SAM synthetase-catalyzed reactions as described herein.[4]

Preparation of ENDOR Samples. ENDOR samples were prepared under anaerobic conditions in a Coy anaerobic chamber. The purified LAM (0.90 mM LAM, ~270 μM active sites) was activated by incubation with 10 mM L-cysteine in the presence of 0.90 mM PLP, 1.0 mM ammonium iron(II) sulfate, and 15% glycerol in 42 mM EPPS buffer at pH 8.0 and 37 °C for 4 h. The activated enzyme was concentrated with Microcon 30 centrifugal filter devices (Millipore) so that the concentration of enzyme active site was ~1.2 mM. The concentrated enzyme was quickly mixed with anSAM (or [methyl-^{13}C]-anSAM), sodium dithionite, and L-lysine (one of the following: unlabeled L-lysine, [u-^{13}C,^{15}N]-L-lysine, [1,2-^{13}C]-D,L-lysine, [2-^{13}C]-D,L-lysine, [2,6,6-^{2}H]-L-lysine, [3,3,4,4,5,5,6,6-^{2}H]-L-lysine, [2-^{15}N]-D,L-lysine) in a 0.65 mL microcentrifuge tube. The mixed sample was rapidly transferred to an ENDOR sample tube and frozen in liquid nitrogen. The time scale from mixing to sample freezing was from 1 to 1.5 min, sufficient time for equilibrium to be attained in the reaction of 0.9 mM LAM. In all samples, the concentrations of the enzyme active site were ~0.9 mM; the concentrations of anSAM, sodium dithionite, and lysine (or its analogue) were 3.0, 6.0, and 40 mM, respectively. All assays were performed in an MBraun anaerobic chamber at <1 ppm oxygen.

EPR and ENDOR Spectroscopy. X-band CW electron paramagnetic resonance (EPR) measurements were performed by a Bruker ESP 300 spectrometer equipped with an Oxford Instruments ESR 910 continuous He flow cryostat.

Q-band CW ENDOR spectra were collected on a spectrometer with a helium immersion dewar previously reported.[36,37] All measurements were done at 2 K. Stochastic field-modulation detected ENDOR technique, which has been first reported by Brueggeman and Niklas,[38] was here utilized for ^{1}H ENDOR measurement. In the stochastic ENDOR sequence, RF is randomly hopped over the range of spectrum region with the subtraction of background signal (RF off) at each frequency.

Pulsed ENDOR spectra were collected on a spectrometer described earlier,[19] equipped with a helium immersion dewar for measurements at 2 K. ENDOR measurements employed the Mims pulse sequence ($\pi/2-\tau-\pi/2-T-\pi/2-\tau-$echo, RF applied during interval T) for small hyperfine couplings or the Davies pulse sequence ($\pi-T-\pi/2-\tau-\pi-\tau-$echo) for large hyperfine couplings.[39] To determine the sign of hyperfine couplings we utilized the recently developed Pulsed ENDOR Saturation and Recovery (PESTRE) technique, which employs a multipulse sequence comprised of the Davies ENDOR sequence.[40]

For nuclei (N) of spin $I = 1/2$ (^{13}C, ^{1}H, ^{15}N) interacting with a $S = 1/2$ paramagnetic center, the first-order ENDOR spectrum for a single molecular orientation is a doublet with frequencies (ν_+/ν_-),

$$\nu_{\pm} = \nu_N \pm A/2 \tag{1}$$

where ν_N is the Larmor frequency and A is the orientation-dependent hyperfine constant. For nuclei with $I = 1$ (^{2}H), the first-order ENDOR condition can be written:

$$\nu_{\pm}(\pm) = \left|\nu_N \pm \frac{A}{2} \pm \frac{3P}{2}\right| \tag{2}$$

where P is the orientation-dependent quadrupolar splitting.

For a nucleus with hyperfine coupling, A, Mims pulsed ENDOR has a response R that depends on the product, $A\tau$, according to the equation,

$$R \sim [1 - \cos(2\pi A\tau)] \tag{3}$$

This function has zeros, corresponding to minima in the ENDOR response (hyperfine "suppression holes"), at $A\tau = n$; $n = 0, 1, ...$, and maxima at $A\tau = (2n + 1)/2$; $n = 0, 1, ...$[8,20] The "holes" at $A = n/\tau$, $n = 1, 2, 3, ...$, can be adjusted by varying τ. However, the "central", $n = 0$, hole at $\nu = \nu_N$ persists regardless. This can be of significance in distinguishing a tensor that is dominated by anisotropic interactions from one that is dominated by isotropic ones. The latter would never lead to ENDOR intensity near ν_N; the former does so for certain orientations, but the $\nu = 0$ Mims hole tends to diminish the differences between the two cases.

Neither the very small dispersion of g values nor the hyperfine coupling to the nuclei of anAdo• radical are resolved in the 35 GHz EPR spectra of state **2** of LAM prepared with anSAM. Consequently,

DOI: 10.1021/jacs.5b00498
J. Am. Chem. Soc. 2015, 137, 7111−7121

ENDOR spectra of nuclei hyperfine-coupled to the radical collected at the field of maximum EPR intensity are an isotropic powder-averaged pattern. Simulation of these powder patterns for nuclei of the anAdo• radical itself are analyzed in terms of the spin distribution among the carbons of the allyl fragment as a test of the reported spin distribution.[16] Simulation of the ENDOR patterns for nuclei of substrate yield hyperfine tensors that allow estimation of distances between the radical center and those nuclei, as well as bonding and orbital overlap properties, but do not yield orientations relative to the g-frame or molecular frame. All simulations were done with the program, ENDORSIM.[41]

The central goal of these measurements is to determine the position of the reactive C5′ carbon relative to the atoms of the L-Lys substrate through analysis of the hyperfine coupling tensor, **A**, between the nuclei of Lys and C5′ of the anAdo• radical. Such a tensor is the sum of a possible contribution from spin delocalization across the noncovalent "interface" between anAdo• radical and atoms of Lys (see Discussion), the so-called isotropic coupling (coupling constant, A_{iso}), and the through-space dipolar coupling between the nucleus of Lys and the spin of the anAdo• radical. The distance-dependence of this latter term yields the sought-for metrical result.

In principle, the dipolar term is the sum of the interactions with the spin density on all three allyl carbons, the two with large spin densities $\rho(C5') \sim \rho(C3') \sim 0.59$, and the one with small spin density, $\rho(C4') \sim -0.18$.[16] However, C5′ of anAdo• is close to or even in van der Waals contact with Lys nuclei, whereas the other carbon with high spin density, C3′, is much farther away, and C4′ has low spin density, and so we began our determination of distances between C5′ and atoms of Lys by ignoring the contribution from spin on the allyl carbons other than C5′. In this case the through-space hyperfine coupling to anAdo• radical spin on C5′ is described by the axial form

$$\mathbf{T} = [T_1, T_2, T_3] = [-T, -T, 2T] \quad (4)$$

In the point-dipole approximation for the electron spin, the parameter **T** is related to the distance from C5′ to the nucleus being examined through the relationship,

$$2T = 2g_N\beta_N g_e\beta_e\rho(C5')/r^3 \quad (5)$$

where $\rho(C5') = +0.59$. As described in the Discussion, at the (relatively) short distances associated with 2-^{13}C and 3-^{2}H: one must take into account a correction to the point-dipole equations associated with the distributed nature of the spin in the 2pπ orbital of C5′ through use of equations presented by McConnell and Strathdee.[42]

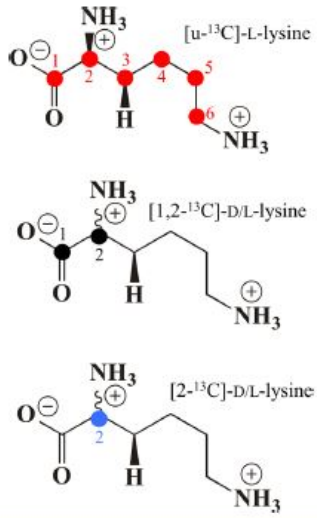
We tested the validity of the ignoring the effects of spin density on C4′ and C3′ in the determination of distances between C5′ and atoms of Lys, in the following fashion. As described below we used the distances between C5′ and various nuclei of Lys as calculated through the use of spin density on C5′ alone to estimate the position of C5′ of anAdo• radical, then approximated the position of the remainder of the radical by simply translating the Ado fragment present in the state 5 crystal structure so as to place C5′ at that position (see Figure 7, below). The positions of C4′ and C3′ within this heuristic structure were then used as input into previously published equations[43] to test whether the spin density on those atoms materially alters the dipolar interaction tensor, **T**, and hence the calculated distances of C5′ to the Lys nuclei. The extended treatment shows that the small negative spin density on C4′ adjacent to C5′, $\rho(C4') = -0.18$, would tend to slightly shorten the estimated distance from C5′ to target atoms and to introduce a small rhombicity ($|T_2| > |T_1|$, eq 4) to the coupling tensor. However, within the precision of these calculations, this effect is countered by the effect of the large positive spin density, $\rho(C3') = +0.59$, on the more remote C3′ to lengthen the calculated distance and to introduce a rhombicity of the opposite sense ($|T_2| < |T_1|$, eq 4), the two effects thus largely cancel each other; most importantly even when the extended model predicted a non-negligible rhombicity, it gave a value of $2T$, the largest dipolar splitting, not significantly different from that obtained by using the distance to C5′ in eq 5. Hence, for the purposes of this paper, the simplified analysis in terms of spin density on C5′ alone is satisfactory.

RESULTS

EPR Measurements and Analysis for Stochastic ^{1}H ENDOR for anAdo• Radical. To help refine the analysis of the anAdo• radical properties, we collected 35 GHz echo-detected EPR spectra and stochastic CW ^{1}H ENDOR spectra, of the radical presented in Figure S1. The simulation parameters that best fit the ^{1}H ENDOR spectra (Table S1) differ only minimally from those previously reported.[16]

Substrate ^{13}C ENDOR Measurements. The 35 GHz Pulsed Davies ^{13}C ENDOR spectra of LAM with anSAM and PLP linked to isotopically labeled lysines (Chart 1;[u-^{13}C]-L-lysine, [1,2-^{13}C]- and [2-^{13}C]- D/L-lysine) are shown in Figure 3.

Chart 1



These spectra were obtained by subtracting the spectrum of a sample prepared with natural-abundance lysine, which exhibits a

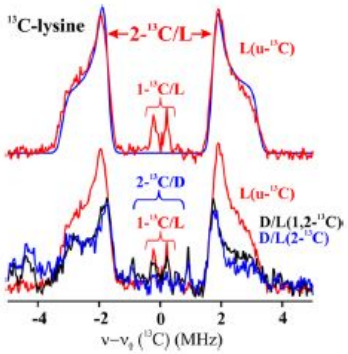


Figure 3. Davies ^{13}C ENDOR for LAM with anSAM, PLP and substrate with simulation spectrum. Spectra were collected at the radical peak. The baseline spectrum from unlabeled Lys has been subtracted for all Davies spectra. Upper: u-^{13}C Lys, with assignments derived from spectra of isotopologues. Simulation, upper, in blue calculated with parameters: A_{iso} = 4.5 MHz, $2T$ = 2.0 MHz, ENDOR line-width, 0.35 MHz. Lower: as described in text using partially labeled Lys (Chart 1). Experimental conditions: MF = 34.6−34.8 GHz, MW pulse length (π) = 120 ns, τ = 600 ns T = 2 K.

DOI: 10.1021/jacs.5b00498
J. Am. Chem. Soc. 2015, 137, 7111−7121

broad signal at $\delta\nu \sim -3$ MHz attributable to the ν_+ partner of the ^{14}N double-quantum transitions (Figure S2 (gray)), and then normalizing the electron spin echo amplitudes.

The spectrum for uniformly labeled Lys consists of two ^{13}C ENDOR doublets, one with couplings (splittings) ranging from ~3 to ~8 MHz, the other with a weak coupling of ~0.4 MHz. The larger coupling is shown to be associated with 2-^{13}C by its persistence in the samples prepared with [1,2-^{13}C]- and [2-^{13}C]-lysine (Figure 3, lower). The weak coupling is associated with 1-^{13}C, as shown by its persistence in the [1,2-^{13}C]-Lys sample and its negligible presence in the [2-^{13}C]- sample (Figure S3, S4); the analysis of the 2-C response is given in the next subsection; that of 1-C is given in SI.[44]

Interestingly, the intensity of both ENDOR signals in Figure 3, which are normalized to the EPR echo intensity from the anAdo• radical formed by anSAM cleavage, is larger in the spectra with [u-^{13}C]-L-Lys, compared to those with D/L-Lys [1,2-^{13}C] and [2-^{13}C]. We interpret this to mean that anSAM is cleaved in ternary complexes with both D- and L-Lys, but that L-Lys is bound preferentially, and with the 2-^{13}C of D-Lys farther from the anAdo• radical. This inference is derived from the spectra of Figure 3, lower and the expansion of the frequency range, ±2 MHz in Figure S5. These spectra show that the ENDOR responses for both D/L-Lys [1,2-^{13}C] and [2-^{13}C] exhibit an extremely weak, sharp doublet with an intermediate coupling ($A_{obs} = \sim 2$ MHz), that we may assign to 2-^{13}C of D-Lys bound in a nonproductive conformation, farther from C5′ of the anAdo• radical.

Analysis of 2-^{13}C ENDOR Response. The shape of the [2-^{13}C]-Lys signal is typical of a powder ENDOR "Pake pattern" (see Materials and Methods) in which an axial anisotropic coupling ($\mathbf{T} = [-T, -T, +2T]$) is combined with an isotropic coupling (A_{iso}), where T and A_{iso} have the same sign; as it is expected that T is dominated by through-space dipolar interactions between spin on C5′ and 2-^{13}C with $T > 0$, this implies that $A_{iso} > 0$. The sign of the 2-^{13}C hyperfine coupling constants is confirmed by pulsed ENDOR saturation and recovery (PESTRE) measurements (Figure S6).

In such a Pake pattern spectrum, the splitting between the intense "perpendicular" peaks of the two branches of the spectrum is $A_\perp = (A_{iso} - T)$, that between the extremal shoulders, is $A_\parallel = (A_{iso} + 2T)$, and the width of each branch is $3T/2$. Simulation of the spectrum gives $A_{iso} = +4.5$ MHz and $T = +1.0$ MHz. As the EPR and ENDOR measurements of anAdo• radical confirm that this radical has not formed a covalent bond to Lys, the observation of a substantial isotropic coupling to the noncovalently bonded 2-^{13}C (C_α) of Lys therefore is remarkable. Such couplings are normally found only when spin is transferred along a covalent pathway between electron spin and coupled nucleus. We show below that this finding instead is the consequence of a tight van der Waals contact between C5′ of anAdo• radical and 2-^{13}C (C_α) of Lys.

The anisotropic coupling matrix in principle is the sum of two axial matrices, the nonlocal contribution ($T_{n\text{-}loc}$) from through-space dipolar interaction between the electron spin of anAdo• radical and the ^{13}C nuclear spin, and a local contribution (T_{loc}), caused by interaction of electron spin density delocalized into the C−H bonds of 2-C of Lys: $\mathbf{T} = T_{loc} + T_{n\text{-}loc}$. Assuming the latter term comes from the point-dipolar interaction between 2-^{13}C nucleus and the spin density on C5′ ($\rho = 0.59$; SI), the distance from C5′ to 2-^{13}C of lysine, r, is estimated (see SI) to be $r \sim 2.7$ Å. However, the point-dipole treatment underestimates the interaction at short distances: the spin on C5′ is not confined to a point, but is distributed within its 2pπ orbital.[42] Application of the McConnell−Strathdee correction to the highly resolved axial 2-^{13}C ENDOR pattern (Figure 3) indicates that 2-C lies along the axis of the 2pπ C5′ orbital, as illustrated in Figure 4;[45] if

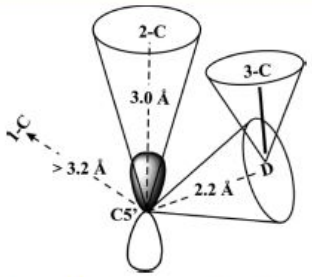


Figure 4. "Cone model" for ENDOR-derived constraints on the distances between C5′ of the anAdo• radical and the carbons and deuterons of Lys. The anAdo• 2pπ orbital is orienated towards the 2-C of Lys. Following the practice of McCracken and co-workers,[45] the direction of a C5′-nucleus vector is shown as lying roughly within the cone associated with the nucleus, and similarly for the 3-C−D vector. All distances are shown in Table 1.

2-C lay appreciably off the π-orbital axis, the anisotropic coupling would acquire a rhombic component absent here. Taking 2-C to lie precisely on-axis for concreteness, the correction yields a C5′ ↔ 2-C distance of ~3 Å,[42] satisfyingly in agreement with the van der Waals distance expected when a 2pπ-orbital contact is involved.

Pauli Spin Delocalization. Given the absence of a covalent bond between anAdo• radical and lysine, the presence of a significant isotropic hyperfine coupling to the 2-C ($C\alpha$) of substrate lysine, $A_{iso} = +4.5$ MHz, might appear surprising, as such couplings normally arise from through-bond spin delocalization. However, such spin transfer across a noncovalent contact is well documented. The paradigm for such spin transfer from a paramagnetic center to a closed-shell neighbor not linked by a covalent bond was provided long ago by H atoms incorporated in a noble gas (e.g., Kr) matrix, which shows a strong hyperfine coupling to matrix nuclei in the absence of covalent bond formation.[46,47]

The analysis of H-atom to noble gas-atom spin transfer[48] considered the consequences of a tight van der Waals contact between a paramagnetic center and a closed-shell neighbor. In such a structure, the electron charge cloud of the paramagnet's spin-bearing orbital overlaps the electron charge cloud(s) of the doubly occupied orbitals of the closed-shell neighbor, and a simple description of the electronic structure in terms of orbitals localized on only one or the other of the two centers violates the Pauli exclusion principle. Such overlap can, however, be properly described by requiring that the one-electron orbital containing the unpaired electron, in this case the C5′ 2pπ orbital ($|2p\pi C5'\rangle$) of the anAdo• allyl radical, be orthogonalized to the one-electron orbital(s) of the closed-shell neighbor, in this case 2-C.[48] This process delocalizes the spin-bearing orbital onto the closed-shell neighbor, 2-C: the spin-bearing C5′ 2pπ orbital ($|2p\pi C5'\rangle$) acquires a small contribution from sp^3 orbitals of 2-C ($|sp^3\rangle_i$), and this "Pauli delocalization" introduces an isotropic hyperfine interaction with the closed-shell neighbor. Thus, the presence of an isotropic coupling to 2-^{13}C reveals that this substrate atom is in tight van der Waals contact with the C5′ π atomic orbital of the spin-bearing allyl, π molecular orbital on the anAdo• radical.

DOI: 10.1021/jacs.5b00498
J. Am. Chem. Soc. 2015, 137, 7111−7121

This delocalization of the odd electron results in a hyperfine coupling for 2-^{13}C that can be approximated as

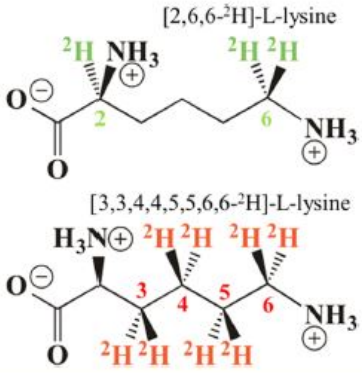
$$\rho_{2s} \approx N^2(1/4)\rho_C \sum_{i,C\alpha} S(2p\pi, sp^3)_i^2 \quad A(2\text{-}^{13}C) \approx +\rho_{2s}a_0 \tag{6}$$

where ρ_{2s} is the spin density transferred into the 2s orbital of Lys 2-C, the sum is over the four sp^3 orbitals of 2-C, $S(2p\pi, sp^3)_i$ is the C5′($2p\pi$) ↔ 2-C(sp^3)$_i$ overlap integral, ρ(C5′) = +0.59 is the spin density in C5′($2p\pi$), the factor of 4 reflects the 2s contribution to the 2sp^3 hybrid orbitals on 2-^{13}C, and N is the normalization factor for the orthogonalized orbital. Insertion of A(2-^{13}C) = 4.3 MHz into this formula shows that the actual spin delocalization onto 2-C is extremely small, $\rho_{2s} \sim 10^{-3}$. The operation of Pauli delocalization is supported by the PESTRE measurements, which show that A(2-^{13}C) > 0, in agreement with the prediction of eq 6.

Mims ENDOR from ^{2}H-Lys. In the conversion of state **2** to state **3** (Figure 1), a hydrogen atom on 3-C of Lys is abstracted by the C5′ radical to generate β-Lys● radical. Thus, the most important distance in state **2** is that between C5′ and the target proton on 3-C. In the X-ray crystal structure of state **0**, the distance from the C5′ in SAM to the nearest H on 3-C of Lys is 2.9 Å. This distance is too great to abstract a hydrogen atom from substrate,[49,50] so in the formation of state **2**, the 5′-dAdo● radical must move toward this hydrogen atom immediately after SAM cleavage, as is definitively shown by the ^{13}C ENDOR results described above.

To determine the distance from the C5′ of anAdo● radical to the substrate hydrogen atoms in state **2**, we collected ^{2}H Mims ENDOR of anAdo● radical in samples prepared with variously deuterated lysines (Chart 2; [3,3,4,4,5,5,6,6-^{2}H]-, [2,6,6-^{2}H]-)

Chart 2



and unlabeled Lys (Figure 5, inset). The [2,6,6-^{2}H]-Lys, which is not deuterated at the target 3-C site, showed a ^{2}H response with observed breadth of, A(^{2}H) ~ 0.6–7 MHz; when scaled by the ratio of nuclear g-factors, this corresponds to a ^{1}H response, A(^{1}H) ~ 4 MHz. The ^{13}C ENDOR discussed above clearly shows that upon cleavage of anSAM the anAdo● radical moves toward 2-C/3-C, which puts C5′ far from the 6-H, so we may assign the breadth of the [2,6,6-^{2}H]-Lys signal as being determined by the dipolar ^{2}H coupling between spin on C5′ of anAdo● radical to 2-H of Lys, giving a rough distance of about 3.8 Å between C5′ and 2-^{2}H.

The ^{2}H Mims ENDOR spectrum for [3,3,4,4,5,5,6,6-^{2}H]-Lys is much broader, Figure 5, and exhibits two well-defined pairs of

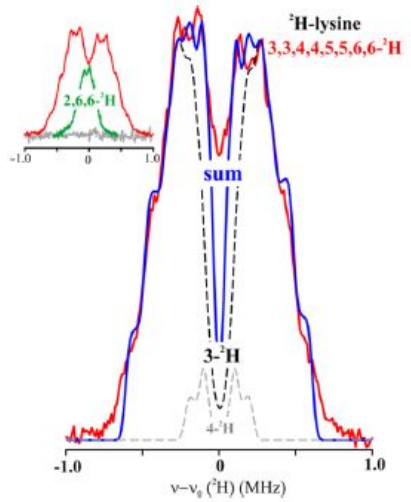


Figure 5. ^{2}H Mims ENDOR of LAM with anSAM/PLP/^{2}H-Lys. Experimental spectrum with [3,3,4,4,5,5,6,6-^{2}H]-Lys (red) overlaid with sum (blue) of the simulations of the 3-^{2}H (black dashed) and 4-^{2}H (gray dashed) signals. Inset: Overlay of experimental spectra for [3,3,4,4,5,5,6,6-^{2}H]-Lys (red) and [2,6,6-^{2}H]-Lys (green) and unlabeled Lys (grey). Simulation in main figure: Point-dipole interaction with 3-^{2}H, 2T = 0.96 MHz, P = [42 42, 84] kHz, ENDOR line width = 0.05 MHz; additional intensity in the frequency range, ±0.4 MHz is assigned to 4-^{2}H, with point-dipole interaction having with 2T = 0.45 MHz and ENDOR line width = 0.05 MHz. Conditions: microwave frequency = 34.77 GHz for [2,6,6-^{2}H]-Lys, 34.61 GHz for [3,3,4,4,5,5,6,6-^{2}H]-Lys, MW pulse length (π/2) = 50 ns, τ = 1000 ns for [2,6,6-^{2}H]-Lys, 500 ns for [3,3,4,4,5,5,6,6-^{2}H]-Lys, and T = 2 K.

shoulders on the "outsides" of the pattern. These shoulders are the quadrupole-split features associated with the maximum dipolar splitting, 2T = 0.96 MHz, by a single target 3-^{2}H nucleus of Lys. A C5′ ↔ 3-^{2}H distance in the reactive state **3** of 2.4 Å is obtained by interpretation of 2T within the point-dipole model, eq 5; incorporation of a McConnell and Strathdee[42] correction lowers the distance slightly, to 2.2–2.3 Å. As shown in the figure, the ENDOR response is well reproduced by a simulation that adopts such a dipolar coupling; the quadrupole coupling of a C–^{2}H bond is well-known to have axial symmetry with the unique axis along the bond,[51] and the magnitude of the observed quadrupolar splitting used in the simulation implies a large angle between the unique axis of the hyperfine tensor, associated with the C5′-3H vector, and the 3C–3H bond. (see Figure 4). Regardless of the precise details of the analysis, the size of the hyperfine coupling to 3-^{2}H, as manifest simply in the breadth of the spectrum, clearly indicates that the reactive C5′ site of the adenosyl radical achieves direct contact with its target proton upon cleavage of SAM.

Finally, we can comment on the other ^{2}H of the deuterated Lys. Considerations of a model for the full structure of state **5** presented below suggest that ENDOR intensity in the inner part of the ENDOR signal likely arises mostly from a 4-^{2}H, and this is included in the simulation. Given the tetrahedral geometry at 3-C and the close contact between one 3-^{2}H and C5′, then the other 3-^{2}H must be pointed "away" such that its distance to C5′ is so great as to yield an unresolvably small hyperfine coupling.

Distance from C5′ Methyl-^{13}C Methionine of anSAM. A 35 GHz Pulsed Mims ^{13}C ENDOR spectra of LAM with

DOI: 10.1021/jacs.5b00498
J. Am. Chem. Soc. 2015, 137, 7111–7121

[methyl-^{13}C]-anSAM, Lys and PLP is shown in Figure 6. The spectrum comprises a hyperfine-split doublet of asymmetric

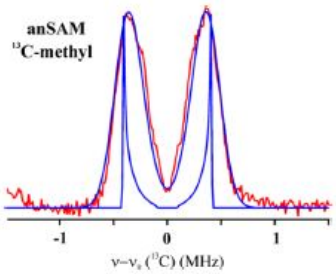


Figure 6. ^{13}C Mims ENDOR for LAM with [^{13}C-methyl]-anSAM, PLP and substrate with simulation spectrum. Spectrum collected at radical peak. Experimental conditions: MF = 34.74 GHz, MW pulse length (π/2) = 50 ns, τ = 400 ns for Mims, and T = 2 K. Simulations (blue) with ENDOR line-widths of 0 and 0.28 MHz; parameters, A_{iso} = −0.61 MHz, T = 0.21 MHz (distance r = 3.6 Å).

peaks in which individual features are unresolved because the line width is comparable to the dipolar coupling and because of Mims holes effects. Because of the poor resolution, simulations yield only a range of possible values for the hyperfine couplings: $0.39 < |A_{iso}| < 0.70$ (MHz); $0.12 < T < 0.43$ (MHz) (Figure S7). As with 2-^{13}C, the presence of an isotropic coupling implies van der Waals contact between the spin-bearing C5′ of the anAdo• radical and [methyl-^{13}C]-anSAM. The point-dipolar coupling corresponds to a range in distance between C5′ and methyl-carbon in methionine, $3.0 < r < 4.7$ (Å), substantially greater than the distance to C5′, with the favored simulation, shown in Figure 6, yielding a distance of C5′ of the anAdo• radical to the methyl carbon of cluster-bound methionine of $r \approx 3.6$ Å. The crystal structure shows that before reductive cleavage of SAM this distance is 2.94 Å. The lengthening of this distance after cleavage is in agreement with the idea that the distance between C5′ of anAdo• radical and the methyl-^{13}C of methionine has slightly lengthened as the radical moved toward the substrate after cleavage of anSAM. The simulation yields a negative value for A_{iso}, which implies the longer distance involves radical contact with a methyl-H, with spin-polarization of the C−H bond yielding a negative spin density of the C.

Constraints on the Distances from C5′ to other Lys Nuclei. ENDOR measurements have also been carried out on Lys 1-^{13}C and 2-^{15}N, as presented in SI. These spectra, like those for [methyl-^{13}C]-anSAM, yield constraints on the distance from C5′- to these nuclei; they are included in Table 1 and visualized in Figure 4.

Table 1

nucleus (N)	C5′ ↔ N distances (Å) (ENDOR)
1-C	>3.2
2-C	3.0
3-C	[a]
3-H	2.2−2.3
2-N	>3.2
methyl-carbon of Met	~3.6
2-H	~3.8

[a]Signal not resolved.

DISCUSSION

Radical SAM enzymes use a site-differentiated [4Fe-4S] cluster and SAM to initiate remarkably diverse radical reactions, nearly all of which are initiated by the 5′-dAdo• radical intermediate generated upon the reductive cleavage of SAM.[1,2] The 5′-dAdo• radical intermediate is a highly reactive primary carbon radical that has never been directly observed, although numerous lines of indirect evidence support its central role in both radical SAM and B_{12} reactions.[12,13,52] Key mechanistic questions for radical SAM enzymes revolve around how the reactivity of this initial radical is controlled and directed toward a single, well-defined hydrogen atom on substrate, in a reaction that is often both regio- and stereospecific. Because the 5′-dAdo• radical is so reactive, however, it has not been possible as of yet to directly observe it in an enzyme active site.

In the present work, we utilize the functional SAM analogue *S*-3′,4′-anhydroadenosyl-L-methionine (anSAM, Scheme 3), which contains a 3′-4′ double bond that provides allylic stabilization to the anAdo• radical, in order to directly probe the initial radical intermediate in lysine 2,3-aminomutase. Use of this stabilized anAdo• radical intermediate in conjunction with isotopically labeled Lys substrates and isotopic labeling of the methionine fragment of anSAM shows that the C5′ of SAM/anSAM moves a small distance toward the substrate site of H atom abstraction and away from the cluster-bound methionyl fragment upon anSAM S−C5′ bond cleavage.

Structural Consequences of SAM Cleavage. The ENDOR-derived metrical information for the relative position and orientation of the C5′ carbon of anAdo• radical analogue for the reactive 5′-dAdo• radical bound at the active site of *C. subterminale* SB4 LAM is summarized in Table 1 and Figure 4. When considered in the context of the crystal structure of *C. subterminale* SB4 LAM with bound SAM and Lys in precursor state **0**, these findings reveal the minimal extent of the active site rearrangements accompanying reductive S−C5′ bond cleavage and H atom abstraction from Lys, and the driving force for that rearrangement.

Of fundamental importance to efficient catalysis is the remarkably intimate positioning of the target H of substrate adjacent to C5′ of SAM in the ternary complex of state **0**, a separation of only 2.8 Å (Figure 2(A)). In conjunction with the dense packing of the LAM active site (Figure S10), this highly constrains the movements of 5′-dAdo• radical, *and* limits possible side reactions on its remarkably short journey to its destined reaction with a 3-H of Lys. To illustrate the efficiency introduced by the compact LAM active site, consider the implications of the two most robust C5′ ↔ substrate distances in state **2** as measured here.

The C5′ ↔ 2-C (Lys) distance in the LAM/SAM/Lys state **0** structure is 4.2 Å, while the S−C5′ bond length in SAM is 1.98 Å. Breaking that S−C5′ bond must force the two atoms apart, to a distance that approximates the sum of their van der Waals radii, ~3.2 Å (assuming 1.8 Å for S and 1.5 Å for the sp^2 carbon of C5′).[53] Thus, the reductive cleavage of the S−C5′ bond would immediately lengthen the S−C5′ distance by ~1.3 Å, quite likely "ballistically" driving the radical toward substrate. If bond-breaking were accompanied by the "most efficient" concomitant movement of C5′, namely displacement directly toward 2-C relative to a motionless S, *no* additional movement would be required to achieve the C5′ ↔ 2-C van der Waals contact distance of ~3 Å as found by ENDOR spectroscopy. Correspondingly, the C5′ distance to the actual target, 3-H

DOI: 10.1021/jacs.5b00498
J. Am. Chem. Soc. 2015, 137, 7111−7121

(Lys), in the LAM/SAM/Lys state **0** structure is 2.79 Å, and C5′ would need to move toward 3-H by only ~0.6 Å, or just half the obligatory elongation of the S−C5′ distance upon reductive cleavage, to achieve the ENDOR-estimated distance in the radical state of ~2.2 Å, indicative of van der Waals contact.

The distance constraints of Figure 4 (Table 1) can in fact be self-consistently combined in a least-squares optimization of the position for C5′ of the anAdo•/5′-dAdo• radical within the LAM/SAM/Lys structure (state **0**), as shown in Figure 7. This

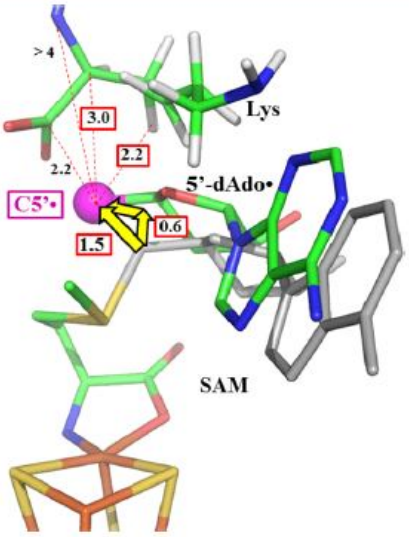


Figure 7. Inferred motion of 5′-dAdo• radical upon reductive cleavage of SAM (state **1** → **2**). The C5′ radical position (magenta) is situated within the X-ray crystal structure (state **0**) based on ENDOR constraints. The rest of the 5′-dAdo• radical is simply shifted from cluster bound SAM (state **0**, shown in gray).

figure further presents an heuristic representation of state **5** by incorporating a representation of the 5′-dAdo• radical generated by translating the corresponding fragment of SAM so as to place C5′ at the location relative to the substrate Lys as obtained with the ENDOR constraints. Of particular note, in this structure the 2pπ orbital on a trigonalized C3′ of the anSAM allyl radical would indeed point toward 2-C of Lys, as inferred above from the analysis of the hyperfine interaction.

There of course will be other, but we suggest secondary, active site rearrangements that contribute to this placement of the 5′-dAdo• radical relative to the substrate target in LAM. The flexibility of the lysyl tail, in particular, is shown by the fact that the X-ray structure does not have resolved density for atoms 3−6 within the tail (Figure S11). This flexibility, among other factors, must lie at the ability of the active site to accommodate both D- and L-lysine, as noted above, although with a preference for the L-isomer. For completeness, we note that one must expect some conformational changes in 5′-dAdo• radical itself.[54] Such refinements to the overall structure of state **5** presented in Figure 7 should be revealed by subsequent molecular dynamics simulations.

Regardless of any possible imperfections in the details, Figure 7 dramatically reveals how the active site of LAM "tames" the highly reactive 5′-dAdo• radical: this "free radical" is never free. As seen in the state **0** structure of LAM (Figure 7) the low steric demands of the radical-generating [4Fe-4S]/SAM construct allows the 3-H target site of L-Lys substrate to bind adjacent to the S−C5′ bond. ENDOR shows that the reductive cleavage of the S−C5′ bond propels the C5′ radical site through a total motion of only ~1.5 Å, essentially equal to the total motion (~1.3 Å) that would be imparted just by S−C5′ bond cleavage and separation of the atoms to the sum of their van der Waals radii.[53] This motion moves C5′ into van der Waals contact with the 3-H target of Lys, having crossed a mere ~0.6 Å gap from its target as implied by the state **0** structure (Figures 2, 4). At this stage the radical site is nestled in a highly constrained pocket where its position is enforced by van der Waals contacts with Lys 2-C and 1-C as well. In addition, C5′ remains in contact with the CH_3−S of methionine.

Placed in context with our earlier study of states **3** and **4**,[14] these observations fill in a picture of how the active site exerts "van der Waals control" of small motions throughout the LAM catalytic cycle. The study of state **3** showed that H atom abstraction creates the α-NH_2 Lys substrate radical in van der Waals contact with the 5′-dAdoH. Substrate rearrangement forms the β-NH_2 product radical in van der Waals contact with the 5′-methyl, state **4**, thereby enforcing the reciprocal abstraction of an H atom from the 5′-dAdoH, 5′-methyl by the product radical, to generate β-NH_2 Lys product and regenerate the 5′-dAdo• radical, state **5**. As noted just above, the constrained environment places the 5′-dAdo• radical in contact with the S of methionine, and thus poised for recombination to regenerate SAM (conversion of state **5** to state **6**) to complete the catalytic cycle.

It is important to note that the short C5′ ↔ 2-C (Lys) target distance in the LAM/SAM/Lys state **0** structure is not unique to this enzyme/substrate pair, but rather comparable distances from the SAM C5′ to the target C of substrate are found in the other structurally characterized radical SAM enzymes (Table 2).[8,10,55−62] Given that the target H of substrate is bound

Table 2

radical SAM enzyme (PDB ID)	C5′ ↔ target C distances (Å) (X-ray)
anSME (4K39)	4.1
BioB (1R30)	3.9
BtrN (4M7T)	3.7
HemN (1OLT)	4.0
MoaA (2FB3)	4.7−5.3
NosL (4R33)	4.1
PFL-AE (3CB8)	4.1
SPL (4FHD)	3.9

adjacent to the S−C5′ bond of SAM in this wide array of radical SAM enzymes, it seems likely to us that this mechanism of "van der Waals control" of small motions for taming the 5′-dAdo• radical, and indeed for such control of the entire catalytic cycle of radical reactions, is common throughout the radical SAM enzyme superfamily.

Lessons from LAM about Coenzyme B_{12} Enzymes. B_{12}-dependent radical enzymes share a common mechanism in which a hydrogen atom and a substituent exchange places on neighboring sp^3-hybridized carbon atoms,[63] precisely as occurs in the isomerization of Lys by LAM. In both B_{12} enzymes and radical-SAM enzymes such as LAM, a 5′-dAdo• radical formed by homolytic bond cleavage, S−C5′ in radical-SAM and Co−C5′ in the B_{12} enzymes, carries out the catalytic conversion of

DOI: 10.1021/jacs.5b00498
J. Am. Chem. Soc. 2015, 137, 7111−7121

substrate to product. In both cases the catalytic cycle is completed by the reformation of the parent cofactor.

The mechanism we describe here for "taming" 5′-dAdo• radical by proximity to substrate coupled with van der Waals control of its motion is, however, in sharp contrast to the behavior of the coenzyme B_{12}-dependent enzymes. The C5′ bound to Co in the B_{12} coenzyme *necessarily* faces into the sterically demanding corrinoid ring, away from any possible substrate, and as a result, necessarily is further screened from the substrate target by the 5′-dAdo moiety, which lies between C5′ and the target, as shown in Figure 2(B). This geometry forces the target site of substrate to lie "far away" from the Co−C5′ bond, restricting access to the target by the C5′ radical formed through Co−C5′ bond cleavage.[64] As a result, the radical *must* migrate long distances to the site of reaction, as explicitly shown in the elegant advanced paramagnetic resonance studies of ethanolamine ammonia-lyase (EAL) by Warncke,[17] LoBrutto,[22] and co-workers, as well as studies of the B_{12}-dependent lysine 5,6-aminomutase by Frey, Ke, and co-workers,[25] which revealed that C5′ of 5′-dAdo• radical migrates over 6 Å from its location in the Co−C5′ bond to the reactive position adjacent to substrate. The migration of C5′ required for reaction with its substrate in EAL was modeled by keeping the adenine ring of 5′-dAdo• radical essentially fixed, and introducing a ribosyl rotation around the *N*-glycosidic bond.[65] For glutamate and methylmalonlyl-coenzyme A mutases, the C5′ appears to undergo migration of at most only a few Å, and in fact the cob(II)alamin intermediate has been proposed to function as a conductor rather than a mere spectator in these radical rearrangements.[66] The smaller movement in these B_{12} enzymes is achieved by rotation of the entire adenosyl group,[67] or by pseudorotation of the ribose moiety from the C2′-endo to the C3′-endo conformation.[23,68]

Why B_{12} enzymes? Iron−sulfur proteins are widely accepted to be evolutionarily ancient, perhaps emerging from prebiotic iron−sulfur minerals that catalyzed the synthesis of key molecular precursors of life.[69] The ubiquitous iron−sulfur protein ferredoxin has been described as a living relic of these primordial FeS catalysts.[70] At the present moment in evolution, radical SAM enzymes are found throughout the life on earth, with over 100 000 predicted radical SAM enzymes[71] and substrates that range from large proteins—such as pyruvate formate lyase, through small molecules—such as lysine, and including key roles in nucleotide chemistry and cofactor biosynthesis.[10,52] Cobalamin, a highly complex radical-generating cofactor, in contrast, is thought to have emerged more recently than radical SAM enzymes,[12] yet there are only 12 known cobalamin enzymes, catalyzing a much more limited range of reactions. These observations lead to two obvious questions.

The first question is, why have radical SAM enzymes retained their dominance among extant radical enzymes? Certainly, one factor must be that "they got here first". However, the results reported here suggest that a significant contributing factor is that these ancient enzymes provide a more flexible architecture for carrying out highly controlled radical catalysis on diverse substrates. For most B_{12} radical enzymes, catalysis requires that the active site control long-distance (~6 Å) migrations of C5′ of 5′-dAdo• radical because steric congestion shrouds the site of radical generation (Figure 2(B)), forcing remote binding of substrate. This may be contrasted with the minimal, roughly 0.6 Å, motion of the C5′ toward the 3-H target of Lys estimated in this study of LAM (Figure 7), which is enabled by the nearly unfettered access of the Lys 3-H substrate target to the radical-generating [4Fe-4S]-SAM machinery of LAM (Figure 2(A)). Available structural data on other radical SAM enzymes points to similar uninhibited access as reported here for LAM (Table 2). We suggest that the low steric constraints of the [4Fe-4S]/SAM construct and resultant accessibility to substrate of the C5′ radical provided a major reason why evolution spread and retained the use of this construct across all of the kingdoms of life, with thousands of family members catalyzing transformations of the widest range of substrates. The contrasting high steric demands of the coenzyme B_{12} force the target in B_{12}-dependent enzymes to bind further from the site of the nascent C5′ radical, and require the radical to migrate longer distances to the target site. It seems plausible that this has contributed strongly to the restricted use of B_{12} radical enzymes.

This analysis, however, raises the evolutionary question: with radical SAM enzymes readily available and apparently more amenable to diverse substrates, why did B_{12} radical enzymes emerge and persist? One possible answer may be that iron−sulfur clusters are notoriously oxygen-sensitive. Perhaps, with the increase in oxygen in the atmosphere after the evolution of oxygenic photosynthesis, cobalamin appeared where oxygen sensitivity and lability of iron−sulfur clusters posed too much of a detriment to the function of radical SAM enzymes. The cobalamin cofactor has the added advantage of being "self-contained", without the need of an external reductant as required by radical SAM enzymes. Another very intriguing hypothesis has been proposed by Bückel and co-workers, who suggest that the cob(II)alamin intermediate plays an integral role in catalysis in some B_{12} radical enzymes, namely glutamate and methylmalonyl-CoA mutases, by interacting with and stabilizing both the 5′-dAdo• radical and product methylene radicals.[66] Because of this intimate interaction between the cob(II)alamin and radical intermediates, it is argued, other radical-generating systems such as [4Fe-4S]-SAM cannot provide a direct replacement of this reactivity. We anticipate further conversations regarding why and how nature evolved the B_{12} enzymes, considering that the low steric constraints of radical SAM enzymes lead to their inherent substrate diversity, a property based on the use of [4Fe-4S]-SAM as "the rich man's adenosyl cobalamin".[52]

■ ASSOCIATED CONTENT

Supporting Information

Additional EPR and ENDOR data and details of analysis are provided. The Supporting Information is available free of charge on the ACS Publications website at DOI: 10.1021/jacs.5b00498.

■ AUTHOR INFORMATION

Corresponding Authors

*jbroderick@chemistry.montana.edu
*bmh@northwestern.edu

Author Contributions

§M.H. and A.S.B. contributed equally.

Notes

The authors declare no competing financial interest.

■ ACKNOWLEDGMENTS

The authors gratefully acknowledge Professor Perry Frey for his seminal contributions to the understanding of LAM and of the parallels between B_{12} and radical SAM enzymes, and for his support as we carried forward this work upon his retirement. The authors acknowledge the contribution of Dr. Susan Veneziano in creating the His-tagged LAM construct. This work has been supported by the NIH (GM54608, JBB; GM 111097, BMH).

DOI: 10.1021/jacs.5b00498
J. Am. Chem. Soc. 2015, 137, 7111−7121

REFERENCES

(1) Broderick, J. B.; Duffus, B. R.; Duschene, K. S.; Shepard, E. M. *Chem. Rev.* **2014**, *114*, 4229.
(2) Frey, P. A.; Hegeman, A. D.; Ruzicka, F. J. *Crit. Rev. Biochem. Mol. Biol.* **2008**, *43*, 63.
(3) Walsby, C. J.; Ortillo, D.; Broderick, W. E.; Broderick, J. B.; Hoffman, B. M. *J. Am. Chem. Soc.* **2002**, *124*, 11270.
(4) Walsby, C. J.; Hong, W.; Broderick, W. E.; Cheek, J.; Ortillo, D.; Broderick, J. B.; Hoffman, B. M. *J. Am. Chem. Soc.* **2002**, *124*, 3143.
(5) Walsby, C. J.; Ortillo, D.; Broderick, W. E.; Broderick, J. B.; Hoffman, B. M. *J. Am. Chem. Soc.* **2002**, *124*, 11270.
(6) Walsby, C. J.; Ortillo, D.; Yang, J.; Nnyepi, M.; Broderick, W. E.; Hoffman, B. M.; Broderick, J. B. *Inorg. Chem.* **2005**, *44*, 727.
(7) Chen, D.; Walsby, C.; Hoffman, B. M.; Frey, P. A. *J. Am. Chem. Soc.* **2003**, *125*, 11788.
(8) Vey, J. L.; Yang, J.; Li, M.; Broderick, W. E.; Broderick, J. B.; Drennan, C. L. *Proc. Natl. Acad. Sci. U. S. A.* **2008**, *105*, 16137.
(9) Lepore, B. W.; Ruzicka, F. J.; Frey, P. A.; Ringe, D. *Proc. Natl. Acad. Sci. U. S. A.* **2005**, *102*, 13819.
(10) Vey, J. L.; Drennan, C. L. *Chem. Rev.* **2011**, *111*, 2487.
(11) Frey, P. A. *Comprehensive Natural Products II Chemistry and Biology*; Elsevier Science: Amsterdam, 2010; Vol. 7, p 501
(12) Frey, P. A. *FASEB J.* **1993**, *7*, 662.
(13) Frey, P. A. *Acc. Chem. Res.* **2014**, *47*, 540.
(14) Lees, N. S.; Chen, D.; Walsby, C.; Behshad, E.; Frey, P. A.; Hoffman, B. M. *J. Am. Chem. Soc.* **2006**, *128*, 10145.
(15) Magnusson, O. T.; Reed, G. H.; Frey, P. A. *J. Am. Chem. Soc.* **1999**, *121*, 9764.
(16) Magnusson, O. T.; Reed, G. H.; Frey, P. A. *Biochemistry* **2001**, *40*, 7773.
(17) Canfield, J. M.; Warncke, K. *J. Phys. Chem. B* **2002**, *106*, 8831.
(18) Canfield, J. M.; Warncke, K. *J. Phys. Chem. B* **2005**, *109*, 3053.
(19) Warncke, K.; Utada, A. S. *J. Am. Chem. Soc.* **2001**, *123*, 8564.
(20) Warncke, K.; Canfield, J. M. *J. Am. Chem. Soc.* **2004**, *126*, 5930.
(21) Warncke, K. *Biochemistry* **2005**, *44*, 3184.
(22) LoBrutto, R.; Bandarian, V.; Magnusson, O. T.; Chen, X.; Schramm, V. L.; Reed, G. H. *Biochemistry* **2001**, *40*, 9.
(23) Gruber, K.; Reitzer, R.; Kratky, C. *Angew. Chem., Int. Ed.* **2001**, *40*, 3377.
(24) Zhu, C.; Warncke, K. *J. Am. Chem. Soc.* **2010**, *132*, 9610.
(25) Maity, A. N.; Hsieh, C.-P.; Huang, M.-H.; Chen, Y.-H.; Tang, K.-H.; Behshad, E.; Frey, P. A.; Ke, S.-C. *J. Phys. Chem. B* **2009**, *113*, 12161.
(26) Marsh, E. N. G.; Meléndez, G. D. R. *Biochim. Biophys. Acta, Proteins Proteomics* **2012**, *1824*, 1154.
(27) Roth, J. R.; Lawrence, J.; Bobik, T. *Annu. Rev. Microbiol.* **1996**, *50*, 137.
(28) Banerjee, R. *Chem. Rev.* **2003**, *103*, 2083.
(29) Toraya, T. *Chem. Rev.* **2003**, *103*, 2095.
(30) Brown, K. L. *Chem. Rev.* **2005**, *105*, 2075.
(31) Bradford, M. M. *Anal. Biochem.* **1976**, *72*, 248.
(32) Fish, W. W. *Methods Enzymol.* **1988**, *158*, 357.
(33) Hinckley, G. T.; Frey, P. A. *Biochemistry* **2006**, *45*, 3219.
(34) Mathews, I. I.; Erion, M. D.; Ealick, S. E. *Biochemistry* **1998**, *37*, 15607.
(35) Park, J.; Tai, J.; Roessner, C. A.; Scott, A. I. *Bioorg. Med. Chem.* **1996**, *4*, 2179.
(36) Werst, M. M.; Davoust, C. E.; Hoffman, B. M. *J. Am. Chem. Soc.* **1991**, *113*, 1533.
(37) Davoust, C. E.; Doan, P. E.; Hoffman, B. M. *J. Magn. Reson.* **1996**, *119*, 38.
(38) Brueggemann, W.; Niklas, J. R. *J. Magn. Reson., Ser. A* **1994**, *108*, 25.
(39) Doan, P. E.; Hoffman, B. M. *Chem. Phys. Lett.* **1997**, *269*, 208.
(40) Doan, P. E. *J. Magn. Reson.* **2011**, *208*, 76.
(41) Doan, P. E.; Lees, N. S.; Shanmugam, M.; Hoffman, B. M. *Appl. Magn. Reson.* **2010**, *37*, 763.
(42) McConnell, H. M.; Strathdee, J. *Mol. Phys.* **1959**, *2*, 129.
(43) Willems, J.-P.; Lee, H.-I.; Burdi, D.; Doan, P. E.; Stubbe, J.; Hoffman, B. M. *J. Am. Chem. Soc.* **1997**, *119*, 9816.
(44) A very weak signal in the 2−13C sample is assigned to a small amount of scrambled label.
(45) Muthukumaran, R. B.; Grzyska, P. K.; Hausinger, R. P.; McCracken, J. *Biochemistry* **2007**, *46*, 5951.
(46) Foner, S. N.; Cochran, E. L.; Bowers, V. A.; Jen, C. K. *J. Chem. Phys.* **1960**, *32*, 963.
(47) Morton, J. R.; Preston, K. F.; Strach, S. J.; Adrian, F. J.; Jette, A. N. *J. Chem. Phys.* **1979**, *70*, 2889.
(48) Adrian, F. J. *J. Chem. Phys.* **1960**, *32*, 972.
(49) Hammes-Schiffer, S. *Acc. Chem. Res.* **2001**, *34*, 273.
(50) Hatcher, E.; Soudackov, A. V.; Hammes-Schiffer, S. *J. Am. Chem. Soc.* **2004**, *126*, 5763.
(51) Lucken, E. A. C. *Nuclear Quadrupole Coupling Constants*; Academic Press: New York, 1969.
(52) Frey, P. A.; Magnusson, O. T. *Chem. Rev.* **2003**, *103*, 2129.
(53) Bondi, A. *J. Phys. Chem.* **1964**, *68*, 441.
(54) In the analogue to State 5 studied here, with anAdo• instead of Ado•, there must of course be an additional change in the conformation of the ribose ring to accommodate the change from tetrahedral to trigonal geometries at C4′ and C3′, associated with the presence of the allyl radical comprising C3′, C4′, C5′.
(55) Goldman, P. J.; Grove, T. L.; Sites, L. A.; McLaughlin, M. I.; Booker, S. J.; Drennan, C. L. *Proc. Natl. Acad. Sci. U. S. A.* **2013**, *110*, 8519.
(56) Berkovitch, F.; Nicolet, Y.; Wan, J. T.; Jarrett, J. T.; Drennan, C. L. *Science* **2004**, *303*, 76.
(57) Goldman, P. J.; Grove, T. L.; Booker, S. J.; Drennan, C. L. *Proc. Natl. Acad. Sci. U. S. A.* **2013**, *110*, 15949.
(58) Layer, G.; Moser, J.; Heinz, D. W.; Jahn, D.; Schubert, W.-D. *EMBO J.* **2003**, *22*, 6214.
(59) Hänzelmann, P.; Schindelin, H. *Proc. Natl. Acad. Sci. U. S. A.* **2004**, *101*, 12870.
(60) Hänzelmann, P.; Schindelin, H. *Proc. Natl. Acad. Sci. U. S. A.* **2006**, *103*, 6829.
(61) Nicolet, Y.; Zeppieri, L.; Amara, P.; Fontecilla-Camps, J. C. *Angew. Chem.* **2014**, *126*, 12034.
(62) Benjdia, A.; Heil, K.; Barends, T. R. M.; Carell, T.; Schlichting, I. *Nucleic Acids Res.* **2012**, *40*, 9308.
(63) Buckel, W.; Friedrich, P.; Golding, B. T. *Angew. Chem.* **2012**, *51*, 9974.
(64) Shibata, N.; Tamagaki, H.; Hieda, N.; Akita, K.; Komori, H.; Shomura, Y.; Terawaki, S.-i.; Mori, K.; Yasuoka, N.; Higuchi, H.; Toraya, T. *J. Biol. Chem.* **2010**, *285*, 26484.
(65) Khoroshun, D. V.; Warncke, K.; Ke, S.-C.; Musaev, D. G.; Morokuma, K. *J. Am. Chem. Soc.* **2003**, *125*, 570.
(66) Buckel, W.; Kratky, C.; Golding, B. T. *Chem.—Eur. J.* **2006**, *12*, 352.
(67) Kim, S. J.; Lester, C.; Begley, T. P. *J. Org. Chem.* **1995**, *60*, 6256.
(68) Buckel, W.; Friedrich, P.; Golding, B. T. *Angew. Chem., Int. Ed.* **2012**, *51*, 9974.
(69) Huber, C.; Wächtershäuser, G. *Science* **1998**, *281*, 670.
(70) Eck, R. V.; Dayhoff, M. O. *Science* **1966**, *152*, 363.
(71) Babbitt, P.; Gerlt, J. *Structure Function Linkage Database*, 2013; http://sfld.rbvi.ucsf.edu/django/superfamily/29/, accessed 05/12/15.

DOI: 10.1021/jacs.5b00498
J. Am. Chem. Soc. 2015, 137, 7111−7121

Supplementary Information

Why Nature Uses Radical SAM Enzymes so Widely: Electron Nuclear Double Resonance Studies of Lysine 2,3-Aminomutase Show the 5'-dAdo• "Free Radical" Is Never Free

Masaki Horitani[¶,§], Amanda S. Byer[Ŧ,§], Krista A. Shisler[Ŧ], Tilak Chandra[Ŧ], Joan B. Broderick[Ŧ,*], Brian M. Hoffman[¶,*]

[¶] Department of Chemistry, Northwestern University, 2145 Sheridan Road, Evanston, Illinois 60208, USA
[Ŧ] Department of Chemistry and Biochemistry, Montana State University, Bozeman, Montana 59717, USA

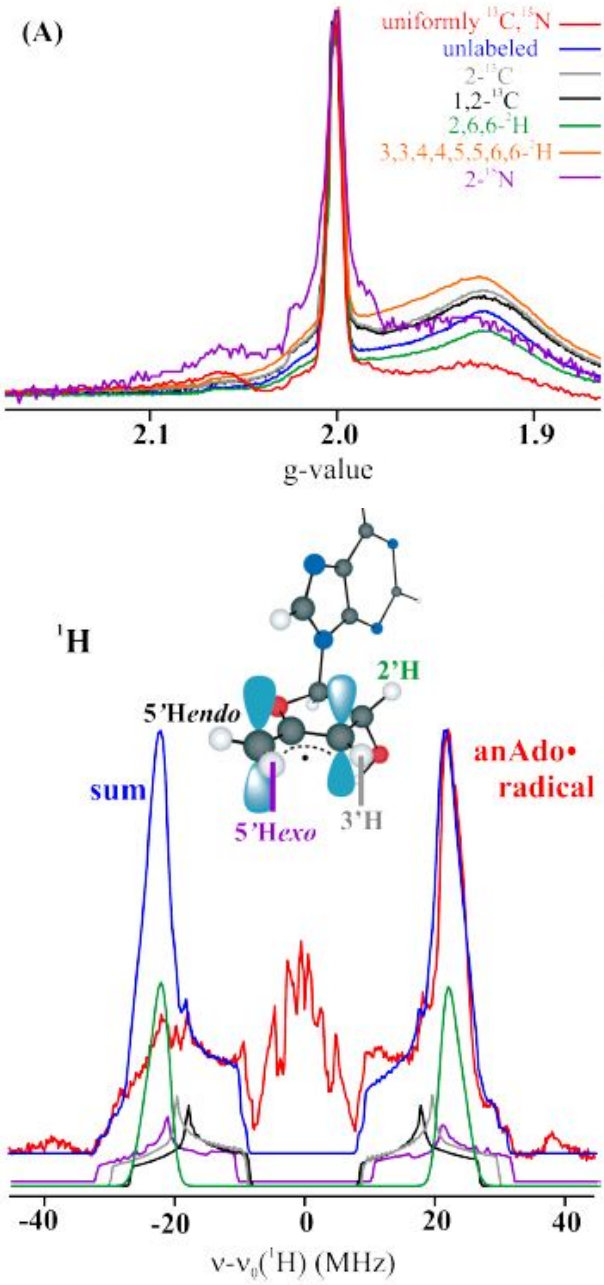


Figure S1. (A) 35 GHz echo-detected EPR spectra for LAM with anSAM, PLP and substrate as indicated (B) 35 GHz stochastic CW ^{1}H ENDOR spectrum of LAM with anSAM, PLP and *α*-Lys.

Experimental conditions: (A) microwave frequency = 34.6 ~ 34.8 GHz, τ = 600 ns, microwave pulse length (π/2) = 40 ns, repetition rate = 2 Hz and T = 2 K (B) microwave frequency = 34.773 GHz, modulation amplitude = 4.0 G, rf on = 5.0 ms, rf off = 5.0 ms, sample collection time = 1.0 ms and temperature = 2 K. (B) CW stochastic ^{1}H ENDOR Spectrum collected at peak of radical EPR (g = 2.00). The experimental spectrum and sum of simulation spectrum were drawn in red and blue, respectively. Each simulation spectrum is colored to correspond to ^{1}H positions in the anAdo• radical picture.

Determination of local contribution to ^{13}C dipolar coupling

The anisotropic coupling matrix in principle is the sum of two axial matrices, the non-local contribution ($T_{n\text{-}loc}$) from through-space dipolar interaction between the electron spin of anAdo• radical and the ^{13}C nuclear spin, and a local contribution (T_{loc}), caused by interaction of electron spin density delocalized into the C-H bonds of 2-C of Lys: , $\boldsymbol{T} = T_{loc} + T_{n\text{-}loc}$. Treating the two as coaxial, as required by the axial experimental matrix, T_{loc} can be estimated from the measured A_{iso}, through the following equation,[1]

$$T_{loc} = \left(\frac{A_{iso}}{a_0}\right) n T_0 \qquad \textbf{(S1)}$$

where n is the hybridization coefficient of the spin-brearing carbon, sp^n, in this case n = 3, and T_0 and a_0 are axial hyperfine constant and isotropic hyperfine constant for carbon, respectively. From this and the parameters obtained from the simulation, T_{loc} = +0.38 MHz, giving $T_{n\text{-}loc}$ = +0.66 MHz. Assuming the latter term comes from the point-dipolar interaction between 2-^{13}C nucleus and the spin density on C5' (ρ = 0.59), the distance from C5' to 2-^{13}C of lysine, r, is estimated from **eq 5** to be $r \sim 2.7$ Å. However the point-dipole treatment needs a correction at such short distances: the spin on C5' is not confined to a point, but is distributed within its 2pπ orbital, and an accurate treatment requires integration of the dipolar interaction over the spin distribution in the 2pπ orbital.[2]

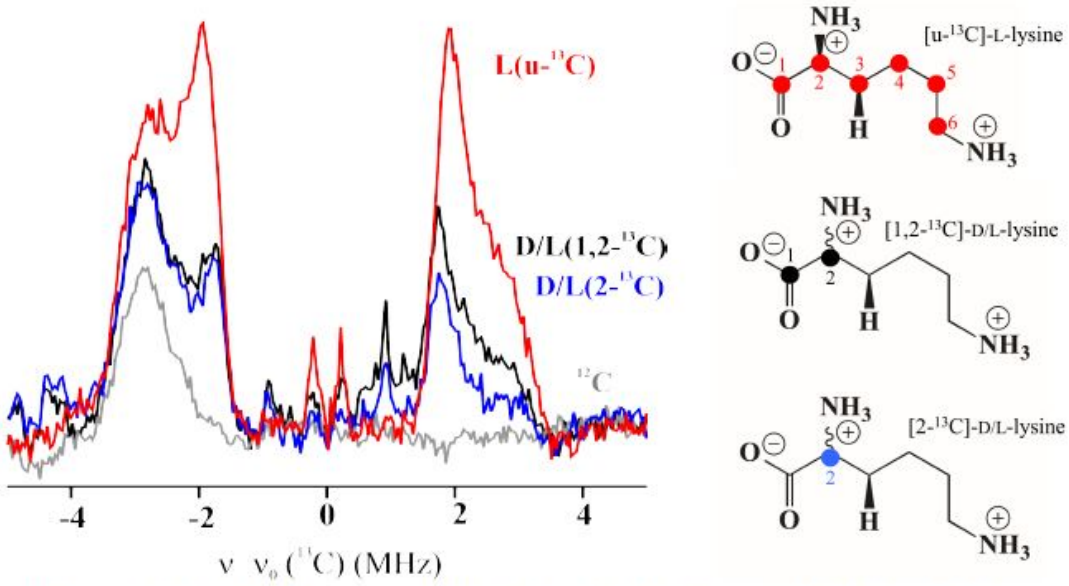


Figure S2. 35 GHz ^{13}C Davies ENDOR for LAM with anSAM, PLP and substrate as indicated.

All experimental conditions are the same as **Figure 3**.

Analysis of 1-^{13}C ENDOR Response

The weakly coupled ENDOR signal from 1-^{13}C of Lys is best visualized by applying the Mims pulse ENDOR technique, **Figure S3**. The small coupling compared to that of 2-^{13}C implies that 1-C is much farther away from C5' of anAdo• radical than is 2-

C, but with such a small coupling the line-width is large compared to the differences between hyperfine coupling matrix components, and the two branches of the spectrum are featureless. Simulations that employed a range of values for A_{iso} and T, indicated a possible range of the hyperfine values: $-0.25 < A_{iso} < -0.10$ (MHz); point-dipole through-space coupling, $0.23 < T < 0.36$ (MHz). The latter corresponds to a range in distances from C5' to 1-C of Lys, $3.2 < r < 3.7$ (Å) (**Figure S4**).

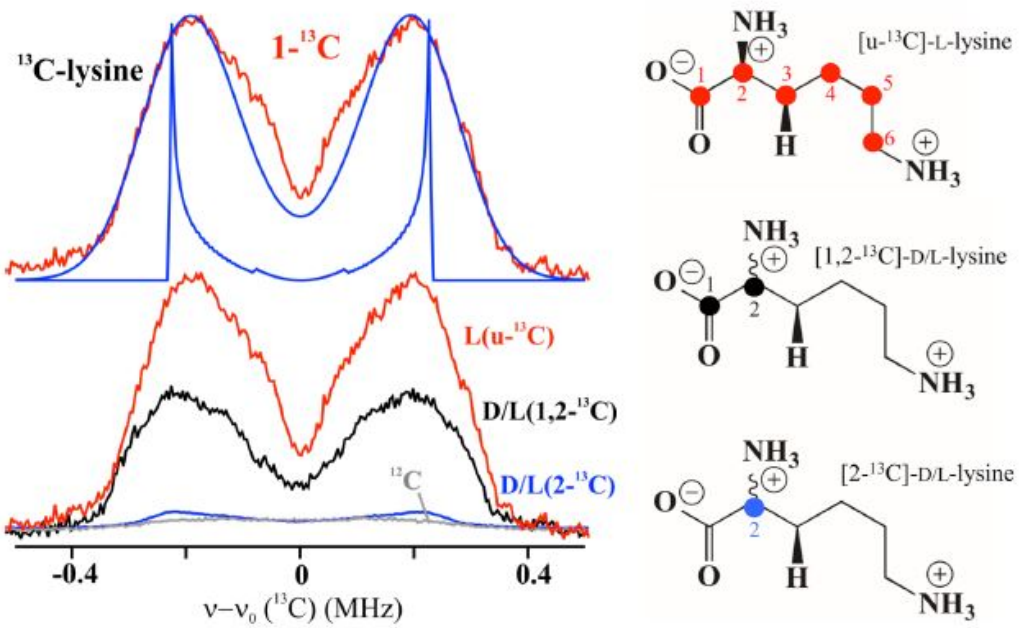


Figure S3. 35 GHz ^{13}C Mims ENDOR and simulation spectra. Spectra were collected at the radical peak. Experimental conditions: MF = 34.6 ~ 34.8 GHz, MW pulse length ($\pi/2$) = 50 ns, τ = 1000 ns and T = 2 K. Simulation spectra are drawn in blue (top); unlabeled lysine sample is gray.

aiso	r	r(real)
-0.25	4.59	3.73
-0.20	4.25	3.45
-0.17	4.12	3.40
-0.16	4.04	3.34
-0.14	3.97	3.29
-0.12	3.90	3.23
-0.11	3.84	3.19
-0.10	3.82	3.18

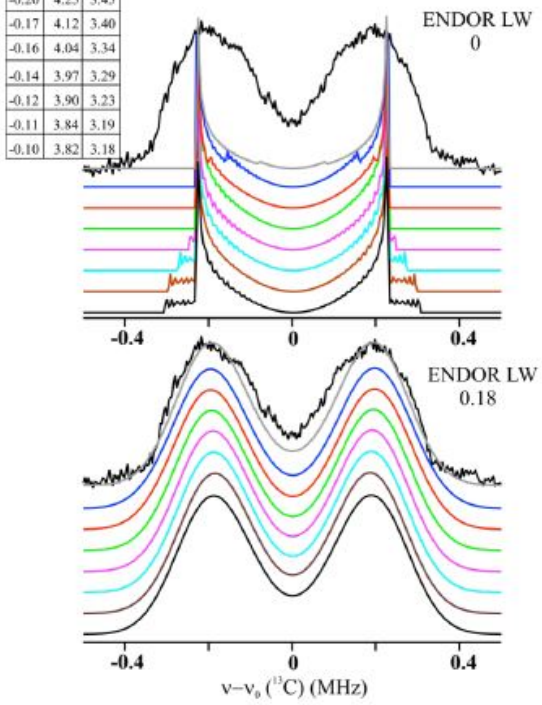


Figure S4. 35 GHz ^{13}C Mims ENDOR and all simulation spectra. Experimental spectrum is ^{13}C Mims ENDOR for LAM with anSAM, PLP and [1,2-^{13}C]-Lys. Experimental conditions are same as **Figure S3**. Simulation parameters are listed in insert table with ENDOR line-width (LW) 0 MHz (top) and 0.18 MHz (bottom).

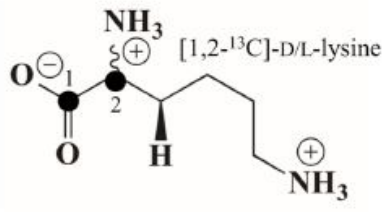
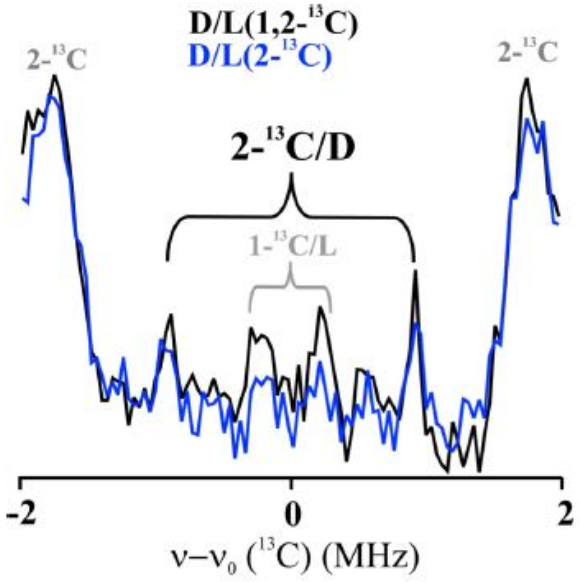
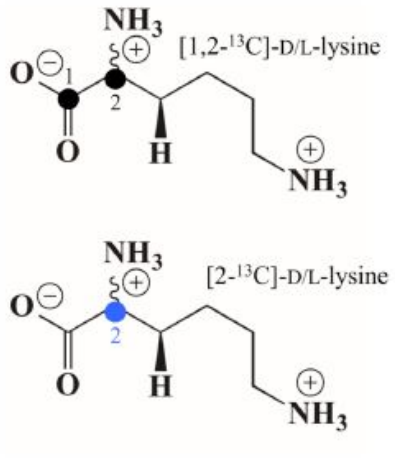


Figure S5. 35 GHz ^{13}C Davies ENDOR (small range) for LAM with anSAM, PLP and substrate as indicated.
All experimental conditions are the same as **Figure 3.**





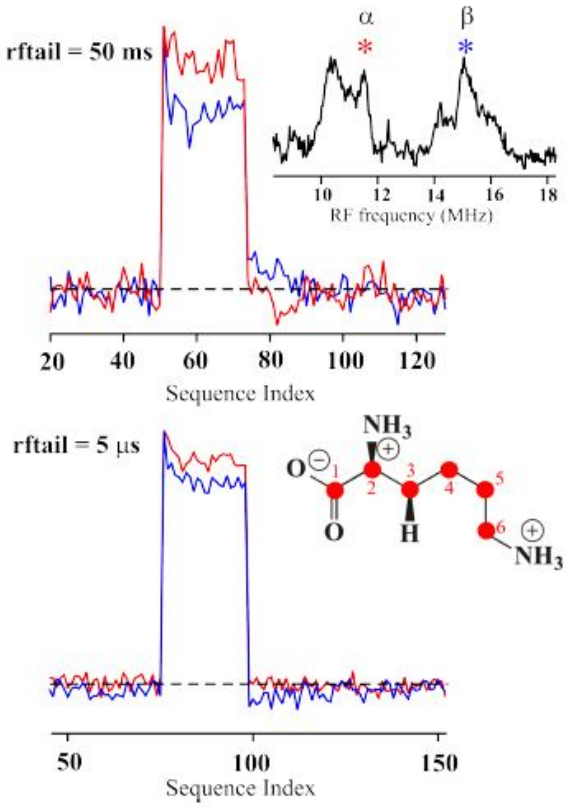
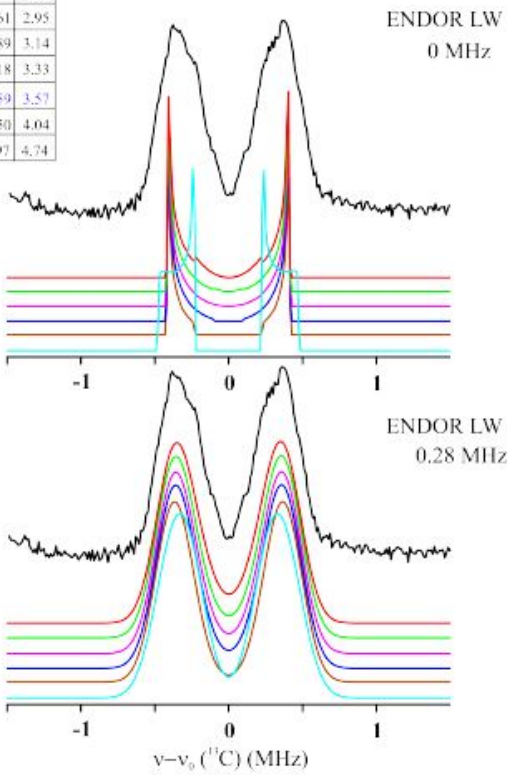


Figure S6. PESTRE technique for LAM with anSAM, PLP and [u-^{13}C]-Lys.

The frequency at which the PESTRE measurements were acquired is denoted by an asterisk in the inset figure, which is the ^{13}C Davies ENDOR spectrum for the LAM/anSAM/PLP sample with [u-^{13}C]-Lys collected g = 2.00. Experimental conditions: microwave frequency = 34.77 GHz, microwave pulse length (π) = 200 ns, τ = 1000 ns, mixing times are indicated in figure as rf-tail and T = 2 K.

aiso	r	r(real)
-0.39	3.61	2.95
-0.48	3.89	3.14
-0.55	4.18	3.33
-0.61	4.59	3.57
-0.70	5.50	4.04
0.62	4.97	4.74



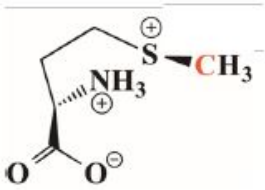


Figure S7. 35 GHz ^{13}C Mims ENDOR and simulation spectra.
Experimental spectrum is ^{13}C Mims ENDOR for LAM with [^{13}C-methyl]-anSAM, PLP and Lys. Experimental conditions are same as **Figure 6**. Simulation parameters are listed in inset table with ENDOR line-width (LW) 0 MHz (top) and 0.28 MHz (bottom).

Distance from the Radical to Amine Nitrogen

Figure S8 (bottom) shows weakly coupled ^{15}N Mims ENDOR signals for uniformly labeled ^{15}N (red), 2-^{15}N (black) and unlabeled Lys (gray) at τ = 1000 ns. The observation of the same signal from the samples prepared with isotopically labeled lysines (**Chart S1**; L-Lys [u-^{15}N] and D/L-Lys [2-^{15}N]) confirms that the signal comes from the weakly-coupled α-amino ^{15}N of Lys bound to PLP.

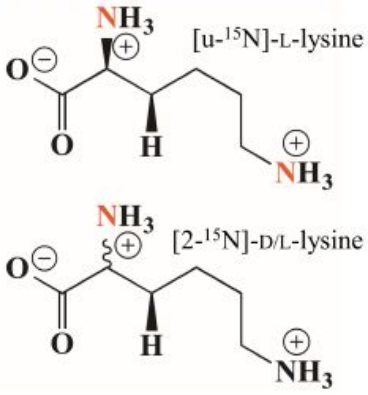


Chart S1.

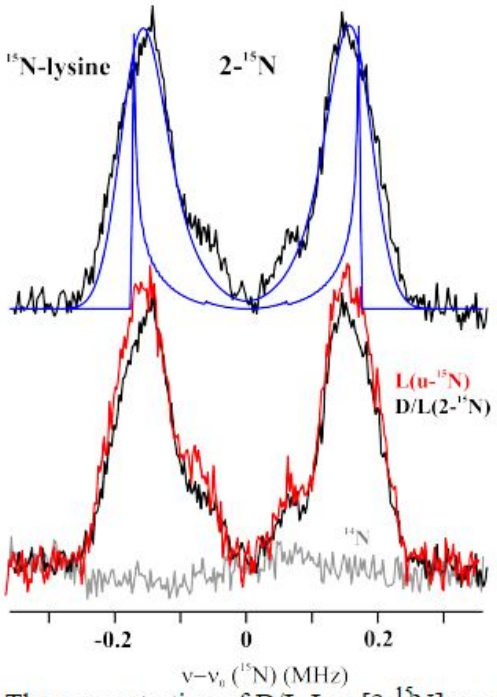


Figure S8. ^{15}N Mims ENDOR for LAM with anSAM, PLP and substrate and simulation spectra. Spectra collected at the peak of radical EPR for each labeled Lys, as indicated; simulation shown in blue (top); unlabeled lysine shown in gray (bottom). Experimental conditions; microwave frequency = 34.74 GHz, MW pulse length (π/2) = 50 ns, τ = 1000 ns and T = 2 K. Simulation parameters; A_{iso} = -0.19 MHz, T = 0.16 MHz, ENDOR line width = 0.07 MHz.

The concentration of D/L-Lys [2-^{15}N] used to prepare the sample is twice as large as that of L-Lys [u- ^{15}N]. The similar intensities of the signals for the two samples again (see above) imply that the L-Lys binds preferentially. The absence of additional features in the [u-^{15}N]-Lys sample indicates, unsurprisingly, that the 6-^{15}N of the side-chain is too far from C5' of anAdo• radical to give a detectable ENDOR response. The distance of C5' of anSAM to 6-N before the reductive cleavage is 6.3 Å, outside the range of detectability, and that distance is not anticipated to decrease appreciably.

The crystal structure shows that the distance of C5' of the SAM to 2-N before the reductive cleavage is 5.5 Å, again probably too far for ^{15}N couplings to be detected. The existence of a detectable signal then implies a shortening of this distance subsequent to anSAM cleavage. However, as with 1-^{13}C, the ^{15}N line width is large compared to the differences between hyperfine matrix components, and the two branches of the ^{15}N spectrum are featureless. As with the ^{13}C Mims simulation, simulations with a range of hyperfine coupling parameters (**Figure S9**) set limits on the possible coupling parameters, but with A_{iso} and T of opposite signs, suggesting a different mechanism for the tiny transfer of spin to 2-N: $-0.28 < A_{iso} < -0.09$ (MHz); $0.07 < T < 0.26$ (MHz). The latter yields a range of distances between C5' of the radical and the 2-^{15}N, $3.2 < r < 4.8$ (Å). We note that in simulations with uniformly narrow or strongly anisotropic line widths, parameters near the middle of this range would predict '$A_{\parallel}$' shoulders corresponding to those observed at ~ ± 0.06 MHz; these are 'washed out' by the uniform line width chosen to reproduce the rest of the spectrum. Whether the observed shoulders reflect an anisotropic line width or a second conformer with smaller coupling cannot be determined.

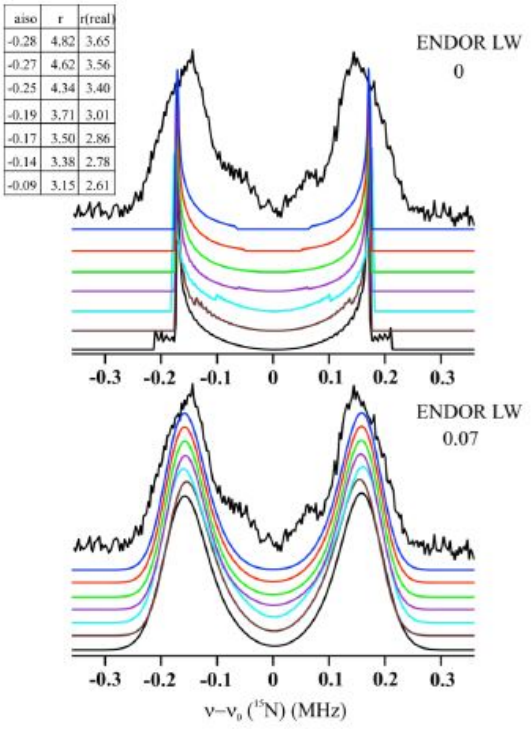
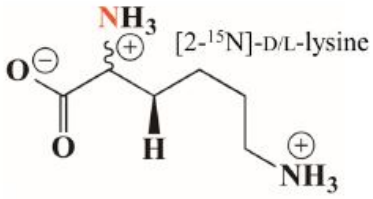


Figure S9. 35 GHz ^{15}N Mims ENDOR and simulation spectra.
Experimental spectrum is ^{15}N Mims ENDOR for LAM with anSAM, PLP and [2-^{15}N]-Lys. Experimental conditions are same as **Figure S8**. Simulation parameters are listed in inset table with ENDOR line-width (LW) 0 MHz (top) and 0.07 MHz (bottom).



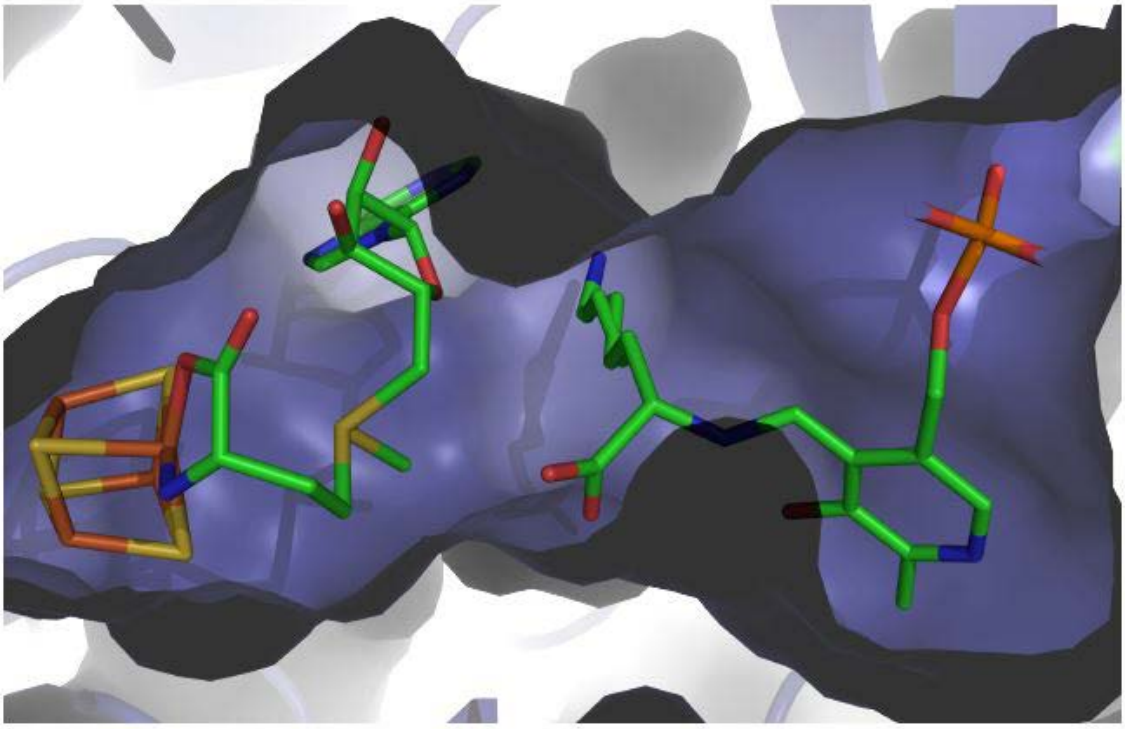


Figure S10. Illustration of the Constraint within the LAM active site.
PDB ID is 2A5H. Color scheme: carbon atoms of lysine, SAM and PLP are green; nitrogen is dark blue; oxygen is red; phosphorous is orange; sulfur is yellow; iron is rust; inside of pocket is highlighted in blue; protein cartoon is blue-gray. This image was made using PyMol.

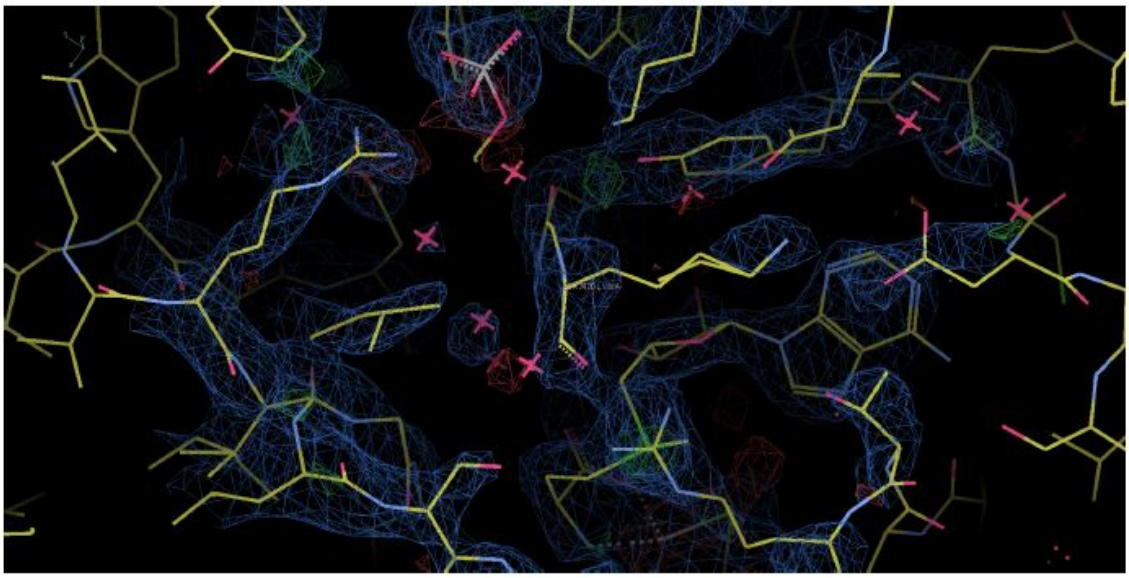


Figure S11. Electron density map of the LAM active site.
PDB ID is 2A5H. Figure is drawn in WinCoot. Carbon, nitrogen and oxygen are colored yellow, blue and red, respectively. The oxygens of the water molecules are shown as red crosses. The electron density map of the substrate lysine is somewhat disordered.

Table S1.

Nucleus	A_1 (MHz)	A_2 (MHz)	A_3 (MHz)	A_{iso} (MHz)
5'H_{exo}	64	21	42	42.3
5'H_{endo}	54	17	36	35.7
3'H	60	18	39.5	39.2
2'H	42.5	42.5	51.5	45.5

References

(1) Manikandan, P.; Choi, E.-Y.; Hille, R.; Hoffman, B. M. *J. Am .Chem. Soc.* **2001**, *123*, 2658.

(2) McConnell, H. M.; Strathdee, J. *Molecular Physics* **1959**, *2*, 129.

CHAPTER TEN

A RAPID FREEZE QUENCH ENDOR STUDY OF AN ORGANOMETALLIC RADICAL INTERMEDIATE IN PFL-AE

Contribution of Authors and Co-Authors

Manuscript(s) in Chapter(s) 4, 5, 6, 7, 9, 10

Author: Krista A Shisler

Contributions: Purified PFL-AE and PFL in addition to synthesis and purified of isotopically labeled and unlabeled SAM molecules. Purification of PFL G734S variant. Traveled to Northwestern University to prepare samples for RFQ analysis. Determined new experimental parameters with different isotopically labeled SAM molecules or isotopically labeled PFL-AE to optimize intermediate signal through the use of different concentrations of PFL-AE, PFL, and SAM and reduction of reducing agents. Attempted RFQ with other radical SAM enzymes to reproduce the intermediate signal.

Co-Author: Masaki Horitani

Contributions: Preformed RFQ experiments at Northwestern University. Collected and analyzed EPR and ENDOR results. Helped prepare manuscript by generating figures.

Co-Author: Kaitlin Duschene

Contributions: Purified PFL-AE, PFL, RNR-AE, and RNR and helped synthesis and purify some of the isotopically labeled SAM molecules. Traveled to Northwestern University to perform some RFQ experiments. Helped optimize intermediate signal and helped determine parameters for testing with the RNR system.

Co-Author: Rachel Hutcheson

Contributions: Purified PFL-AE and PFL and helped synthesis and purify some of the isotopically labeled SAM molecules. Traveled to Northwestern University to perform some of the RFQ experiments.

Contribution of Authors and Co-Authors Continued

Co-Author: Amy Marts

Contributions: Preformed some of the RFQ experiments at Northwestern University. Helped collect and analyzed EPR and ENDOR results.

Co-Author: George Cutsail III

Contributions: Preformed some of the RFQ experiments at Northwestern University.

Co-Author: William Broderick

Contributions: Preformed initial RFQ experiments and first discovered the intermediate. Provided insights into possible mechanisms.

Co-Author: Brian M Hoffman

Contributions: Provided interpretation of the ENDOR results and aided in preparation of manuscript and figures.

Co-Author: Joan B Broderick

Contributions: Provided interpretation of the ENDOR results, provided insights into the preparation of RFQ samples, and aided in preparation of manuscript and figures.

Manuscript Information Page

Krista A Shisler, Masaki Horitani, Kaitlin Duschene, Rachel U Hutcheson, Amy Marts, George Cutsail III, William Broderick, Brian M Hoffman, and Joan B Broderick
Journal of the American Chemical Society
Status of Manuscript:
__X__ Prepared for submission to a peer-reviewed journal
____ Officially submitted to a peer-review journal
____ Accepted by a peer-reviewed journal
____ Published in a peer-reviewed journal

Publisher ACS Publications

CHAPTER 10

A RAPID FREEZE QUENCH ENDOR STUDY OF AN ORGANOMETALLIC RADICAL INTERMEDIATE IN PFL-AE

Introduction

Radical *S*-adenosyl-L-methionine (SAM) chemistry is based on the production of the 5'-deoxyadenosyl radical (5'-dAdo•) intermediate during the reductive cleavage of SAM catalyzed by radical SAM enzymes (Figure 10.1) [1]. Although this highly reactive

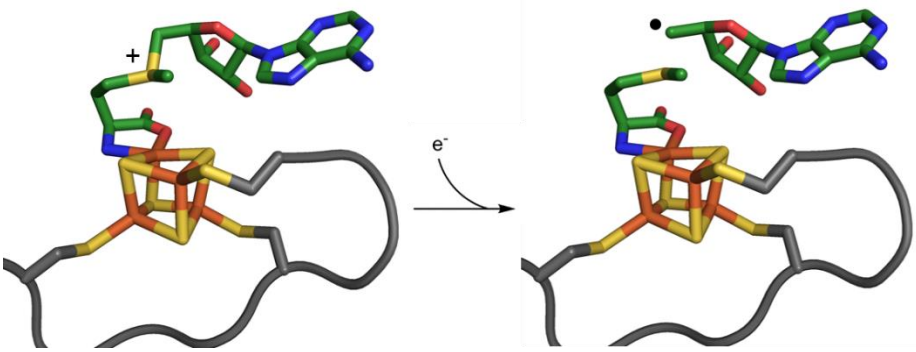


Figure 10.1. Reductive cleavage of SAM. Upon one electron reduction of the $[4Fe\text{-}4S]^{2+}$ cluster coordinated by three cysteines (grey carbons), an electron is transferred to SAM (green carbons) to produce the 5'-dAdo• radical and methionine.

radical has never been spectroscopically observed, the SAM analog *S*-3',4'-anhydroadenosyl-L-methionine (anSAM) produces a stable allylic 5'-deoxy-3',4'-anhydroadenosine-5'-yl radical (anAdo•) [2-4] that builds up to sufficient levels under steady-state turnover conditions to allow characterization using magnetic resonance techniques. Exploiting the stability of the anAdo• radical in LAM, the only radical SAM enzyme for which anAdo• has been observed to date, electron nuclear double resonance

(ENDOR) spectroscopy was used to analyze movement of the radical with respect to substrate lysine in the active site. It was determined that the 5'-C undergoes only minimal motions post cleavage, ~0.6 Å towards the abstracted H of lysine [4]. This movement is highly restrictive compared to the adenosylcobalamin (AdoCbl) dependent enzymes where the 5'-dAdo• radical is generated post cleavage of a Co-C bond and must travel up to 6 Å or more to interact with substrate [5-7].

Radical SAM chemistry is mediated by a [4Fe-4S] cluster where the amino N and carboxyl O of SAM are ligated to a site-differentiated Fe to place the active center of SAM (the 5'-C) in an axial position to the unique Fe. Upon reduction of the $[4Fe\text{-}4S]^{2+}$ cluster, inner sphere electron transfer induces homolytic cleavage of SAM to produce 5'-dAdo• and methionine. This 5'-dAdo• can then abstract a hydrogen from a variety of substrates; in pyruvate formate lyase activating enzyme (PFL-AE), 5'-dAdo• abstracts a hydrogen from a glycine residue (G734) on the homodimeric protein pyruvate formate lyase (PFL) (Figure 10.2). Once activated, PFL catalyzes the conversion of pyruvate and coenzyme A (CoA) to formate and acetyl-CoA through a succession of radical transfers from G734 to C419 and then C418 before reacting with pyruvate [8-12].

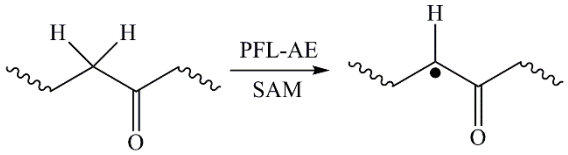


Figure 10.2. Activation of PFL by PFL-AE through H-atom abstraction at G734 to produce a glycyl radical.

Rapid freeze quench (RFQ), combined with spectroscopic techniques such as electron paramagnetic resonance (EPR) and ENDOR, can provide insights into radical

intermediate species. To investigate the reactions of PFL-AE and to trap possible intermediates, we utilized RFQ techniques and revealed a previously unknown EPR signal that did not correspond to the already characterized $[4Fe\text{-}4S]^{+}$ cluster nor the glycyl radical of PFL. ENDOR analysis of the intermediate coupled with isotopically labeled SAM molecules and an isotopically ^{57}Fe labeled [4Fe-4S] cluster in PFL-AE revealed novel insights into the PFL-AE catalyzed reaction.

Materials and Methods

Materials

[Methyl-$^{2}H_3$]-L-methionine and [3,3,4,4-$^{2}H_4$]-L-methionine were purchased from C/D/N Isotopes Inc. [Methyl-^{13}C]-L-methionine and [U-$^{2}H_8$]-adenosine 5'-triphosphate lithium salt were purchased from Cambridge Isotope Laboratories, Inc. [$^{13}C_{10}$,$^{15}N_5$]-adenosine 5'-triphosphate sodium salt solution was purchased from Sigma. Seleno-L-methionine was purchased from Fisher Scientific.

Protein Growth and Purification

PFL-AE and ^{57}Fe-enriched PFL-AE were grown and purified as previous described [13,14]. PFL-AE and ^{57}Fe labeled PFL-AE were purified in a 50 mM Tris, pH 7.5 buffer containing 200 mM NaCl and 1 mM DTT in an anerobic Coy chamber. PFL was grown and purified as previously described [13] aerobically in a 20 mM Tris, pH 7.2 or Hepes, pH 7.2 with 1 mM DTT buffer. After purification, PFL was degassed on a Schlenk line, aliquoted, and frozen.

SAM Purification

Unlabeled SAM or labeled [U-$^{13}C_{10}$,$^{15}N_5$-adenosine]-SAM, [U-$^{2}H_8$-adenosine]-SAM, [methyl-$^{13}C_3$]-SAM, [methyl-$^{2}H_2$]-SAM, and [3,3,4,4-$^{2}H_4$]-SAM were synthesized from their respective labeled L-methionine or ATP and purified as previously described [15,16]. Se-SAM was synthesized as previously described [15,16] from seleno-L-methionine except the reaction was quenched with 1 M HCl after 2 hours. Lyophilized SAM was reconstituted in a degassed 100 mM Tris, pH 8.1 buffer and brought up to a pH between 7.0 and 8.0. The SAM analogue, anSAM, was synthesized and purified as previously described [4].

Rapid Freeze Quench Sample Preparation

For all RFQ experiments, the same sample preparation was carried out for WT proteins, variants, and unlabeled or different isotopically labeled SAM molecules or PFL-AE in an anaerobic Coy chamber. A stock solution of PFL-AE and PFL were prepared and photoreduced (discussed below) with enough protein to conduct 3-4 quenching trials. After the appropriate amount of PFL-AE was removed for one mixing trial, the remaining stock solution was photoreduced again until another quenching trial was conducted. This helped keep PFL-AE in a reduced state between quench trials. PFL was only photoreduced once, capped, and put on ice in the anaerobic Coy chamber. For ENDOR analysis, RFQ samples were prepared to contain only one labeled molecule and either labeled SAM or labeled PFL-AE was added. Incorporating a label on both SAM and PFL-AE can complicate the ENDOR spectrum and thus, we only used one isotopically labeled molecule for each sample. To photoreduce PFL-AE, a PFL-AE stock

solution containing 550 μM PFL-AE (unlabeled or ^{57}Fe labeled), 200 μM 5-deazariboflavin and 1 mM DTT in a 50 mM Tris, pH 7.6 buffer containing 100 mM KCl was photoreduced by illumination using a 300 W halogen lamp for one hour (for the first mixing trial with an additional 20-30 minutes for each subsequent trial) in an ice bath. A separate PFL mixture containing 550 μM PFL, 50 μM 5-deazariboflavin, 10 mM oxamate, and 1 mM DTT in a 50 mM Tris, pH 7.6 buffer with 100 mM KCl was also illuminated to remove excess oxygen for 30 minutes to one hour in an ice bath. After photoreduction, 100 μL of the PFL-AE (unlabeled or ^{57}Fe labeled) mixture was loaded into one drive syringe (syringe 1) at a concentration of 550 μM. In a separate drive syringe (syringe 2), 100 μL of the PFL mixture and SAM (either unlabeled or labeled) was added. SAM was added after PFL was photoreduced to decrease the possibility of degradation. Due to the instability of PFL, 550 μM was the highest concentration obtained prior to mixing and this concentration would decrease after SAM was added. For SAM addition, two different methods were employed. For the first method, 90 μL of PFL was mixed with SAM for a final concentration of 5.5 mM of SAM (prior to mixing and quenching with PFL-AE) for a total volume of 100 μL. Buffer was added up to 10 μL to the PFL/SAM mixture to accommodate for the different stock concentrations of SAM. This led to a final concentration of 495 μM PFL. For the second method, SAM was added to a final concentration of 5.5 mM (prior to mixing and quenching with PFL-AE) to 100 μL of PFL. The volume of SAM added was < 10 μL (~4-8 μL) which led to a final concentration of ~530 μM to ~510 μM PFL. For these samples, buffer was added to PFL-AE to accommodate for the SAM addition to PFL to obtain a final concentration

of ~530 μM to ~510 μM PFL-AE, leading to a 1:1 ratio of PFL-AE:PFL. This second method was generally employed for RFQ sample preparation. Prior to mixing, the ratio of PFL-AE:PFL:SAM was 1:0.9:10 for the first method or 1:1:10 for the second method of SAM addition. Post mixing, these concentrations were halved but the ratio of PFL-AE:PFL:SAM was maintained. All concentrations reported are the final concentrations prior to mixing of PFL-AE with PFL/SAM during a quenching experiment. To ensure all protein exited the syringes into the mixing chamber and onto the copper wheels (described below), a 100 mM dithionite buffer (in water) was placed on each side of the protein. A pocket of air was introduced in the tube between the dithionite buffer and the protein. Dithionite was used to react with any oxygen to help protect the protein since the RFQ instrument was not housed in an anaerobic chamber.

For preparation of samples with the PFL variants G734A and G734S, the relatively low solubility of the variants resulted in a lower initial concentration of both PFL and PFL-AE prior to mixing. Sample preparation was performed identically to second method of SAM addition described above. Even with lower concentrations of the PFL variants, oxamate and DTT were still added to a final concentration of 10 mM prior to mixing and 5-deazariboflavin was added to a final concentration of 50 μM prior to mixing. For PFL-AE, 200 μM 5-deazariboflavin and 1 mM DTT was added prior to photoreduction, as described above. PFL-AE and PFL variants were photoreduced as described above. For both variants, only one label, either a labeled SAM molecule or the ^{57}Fe labeled PFL-AE, was used for individual samples. For the PFL G734S samples, PFL-AE (unlabeled or labeled) and PFL G734S were loaded into separate syringes at an

initial concentration of 292 μM prior to mixing. Into syringe 1, 100 μL of PFL-AE was loaded while into syringe 2, 100 μL of PFL G734S and 2.5 mM of either labeled or unlabeled SAM (prior to mixing and quenching with PFL-AE) was loaded. Buffer was added to PFL-AE to compensate for the SAM volume added to PFL. For the PFL G734A variant, sample preparation was identical for the G734S variant except PFL-AE and PFL were at final concentration of 250 μM prior to mixing and 2.5 mM SAM (final concentration prior to mixing) was added to PFL G734A. The ratio of PFL-AE:PFL variant:SAM for PFL G734A was 1:1:10 but 1:1:8 for PFL G734S.

Sample preparation with anSAM was performed like the second method of SAM addition described above. Unlabeled PFL-AE was photoreduced at a final concentration of 300 μM, as described above with 200 μM 5-deazariboflavin and 1 mM DTT, and 100 μL was loaded into syringe 1. PFL WT was photoreduced at a final concentration of 600 μM, as described above, with 10 mM oxamate and DTT and 50 μM 5-deazariboflavin (all concentrations prior to mixing). After photoreduction of PFL, 1 mM anSAM was added to 100 μL of PFL and loaded into syringe 2. Buffer was added to 100 μL of PFL-AE again to compensate for anSAM addition to PFL and loaded into syringe 1. The ratio of PFL-AE:PFL:anSAM was 1:2:3.3.

Rapid freeze-quench experiments were performed with a System 100 apparatus from Update Instrument by mixing the reduced PFL-AE with PFL/SAM. The mixture was quenched by spraying onto two rotating copper wheels cooled to liquid nitrogen temperatures as previously described [17,18] after 25 ms, 100 ms, 300 ms, 500 ms, or 1 s mixing times. For the PFL variants, only the 500 ms was conducted while 500 ms and 1 s

mixing times were conducted on the anSAM samples. The powder was collected in a funnel and packed into Q-band tubes for EPR and ENDOR analysis.

Static EPR Sample Preparation

For the reduced $[4Fe\text{-}4S]^{+}$ cluster and the PFL glycyl radical controls, static EPR samples were prepared. For a reduced cluster with bound SAM control, 250 μM PFL-AE unlabeled or ^{57}Fe labeled, was added to 200 μM 5-deazariboflavin, 1 mM DTT in a 50 mM Tris, pH 7.6 buffer with 100 mM KCl. PFL-AE was photoreduced with a 300 W halogen lamp for at least one hour in an ice bath at which time 2 mM SAM was added and the sample flash frozen. For analysis of the glycyl radical, 376 μM PFL was added to 125 μM PFL-AE and 2 mM SAM (final concentrations) prior to flash freezing.

EPR and ENDOR Analysis

EPR and ENDOR spectroscopic experiments were conducted as previously described [4]. X-band CW EPR spectroscopy was conducted on a Bruker ESP 300 spectrometer equipped with an Oxford Instruments ESR 910 continuous helium flow cryostat. Typical experimental parameters were at 10 K, 9.38 GHz, 10 mW microwave power, 100 kHz modulation, and 10 G modulation amplitude. Q-band CW and pulsed ENDOR techniques were recorded on a Varian Associates E-109 spectrometer with an E-110 microwave bridge at 35 GHz and 2 K as previously described [4].

Annealing

RFQ samples were annealed as previously described [19] at the desired temperatures by transferring the samples from liquid nitrogen to an isopentane bath at a

fixed temperature for 1 min, unless specified otherwise. Temperatures were monitored by stirring and addition of liquid nitrogen. The sample was then transferred back to liquid nitrogen and an EPR spectrum was recorded. EPR spectroscopy was performed at 12 K and 40 K and the initial intermediate signal in the 500 ms quench (at 12 K) was subtracted from the spectrum at 40 K.

Results

RFQ Reveals a Unique Signal

Two paramagnetic species in the PFL-AE catalyzed reaction have been previously characterized: the catalytically essential $[4Fe\text{-}4S]^{+}$ on PFL-AE, which undergoes characteristic spectral changes upon binding SAM, and the product glycyl radical on PFL [20,21]. In contrast, the 5'-dAdo• radical and any other PFL-AE intermediates have escaped detection. Rapid freeze quench (RFQ) of PFL-AE mixed with PFL and SAM revealed a unique EPR signal not identifiable as the reduced $[4Fe\text{-}4S]^{+}$ cluster nor the glycyl radical on PFL (Figure 10.3). This new signal begins to appear at approximately 25 ms mixing time, reaches a maximum at 500 ms, and after ~1 sec, the signal has been replaced by the more dominant glycyl radical signal (Figure SI.10.1) This signal was thus proposed to arise from an intermediate species in the PFL-AE-catalyzed reaction. Since the signal intensity is greatest at 500 ms, we used this quench time to prepare samples for ENDOR analysis.

This intermediate signal is slightly up-field with respect to the gly radical ($g_{\perp}$ ~ 2.01) and contains more broadening and an additional feature at approximately g = 2.03.

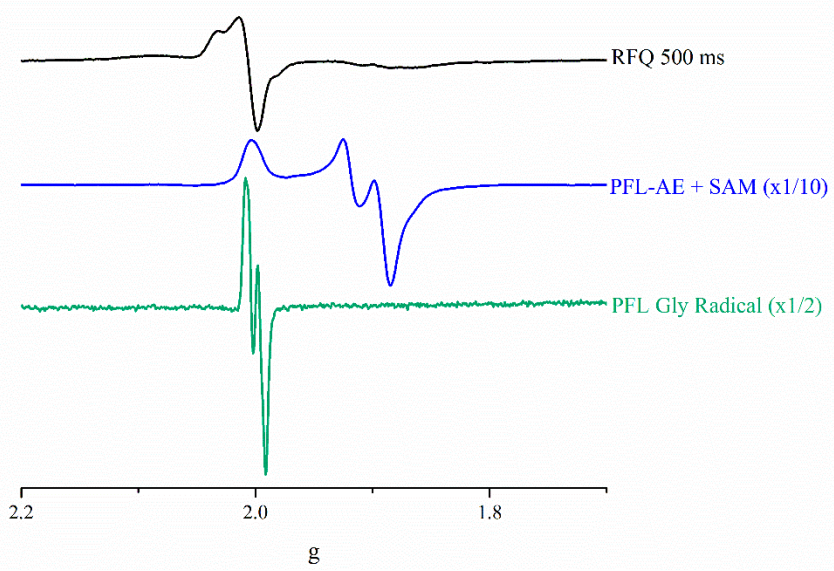


Figure 10.3. Comparison of the EPR spectra of the reaction quenched at 500 ms after mixing (black), the reduced $[4Fe\text{-}4S]^{+}$ cluster in PFL-AE with SAM bound (one tenth the scale, blue), and the PFL glycyl radical (half the scale, green). The 500 ms quenched signal is much broader than the gly radical. The 500 ms quench and the $[4Fe\text{-}4S]^{+}$ reduced cluster with SAM EPR spectra were obtained at 12 K while the glycyl radical spectrum was obtained at 70 K.

The signal is much sharper and more isotropic than a $[4Fe\text{-}4S]^{+}$ cluster. The feature at approximately g = 2.1 is due to cavity (Figure SI.10.2) while the feature at approximately g = 1.88 is due to reduced $[4Fe\text{-}4S]^{+}$ cluster in the presence of SAM. Temperature dependence studies reveal an optimal temperature at 5 K and power saturation studies reveal an optimal power of 5 mW (Figure SI.10.3). The signal is more susceptible to power saturation than a $[4Fe\text{-}4S]^{+}$ cluster but less susceptible than an organic radical signal.

Optimization of the Intermediate Signal

To optimize the intermediate signal and decrease the reduced cluster component at g = 1.88, we eliminated sodium dithionite from the PFL-AE and the PFL

photoreduction solutions. Sodium dithioinine was added initially to help minimize any O_2 destruction of the cluster or to minimize any other radical species since the RFQ instrument resides outside an anaerobic Coy chamber. We also increased the ratio of PFL-AE:SAM to 1:10 and later attempted an increase in the PFL-AE:PFL ratio to 1:1.5 which intensified the signal. The 1:10 PFL-AE:SAM ratio was optimized and used in all sample preparations while the increase in PFL-AE:PFL ratio was only performed once and more trials with this higher PFL concentration needs to be performed.

We also tried PFL variants to enhance the intermediate signal. Unfortunately, the variants are more insoluble than WT and we could not exceed a concentration of 300 μM of each PFL variant prior to mixing. The intermediate signal was still observed (Figure SI.10.4) albeit with less signal intensity than the WT PFL. Interestingly, there was a rounding of the signal in some of the samples. Further analysis needs to be conducted to understand this rounding.

The SAM analog, anSAM, produces a stable allylic radical upon cleavage by the radical SAM enzyme LAM [2,4]. Currently, no other radical SAM enzyme has produced the anAdo• radical, including PFL-AE. In hopes to trap either the anAdo• or the intermediate signal, we attempted a 500 ms and a 1 s quench with PFL-AE, anSAM, and PFL and observed the intermediate signal at 500 ms and a currently unknown signal at 1 s (Figure 10.4). The 500 ms signal has slightly greater intensity than most of the samples performed with labeled or unlabeled SAM. The anSAM studies did contain a larger PFL-AE:PFL ratio (1:2) compared to those with SAM and might explain the increase in signal. But the ratio of PFL-AE:anSAM was lower (1:3.3) suggesting less anSAM is

required to obtain an intermediate signal. The signal still decays after 1 s but does not produce the anAdo• nor the glycyl radical. The signal at 1 s could be attributed to a [3Fe-4S] cluster but the origin of this signal is still unknown. We would like to perform further studies with labeled and unlabeled anSAM to optimize and further understand the 500 ms quench signal.

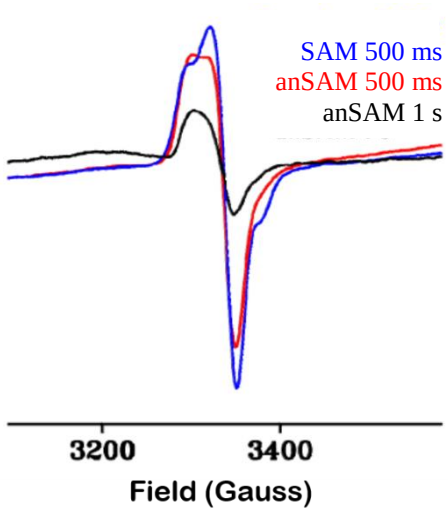


Figure 10.4. Comparison of the EPR signal of the intermediate when either SAM (blue) or anSAM (red and black) were used in the reaction mixture. The most intense quench with SAM is shown. Two different quench times were conducted with anSAM with unlabeled PFL-AE at a 500 ms quench (red) and 1 s quench (black).

Annealing Studies Reveal Progression to the Glycyl Radical

In order to analyze the progression of the intermediate to the glycyl radical and provide evidence whether this intermediate is on-pathway, we conducted annealing studies on the 500 ms quench sample (Figure 10.5). Prior to annealing, some glycyl radical signal is present in the 500 ms quench (observable at 40 K, Figure 10.5). Progression through the reaction by slightly warming the sample to allow minimal

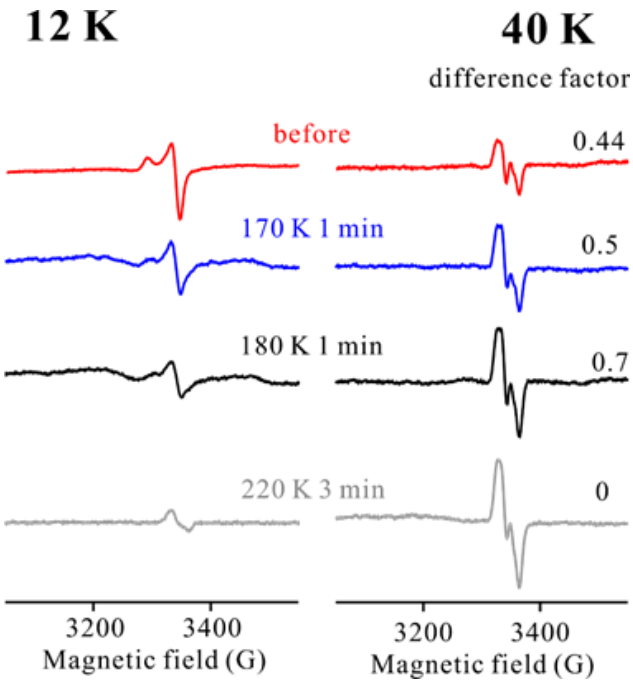


Figure 10.5. Annealing studies of the 500 ms quench. The intermediate signal is mostly visible at 12 K (left) but due to spin relaxation, the signal has very little signal intensity at 40 K (right). The glycyl radical of PFL has a very weak signal at 12 K but its signal is stronger at 40 K. Any contributions from the intermediate signal are removed from the spectra reported at 40 K. This was done by plotting the difference between the spectrum taken at 40 K and subtracting it from the intermediate signal (12 K before, red) and multiplying by a difference factor. After annealing, or warming of the sample to higher temperatures for specified amounts of time, as indicated, the intermediate signal weakens and the glycyl radical signal intensifies. After 3 minutes at 220 K (grey), the intermediate has fully converted to the glycyl radical, shown by a difference factor of zero.

molecular motions while maintaining a frozen state, the intermediate signal (observable at 12 K, Figure 10.5) weakens and the glycyl radical signal intensifies. After the sample was warmed to 220 K for 3 minutes, the intermediate signal has disappeared with conversion to the glycyl radical. The small signal observed at 12 K in the 220 K sample is assigned to the glycyl radical which is still observable at 12 K, albeit with very low signal intensity. We concluded from these results that this signal is indeed an intermediate in the PFL-AE reaction prior to activation of PFL.

ENDOR Analysis of ^{57}Fe Labeled PFL-AE

Due to the line broadening in the EPR spectrum (compared to a glycyl radical signal) of the 500 ms quenched sample and its relaxation properties in varying temperatures and microwave powers, we hypothesized that the paramagnetic center is thus interacting with cluster. Therefore, we used ^{57}Fe labeled PFL-AE ([4^{57}Fe-4S]) to probe any interaction of the unpaired electron with the I = ½ ^{57}Fe isotope. X-band EPR spectroscopy revealed broadening and some perturbation in the ^{57}Fe labeled PFL-AE signal with respect to unlabeled PFL-AE (Figure 10.6a). CW ENDOR analysis of this

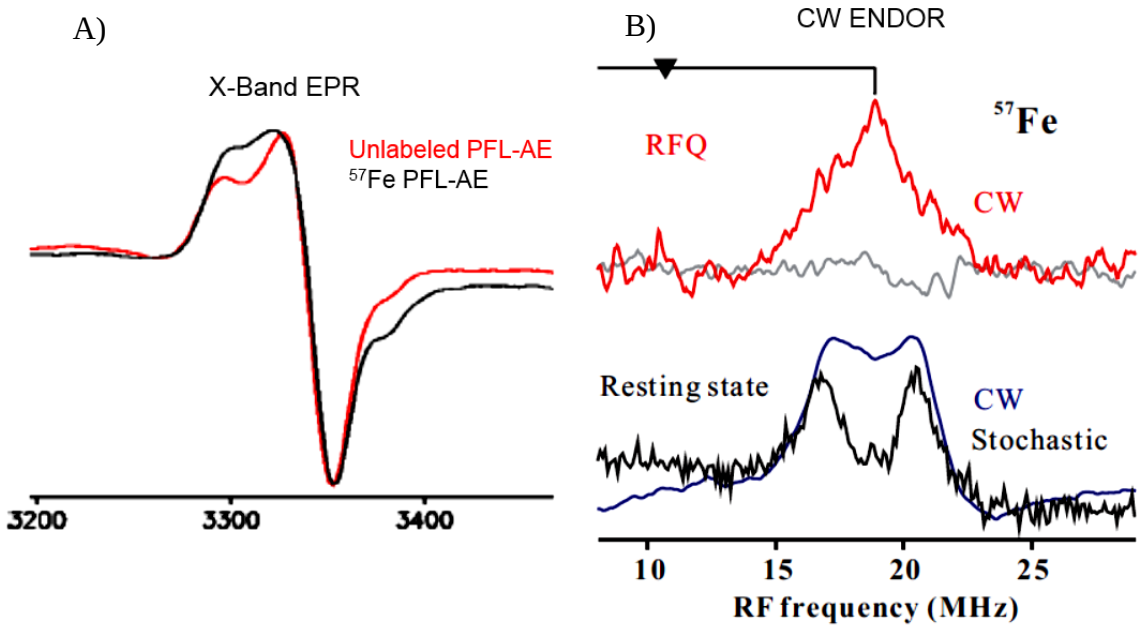


Figure 10.6. X-band EPR spectra and CW ^{57}Fe ENDOR spectra of the 500 ms quench with ^{57}Fe labeled PFL-AE and unlabeled SAM. A) The X-band EPR spectrum shows broadening of the signal in the ^{57}Fe labeled PFL-AE (black) versus the unlabeled PFL-AE (red) in the 500 ms quench sample. B) The Q-band CW ENDOR spectra of the 500 ms quench sample with [4^{57}Fe-4S] PFL-AE (red) and unlabeled PFL-AE (grey). The static, or resting state, [4^{57}Fe-4S] PFL-AE CW ENDOR spectrum (blue) and the spectrum under stochastic conditions (black) are shown for comparison. The coupling of ^{57}Fe in the 500 ms quench sample is very similar to that of the resting state.

sample revealed strong coupling of ^{57}Fe with the unpaired electron centered at the Laramor frequency of ^{57}Fe, which is absent in the 500 ms quench with unlabeled PFL-AE. The extent of coupling between the paramagnetic center and the ^{57}Fe in the intermediate is very similar to that of a static PFL-AE [4^{57}Fe-4S]$^{+}$ cluster (Figure 10.6b) where the unpaired electron resides on the cluster. From these ENDOR results, we have concluded that the intermediate is an unknown paramagnetic [4Fe-4S] cluster.

ENDOR Analysis of Isotopically Labeled SAM Molecules

Since this intermediate signal at 500 ms is an unknown cluster state, we wanted to further characterize the signal with labeled SAM molecules to observed any coupling via ENDOR. First, we needed to introduce specific NMR-active nuclei into SAM by synthesizing SAM from [U-$^{13}C_{10}$,$^{15}N_5$]-adenosine 5'-triphosphate and [U-$^{2}H_8$]-adenosine 5'-triphosphate to provide SAM labeled in the adenosine portion and [methyl-^{13}C]-L-methionine, [methyl-$^{2}H_3$]-L-methionine, [3,3,4,4-$^{2}H_4$]-L-methionine, and seleno-L-methionine for labeling of the methionine portion of SAM (Figure 10.7). With the

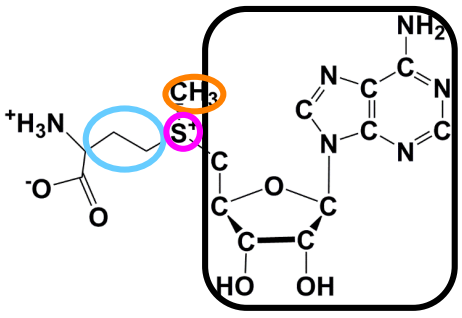


Figure 10.7. Labeled SAM molecules used in this study. Circled areas with different colors correspond to either ^{13}C, ^{15}N, ^{2}H, or Se labeling in either the methionine portion or the adenosine portion.

addition of [U-$^{13}C_{10}$,$^{15}N_5$-adeonsine]-SAM and [methyl-^{13}C]-SAM, slight broadening of the X-band EPR intermediate signal was observed, suggesting an interaction between those nuclei and the paramagnetic [4Fe-4S] cluster (Figure 10.8). We therefore focused on these SAM labels.

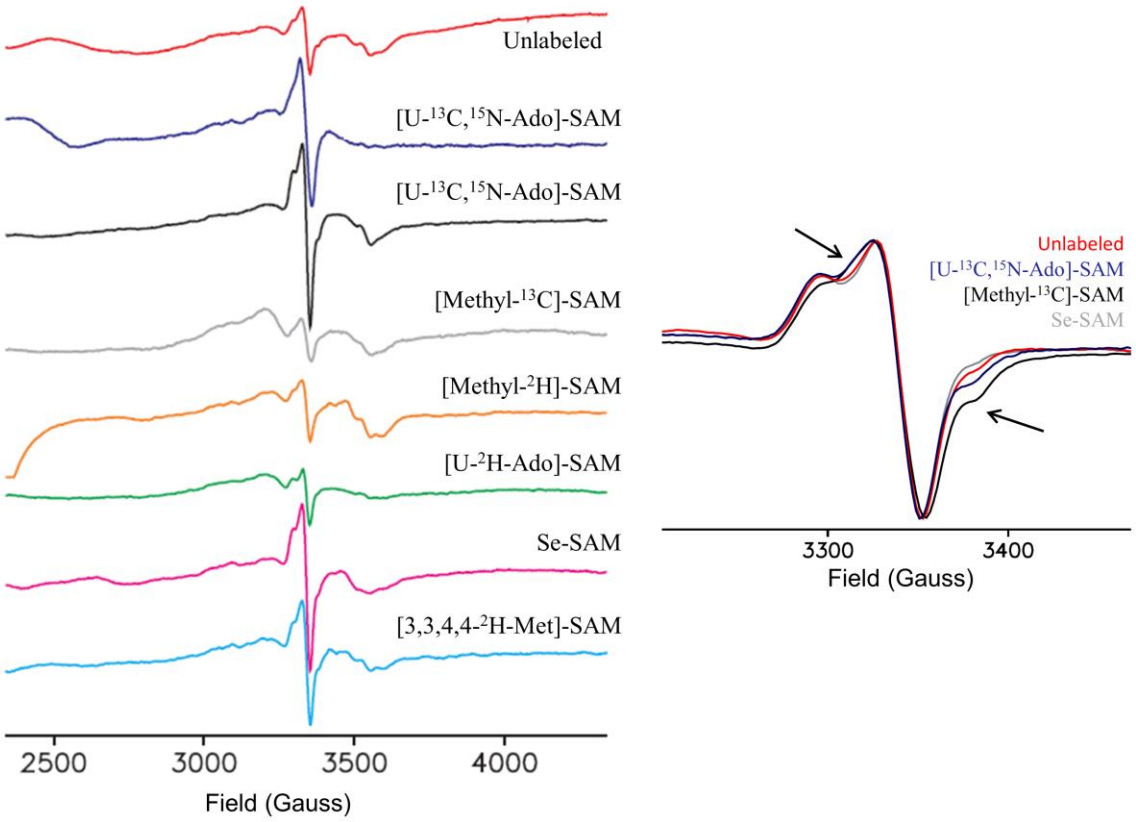


Figure 10.8. X-band EPR spectra of the 500 ms quench of PFL-AE with different isotopically labeled SAM molecules (left). On the right, comparison of unlabeled (red), [U-$^{13}C_{10}$,$^{15}N_5$-adeonsine]-SAM (blue), methyl-^{13}C-SAM (black), and Se-SAM (grey) are shown. Black arrows indicate broadened features due to the different labeled SAM molecules.

CW ENDOR analysis of [U-$^{13}C_{10}$,$^{15}N_5$-adeonsine]-SAM revealed one strongly coupled carbon (Figure 10.9). This signal contains a very strong A_{iso} = 9.4 MHz coupling giving rise to a distance of 1.72 Å from the paramagnetic species. This

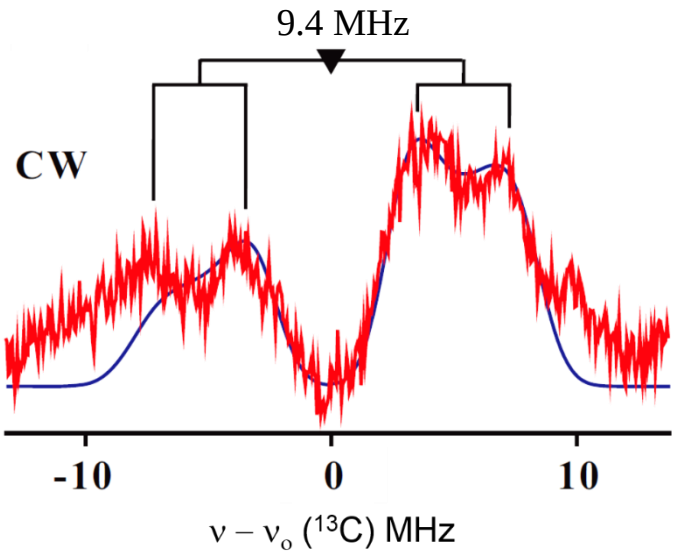


Figure 10.9. Q-band CW ^{13}C ENDOR spectrum of the 500 ms quenched sample with [U-$^{13}C_{10}$,$^{15}N_5$-adeonsine]-SAM. The simulated spectrum (blue) gives an A_{iso} = 9.4 MHz with a radius of 1.72 Å from the paramagnetic [4Fe-4S] cluster.

coupling is much weaker than a carbon based radical. For example, ENDOR analysis on triphenylmethyl radicals (Figure 10.10) in solution with natural abundant ^{13}C revealed a 66.87 MHz coupling for the perdeuterotriphenylmethyl radical on the central carbon. A strong 31.93 MHz coupling was also observed on the attached carbon [22]. Another example is the methoxy substituted pentaphenylcyclopentadienyl radical with ^{13}C labeling on one carbon in the ring (Figure 10.10) resulting in an ENDOR coupling of 27.41 MHz [23]. This radical is delocalized within the ring, accounting for the lower coupling constant compared to the triphenylmethyl radical centered on one carbon. Compared to the coupling of 9.4 MHz in the PFL-AE intermediate, our coupling is too weak to be a carbon based radical, ruling out the elusive 5'-dAdo•. Rather, a carbon is directly interacting with the [4Fe-4S] cluster. Due to the current understanding of radical

SAM chemistry where reductive cleavage of the S-5'-C bond produces a radical on the 5'-C, we have assigned the strongly coupled ^{13}C as the 5'-C.

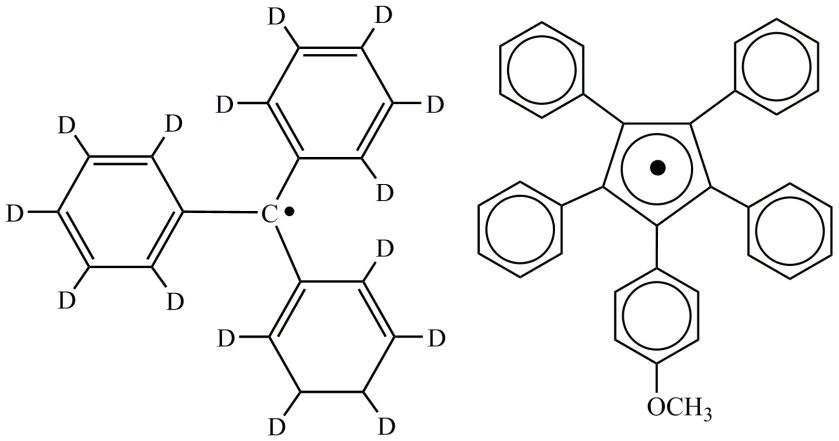


Figure 10.10. Carbon based radicals used for comparison of the ^{13}C coupling found in the PFL-AE intermediate. The carbon based radical coupling from the triphenylmethyl radical (left) and the methoxy substituted pentaphenylcyclopentadienyl radical (right) were much greater than that observed in the PFL-AE intermediate.

Mims ENDOR spectroscopy is used to analyze weak coupling between a paramagnetic species and a nucleus. Mims ENDOR analysis revealed two weakly coupled ^{13}C to the [4Fe-4S] cluster in the [U-$^{13}C_{10}$,$^{15}N_5$-adeonsine]-SAM sample. The coupling constants of these two carbons were calculated as $A_1 = 0.7$ MHz and $A_2 = 0.1$ MHz and these signals presumably arise from the 4'-C and 3'-C, respectively (Figure 10.11). The [methyl-^{13}C]-SAM sample contained a coupling constant of A = 0.5 MHz which is very similar to the coupling observed in static PFL-AE prepared with [methyl-^{13}C]-SAM [15], suggesting the methyl-C is still within the same distance of the [4Fe-4S] cluster.

In addition to ^{13}C ENDOR experiments, ^{14}N ENDOR analysis was conducted on the intermediate samples to determine whether the amino N is coordinated to the unique

Fe. Initial experiments revealed no coupling between the [4Fe-4S] cluster and ^{14}N (data not shown). It is difficult to say whether this is due to the dissociation of the methionine portion or whether the relatively weak intermediate EPR signal is suppressing any coupling from the amino N. Further methionine labeling with amino ^{15}N and carboxyl ^{17}O needs to be conducted.

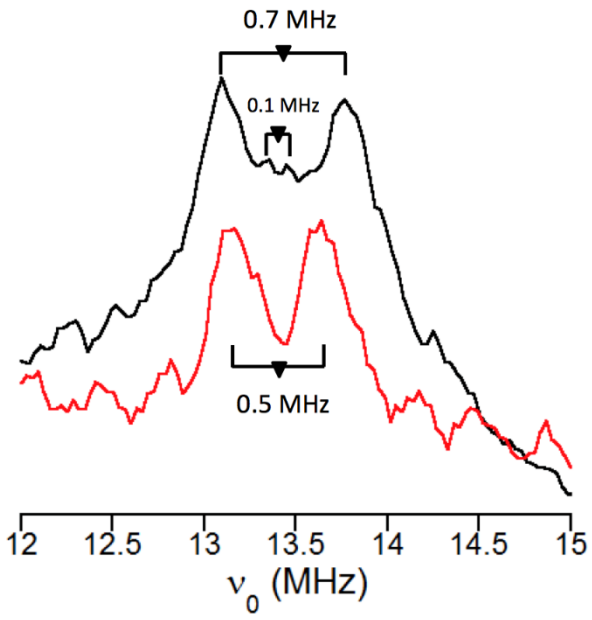


Figure 10.11. Mims ^{13}C ENDOR spectra of the 500 ms quench sample with [U-$^{13}C_{10}$,$^{15}N_5$-adeonsine]-SAM (black) or [methyl-^{13}C]-SAM (red).

Discussion

Rapid freeze techniques revealed an unknown signal which dominates after a 500 ms quench but does not correspond to a reduced [4Fe-4S] cluster nor a glycyl radical previously characterized in the PFL-AE reaction (Figure 10.12). Shorter and longer

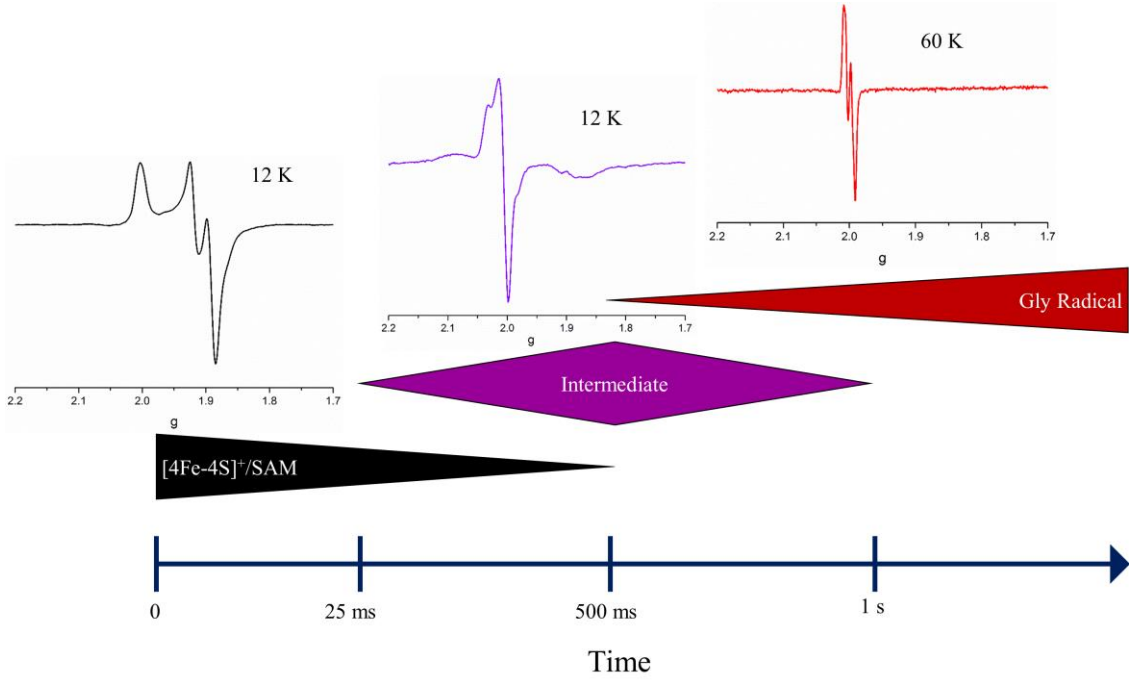


Figure 10.12. Progression of the observed paramagnetic species in the PFL-AE reaction. At time zero, the $[4Fe\text{-}4S]^{+}$/SAM signal (black) precedes the intermediate signal (purple) which maximizes at 500 ms but can be observed beginning with a 25 ms quench through a 1 s quench. The intermediate is then turned over to the glycyl radical (red) which dominates after 1 s.

mixing times in addition to annealing studies suggest that this signal is a valid intermediate in the PFL-AE reaction. The signal was characterized through ENDOR analysis of isotopically labeled PFL-AE and SAM molecules. Labeling of the $[4^{57}Fe\text{-}4S]$ cluster revealed a strong coupling between the paramagnetic species and ^{57}Fe of the cluster, similar to the resting state of a $[4^{57}Fe\text{-}4S]^{+}$ cluster, suggesting the unpaired electron resides on the cluster. Due to antiferromagnetic coupling, the cluster must be either a reduced $[4Fe\text{-}4S]^{+}$ or an oxidized $[4Fe\text{-}4S]^{3+}$ cluster. We believe this intermediate corresponds to a $[4Fe\text{-}4S]^{3+}$ state due to a direct bond between the cluster and the 5'-C of SAM. Strong coupling between the $[4Fe\text{-}4S]^{3+}$ to a ^{13}C in [U-$^{13}C_{10}$,$^{15}N_5$-adeonsine]-SAM revealed a distance of 1.72 Å between the ^{13}C and the paramagnetic

center. The extent of this coupling suggests there's a direct bond between the cluster and a carbon of SAM. From our current understanding of radical SAM enzymes, we identify this strongly coupled carbon as the 5'-C which is thus bound to the $[4Fe\text{-}4S]^{3+}$ cluster to produce an unprecedented organometallic intermediate (Figure 10.13). Support for this unusual cluster Fe-C bond was observed in the [4Fe-4S] containing IspH and IspG

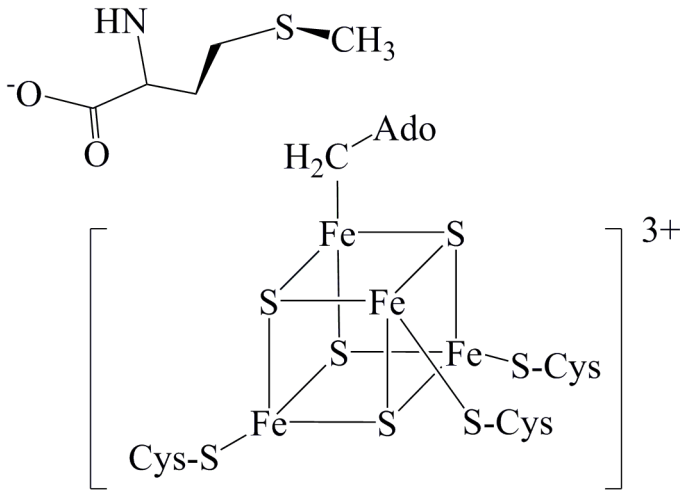


Figure 10.13. Proposed intermediate in the PFL-AE reaction.

enzymes in which an intermediate signal is thought to originated from a direct cluster-substrate bond between the unique iron and a carbon of the substrate (Figure 10.14). These enzymes are involved in the conversion of 2-C-methylerythritol-cyclo-2,4-diphosphate (MEcPP) to (E)-1-hydroxy-2-methyl-but-2-enyl-4-diphosphate (HMBPP) by IspG followed by conversion of HMBPP to isopentenyl diphosphate and dimethylallyl diphosphate by IspH, each through a proposed substrate carbon-unique Fe bound intermediate (Figure 10.14) [24-26]. The reported intermediate has very similar EPR g-values (g = 2.173, 2.013, and 1.997 for IspH) [26] as the PFL-AE intermediate (g = 2.04, 2.01), although IspH does contain a higher field feature at g = 2.173 which is absent

in PFL-AE. Even though no ^{57}Fe coupling has been reported for IspH nor IspG, the cluster is believed to have donated two electrons to substrate, oxidizing the cluster to a paramagnetic [4Fe-4S]$^{3+}$ state. The ^{13}C coupling in the IspG protein to the paramagnetic cluster (17.7 MHz) [25] is slightly larger than obtained in our intermediate (9.4 MHz) but is still similar to our observed ^{13}C coupling, supporting our hypothesis of a cluster Fe-C bond.

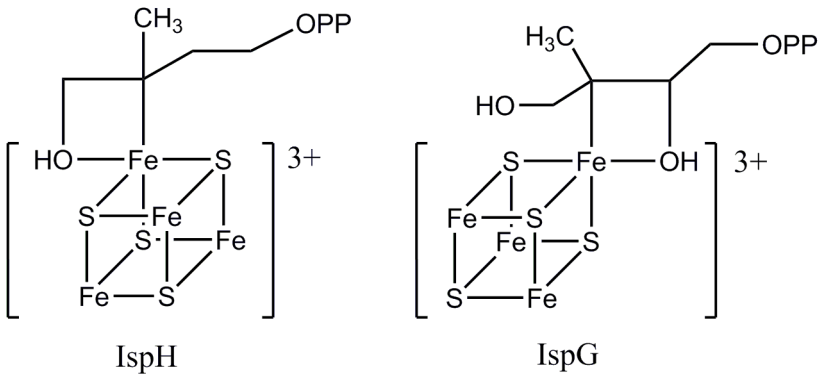


Figure 10.14. Proposed intermediates in the IspH (left) and IspG (right) enzymes.

In the PFL-AE intermediate, we believe SAM has been cleaved and the methyl-C of methionine is within 4.0 Å of the cluster, similar to un-cleaved SAM. Presumably, if SAM were intact, a strong methyl-^{13}C signal would be detected; however, almost identical methyl-^{13}C coupling to static samples prepared with [methyl-^{13}C]-SAM was observed. To determine whether methionine has dissociated from the cluster in the intermediate, ENDOR analysis was conduct to observe any coupling between the [4Fe-4S]$^{3+}$ cluster and the amino ^{14}N of SAM. No ^{14}N coupling (data not shown) was observed in the intermediate species. Whether this is due to the amino N dissociating from the cluster is undetermined. With these ENDOR results, we have proposed the

intermediate is a paramagnetic $[4Fe\text{-}4S]^{3+}$ cluster with a unique Fe-adenosyl bound with methionine dissociated upon Fe-C bond formation (Figure 10.13).

A direct metal-adenosyl bond is not unusual in metalloenzymes: the adenosylcobalamin-dependent enzymes utilize the adenosylcobalamin (AdoCbl) cofactor to generate substrate radicals through cleavage of a Co-adenosyl bond to produce 5'-dAdo• [27]. Our cluster-adenosyl intermediate is very similar to the AdoCbl cofactor and suggests these two enzymes are more closely related than initially thought. The AdoCbl-dependent enzymes may provide clues into a possible reaction mechanism in PFL-AE since the exact mechanism by which the organometallic intermediate forms and then proceeds to abstract a H from PFL is still under investigation. One scenario involves inner sphere electron transfer from the reduced cluster to SAM, followed by homolytic cleavage of SAM to produce the 5'-dAdo• radical in conjunction with the oxidation of the cluster to the $[4Fe\text{-}4S]^{2+}$ state. The unique Fe then donates another electron to form a bond with the 5'-C, resulting in an EPR active $[4Fe\text{-}4S]^{3+}$ cluster state. Like the AdoCbl-dependent enzymes, this Fe-adenosyl bond is them cleaved to produce the 5'-dAdo• radical, resulting in reduction of the cluster to the $[4Fe\text{-}4S]^{2+}$ state (Figure 10.15). An alternative scenario could involve an S_N2-type reaction where a lone pair on the unique Fe attacks the 5'-C of SAM, displacing methionine and resulting in a net oxidation of the cluster to the $[4Fe\text{-}4S]^{3+}$ state with the adenosyl moiety bound (Figure 10.16). This mechanism is similar to the proposed addition of adenosine to the cobalt center to form the AdoCbl cofator. In order for this reaction to occur in PFL-AE, the sulfonium must

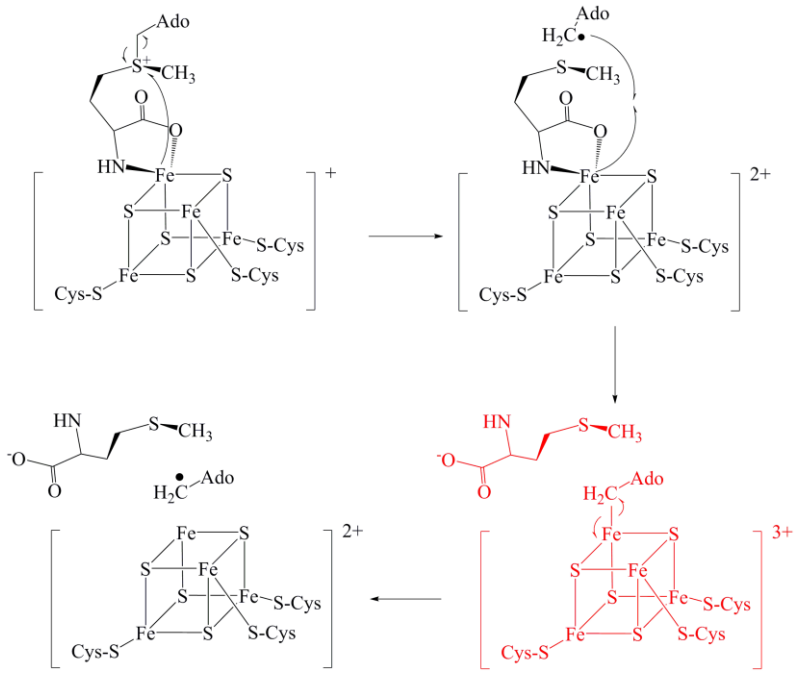


Figure 10.15. A proposed mechanism for the production of the proposed Fe-adenosyl intermediate (red) and 5'-Ado• in PFL-AE. The reaction begins with one electron transfer for reductive cleavage of SAM to produce 5'-dAdo•. Another electron from the cluster attacks 5'-dAdo• to form the Fe-adenosyl intermediate (red). The Fe-C bond is then cleaved to produce 5'-dAdo• which can then abstract a hydrogen from PFL.

move to allow the 5'-C to rotate towards the unique Fe. Again, this Fe-adenosyl bond can then be cleaved for 5'-dAdo• production.

Many questions still remain and this report is just the beginning of what will be an extended study of radical intermediates in radical SAM enzymes. The mechanism to generate this organometallic intermediate is unknown but we have concluded that this intermediate is generated prior to PFL activation. Annealing studies validated that the intermediate signal converts to a PFL based glycyl radical. We believe the Fe-adenosyl bond is cleaved to produce the 5'-dAdo• radical to abstract the H-atom of G734. One big question is whether 5'-dAdo• is produced during catalysis. The Fe-adenosyl bond

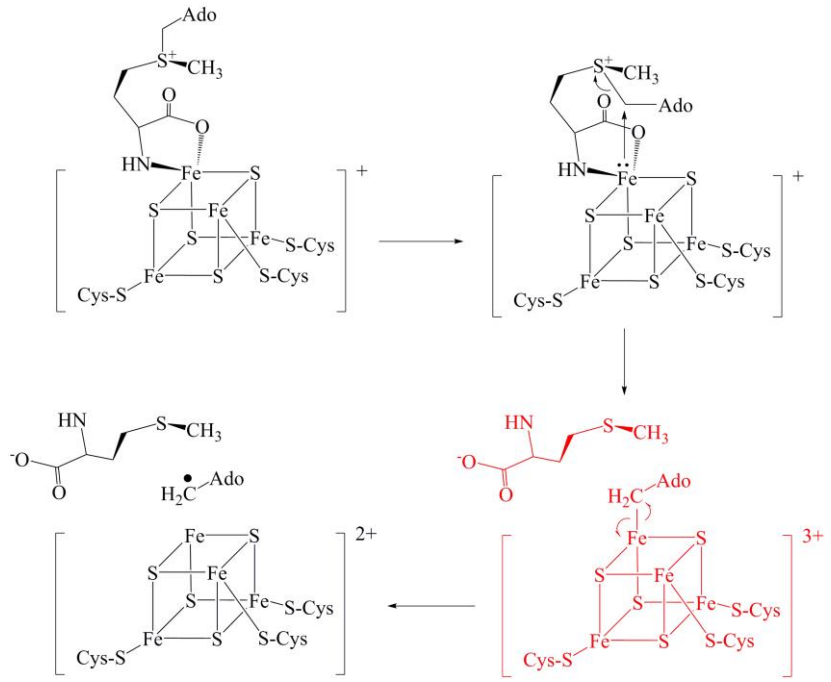


Figure 10.16. Another proposed mechanism for formation of the Fe-adenosyl intermediate (red) via an S_N2-like reaction with methionine as a leaving group. In this mechanism, the 5'-C must first rotate towards the unique Fe. Then, a lone pair on the unique Fe attacks the 5'-C of SAM, forming a Fe-C bond (red). The Fe-adenosyl bond is then cleaved to form 5'-dAdo•.

increases the distance between the unique Fe and the abstracted hydrogen on PFL, forming a 7.4 Å gap between the two. This contradicts the results that the anAdo• radical only undergoes a 0.6 Å shift towards the lysine substrate in the LAM/anSAM complex [4]. However, work on the radical SAM enzyme LAM showed that upon cleavage of anSAM, a stable anAdo• can be observed and LAM was able to turnover substrate [2-4], suggesting that the anAdo•, and thus 5'-dAdo•, is an intermediate in radical SAM enzymes. PFL-AE, on the other hand, has not been shown to cleave anSAM. However, the intermediate signal was observed in the presence of anSAM, and produced a more intense EPR signal than SAM, suggesting that PFL-AE can cleave anSAM and form a Fe-C bond. We would like to conduct annealing studies on the anSAM 500 ms quench

sample for it may reveal whether the Fe-C bond can be cleaved to produce an anAdo• radical or ultimately the glycyl radical.

Another question thus arises as to why this intermediate would be formed in PFL-AE which increases the distance between SAM and substrate. One possibility is that the intermediate may be a control mechanism in which PFL-AE awaits proper coordination of substrate. PFL is believed to contain two conformations in which an open conformation interacts with PFL-AE and a closed conformation carries out the conversion of pyruvate and CoA to formate and acetyl-CoA [28]. The open conformation involves a loop region, which includes the catalytic G734 residue, to swing out for activation by PFL-AE. This loop then swings back into the interior of the protein to interact with the catalytic cysteine residues. Since PFL must undergo a large conformational change to interact with PFL-AE, the intermediate may be a way for PFL-AE to store 5'-dAdo• while the PFL loop orients properly in the active site. Once the G734 residue is in place, the Fe-adenosyl bond is thus cleaved and immediate H-atom abstraction can occur. We do not know whether this intermediate is exclusive to PFL-AE, other activating enzymes, or if all radical SAM enzymes contain this unprecedented organometallic intermediate but this intermediate is changing our view of how radical SAM enzymes are able to carry out diverse reactions with a simple molecule.

Supplementary Information

SI Figures

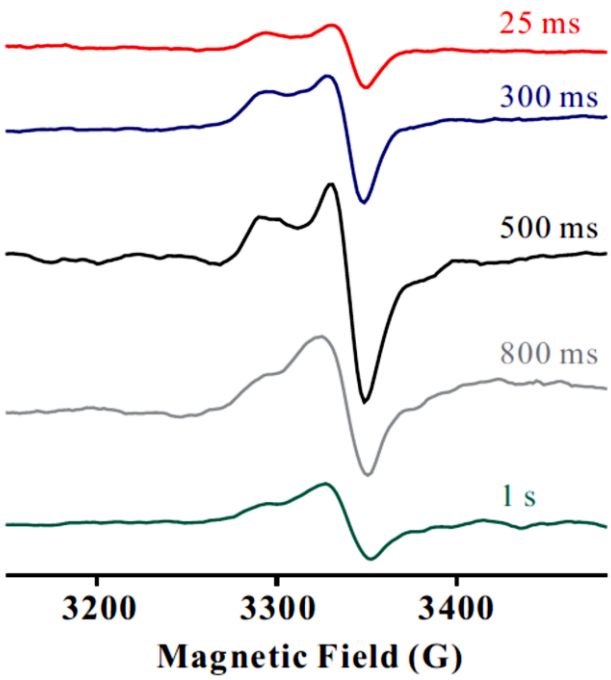


Figure SI.10.1. EPR spectra of different quench times. Some intermediate is observed at the 25 ms quench which maximizes at the 500 ms quench, followed by a decrease at the 800 ms and 1 s quench times.

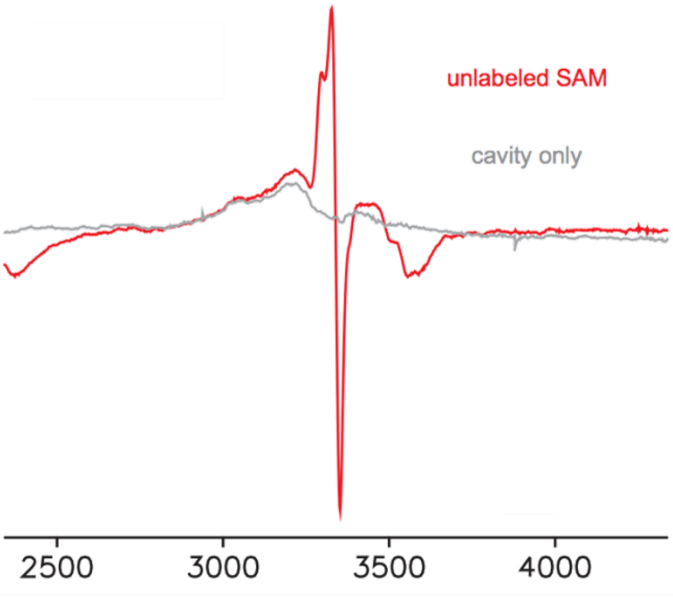


Figure SI.10.2. EPR spectra comparing the 500 ms quenched sample with unlabeled SAM (red) and the empty cavity (grey). The feature at ~3200 G is due to cavity while the feature ~ 3550 G is due to $[4Fe\text{-}4S]^{+}$/SAM signal.

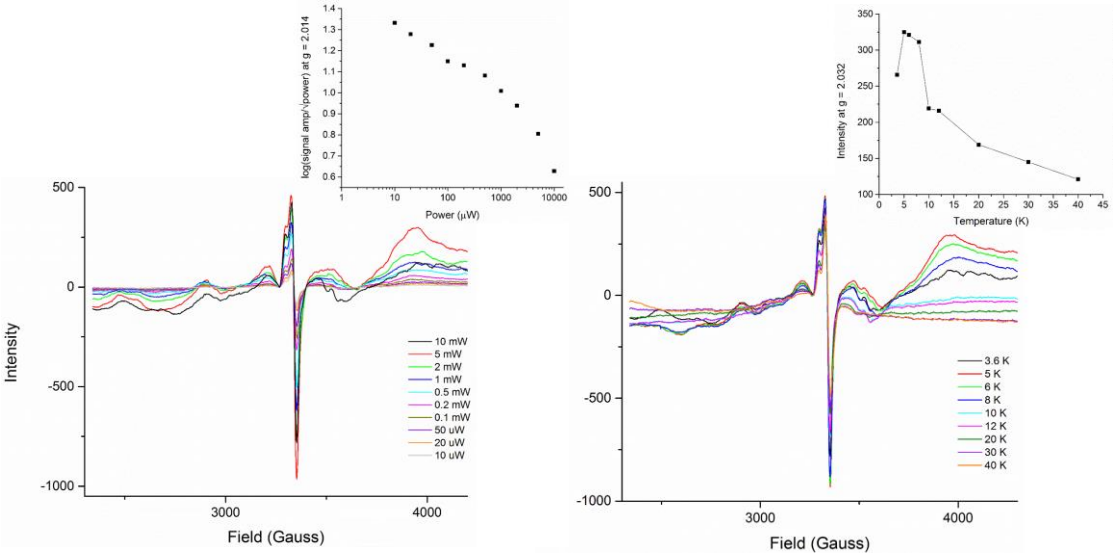


Figure SI.10.3. EPR power saturation (left) and temperature dependence (right) of the 500 ms intermediate signal. Power studies were conducted at 3.6 K while temperature studies were conducted at 10 mW.

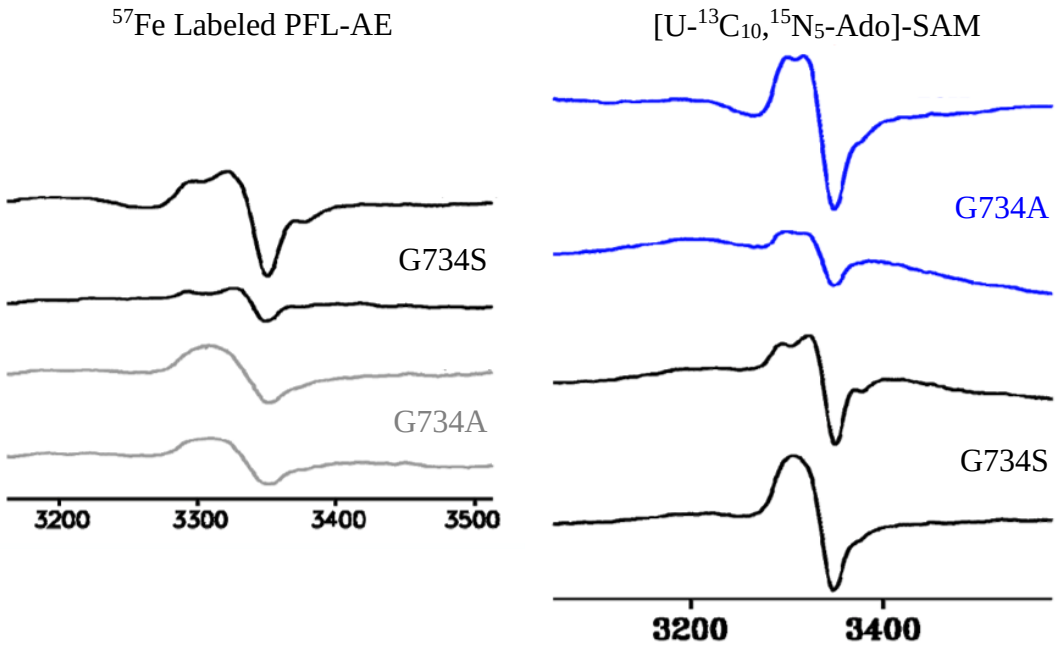


Figure SI.10.4. EPR spectra of different 500 ms quench samples containing either ^{57}Fe labeled PFL-AE, SAM, and the two PFL G734 variants (left) or unlabeled PFL-AE, [U-$^{13}C_{10}$,$^{15}N_5$-Ado]-SAM, and the two PFL G734 variants (right). All the spectra are normalized. The G734S variant spectra are shown in black while the G734A variant spectra are shown in grey and blue.

References

1. Broderick, J. B.; Duffus, B. R.; Duschene, K. S.; Shepard, E. M. *Chem. Rev.* **2014**, *114*, 4229-4317.

2. Magnusson, O. T.; Reed, G. H.; Frey, P. A. *J. Am. Chem. Soc.* **1999**, *121*, 9764-9765.

3. Magnusson, O. T.; Reed, G. H.; Frey, P. A. *Biochemistry* **2001**, *40*, 7773-7782.

4. Horitani, M.; Byer, A. S.; Shisler, K. A.; Chandra, T.; Broderick, J. B.; Hoffman, B. M. *J. Am. Chem. Soc.* **2015**, *137*, 7111-7121.

5. Maity, A. N.; Hsieh, C.-P.; Huang, M.-H.; Chen, Y.-H.; Tang, K.-H.; Behshad, E.; Frey, P. A.; Ke, S.-C. *J. Phys. Chem. B* **2009**, *113*, 12161-12163.

6. Canfield, J. M.; Warncke, K. *J. Phys. Chem. B* **2002**, *106*, 8831-8841.

7. LoBrutto, R.; Bandarian, V.; Magnusson, O. T.; Chen, X.; Schramm, V. L.; Reed, G. H. *Biochemistry* **2001**, *40*, 9-14.

8. Becker, A.; Fritz-Wolf, K.; Kabsch, W.; Knappe, J.; Schultz, S.; Volker Wagner, A. F. *Nature structural biology* **1999**, *6*, 969-975.

9. Frey, M.; Rothe, M.; Wagner, A. F.; Knappe, J. *J. Biol. Chem.* **1994**, *269*, 12432-12437.

10. Knappe, J.; Sawers, G. *FEMS Microbiol. Rev.* **1990**, *75*, 383-398.

11. Plaga, W.; Vielhaber, G.; Wallach, J.; Knappe, J. *FEBS Lett.* **2000**, *466*, 45-48.

12. Becker, B. F.; Gilles, S.; Sommerhoff, C. P.; Zahler, S. *J. Biol. Chem.* **2002**, *383*, 1821-1826.

13. Broderick, J. B.; Henshaw, T. F.; Cheek, J.; Wojtuszewski, K.; Smith, S. R.; Trojan, M. R.; McGhan, R. M.; Kopf, A.; Kibbey, M.; Broderick, W. E. *Biochem. Biophys. Res. Commun.* **2000**, *269*, 451-456.

14. Krebs, C.; Henshaw, T. F.; Cheek, J.; Huynh, B.; Broderick, J. B. *J. Am. Chem. Soc.* **2000**, *122*, 12497-12506.

15. Walsby, C. J.; Hong, W.; Broderick, W. E.; Cheek, J.; Ortillo, D.; Broderick, J. B.; Hoffman, B. M. *J. Am. Chem. Soc.* **2002**, *124*, 3143-3151.

16. Walsby, C. J.; Ortillo, D.; Broderick, W. E.; Broderick, J. B.; Hoffman, B. M. *J. Am. Chem. Soc.* **2002**, *124*, 11270-11271.

17. Kim, S. H.; Perera, R.; Hager, L. P.; Dawson, J. H.; Hoffman, B. M. *J. Am. Chem. Soc.* **2006**, *128*, 5598-5599.

18. Lin, Y.; Gerfen, G. J.; Rousseau, D. L.; Yeh, S.-R. *Analytical Chemistry* **2003**, *75*, 5381-5386.

19. Davydov, R.; Kofman, V.; Fujii, H.; Yoshida, T.; Ikeda-Saito, M.; Hoffman, B. M. *J. Am. Chem. Soc.* **2002**, *124*, 1798-1808.

20. Broderick, J. B.; Duderstadt, R. E.; Fernandez, D. C.; Wojtuszewski, K.; Henshaw, T. F.; Johnson, M. K. *J. Am. Chem. Soc.* **1997**, *119*, 7396-7397.

21. Henshaw, T. F.; Cheek, J.; Broderick, J. B. *J. Am. Chem. Soc.* **2000**, *122*, 8331-8332.

22. Kirste, B. *J. Magn. Reson. 1969* **1985**, *62*, 242-259.

23. Kieslich, W.; Kurreck, H. *J. Am. Chem. Soc.* **1984**, *106*, 4328-4335.

24. Wang, W.; Li, J.; Wang, K.; Huang, C.; Zhang, Y.; Oldfield, E. *Proc. Natl. Acad. Sci. USA* **2010**, *107*, 11189-11193.

25. Wang, W.; Wang, K.; Li, J.; Nellutla, S.; Smirnova, T. I.; Oldfield, E. *J. Am. Chem. Soc.* **2011**, *133*, 8400-8403.

26. Xu, W. Y.; Lees, N. S.; Hall, D.; Welideniya, D.; Hoffman, B. M.; Duin, E. C. *Biochemistry* **2012**, *51*, 4835-4849.

27. Marsh, E. N.; Melendez, G. D. *Biochim. Biophys. Acta, Proteins Proteomics* **2012**, *1824*, 1154-1164.

28. Peng, Y.; Veneziano, S. E.; Gillispie, G. D.; Broderick, J. B. *J. Biol. Chem.* **2010**, *285*, 27224-27231.

CHAPTER 11

CONCLUSIONS

Radical SAM (*S*-adenosyl-L-methionine) enzymes are a large superfamily of enzymes capable of carrying out very diverse chemical reactions through a proposed common mechanism: the production of the 5'-deoxyadeonsyl radical (5'-dAdo•) which abstracts a hydrogen from substrate. Although 5'-dAdo• has never been observed, it has been accepted as an intermediate during catalysis [1]. An observed SAM analogue, *S*-3',4'-anhydroadenosylmethionine (anSAM), produces an allylic stable 5'-deoxy-3',4'-anhydroadenosine-5'-yl (anAdo•) radical which can provide clues into radical SAM mechanisms. This anAdo• radical was analyzed previously by electron paramagnetic resonance (EPR) in the radical SAM enzyme lysine 2,3-aminomutase (LAM) with different isotopically labeled anSAM and α-lysine molecules at different temperatures [2,3]; however, no electron nuclear double resonance (ENDOR) analysis of the coupling between lysine and the anAdo• radical has been conducted. Thus, we wanted to observe any movements of anAdo• with respect to the lysine substrate during catalysis via ENDOR spectroscopy. Strong coupling between anAdo• and the 2-^{13}C of lysine (the α-C) implied that the radical is within van der Waals contact with this carbon at a distance of 3.0 Å. This distance is crucial for regeneration of 5'-dAdo• via radical transfer from the 2-C in lysine back to the 5'-C of 5'-deoxyadenosine (5'-dAdo). ENDOR analysis of ^{2}H coupling to anAdo• revealed a distance of ~3.8 Å from a 2-^{2}H and 2.2 Å from a 3-^{2}H to the 5'-C. To analyze movement of the 5'-C from the methyl-C

portion of methionine post cleavage, methyl-^{13}C labeled anSAM was used. The distance from the methyl-^{13}C to anAdo• was approximated at 3.6 Å, further than the resting state distance of 2.94 Å. Using the crystal structure of LAM/SAM/Lys and the ENDOR results, it was concluded that the 5'-C only moves ~0.6 Å upon reductive cleavage which is a highly controlled reaction.

Currently, only the anAdo• has only been observed in LAM. In order to probe other possible intermediates, including the highly reactive 5'-dAdo• radical, rapid freeze quench (RFQ) techniques were employed on pyruvate formate lyase activating enzyme (PFL-AE). During RFQ experiments, an unusual signal was observed after a 25 ms quench, albeit with weak signal intensity, which maximized at 500 ms and disappeared after 1 s. This signal did not correspond to a $[4Fe\text{-}4S]^{+}$ reduced PFL-AE cluster in the presence or absence of SAM (which is observed at time = 0), nor a glycyl radical, which dominates the signal after ~1 s. Thus, the signal was identified as an intermediate of unknown origin. Annealing experiments, where the 500 ms quench sample was warmed to allow minimal molecular motion while still maintaining freezing conditions, the intermediate signal was able to convert to the glycyl radical, suggesting the intermediate is a valid intermediate in the PFL-AE reaction. To investigate the origin of the signal, the intermediate signal was coupled with specific isotopically labeled SAM molecules and an ^{57}Fe labeled PFL-AE cluster ([4^{57}Fe-4S]) for ENDOR analysis. When RFQ samples were prepared with [4^{57}Fe-4S] PFL-AE, a very strong coupling was observed between the paramagnetic species and ^{57}Fe. This coupling was very similar to a reduced $[4^{57}Fe\text{-}4S]^{+}$ cluster prior to quenching, suggesting the unpaired electron resides on the

cluster and the intermediate is a new paramagnetic state of the cluster. Due to antiferromagnetic coupling, only a $[4Fe\text{-}4S]^{+}$ cluster or a $[4Fe\text{-}4S]^{3+}$ cluster is paramagnetic. To further explore the origin of the intermediate signal, isotopically labeled SAM molecules were utilized to analyze interactions of SAM with the unknown cluster state. ENDOR analysis was conducted on samples containing labeled SAM molecules that caused broadening of the EPR signal. With the addition of [U-$^{13}C_{10}$,$^{15}N_5$-adenosine]-SAM, strong ^{13}C coupling was observed via ENDOR spectroscopy, presumably from the 5'-C, and it was hypothesized that the 5'-C is bound to the unique Fe of a $[4Fe\text{-}4S]^{3+}$ cluster. Similar ^{13}C coupling was observed in the 500 ms quench sample containing [methyl-^{13}C]-SAM as that observed in static samples containing a reduced $[4Fe\text{-}4S]^{+}$ cluster and [methyl-^{13}C]-SAM. It was thus hypothesized that SAM was cleaved and the methyl-C is within the same distance of the cluster as un-cleaved SAM. No amino ^{14}N coupling was observed via ENDOR spectroscopy suggesting that the methionine portion has dissociated in the intermediate. The organometallic Fe-adenosyl intermediate species is identical to the adenosylcobalamin (AdoCbl) cofactor which contains an adenosyl group bound to cobalt oriented in a corrin ring. During catalysis, the Co-adenosyl bond is broken to produce 5'-dAdo• which then abstracts a hydrogen from substrate [4]. PFL-AE (and possibly other radical SAM enzymes) may be closer related to AdoCbl-dependent enzymes than previously thought since an Fe-adenosyl intermediate was isolated in PFL-AE.

The Fe-adenosyl PFL-AE intermediate is very perplexing. It has changed our view of radical generation in radical SAM enzymes and has raised many more questions.

The formation of the Fe-adenosyl bond increases the distance of the 5'-C with respect to substrate, contrary to the results with anSAM and LAM. The pro-*S* hydrogen of the PFL G734 residue is 7.4 Å from the unique Fe in the crystal structure of PFL-AE. Why would PFL-AE increase this distance? One possibility is for control of the 5'-dAdo• radical while the PFL loop region containing G734 aligns properly in PFL-AE. This loop region is very dynamic and must flip out to interact with PFL-AE and then swing back into the active site of PFL [5]. Due to the highly reactive manner of 5'-dAdo•, the cluster may tame the radical while the PFL loop swings into the active site. Presumably, other radical SAM enzymes that act upon other large protein substrates, such as other glycyl activating enzymes, would undergo the same intermediate. Other radical SAM enzymes which contain small molecule substrates may not need to tame the 5'-dAdo• and this intermediate may not occur. If we can isolate this intermediate in other radical SAM enzymes, it can provide clues as to why PFL-AE undergoes a very unusual pathway for substrate activation.

Another question that arises with this Fe-adenosyl intermediate is how and if the 5'-dAdo• radical is formed. Currently, it is proposed that 5'-dAdo• is generated by inner sphere electron transfer from the unique Fe to the sulfonium to induce homolytic cleavage of the S-C bond [6]. Since PFL-AE contains an Fe-adenosyl intermediate, the mechanism for 5'-dAdo• production needs to be revised. Two possible methods have been proposed: oxidative addition of 5'-dAdo• to the unique Fe or an S_N2-like reaction. In an oxidative addition mechanism, 5'-dAdo• is produced by reductive cleavage of SAM followed by formation of the Fe-adenosyl bond while in an S_N2-like reaction, methionine

acts as a leaving group. We believe 5'-dAdo• is then produce following cleavage of the Fe-adenosyl bond similar to the AdoCbl-dependent enzymes and the hydrogen of substrate is then abstracted. The allylic anAdo• radical produced upon cleavage of the SAM analogue anSAM supports that a 5'-dAdo• is produced during catalysis. Previous results of LAM with anSAM showed that the rate of anAdo• formation makes it a kinetically competent intermediate in the LAM reaction [2].

Another project involved further investigation into previous Mössbauer experiments that revealed a valence localized $[4Fe\text{-}4S]^{2+}$ cluster in PFL-AE in whole cells which could be induced with the addition of adenosine monophosphate (AMP), 5'-deoxyadenosine (5'-Ado), methylthioadenosine (MTA), and adenosine diphosphate (ADP) [7]. To understand how these adenosyl-containing molecules interact with the cluster, EPR and ENDOR analysis was conducted in the presence of small molecules. These experiments were conducted in the EPR active, $[4Fe\text{-}4S]^{+}$ reduced state. Spectral changes were observed in the presence of AMP, MTA, 5'-dAdo, adenine, and ADP, consistent with Mössbauer results in which these small molecules induce valence localization. ENDOR spectroscopy was used to observe any coupling between the cluster and labeled [U-$^{13}C_{10}$,$^{15}N_5$]-AMP and [ribose-$^{13}C_5$]-adenosine which can be used to obtain structural information. Two weak couplings with different coupling constants were detected in the [U-$^{13}C_{10}$,$^{15}N_5$]-AMP sample with only the weaker coupling observed in the labeled [ribose-$^{13}C_5$]-adenosine sample, suggesting the adenine ring is oriented closer to the cluster. Synthesized [ribose-$^{13}C_5$]-AMP only contained the weak signal, confirming that the adenine ring was closer to the cluster and the phosphate group did not

significantly change the small molecule orientation. No ^{15}N coupling was observed in the presence of [U-$^{13}C_{10}$,$^{15}N_5$]-AMP, suggesting that the adenine ring is not directly interacting with the cluster through an Fe-N bond. This result was peculiar because the extent of the ^{13}C coupling from the adenine ring was strong enough to suggest that the cluster was directly interacting with a neighboring atom. Further ENDOR analysis with samples prepared in ^2H_2O confirmed that H_xO was bound to the unique Fe. Docking studies of AMP into the active site of PFL-AE revealed three possible binding modes of AMP that agree with ENDOR results. These included a SAM-like mode where the adenosine ring of AMP was positioned similarly to that of SAM in the crystal structure of PFL-AE; a π-cation mode where the adenine ring of AMP is sandwiched between the cluster and a unique cation site in PFL-AE; and a rotated SAM-like mode which was the most plausible model. In this model, the adenine ring is rotate with respect to SAM binding but places the adenine ring and the ribose ring at distances consistent with ENDOR results. The phosphate group was protected within the active site and was position to interact with the H_xO bound species. More analysis needs to be conducted to determine the actual binding mode for these small molecules, to determine exactly how they are inducing valence localization, and to understand why a valence localization event occurs.

Further refinement of the crystal structure of PFL-AE revealed a cation binding site within the active site. The cation contained a distorted trigonal bipyramidal geometry with five oxygens ligands from two aspartate side chains (D104 and D129), a threonine (T105) backbone, a methionine (M127) backbone, and the free carboxyl O of SAM. The

identity of this monovalent cation affected the activity of PFL-AE, the EPR signal, and the circular dichroism (CD) signal. The lowest activity was observed in the absence of monovalent cation with an increase in activity in the presence of the smallest monovalent cations Li^+<Na^+, a maximum in the presence of K^+, followed by a decrease in activity with the addition of the larger cations NH_4^+>Rb^+>Cs^+. The divalent cations tested (Ca^{2+}, Mg^{2+}, and Zn^{2+}) inhibited activity. Activity was also dependent on the concentration of K^+, revealing an optimal concentration between 100 mM and 200 mM K^+. The most significant EPR and CD spectral changes were observed in the presence of different monovalent cations when SAM was present suggesting that cation size affected SAM coordination. To observe any changes in SAM coordination in the presence of K^+, Na^+, and another monovalent cation Tl^+, ^{14}N ENDOR spectroscopy was conducted to observe changes in the amino N coordination and ^{13}C ENDOR spectroscopy was conducted on [methyl-^{13}C]-SAM containing samples to observe changes in the methyl-C. SAM has slightly different coordination in the presence of the three different cations with a more defined SAM structure in the K^+ sample which might correlate with its highest activity. ENDOR spectroscopy was also conducted to observe any coupling between a monovalent cation and the $[4Fe\text{-}4S]^+$ cluster. In the presence of Tl^+, the EPR spectrum of the cluster produced an unusual signal that was originally thought to be hyperfine splitting due to nuclear spin of $^{203}Tl/^{205}Tl$ (I = ½) and these samples were good candidates for ENDOR spectroscopy. With the use of Q-band EPR, the “splitting” observed in the EPR signal was determined to be two different conformations of the cluster not hyperfine interactions. However, during ENDOR experiments, coupling between the cluster and

Tl^+ (I = ½) was observed and a distance of >5.5 Å was calculated, consistent with the 6.5Å distance to the center of the cation in the crystal structure of PFL-AE [8]. Coupling between the cluster and Na^+ was also observed with an estimated distance of 5-6 Å from the cluster. No K^+ coupling, however, was observed.

Alignment of PFL-AE with other radical SAM enzymes revealed that other activating enzymes including RNR-AE, Bss-AE, Hpd-AE, and GD-AE may contain a cation binding site. These radical SAM enzymes share a common cation binding motif of $DTX_{18\text{-}21}MXD$ (X = 21 for PFL-AE) although they differ with respect to the aspartate and methionine residues. The activating enzymes contain an aspartate (RNR-AE) or a glutamate in the first aspartate position (D104 in PFL-AE) and a conserved aspartate in the last position (D129 in PFL-AE). A conserved threonine is found in the second position for all these enzymes with high variability with respect to the methionine. Further analysis on other activating enzymes will determine whether a cation can stimulate activity in other activating enzymes.

The cation may play a more significant role than coordinating SAM and orienting SAM properly in the active site. It may be involved in the organometallic intermediate state by stabilizing the dissociated amino N and carboxyl O atoms of the methionine portion post SAM cleavage and formation of the Fe-adenosyl bond. Methyl-^{13}C coupling is observed in the intermediate which demonstrates that methionine is still present in the active site; however, no ^{14}N coupling was observed, suggesting the amino N and carboxyl O have dissociated upon Fe-adenosyl formation. The cation may help stabilize methionine until the Fe-adenosyl bond is cleaved, activing PFL.

PFL-AE is a well-characterized radical SAM enzyme, which allows for more advanced spectroscopic techniques to be conducted to further understand the mechanisms of radical SAM enzymes. However, using these advanced spectroscopic techniques, it was determined that PFL-AE contains some highly unusual qualities that have yet to be observed in other radical SAM enzymes. It contains a monovalent cation site and in the presence of different monovalent cations, activity is stimulated by vary degrees. The monovalent cation identity also affects the EPR and CD spectrum of PFL-AE with more prominent changes in the presence of SAM. SAM binding differs in the presence of different monovalent cations and this change in orientation may be the cause of the variability in activity observed in PFL-AE. The $[4Fe\text{-}4S]^{2+}$ cluster in PFL-AE also exhibits a highly unusual valence localized state in the presence of small molecules that, surprisingly, are not directly interacting with the unique Fe but rather a water molecule is bound. How these small molecules are inducing valence localization is still unclear. PFL-AE and LAM were used as models to analyze intermediates in radical SAM catalysis and provide further details into the mechanisms of radical SAM enzymes. An unusual organometallic intermediate was observed in PFL-AE that is changing our view of how radical SAM enzymes abstract a hydrogen from substrate. LAM was used to observe a stable anAdo• radical through cleavage of the SAM analogue anSAM. This work further supported that 5'-dAdo• is produced during catalysis even though the Fe-adenosyl intermediate brings into question whether 5'-dAdo• is formed. In PFL-AE, the Fe-adenosyl intermediate increases the distance of the 5'-C to the substrate which contradicts anSAM results showing the production of 5'-dAdo• is highly controlled with

minimal movement upon SAM cleavage. In the adenosylcobalmin (AdoCbl)-dependent enzymes, however, the distance from the 5'-C and substrate is also large. The Fe-adenosyl intermediate provides yet another link between radical SAM enzymes and the AdoCbl-dependent enzymes which both share a common 5'-dAdo• radical.

References

1. Broderick, J. B.; Duffus, B. R.; Duschene, K. S.; Shepard, E. M. *Chem. Rev.* **2014**, *114*, 4229-4317.

2. Magnusson, O. T.; Reed, G. H.; Frey, P. A. *Biochemistry* **2001**, *40*, 7773-7782.

3. Magnusson, O. T.; Reed, G. H.; Frey, P. A. *J. Am. Chem. Soc.* **1999**, *121*, 9764-9765.

4. Marsh, E. N.; Melendez, G. D. *Biochim. Biophys. Acta, Proteins Proteomics* **2012**, *1824*, 1154-1164.

5. Peng, Y.; Veneziano, S. E.; Gillispie, G. D.; Broderick, J. B. *J. Biol. Chem.* **2010**, *285*, 27224-27231.

6. Nicolet, Y.; Amara, P.; Mouesca, J. M.; Fontecilla-Camps, J. C. *Proc. Natl. Acad. Sci. USA* **2009**, *106*, 14867-14871.

7. Yang, J.; Naik, S. G.; Ortillo, D. O.; Garcia-Serres, R.; Li, M.; Broderick, W. E.; Huynh, B. H.; Broderick, J. B. *Biochemistry* **2009**, *48*, 9234-9241.

8. Vey, J. L.; Yang, J.; Li, M.; Broderick, W. E.; Broderick, J. B.; Drennan, C. L. *Proc. Natl. Acad. Sci. USA* **2008**, *105*, 16137-16141.

REFERENCES CITED

Adrian, F. J. J. Chem. Phys. 1960, 32, 972-981.

Allen, R. M.; Chatterjee, R.; Ludden, P. W.; Shah, V. K. J. Biol. Chem. 1995, 270, 26890-26896.

Andrei, P. I.; Pierik, A. J.; Zauner, S.; Andrei-Selmer, L. C.; Selmer, T. Eur. J. Biochem. 2004, 271, 2225-2230.

Anton, B. P.; Russell, S. P.; Vertrees, J.; Kasif, S.; Raleigh, E. A.; Limbach, P. A.; Roberts, R. J. Nucleic Acids Res. 2010, 38, 6195-6205.

Arragain, S.; Garcia-Serres, R.; Blondin, G.; Douki, T.; Clemancey, M.; Latour, J. M.; Forouhar, F.; Neely, H.; Montelione, G. T.; Hunt, J. F.; Mulliez, E.; Fontecave, M.; Atta, M. J. Biol. Chem. 2010, 285, 5792-5801.

Arragain, S.; Handelman, S. K.; Forouhar, F.; Wei, F.-Y.; Tomizawa, K.; Hunt, J. F.; Douki, T.; Fontecave, M.; Mulliez, E.; Atta, M. J. Biol. Chem. 2010, 285, 28425-28433.

Ayala-Castro, C.; Saini, A.; Outten, F. W. Microbiol. Mol. Biol. Rev. 2008, 72, 110-125, table of contents.

Banerjee, R. Chem. Rev. 2003, 103, 2083-2094.

Becker, A.; Fritz-Wolf, K.; Kabsch, W.; Knappe, J.; Schultz, S.; Volker Wagner, A. F. Nature structural biology 1999, 6, 969-975.

Becker, A.; Kabsch, W. J. Biol. Chem. 2002, 277, 40036-40042.

Becker, B. F.; Gilles, S.; Sommerhoff, C. P.; Zahler, S. J. Biol. Chem. 2002, 383, 1821-1826.

Beinert, H. J. Biol. Inorg. Chem. 2000, 5, 2-15.

Beinert, H. Methods Enzymol. 1978, 54, 435-445.

Beinert, H.; Holm, R. H.; Munck, E. Science 1997, 277, 653-659.

Beller, H. R.; Spormann, A. M. FEMS Microbiol. Lett. 1999, 178, 147-153.

Benjdia, A.; Heil, K.; Barends, T. R.; Carell, T.; Schlichting, I. Nucleic Acids Res. 2012, 40, 9308-9318.

Benjdia, A.; Subramanian, S.; Leprince, J.; Vaudry, H.; Johnson, M. K.; Berteau, O. FEBS J. 2010, 277, 1906-1920.

Berkovitch, F.; Nicolet, Y.; Wan, J. T.; Jarrett, J. T.; Drennan, C. L. Science 2004, 303, 76-79.

Bharadwaj, V. S.; Dean, A. M.; Maupin, C. M. J. Am. Chem. Soc. 2013, 135, 12279-12288.

Bianchi, V.; Eliasson, R.; Fontecave, M.; Mulliez, E.; Hoover, D. M.; Matthews, R. G.; Reichard, P. Biochem. Biophys. Res. Commun. 1993, 197, 792-797.

Blaschkowski, H. P.; Neuer, G.; Ludwig-Festl, M.; Knappe, J. Eur. J. Biochem. 1982, 123, 563-569.

Boal, A. K.; Grove, T. L.; McLaughlin, M. I.; Yennawar, N. H.; Booker, S. J.; Rosenzweig, A. C. Science 2011, 332, 1089-1092.

Bondi, A. J. Phys. Chem. 1964, 68, 441-&.

Bonomi, F.; Iametti, S.; Morleo, A.; Ta, D.; Vickery, L. E. Biochemistry 2008, 47, 12795-12801.

Bradford, M. M. Anal. Biochem. 1976, 72, 248-254.

Broderick, J. B. Nature 2010, 465, 877-878.

Broderick, J. B.; Duderstadt, R. E.; Fernandez, D. C.; Wojtuszewski, K.; Henshaw, T. F.; Johnson, M. K. J. Am. Chem. Soc. 1997, 119, 7396-7397.

Broderick, J. B.; Duffus, B. R.; Duschene, K. S.; Shepard, E. M. Chem. Rev. 2014, 114, 4229-4317.

Broderick, J. B.; Henshaw, T. F.; Cheek, J.; Wojtuszewski, K.; Smith, S. R.; Trojan, M. R.; McGhan, R. M.; Kopf, A.; Kibbey, M.; Broderick, W. E. Biochem. Biophys. Res. Commun. 2000, 269, 451-456.

Brown, K. L. Chem. Rev. 2005, 105, 2075-2149.

Bruggemann, W.; Niklas, J. R. J. Magn. Reson., Ser. A 1994, 108, 25-29.

Brush, E. J.; Lipsett, K. A.; Kozarich, J. W. Biochemistry 1988, 27, 2217-2222.

Buckel, W.; Friedrich, P.; Golding, B. T. Angew. Chem. Int. Ed. Engl. 2012, 51, 9974-9976.

Buckel, W.; Kratky, C.; Golding, B. T. Chem.- Eur. J. 2006, 12, 352-362.

Cammack, R.; MacMillan, F. In Metals in Biology: Applications of High-Resolution EPR to Metalloenzymes; Hanson, G., Berliner, L., Eds.; Springer: New York, 2010; Vol. 29.

Canfield, J. M.; Warncke, K. J. Phys. Chem. B 2005, 109, 3053-3064.

Canfield, J. M.; Warncke, K. J. Phys. Chem. B 2002, 106, 8831-8841.

Chahal, H. K.; Dai, Y.; Saini, A.; Ayala-Castro, C.; Outten, F. W. Biochemistry 2009, 48, 10644-10653.

Chandra, T.; Silver, S. C.; Zilinskas, E.; Shepard, E. M.; Broderick, W. E.; Broderick, J. B. J. Am. Chem. Soc. 2009, 131, 2420-2421.

Chatterjee, A.; Li, Y.; Zhang, Y.; Grove, T. L.; Lee, M.; Krebs, C.; Booker, S. J.; Begley, T. P.; Ealick, S. E. Nat. Chem. Biol. 2008, 4, 758-765.

Chen, D.; Walsby, C.; Hoffman, B. M.; Frey, P. A. J. Am. Chem. Soc. 2003, 125, 11788-11789.

Cho, K. B.; Himo, F.; Gräslund, A.; Siegbahn, P. E. M. J. Phys. Chem. B 2001, 105, 6445-6452.

Cicchillo, R. M.; Lee, K. H.; Baleanu-Gogonea, C.; Nesbitt, N. M.; Krebs, C.; Booker, S. J. Biochemistry 2004, 43, 11770-11781.

Conradt, H.; Hohmann-Berger, M.; Hohmann, H. P.; Blaschkowski, H. P.; Knappe, J. Arch. Biochem. Biophys. 1984, 228, 133-142.

Covert, K. J.; Neithamer, D. R.; Zonnevylle, M. C.; Lapointe, R. E.; Schaller, C. P.; Wolczanski, P. T. Inorg. Chem. 1991, 30, 2494-2508.

Craciun, S.; Balskus, E. P. Proc. Natl. Acad. Sci. USA 2012, 109, 21307-21312.

Crain, A. V.; Broderick, J. B. Biochim. Biophys. Acta. 2013, 1834, 2512-2519.

Cutsail, G. E., 3rd; Telser, J.; Hoffman, B. M. Biochim. Biophys. Acta 2015, 1853, 1370-1394.

Davoust, C. E.; Doan, P. E.; Hoffman, B. M. J. Magn. Reson. 1996, A119, 38-44.

Davydov, R.; Kofman, V.; Fujii, H.; Yoshida, T.; Ikeda-Saito, M.; Hoffman, B. M. J. Am. Chem. Soc. 2002, 124, 1798-1808.

Demick, J. M.; Lanzilotta, W. N. Biochemistry 2011, 50, 440-442.

Dey, A.; Peng, Y.; Broderick, W. E.; Hedman, B.; Hodgson, K. O.; Broderick, J. B.; Solomon, E. I. J. Am. Chem. Soc. 2011, 133, 18656-18662.

Di Cera, E. J. Biol. Chem. 2006, 281, 1305-1308.

Doan, P. E. J. Magn. Reson. 2011, 208, 76-86.

Doan, P. E.; Hoffman, B. M. Chem. Phys. Lett. 1997, 269, 208-214.

Doan, P. E.; Lees, N. S.; Shanmugam, M.; Hoffman, B. M. Appl. Magn. Reson. 2010, 37, 763-779.

Dowling, D. P.; Bruender, N. A.; Young, A. P.; McCarty, R. M.; Bandarian, V.; Drennan, C. L. Nat. Chem. Biol. 2014, 10, 106-112.

Dowling, D. P.; Vey, J. L.; Croft, A. K.; Drennan, C. L. Biochim. Biophys. Acta, Proteins Proteomics 2012, 1824, 1178-1195.

Driesener, R. C.; Challand, M. R.; McGlynn, S. E.; Shepard, E. M.; Boyd, E. S.; Broderick, J. B.; Peters, J. W.; Roach, P. L. Angew. Chem. Int. Ed. Engl. 2010, 49, 1687-1690.

Duffus, B. R.; Hamilton, T. L.; Shepard, E. M.; Boyd, E. S.; Peters, J. W.; Broderick, J. B. Biochim. Biophys. Acta 2012.

Duschene, K. S.; Broderick, J. B. FEBS Lett. 2010, 584, 1263-1267.

Duschene, K. S.; Broderick, J. B. BioMol. Concepts 2012, 3, 255-266.

Duschene, K. S.; Veneziano, S. E.; Silver, S. C.; Broderick, J. B. Curr. Opin. Chem. Biol. 2009, 13, 74-83.

Eaton, G. R.; Eaton, S. S.; Barr, D. P.; Weber, R. T. Quantitative EPR; Springer Vienna, 2010.

Eck, R. V.; Dayhoff, M. O. Science 1966, 152, 363-366.

Eklund, H.; Fontecave, M. Structure 1999, 7, R257-262.

Epstein, W.; Schultz, S. G. J. Gen. Physiol. 1965, 49, 221-234.

Evans, H. J.; Wildes, R. A. In Potassium in Biochemistry and Physiology; International Potash Institute: Berne, Switzerland, 1971.

Feliks, M.; Martins, B. M.; Ullmann, G. M. J. Am. Chem. Soc. 2013, 135, 14574-14585.

Feliks, M.; Ullmann, G. M. The journal of physical chemistry. B 2012, 116, 7076-7087.

Finke, R. G.; Hay, B. P. Inorg. Chem. 1984, 23, 3041-3043.

Fish, W. W. Methods Enzymol. 1988, 158, 357-364.

Flaherty, K. M.; DeLuca-Flaherty, C.; McKay, D. B. Nature 1990, 346, 623-628.

Fluhe, L.; Knappe, T. A.; Gattner, M. J.; Schafer, A.; Burghaus, O.; Linne, U.; Marahiel, M. A. Nat. Chem. Biol. 2012, 8, 350-357.

Foner, S. N.; Cochran, E. L.; Bowers, V. A.; Jen, C. K. J. Chem. Phys. 1960, 32, 963-971.

Fontecave, M.; Mulliez, E.; Logan, D. T. Progress in nucleic acid research and molecular biology 2002, 72, 95-127.

Fontecave, M.; Ollagnier-de-Choudens, S. Arch. Biochem. Biophys. 2008, 474, 226-237.

Frazzon, J.; Dean, D. R. Curr. Opin. Chem. Biol. 2003, 7, 166-173.

Frey, M.; Rothe, M.; Wagner, A. F.; Knappe, J. J. Biol. Chem. 1994, 269, 12432-12437.

Frey, P. A. Comprehensive Natural Products II Chemistry and Biology Amsterdam, 2010; Vol. 7.

Frey, P. A. FASEB J. 1993, 7, 662-670.

Frey, P. A. Acc. Chem. Res. 2014, 47, 540-549.

Frey, P. A.; Hegeman, A. D.; Ruzicka, F. J. Crit. Rev. Biochem. Mol. Biol. 2008, 43, 63-88.

Frey, P. A.; Magnusson, O. T. Chem. Rev. 2003, 103, 2129-2148.

Fugate, C. J.; Jarrett, J. T. Biochim. Biophys. Acta. 2012, 1824, 1213-1222.

Fugate, C. J.; Stich, T. A.; Kim, E. G.; Myers, W. K.; Britt, R. D.; Jarrett, J. T. J. Am. Chem. Soc. 2012.

Goldman, P. J.; Grove, T. L.; Booker, S. J.; Drennan, C. L. Proc. Natl. Acad. Sci. USA 2013, 110, 15949-15954.

Goldman, P. J.; Grove, T. L.; Sites, L. A.; McLaughlin, M. I.; Booker, S. J.; Drennan, C. L. Proc. Natl. Acad. Sci. USA 2013, 110, 8519-8524.

Goto-Ito, S.; Ishii, R.; Ito, T.; Shibata, R.; Fusatomi, E.; Sekine, S. I.; Bessho, Y.; Yokoyama, S. Acta crystallographica. Section D, Biological crystallography 2007, 63, 1059-1068.

Grove, T. L.; Ahlum, J. H.; Sharma, P.; Krebs, C.; Booker, S. J. Biochemistry 2010, 49, 3783-3785.

Grove, T. L.; Benner, J. S.; Radle, M. I.; Ahlum, J. H.; Landgraf, B. J.; Krebs, C.; Booker, S. J. Science 2011, 332, 604-607.

Grove, T. L.; Lee, K. H.; St Clair, J.; Krebs, C.; Booker, S. J. Biochemistry 2008, 47, 7523-7538.

Grove, T. L.; Radle, M. I.; Krebs, C.; Booker, S. J. J. Am. Chem. Soc. 2011, 133, 19586-19589.

Gruber, K.; Reitzer, R.; Kratky, C. Angew. Chem., Int. Ed. Engl. 2001, 40, 3377-3380.

Haldar, S.; Paul, S.; Joshi, N.; Dasgupta, A.; Chattopadhyay, K. PLoS One 2012, 7, e31797.

Hales, B. J. In Applications of Physical Methods to Inorganic and Bioinorganic Chemistry; Scott, R. A., Lukehart, C. M., Eds.; John Wiley and Sons, Ltd.: England, 2007, p 40-53.

Halpern, J.; Kim, S. H.; Leung, T. W. J. Am. Chem. Soc. 1984, 106, 8317-8319.

Hammes-Schiffer, S. Acc. Chem. Res. 2001, 34, 273-281.

Hanzelmann, P.; Schindelin, H. Proc. Natl. Acad. Sci. USA 2006, 103, 6829-6834.

Hanzelmann, P.; Schindelin, H. Proc. Natl. Acad. Sci. USA 2004, 101, 12870-12875.

Harding, M. M. Acta Crystallogr. D Biol. Crystallogr. 2002, 58, 872-874.

Hatcher, E.; Soudackov, A. V.; Hammes-Schiffer, S. J. Am. Chem. Soc. 2004, 126, 5763-5775.

Heider, J. Curr. Opin. Chem. Bio. 2007, 11, 188-194.

Heil, K.; Kneuttinger, A. C.; Schneider, S.; Lischke, U.; Carell, T. Chem. Eur. J. 2011, 17, 9651-9657.

Henshaw, T. F.; Cheek, J.; Broderick, J. B. J. Am. Chem. Soc. 2000, 122, 8331-8332.

Hilberg, M.; Pierik, A. J.; Bill, E.; Friedrich, T.; Lippert, M. L.; Heider, J. J. Biol. Inorg. Chem. 2012, 17, 49-56.

Hinckley, G. T.; Frey, P. A. Biochemistry 2006, 45, 3219-3225.

Hioe, J.; Zipse, H. Faraday Discuss. 2010, 145, 301-313.

Hoffman, B. M. Acc. Chem. Res. 1991, 24, 164-170.

Hoffman, B. M. Proc. Natl. Acad. Sci. USA 2003, 100, 3575-3578.

Hoffman, B. M. Acc. Chem. Res. 2003, 36, 522-529.

Horitani, M.; Byer, A. S.; Shisler, K. A.; Chandra, T.; Broderick, J. B.; Hoffman, B. M. J. Am. Chem. Soc. 2015, 137, 7111-7121.

Huang, W.; Xu, H. H.; Li, Y.; Zhang, F.; Chen, X.-Y.; He, Q.-L.; Igarashi, Y.; Tang, G.-L. J. Am. Chem. Soc. 2012, 134, 8831-8840.

Huber, C.; Wachtershauser, G. Science 1998, 281, 670-672.

Ifuku, O.; Koga, N.; Haze, S.; Kishimoto, J.; Wachi, Y. Eur. J. Biochem. 1994, 224, 173-178.

Jiang, D.; Guo, H.; Xu, C.; Chang, J.; Gu, B.; Wang, L.; Block, T. M.; Guo, J. T. J. Virol. 2008, 82, 1665-1678.

Johnson, D. C.; Dean, D. R.; Smith, A. D.; Johnson, M. K. Annu. Rev. Biochem. 2005, 74, 247-281.

Jordan, A.; Reichard, P. Annu. Rev. Biochem. 1998, 67, 71-98.

Kachmar, J. F.; Boyer, P. D. J. Biol. Chem. 1953, 200, 669-682.

Kampmeier, J. A. Biochemistry 2010, 49, 10770-10772.

Kappl, R.; Bracic, G.; Huttermann, J. In High Resolution EPR: Applications to Metalloenzymes and Metals in Medicine; Hanson, G., Berliner, L., Eds.; Springer: New York, 2009; Vol. 28, p 63-103.

Khoroshun, D. V.; Warncke, K.; Ke, S. C.; Musaev, D. G.; Morokuma, K. J. Am. Chem. Soc. 2003, 125, 570-579.

Kieslich, W.; Kurreck, H. J. Am. Chem. Soc. 1984, 106, 4328-4335.

Kiley, P. J.; Beinert, H. Curr. Opin. Microbiol. 2003, 6, 181-185.

Kim, S. H.; Perera, R.; Hager, L. P.; Dawson, J. H.; Hoffman, B. M. J. Am. Chem. Soc. 2006, 128, 5598-5599.

Kim, S. J.; Lester, C.; Begley, T. P. J. Org. Chem. 1995, 60, 6256-6257.

Kirste, B. J. Magn. Reson. 1969 1985, 62, 242-259.

Knappe, J.; Blaschkowski, H. P.; Edenharder, R. Enzyme-dependent activation of pyruvate formate-lyase of Escherichia coli; Springer: Berlin Heidelberg New York, 1972.

Knappe, J.; Elbert, S.; Frey, M.; Wagner, A. F. Biochemical Society transactions 1993, 21 (Pt 3), 731-734.

Knappe, J.; Neugebauer, F. A.; Blaschkowski, H. P.; Ganzler, M. Proc. Natl. Acad. Sci. USA 1984, 81, 1332-1335.

Knappe, J.; Sawers, G. FEMS Microbiol. Rev. 1990, 75, 383-398.

Knappe, J.; Schacht, J.; Mockel, W.; Hopner, T.; Vetter, H., Jr.; Edenharder, R. Eur. J. Biochem. 1969, 11, 316-327.

Knappe, J.; Schmitt, T. Biochem. Biophys. Res. Commun. 1976, 71, 1110-1117.

Kolberg, M.; Strand, K. R.; Graff, P.; Andersson, K. K. Biochim. Biophys. Acta. 2004, 1699, 1-34.

Krebs, C.; Broderick, W. E.; Henshaw, T. F.; Broderick, J. B.; Huynh, B. J. Am. Chem. Soc. 2002, 124, 912-913.

Krebs, C.; Henshaw, T. F.; Cheek, J.; Huynh, B.; Broderick, J. B. J. Am. Chem. Soc. 2000, 122, 12497-12506.

Krieger, C. J.; Roseboom, W.; Albracht, S. P.; Spormann, A. M. J. Biol. Chem. 2001, 276, 12924-12927.

Kuchenreuther, J. M.; George, S. J.; Grady-Smith, C. S.; Cramer, S. P.; Swartz, J. R. PLoS One 2011, 6, e20346.

Kulik, L.; Lubitz, W. Photosynth. Res. 2009, 102, 391-401.

Kulzer, R.; Pils, T.; Kappl, R.; Huttermann, J.; Knappe, J. J. Biol. Chem. 1998, 273, 4897-4903.

Kung, F. C.; Raymond, J.; Glaser, D. A. J. Bacteriol. 1976, 126, 1089-1095.

Lanz, N. D.; Booker, S. J. Biochim. Biophys. Acta 2012, 1824, 1196-1212.

Larsen, T. M.; Benning, M. M.; Rayment, I.; Reed, G. H. Biochemistry 1998, 37, 6247-6255.

Larsson, K. M.; Andersson, J.; Sjoberg, B. M.; Nordlund, P.; Logan, D. T. Structure 2001, 9, 739-750.

Layer, G.; Moser, J.; Heinz, D. W.; Jahn, D.; Schubert, W. D. EMBO J. 2003, 22, 6214-6224.

Lee, K. H.; Saleh, L.; Anton, B. P.; Madinger, C. L.; Benner, J. S.; Iwig, D. F.; Roberts, R. J.; Krebs, C.; Booker, S. J. Biochemistry 2009, 48, 10162-10174.

Lees, N. S.; Chen, D.; Walsby, C. J.; Behshad, E.; Frey, P. A.; Hoffman, B. M. J. Am. Chem. Soc. 2006, 128, 10145-10154.

Lees, N. S.; Hanzelmann, P.; Hernandez, H. L.; Subramanian, S.; Schindelin, H.; Johnson, M. K.; Hoffman, B. M. J. Am. Chem. Soc. 2009, 131, 9184-9185.

Lepore, B. W.; Ruzicka, F. J.; Frey, P. A.; Ringe, D. Proc. Natl. Acad. Sci. USA 2005, 102, 13819-13824.

Leuthner, B.; Leutwein, C.; Schulz, H.; Horth, P.; Haehnel, W.; Schiltz, E.; Schagger, H.; Heider, J. Mol. Microbiol. 1998, 28, 615-628.

Li, L.; Patterson, D. P.; Fox, C. C.; Lin, B.; Coschigano, P. W.; Marsh, E. N. Biochemistry 2009, 48, 1284-1292.

Lin, Y.; Gerfen, G. J.; Rousseau, D. L.; Yeh, S.-R. Analytical Chemistry 2003, 75, 5381-5386.

LoBrutto, R.; Bandarian, V.; Magnusson, O. T.; Chen, X.; Schramm, V. L.; Reed, G. H. Biochemistry 2001, 40, 9-14.

LoBrutto, R.; Bandarian, V.; Magnusson, O. T.; Chen, X.; Schramm, V. L.; Reed, G. H. Biochemistry 2001, 40, 9-14.

Logan, D. T.; Andersson, J.; Sjoberg, B. M.; Nordlund, P. Science 1999, 283, 1499-1504.

Logan, D. T.; Mulliez, E.; Larsson, K. M.; Bodevin, S.; Atta, M.; Garnaud, P. E.; Sjoberg, B. M.; Fontecave, M. Proc. Natl. Acad. Sci. USA 2003, 100, 3826-3831.

Lucken, E. A. C. Nuclear Quadrupole Coupling Constants; Academic Press: New York, 1969.

Lund, A.; Shiotani, M.; Shimada, S. Principles and Applications of ESR Spectroscopy; Springer: New York, 2011.

Lusk, J. E.; Williams, R. J. P.; Kennedy, E. P. J. Biol. Chem. 1968, 243, 2618-2624.

Luttringer, F.; Mulliez, E.; Dublet, B.; Lemaire, D.; Fontecave, M. J. Biol. Inorg. Chem. 2009, 14, 923-933.

Magnusson, O. T.; Reed, G. H.; Frey, P. A. Biochemistry 2001, 40, 7773-7782.

Magnusson, O. T.; Reed, G. H.; Frey, P. A. J. Am. Chem. Soc. 1999, 121, 9764-9765.

Maity, A. N.; Hsieh, C.-P.; Huang, M.-H.; Chen, Y.-H.; Tang, K.-H.; Behshad, E.; Frey, P. A.; Ke, S.-C. J. Phys. Chem. B 2009, 113, 12161-12163.

Markham, G. D.; Leyh, T. S. J. Am. Chem. Soc. 1987, 109, 599-600.

Marsh, E. N.; Melendez, G. D. Biochim. Biophys. Acta, Proteins Proteomics 2012, 1824, 1154-1164.

Martins, B. M.; Blaser, M.; Feliks, M.; Ullmann, G. M.; Buckel, W.; Selmer, T. J. Am. Chem. Soc. 2011, 133, 14666-14674.

Mathews, I. I.; Erion, M. D.; Ealick, S. E. Biochemistry 1998, 37, 15607-15620.

McCarty, R. M.; Krebs, C.; Bandarian, V. Biochemistry 2013, 52, 188-198.

Mcconnell, H. M.; Strathdee, J. Mol. Phys. 1959, 2, 129-138.

McGlynn, S. E.; Boyd, E. S.; Shepard, E. M.; Lange, R. K.; Gerlach, R.; Broderick, J. B.; Peters, J. W. J. Bacteriol. 2010, 192, 595-598.

Meyer, J. J. Biol. Inorg. Chem. 2008, 13, 157-170.

Miller, D. J.; Ouellette, N.; Evdokimova, E.; Savchenko, A.; Edwards, A.; Anderson, W. F. Protein Sci. 2003, 12, 1432-1442.

Morton, J. R.; Preston, K. F.; Strach, S. J.; Adrian, F. J.; Jette, A. N. J. Chem. Phys. 1979, 70, 2889-2893.

Mulder, D. W.; Boyd, E. S.; Sarma, R.; Lange, R. K.; Endrizzi, J. A.; Broderick, J. B.; Peters, J. W. Nature 2010, 465, 248-251.

Mulder, D. W.; Ortillo, D. O.; Gardenghi, D. J.; Naumov, A. V.; Ruebush, S. S.; Szilagyi, R. K.; Huynh, B.; Broderick, J. B.; Peters, J. W. Biochemistry 2009, 48, 6240-6248.

Mulder, D. W.; Shepard, E. M.; Meuser, J. E.; Joshi, N.; King, P. W.; Posewitz, M. C.; Broderick, J. B.; Peters, J. W. Structure 2011, 19, 1038-1052.

Murphy, D. M.; Farley, R. D. Chem. Soc. Rev. 2006, 35, 249-268.

Muthukumaran, R. B.; Grzyska, P. K.; Hausinger, R. P.; McCracken, J. Biochemistry 2007, 46, 5951-5959.

Neithamer, D. R.; Parkanyi, L.; Mitchell, J. F.; Wolczanski, P. T. J. Am. Chem. Soc. 1988, 110, 4421-4423.

Nicolet, Y.; Amara, P.; Mouesca, J. M.; Fontecilla-Camps, J. C. Proc. Natl. Acad. Sci. USA 2009, 106, 14867-14871.

Nicolet, Y.; Drennan, C. L. Nucleic Acids Res. 2004, 32, 4015-4025.

Nicolet, Y.; Martin, L.; Tron, C.; Fontecilla-Camps, J. C. FEBS Lett. 2010, 584, 4197-4202.

Nicolet, Y.; Rubach, J. K.; Posewitz, M. C.; Amara, P.; Mathevon, C.; Atta, M.; Fontecave, M.; Fontecilla-Camps, J. C. J. Biol. Chem. 2008, 283, 18861-18872.

Nicolet, Y.; Zeppieri, L.; Amara, P.; Fontecilla-Camps, J. C. Angew. Chem. 2014, 126, 12034-12038.

Nnyepi, M. R.; Peng, Y.; Broderick, J. B. Arch. Biochem. Biophys. 2007, 459, 1-9.

O'Brien, J. R.; Raynaud, C.; Croux, C.; Girbal, L.; Soucaille, P.; Lanzilotta, W. N. Biochemistry 2004, 43, 4635-4645.

Ollagnier, S.; Mulliez, E.; Gaillard, J.; Eliasson, R.; Fontecave, M.; Reichard, P. J. Biol. Chem. 1996, 271, 9410-9416.

Page, M. J.; Di Cera, E. Physiol. Rev. 2006, 86, 1049-1092.

Pandelia, M. E.; Lanz, N. D.; Booker, S. J.; Krebs, C. Biochim. Biophys. Acta 2015, 1853, 1395-1405.

Parast, C. V.; Wong, K. K.; Lewisch, S. A.; Kozarich, J. W.; Peisach, J.; Magliozzo, R. S. Biochemistry 1995, 34, 2393-2399.

Park, J.; Tai, J.; Roessner, C. A.; Scott, A. I. Bioorg. Med. Chem. 1996, 4, 2179-2185.

Peng, Y.; Veneziano, S. E.; Gillispie, G. D.; Broderick, J. B. J. Biol. Chem. 2010, 285, 27224-27231.

Peters, J. W.; Broderick, J. B. Annu. Rev. Biochem. 2012, 81, 429-450.

Peters, J. W.; Lanzilotta, W. N.; Lemon, B. J.; Seefeldt, L. C. Science 1998, 282, 1853-1858.

Petrovich, R. M.; Ruzicka, F. J.; Reed, G. H.; Frey, P. A. Biochemistry 1992, 31, 10774-10781.

Pierre, S.; Guillot, A.; Benjdia, A.; Sandstrom, C.; Langella, P.; Berteau, O. Nat. Chem. Biol. 2012, 8, 957-959.

Pierrel, F.; Douki, T.; Fontecave, M.; Atta, M. J. Biol. Chem. 2004, 279, 47555-47563.

Plaga, W.; Frank, R.; Knappe, J. Eur. J. Biochem. 1988, 178, 445-450.

Plaga, W.; Vielhaber, G.; Wallach, J.; Knappe, J. FEBS Lett. 2000, 466, 45-48.

PyMOL Molecular Graphics System 1.7.4. Schrodinger, LLC.

Que, L. J. Physical Methods in Bioinorganic Chemistry : Spectroscopy and Magnetism; University Science Books: Sausalito, CA, 2000.

Rana, S.; Pozzi, N.; Pelc, L. A.; Di Cera, E. Proc. Natl. Acad. Sci. USA 2011, 108, 5221-5225.

Raynaud, C.; Sarçabal, P.; Meynial-Salles, I.; Croux, C.; Soucaille, P. Proc. Natl. Acad. Sci. USA 2003, 100, 5010-5015.

Rödel, W.; Plaga, W.; Frank, R.; Knappe, J. Eur. J. Biochem. 1988, 177, 153-158.

Roth, J. R.; Lawrence, J. G.; Bobik, T. A. Annu. Rev. Microbiol. 1996, 50, 137-181.

Rubach, J. K.; Brazzolotto, X.; Gaillard, J.; Fontecave, M. FEBS Lett. 2005, 579, 5055-5060.

Rupp, H.; Rao, K. K.; Hall, D. O.; Cammack, R. Biochim. Biophys. Acta 1978, 537, 255-269.

Selmer, T.; Andrei, P. I. Eur. J. Biochem. 2001, 268, 1363-1372.

Selmer, T.; Pierik, A. J.; Heider, J. Biol. Chem. 2005, 386, 981-988.

Selvaraj, B.; Pierik, A. J.; Bill, E.; Martins, B. M. J. Bio. Inorg. Chem. 2013, 1-11.

Shao, X.; Grishin, N. V. Nucleic Acids Res. 2000, 28, 2643-2650.

Shaveta, G.; Shi, J. H.; Chow, V. T. K.; Song, J. X. Biochem. Biophys. Res. Commun. 2010, 391, 1390-1395.

Shelburne, C. E.; An, F. Y.; Dholpe, V.; Ramamoorthy, A.; Lopatin, D. E.; Lantz, M. S. J. Antimicrob. Chemother. 2007, 59, 297-300.

Shepard, E. M.; Boyd, E. S.; Broderick, J. B.; Peters, J. W. Curr. Opin. Chem. Biol. 2011, 15, 319-327.

Shepard, E. M.; Broderick, J. B. In Comprehensive Natural Products II Chemistry and Biology; Editors-in-Chief: Lew, M., Hung-Wen, L., Eds.; Elsevier: Oxford, 2010, p 625-661.

Shepard, E. M.; Broderick, J. B. In Comprehensive Natural Products Chemistry; Elsevier: 2009.

Shepard, E. M.; Duffus, B. R.; George, S. J.; McGlynn, S. E.; Challand, M. R.; Swanson, K. D.; Roach, P. L.; Cramer, S. P.; Peters, J. W.; Broderick, J. B. J. Am. Chem. Soc. 2010, 132, 9247-9249.

Shepard, E. M.; McGlynn, S. E.; Bueling, A. L.; Grady-Smith, C. S.; George, S. J.; Winslow, M. A.; Cramer, S. P.; Peters, J. W.; Broderick, J. B. Proc. Natl. Acad. Sci. USA 2010, 107, 10448-10453.

Shibata, N.; Masuda, J.; Tobimatsu, T.; Toraya, T.; Suto, K.; Morimoto, Y.; Yasuoka, N. Structure 1999, 7, 997-1008.

Shibata, N.; Tamagaki, H.; Hieda, N.; Akita, K.; Komori, H.; Shomura, Y.; Terawaki, S.; Mori, K.; Yasuoka, N.; Higuchi, Y.; Toraya, T. J. Biol. Chem. 2010, 285, 26484-26493.

Shisler, K. A.; Broderick, J. B. Curr. Opin. Struct. Biol. 2012, 22, 701-710.

Shisler, K. A.; Broderick, J. B. Arch. Biochem. Biophys. 2014, 546, 64-71.

Sofia, H. J.; Chen, G.; Hetzler, B. G.; Reyes-Spindola, J. F.; Miller, N. E. Nucleic Acids Res. 2001, 29, 1097-1106.

Span, I.; Wang, K.; Eisenreich, W.; Bacher, A.; Zhang, Y.; Oldfield, E.; Groll, M. J. Am. Chem. Soc. 2014, 136, 7926-7932.

Stich, T. A.; Myers, W. K.; Britt, R. D. Acc. Chem. Res. 2014, 47, 2235-2243.

Stoll, S.; Schweiger, A. J. Magn. Reson. 2006, 178, 42-55.

Stubbe, J.; Ge, J.; Yee, C. S. Trends in biochemical sciences 2001, 26, 93-99.

Swanson, K. D.; Duffus, B. R.; Beard, T. E.; Peters, J. W.; Broderick, J. B. Eur. J. Inorg. Chem. 2011, 935-947.

Sweeney, W. V.; Rabinowitz, J. C. Annu. Rev. Biochem. 1980, 49, 139-161.

Tan, L.; Chi-lung, Y. Int. Geol. Rev. 1970, 12, 778-786.

Taylor, A. M.; Stoll, S.; Britt, R. D.; Jarrett, J. T. Biochemistry 2011, 50, 7953-7963.

Telser, J. In Applications of Physical Methods to Inorganic and Bioinorganic Chemistry; Scott, R. A., Lukehart, C. M., Eds.; John Wiley and Sons, Ltd.: England, 2007, p 99-124.

Thibodeaux, C. J.; van der Donk, W. A. Proc. Natl. Acad. Sci. USA 2012, 109, 21184-21185.

Toraya, T. Chem. Rev. 2003, 103, 2095-2127.

Toraya, T.; Sugimoto, Y.; Tamao, Y.; Shimizu, S.; Fukui, S. Biochemistry 1971, 10, 3475-3484.

Trott, O.; Olson, A. J. J Comput Chem 2010, 31, 455-461.

Van Doorslaer, S.; Vinck, E. Phys. Chem. Chem. Phys. 2007, 9, 4620-4638.

Vey, J. L.; Drennan, C. L. Chem. Rev. 2011, 111, 2487-2506.

Vey, J. L.; Yang, J.; Li, M.; Broderick, W. E.; Broderick, J. B.; Drennan, C. L. Proc. Natl. Acad. Sci. USA 2008, 105, 16137-16141.

Wagner, A. F.; Frey, M.; Neugebauer, F. A.; Schafer, W.; Knappe, J. Proc. Natl. Acad. Sci. USA 1992, 89, 996-1000.

Wagner, A. F.; Schultz, S.; Bomke, J.; Pils, T.; Lehmann, W. D.; Knappe, J. Biochem. Biophys. Res Commun. 2001, 285, 456-462.

Walsby, C. J.; Hong, W.; Broderick, W. E.; Cheek, J.; Ortillo, D.; Broderick, J. B.; Hoffman, B. M. J. Am. Chem. Soc. 2002, 124, 3143-3151.

Walsby, C. J.; Ortillo, D.; Broderick, W. E.; Broderick, J. B.; Hoffman, B. M. J. Am. Chem. Soc. 2002, 124, 11270-11271.

Walsby, C. J.; Ortillo, D.; Yang, J.; Nnyepi, M. R.; Broderick, W. E.; Hoffman, B. M.; Broderick, J. B. Inorg. Chem. 2005, 44, 727-741.

Walters, E. M.; Garcia-Serres, R.; Jameson, G. N.; Glauser, D. A.; Bourquin, F.; Manieri, W.; Schurmann, P.; Johnson, M. K.; Huynh, B. H. J. Am. Chem. Soc. 2005, 127, 9612-9624.

Wang, S. C.; Frey, P. A. Biochemistry 2007, 46, 12889-12895.

Wang, W.; Li, J.; Wang, K.; Huang, C.; Zhang, Y.; Oldfield, E. Proc. Natl. Acad. Sci. USA 2010, 107, 11189-11193.

Wang, W.; Wang, K.; Li, J.; Nellutla, S.; Smirnova, T. I.; Oldfield, E. J. Am. Chem. Soc. 2011, 133, 8400-8403.

Wang, X.; Hinson, E. R.; Cresswell, P. Cell host & microbe 2007, 2, 96-105.

Warncke, K. Biochemistry 2005, 44, 3184-3193.

Warncke, K.; Canfield, J. M. J. Am. Chem. Soc. 2004, 126, 5930-5931.

Warncke, K.; Utada, A. S. J. Am. Chem. Soc. 2001, 123, 8564-8572.

Wecksler, S. R.; Stoll, S.; Tran, H.; Magnusson, O. T.; Wu, S. P.; King, D.; Britt, R. D.; Klinman, J. P. Biochemistry 2009, 48, 10151-10161.

Wei, F.-Y.; Suzuki, T.; Watanabe, S.; Kimura, S.; Kaitsuka, T.; Fujimura, A.; Matsui, H.; Atta, M.; Michiue, H.; Fontecave, M.; Yamagata, K.; Suzuki, T.; Tomizawa, K. J. Clin. Invest. 2011, 121, 3598-3608.

Weil, J. A.; Bolton, J. R. Electron Paramagnetic Resonance: Elementary Theory and Practical Applications; 2 ed.; Wiley-Interscience, 2007.

Welander, P. V.; Coleman, M. L.; Sessions, A. L.; Summons, R. E.; Newman, D. K. Proc. Natl. Acad. Sci. USA 2010, 107, 8537-8542.

Werst, M. M.; Davoust, C. E.; Hoffman, B. M. J. Am. Chem. Soc. 1991, 113, 1533-1538.

Werst, M. M.; Kennedy, M. C.; Beinert, H.; Hoffman, B. M. Biochemistry 1990, 29, 10526-10532.

Wiig, J. A.; Hu, Y. L.; Lee, C. C.; Ribbe, M. W. Science 2012, 337, 1672-1675.

Wilbanks, S. M.; McKay, D. B. J. Biol. Chem. 1995, 270, 2251-2257.

Willems, J. P.; Lee, H. I.; Burdi, D.; Doan, P. E.; Stubbe, J.; Hoffman, B. M. J. Am. Chem. Soc. 1997, 119, 9816-9824.

Wilson, R. H.; Evans, H. J. In The Role of Potassium in Agriculture; Kilmer, V. J., Younts, S. E., Brady, N. C., Eds.; ASA, CSSA, SSSA: Madison, WI, 1968, p 189-202.

Wong, K. K.; Murray, B. W.; Lewisch, S. A.; Baxter, M. K.; Ridky, T. W.; Ulissi-DeMario, L.; Kozarich, J. W. Biochemistry 1993, 32, 14102-14110.

Xu, W. Y.; Lees, N. S.; Hall, D.; Welideniya, D.; Hoffman, B. M.; Duin, E. C. Biochemistry 2012, 51, 4835-4849.

Yan, F.; Fujimori, D. G. Proc. Natl. Acad. Sci. USA 2011, 108, 3930-3934.

Yan, F.; LaMarre, J. M.; Rohrich, R.; Wiesner, J.; Jomaa, H.; Mankin, A. S.; Fujimori, D. G. J. Am. Chem. Soc. 2010, 132, 3953-3964.

Yang, J.; Naik, S. G.; Ortillo, D. O.; Garcia-Serres, R.; Li, M.; Broderick, W. E.; Huynh, B. H.; Broderick, J. B. Biochemistry 2009, 48, 9234-9241.

Yu, L.; Blaser, M.; Andrei, P. I.; Pierik, A. J.; Selmer, T. Biochemistry 2006, 45, 9584-9592.

Yu, Y.; Duan, L. A.; Zhang, Q.; Liao, R.; Ding, Y.; Pan, H.; Wendt-Pienkowski, E.; Tang, G.-L.; Shen, B.; Liu, W. ACS Chem. Biol. 2009, 4, 855-864.

Zhang, Q.; Chen, D. D.; Lin, J.; Liao, R.; Tong, W.; Xu, Z.; Liu, W. J. Biol. Chem. 2011, 286, 21287-21294.

Zhang, Q.; Li, Y.; Chen, D. D.; Yu, Y.; Duan, L.; Shen, B.; Liu, W. Nat. Chem. Biol. 2011, 7, 154-160.

Zhang, Q.; Yu, Y. Chembiochem: a European journal of chemical biology 2012, 13, 1097-1099.

Zhang, Y.; Dougherty, M.; Downs, D. M.; Ealick, S. E. Structure 2004, 12, 1809-1821.

Zhang, Y.; Zhu, X.; Torelli, A. T.; Lee, M.; Dzikovski, B.; Koralewski, R. M.; Wang, E.; Freed, J.; Krebs, C.; Ealick, S. E.; Lin, H. Nature 2010, 465, 891-896.

Zheng, H.; Chruszcz, M.; Lasota, P.; Lebioda, L.; Minor, W. J. Inorg. Biochem. 2008, 102, 1765-1776.

Zhu, C.; Warncke, K. J. Am. Chem. Soc. 2010, 132, 9610-9615.